

**SoLID (Solenoidal Large Intensity Device)**  
**Updated Preliminary Conceptual Design Report**

The SoLID Collaboration

June 26, 2017

# Contents

<b>1</b>	<b>Executive Summary of the Responses to Recommendations from the Jefferson Lab Director's Review Committee</b>	<b>1</b>
1.1	Overview	1
1.2	Physics Program	2
1.2.1	SIDIS Production of Charged Pions	2
1.2.2	PVDIS	3
1.2.3	$J/\psi$ Production	4
1.3	Possible Expansions in the Physics Reach of SoLID	4
1.3.1	Generalized Parton Distributions (GPD)	4
1.3.2	SIDIS Production of Charged Kaons	5
1.4	Experimental Design, Simulation and Feasibility	5
1.4.1	Solenoidal Magnet	5
1.4.2	Acceptance, Efficiency and Systematics	6
1.4.3	Rates and Data Acquisition	8
1.5	Summary	8
<b>2</b>	<b>Introduction and Overview of SoLID Experimental Programs</b>	<b>9</b>
2.1	SoLID Project Introduction/Overview	9
2.1.1	Base Equipment Description	9
2.1.2	Dependencies to Base Equipment	9
2.1.3	Experiment-specific Dependencies	10
2.1.4	Research Program	10
2.2	SIDIS Program	11
2.2.1	Introduction	11
2.2.2	Transverse Structure and Semi-Inclusive Deep Inelastic Scattering	13
2.2.3	The Phenomenology TSSAs and TMDs	15
2.2.4	Overview of SIDIS program	16
2.2.5	Beam Time and Projections	17
2.2.6	Comparisons with SBS and CLAS12 SIDIS programs	19
2.3	PVDIS Program	26
2.3.1	Motivation for PVDIS	26
2.3.2	Review of the Theory	26
2.3.3	Charge Symmetry Violation	28
2.3.4	Higher Twist	30
2.3.5	Data Sample and analysis	31
2.3.6	Beam Time and Projections	32
2.4	$J/\psi$ Program	34
2.4.1	Motivation	34
2.4.2	Program Overview	38
2.4.3	Beam Time and Projection	39
2.5	Possible Expansion in Physics Reach	41
2.5.1	GPD Program	41
2.5.2	SIDIS Production of Charged Kaons	42



<b>3</b>	<b>Technical Requirements and Experimental Setup</b>	<b>44</b>
3.1	Summary of Requirements . . . . .	44
3.2	SIDIS- <sup>3</sup> He Experiments . . . . .	49
3.3	SIDIS-proton Experiment . . . . .	52
3.4	PVDIS Experiment . . . . .	54
3.5	$J/\psi$ Experiment . . . . .	56
<b>4</b>	<b>Magnet</b>	<b>60</b>
4.1	Requirements . . . . .	60
4.2	SoLID magnet . . . . .	60
4.3	Planned Modifications . . . . .	61
4.4	Current Status and Planned Test . . . . .	63
<b>5</b>	<b>Targets</b>	<b>66</b>
5.1	Polarized <sup>3</sup> He Target . . . . .	66
5.2	Transversely Polarized Proton Target . . . . .	66
5.3	Cryogenic Target for PVDIS . . . . .	69
<b>6</b>	<b>Baffles</b>	<b>72</b>
<b>7</b>	<b>GEM Tracker</b>	<b>78</b>
7.1	Design . . . . .	78
7.2	GEM tracker R&D . . . . .	82
7.2.1	GEM chamber R&D program in UVa . . . . .	82
7.2.2	GEM chamber R&D programs in China . . . . .	85
7.3	Collaboration Status and Construction Outlook . . . . .	88
<b>8</b>	<b>Light Gas Cherenkov</b>	<b>90</b>
8.1	Design . . . . .	90
8.1.1	Tank and Cherenkov Gas . . . . .	90
8.1.2	Mirrors . . . . .	90
8.1.3	PMTs . . . . .	91
8.1.4	Magnetic Shielding and Winston Cones . . . . .	92
8.2	Tank Support . . . . .	93
8.3	Simulations . . . . .	94
8.3.1	Collection Efficiencies . . . . .	94
8.3.2	Background Rates . . . . .	94
8.3.3	Pion Rejection . . . . .	94
<b>9</b>	<b>Heavy Gas Cherenkov</b>	<b>99</b>
9.1	Optical System Design . . . . .	99
9.2	Simulation . . . . .	100
9.2.1	Photoelectron Yield . . . . .	100
9.2.2	Pion Detection Efficiency and Kaon Rejection Factor . . . . .	100
9.3	Performance of the PMTs in Magnetic Field . . . . .	101
9.4	Engineering Design . . . . .	102
9.5	Gas and Gas System . . . . .	102

<b>10</b>	<b>Electromagnetic Calorimeter</b>	<b>106</b>
10.1	Overview	106
10.2	Shower Detector Design Considerations	108
10.2.1	Total Length of the Calorimeter	108
10.2.2	Sampling Ratio of the Shower Detector	109
10.2.3	Lateral Size of the Calorimeter Module	110
10.3	Preshower Detector	111
10.4	Layout and Support	113
10.5	Light Readout	113
10.6	Radiation Effects	115
10.7	Performance	115
10.7.1	Intrinsic electron-pion separation	115
10.7.2	PID performance under realistic background simulation	118
10.7.3	Trigger capability	120
10.7.4	Shower Position Measurement	124
10.7.5	Supplemental Information: PID Selection Cuts	124
10.8	Scintillator Pad Detector for SIDIS Experiments	126
10.9	EC Collaboration Status and Construction Outlook	128
<b>11</b>	<b>MRPC</b>	<b>129</b>
11.1	Overview	129
11.2	Structure of the MRPC Prototype	129
11.3	Gas system	130
11.4	Cosmic Ray Test	130
11.5	Beam Test at Hall A	131
11.5.1	Test Setup	131
11.5.2	HV Scan Result	132
11.5.3	Rate Scan Result	132
11.6	Radiation hardness and aging	132
11.7	Conclusions	133
11.8	R&D Plan for Better Time Resolution	133
<b>12</b>	<b>Simulation and Reconstruction</b>	<b>141</b>
12.1	End-to-End Software Framework	141
12.2	Simulation	142
12.2.1	Simulation Software	142
12.2.2	Simulation Status	144
12.2.3	Physics Event Generators	145
12.2.4	GEM Digitization	146
12.3	Reconstruction	149
12.3.1	Tracking	149
12.3.2	Additional Reconstruction Algorithms	151
<b>13</b>	<b>Integration and Expected Performance</b>	<b>152</b>
13.1	Overview	152
13.2	SIDIS Program	152
13.3	PVDIS Program	156
13.3.1	Acceptances, efficiencies, and systematic uncertainties for PVDIS	156

13.3.2	Kinematics, Resolution and Calibration for PVDIS	158
13.4	$J/\psi$ Program	162
<b>14</b>	<b>Data Acquisition</b>	<b>165</b>
14.1	Introduction and Requirements	165
14.1.1	SIDIS Trigger and Rate Estimate	166
14.1.2	$J/\psi$ Trigger and Rate Estimate	166
14.1.3	PVDIS Trigger and Rate Estimate	166
14.2	DAQ Hardware and Trigger	167
14.2.1	GEM readout	167
14.2.2	SIDIS Configuration	169
14.2.3	PVDIS Configuration	170
14.3	Event size from FADC	172
14.4	Data rates,event size,tape SILO footprint and L3 Farm	173
14.5	Hall DAQ installation	174
14.5.1	Experiment switch over	174
14.6	Managing data rates	174
14.7	Summary and Pre R&D plans	175
<b>15</b>	<b>Radiation damage estimates and Activation</b>	<b>180</b>
15.1	Radiation damage to GEM electronics	180
15.2	Power deposited	181
15.2.1	Power in 1st baffle (due to Möllers), (Cooling, activation)	182
15.2.2	Power in exit hole in magnet (elastics) (Cooling, activation)	182
15.2.3	Power in the entrance surface of the magnet (Cooling, activation) (external target configurations)	183
15.2.4	Heat load in magnet cryostat	184
15.3	Estimates for radiation damage in the Hall	185
15.3.1	Radiation damage to electronics in Hall	185
15.3.2	Radiation from beam pipe	186
15.3.3	Radiation with external targets	187
<b>16</b>	<b>Slow Controls</b>	<b>194</b>
16.1	General Requirements	194
16.2	Frontend GUIs	194
16.3	High/Low Voltage Controls	195
16.4	DAQ Crate Control	195
16.5	Gas Systems Requirements	195
16.6	Detector Systems	195
<b>17</b>	<b>Electron Beam Polarimetry</b>	<b>196</b>
17.1	Compton Polarimetry	196
17.2	The Hall A Compton Polarimeter Baseline Upgrade	196
17.3	Upgrades Beyond the Baseline	198
17.3.1	Laser System and Luminosity	199
17.3.2	Alternative Laser System	201
17.3.3	Chicane Magnet Modification	203
17.3.4	Photon Detection	203

17.4	Systematic Uncertainties . . . . .	204
17.4.1	Sources of Correlated Error . . . . .	204
17.4.2	Systematic Errors for the Electron Detector . . . . .	204
17.4.3	Systematic Errors for the Photon Detector . . . . .	207
17.5	Summary of Compton Polarimetry . . . . .	208
17.6	Møller Polarimetry . . . . .	208
17.7	The Hall A Upgrade: “High Field” Iron Foil Targets . . . . .	209
17.7.1	Ferromagnetic Foil Targets . . . . .	210
17.7.2	Simplified Møller Scattering Target Assembly . . . . .	212
<b>18</b>	<b>Supports and Infrastructure</b>	<b>214</b>
18.1	Magnet Support . . . . .	214
18.2	Endcap Support Structure and Motion Mechanism . . . . .	214
18.3	Support Structure for Equipment Located Inside Cryostat Bore . . . . .	214
18.4	Power Requirements . . . . .	214
<b>19</b>	<b>Installation</b>	<b>216</b>
19.1	Experimental Layout . . . . .	216
19.2	Magnet Moving and Placement . . . . .	216
19.3	Helium Dewar Support and Upper Access Platform . . . . .	220
19.4	Endcap Forward Angle Detector Package Installation Structure . . . . .	220
19.5	Large Angle Detector and Baffle Installation Mechanism . . . . .	220
19.6	Light Gas Cherenkov Installation Structure . . . . .	221
<b>20</b>	<b>Project Status and Proposed Management Organization</b>	<b>222</b>
20.1	Collaboration and Organization . . . . .	222
20.2	Cost estimation . . . . .	224
	<b>Bibliography</b>	<b>225</b>
	<b>Appendices</b>	<b>241</b>
	<b>Appendix A Summary of Recommendations from the 2015 SoLID Director’s Review and the Responses With Notes Where They Are Addressed</b>	<b>241</b>
A.1	On the physics relevance and risks . . . . .	241
A.2	On the viability of approach and the experimental technique . . . . .	242
A.3	On the understanding, completeness, and credibility of the resources needed for the SoLID project. . . . .	244
	<b>Appendix B Summary of Subsystems</b>	<b>246</b>
B.1	Magnet . . . . .	246
B.2	GEM . . . . .	246
B.3	Light Gas Cherenkov . . . . .	247
B.4	Heavy Gas Cherenkov . . . . .	247
B.5	Electromagnetic Calorimeter and Scintillator-Pad Detector . . . . .	247
B.6	MRPC . . . . .	248
B.7	DAQ . . . . .	248
	<b>Appendix C Software Development Effort Estimate</b>	<b>250</b>

# 1 Executive Summary of the Responses to Recommendations from the Jefferson Lab Director’s Review Committee

## 1.1 Overview

To exploit the full potential of the Jefferson Lab (JLab) 12 GeV energy upgrade, a large acceptance high luminosity device, SoLID (Solenoidal Large Intensity Detector), was proposed for a rich and vibrant set of experiments. Five SoLID experiments, one PVDIS, three SIDIS and one  $J/\psi$  production, were approved with high ratings in 2010–2012 by the JLab Program Advisory Committee. After years of work by the collaboration, a preliminary conceptual design report (pCDR) was submitted to the JLab Director in 2014. A JLab Director’s Review for SoLID was held in February 2015. The review committee felt that SoLID was in a good state to move forward, but also identified a number of areas where additional work would be needed. Thirty-six recommendations were made in total (see Appendix A), with some aiming at longer term efforts required by any project of similar magnitude, and others more specifically relevant for the nearer term. After discussions with the Physics Division and JLab management, the collaboration aimed at the first step to address recommendations that are necessary to proceed with a Science Review as required for the DOE Critical Decision CD-0, while continuing to also address the longer term recommendations to the extent possible with available resources. The collaboration has completed the first step and the progress is reported in this updated pCDR.

This chapter summarizes the preparatory work to reach the milestone of the DOE Science Review. It includes the experiment specific recommendations related to the three core measurements (SIDIS, PVDIS and  $J/\psi$  production), as well as ones related to the general performance of the instrumentation to reach the scientific goals. For PVDIS, the viability of the calibration procedure to determine  $Q^2$  was studied including realistic misalignments of the detectors. The design of the baffles was re-examined including the choice of materials. For SIDIS, careful studies were performed to show the impact of SoLID compared to world data and other programs, including comparisons to projected data from JLab CLAS12 and SBS programs. Examples of physics reach, such as measurements of the transversity distribution and tensor charge, were simulated and are presented. For  $J/\psi$ , bin migration effects and trigger rates were simulated. Additional science topics that can be facilitated by SoLID, such as Generalized Parton Distributions and kaon identification in SIDIS, recommended in the review, were also considered and presented here.

Realistic simulations, as well as tracking and data acquisition development, have shown that the performance of the instrumentation will allow realization of SoLID scientific goals with the proposed design. The acceptances, efficiencies and systematic uncertainties were simulated in detail for each of the three core measurements. Meticulous magnet field modeling confirmed that the forces are tolerable and the fringe field at the polarized target location can be controlled to the desired level. Effects of possible radiation damage were carefully evaluated. Significant progress has also been made in the development of a full analysis simulation and software framework.

Beyond the items listed above which were deemed critical to the near term path to a Science Review, work is continuing on the many recommended fronts. The coils and cryostat of the CLEO-II magnet have arrived at JLab and the exterior steel is being shipped. Other activities include the development of GEM foil production in China and assessment of the risk factor, communication with expert groups in calorimeter design and R&D, and stability testing of the conductivity of MRPC glass. An initial study of the slow control system has been performed. A pre-R&D plan including a cost estimation was developed with inputs from the JLab management and has been submitted to DOE. Meanwhile, detector pre-R&D activities for some sub-systems are continuing and are supported by international collaborations (China and Canada), such as the calorimeter and the MRPC,

and the heavy gas cherenkov systems.

Our answers to all thirty-six recommendations will be summarized in the next few subsections, or merged into the original pCDR along with a map in Appendix A pointing to where the changes are made in the document to address each recommendation.

As a whole, the collaboration considers the progress on SoLID to be adequately substantial and positive to enable the next phase to begin, in particular a DOE Science Review. We therefore submit this revised pCDR as a first formal response to the 2015 JLab Director's Review, and look forward to the committee's evaluation and subsequent guidance from the laboratory.

## 1.2 Physics Program

### 1.2.1 SIDIS Production of Charged Pions

The SoLID SIDIS program includes three approved experiments using transversely and longitudinally polarized  $^3\text{He}$  targets and a transversely polarized proton ( $\text{NH}_3$ ) target, respectively. With the combination of the high luminosity and the large acceptance with a full azimuthal coverage, the SoLID SIDIS experiments will allow measurements in 4-dimensional bins with high statistics and well controlled systematics. Compared to CLAS12 and SBS SIDIS programs, SoLID has better FOM and thus higher statistics in the region  $x = (0.05, 0.55)$ , as shown in Figure 1. To demonstrate the physics impact of the SoLID SIDIS program, we performed the transversity extraction based on [1, 2] with simulated data of CLAS12, SBS and SoLID, and compare their results in Figure 2. SoLID can improve the transversity uncertainty for  $u$  ( $d$ ) quark by a factor of 3 (7) over CLAS12, and by a factor of 5 (10) compared to SBS. The tensor charge determination will have similar improvements which together with neutron EDM measurements will provide constraints on quark EDMs and thus new physics beyond the Standard Model. It is also evident that the projected high precision results from SoLID will provide powerful tests of Lattice QCD and much more quantitative information about TMDs and quark OAMs inside the nucleon.

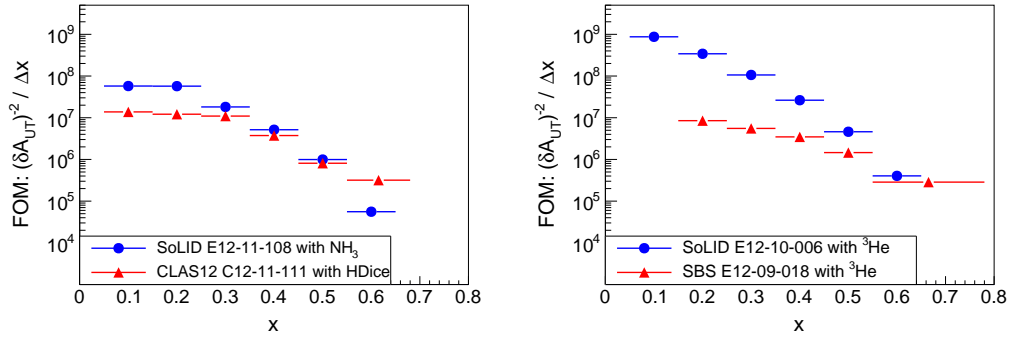


Figure 1: Comparisons of the FOM, defined as the sum of the inverse square of the statistical uncertainties of the single spin asymmetry (roughly proportional to statistics). The SoLID SIDIS experiment with the polarized  $\text{NH}_3$  target is compared with the CLAS12 experiment in the left panel. The SoLID SIDIS experiments with polarized  $^3\text{He}$  targets are compared with the SBS experiment in the right panel. In both comparisons, kinematic cuts of  $W > 2.3 \text{ GeV}$  and  $0.3 < z < 0.7$  are applied.

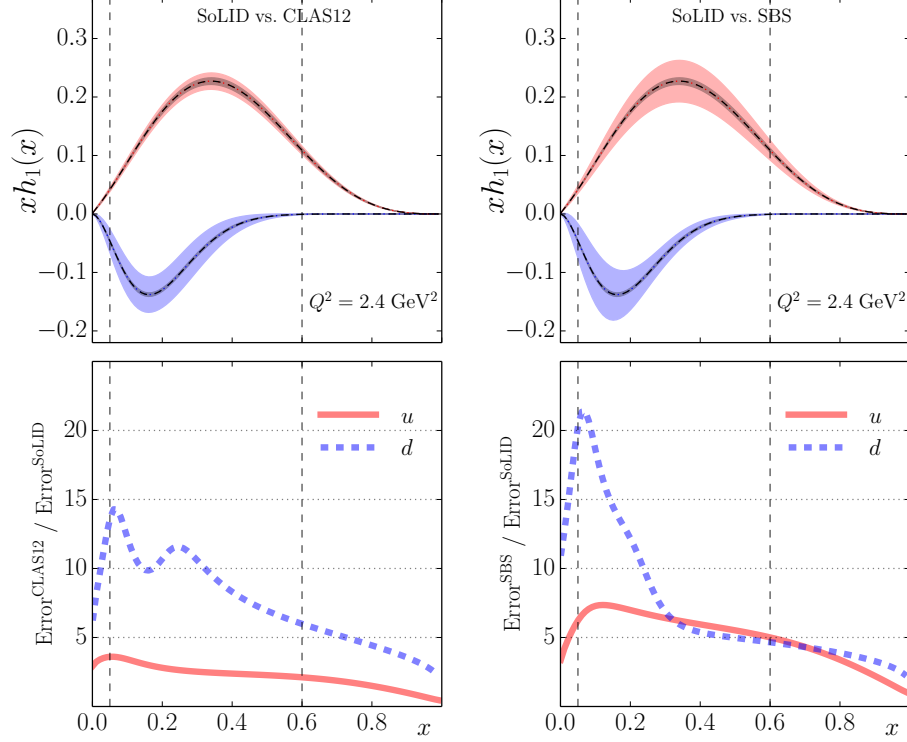


Figure 2: Comparisons of the impact on transversity extractions for up (red) and the down (blue) quarks, as the extension of published works [1, 2]. The left column shows the comparison between SoLID and CLAS12, and the right column shows the comparison between SoLID and SBS. In the upper panels, the light shaded bands show the uncertainties of the transversity function  $h_1(x)$  expected from SBS or CLAS12, and the dark shaded bands show the uncertainties expected from SoLID. The ratio of CLAS12 or SBS expected results to those from SoLID are shown in the lower panels. All results are plotted at a typical JLab12 scale  $Q^2 = 2.4 \text{ GeV}^2$ .

### 1.2.2 PVDIS

The unique feature of SoLID, combining high luminosity and large acceptance, makes it possible to achieve the high precision needed to reach a high physics impact: using PVDIS to probe physics beyond the Standard Model (SM). Measurements of PVDIS on a deuterium target will determine the effective electron-quark neutral-weak coupling constants  $2C_{2u} - C_{2d}$  that is inaccessible with other means. PVDIS measurements can also access a number of topics in hadronic physics, including searching for charge symmetry violation in the parton distribution functions, determining the  $d/u$  ratio in the proton without nuclear effects, and a clean extraction of higher-twist effects caused by quark-quark correlations. The 6-GeV PVDIS collaboration [3] has recently published in Nature a new experimental result  $2C_{2u} - C_{2d} = -0.145 \pm 0.068$ , the first measurement sufficiently sensitive to show that the  $C_{2q}$  are non-zero as predicted by the SM. One way to quantify the reach of various experiments is to quote mass limits suitable for composite models [4], where the couplings are on the order of  $4\pi/\Lambda^2$  where  $\Lambda$  is the compositeness mass scale. Such limits for the 6-GeV PVDIS collaboration and the SoLID PVDIS experiment [5] are shown in Figure 3. The sensitivity to be reached by SoLID is at the same level as LHC's for non-parity-violating couplings.

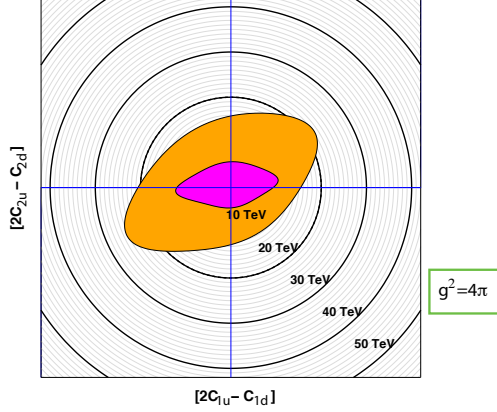


Figure 3: Projected mass limits for composite models from PVDIS. Purple region is excluded by published 6 GeV data and the orange region is the projected reach with SoLID and the final Qweak result.

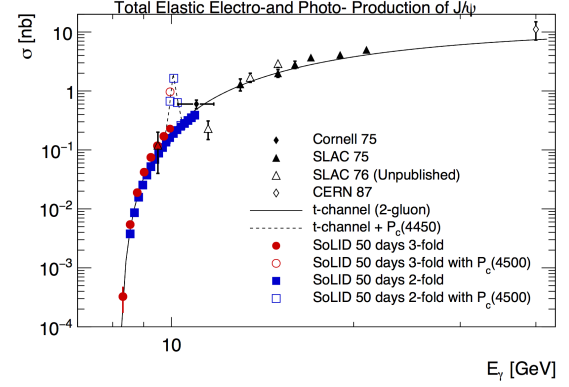


Figure 4: Projected uncertainties of total elastic  $J/\psi$  electro- and photo-production cross sections based on a 2-gluon exchange model including a projection of the LHCb pentaquark production assuming a coupling of 5%.

### 1.2.3 $J/\psi$ Production

Hadrons, the emergent phenomena of QCD, are in the realm of the strong interaction regime where much of its dynamics remains to be understood. While significant progress has been achieved in exploring QCD in its asymptotically free regime, the theory in the strong coupling regime is hardly tractable without numerical techniques. For example, an impressive success was achieved with the recent lattice QCD determination of the low-lying levels of the baryon spectrum [6] but there is a long road ahead to fully grasp the implications of QCD in this regime, for example, to understand the origin of the nucleon mass.

The impressive luminosity offered by SoLID combined with the large acceptance detection opens new opportunities for measurements of rare processes with unprecedented precision. In particular, measurement of the elastic production of  $J/\psi$  on the proton near threshold could provide unique and much needed information on the pure gluonic component of the QCD interaction, as well as to verify the nature of the charmed “pentaquark” states recently observed at LHCb [7]. A measurement very close to the threshold (Figure 4) where the cross section drops rapidly can provide important information on the trace anomaly, which is responsible for a large fraction of the proton mass, and will possibly impact our understanding of QCD in the strong-coupling regime.

## 1.3 Possible Expansions in the Physics Reach of SoLID

### 1.3.1 Generalized Parton Distributions (GPD)

The unique features of SoLID’s large acceptance and high luminosity make it an attractive device for the experimental study of GPDs. A number of groups have been working on developing a SoLID-GPD program. There are several GPD experiments in different stages of study/approval. A run-group proposal of Time-like Compton Scattering (TCS) from an unpolarized LH2 target has been approved to test the universality of GPD, to explore the underlying principles of factorization and to quantify the importance of higher twist effects. Double Deeply Virtual Compton Scattering (DDVCS) in the di-lepton channel on an unpolarized LH2 target was reviewed by the JLab PAC as a Letter-Of-Intent and the collaboration was encouraged to develop it into a two-stage program with



an initial focus to have a first significant DDVCS measurement (over a limited kinematic region) using the baseline SoLID setup. Measurements of DVCS and Deep Exclusive Meson Production (DEMP) with the transversely polarized  $^3\text{He}$  target are under development and the DEMP run-group proposal was reviewed by the SoLID Collaboration and received a strong encouragement. These measurements, together with the planned CLAS12 and Hall A/C GPD experiments, will make a significant contributions in disentangling different GPDs in the JLab 12-GeV kinematic region.

### 1.3.2 SIDIS Production of Charged Kaons

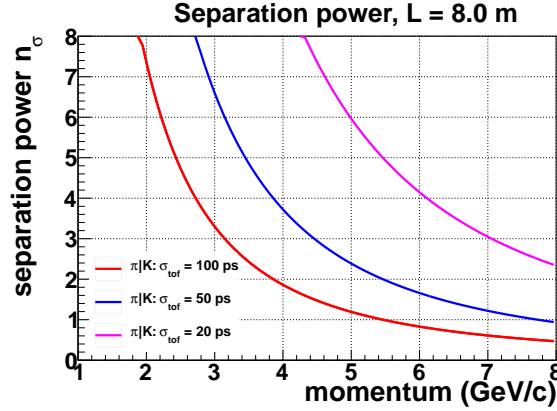


Figure 5: Kaon identification by TOF.

We have studied kaon identification for SoLID to potentially extend its physics programs. A full RICH detector for kaon detection is likely to be too costly to consider. High resolution TOF is a more practical solution. SoLID needs kaon identification over a momentum range of 1 GeV/c to 7 GeV/c. Given the  $\sim 8$  meter flight distance, a TOF time resolution of 20 ps is required to obtain a 3 sigma separation between pions and kaons as shown in Figure 5. A promising avenue is to improve the timing of the planned SoLID TOF-MRPC detector. The baseline MRPC is designed to reach 80 ps time resolution in the SoLID high-rate environment. Bench testings of thin-gap MRPC prototype detectors demonstrated the potential to reach a resolution of sub-20 ps [8, 9]. A planned R&D effort by a Chinese collaboration (Tsinghua University, USTC and CCNU) on the next generation MRPC jointly for SoLID, sPHENIX and EIC is being pursued, aiming for 20 ps resolution in a high-rate environment. The plan is to develop a prototype and readout electronics system next year. Beam test and finalizing of the detector and electronics design will be done in the following year.

## 1.4 Experimental Design, Simulation and Feasibility

### 1.4.1 Solenoidal Magnet

The CLEO II magnet was removed from the CESR beamline by Cornell University and JLab personnel during the 2016 summer down. All ancillary power, cryogenic and control services were disconnected from the magnet in preparation for iron removal. The iron was removed layer by layer and stored at Cornell's laydown yard until 2017 when it will be shipped to JLab. With the cryostat exposed, the axial transport brackets were installed and the cryostat moved to the transport frame. The service turret and neck were removed to reduce the height of the cryostat for safe highway transit. The entire unit was wrapped in marine grade shrink wrap to provide a weather barrier for

the trip to JLab. Three-axis accelerometers were mounted to the cryostat to monitor loads during the road trip. All loads remained under allowable thresholds specified in the Oxford CLEO II Operating Manual. Upon arrival at JLab in November 2016, the magnet was rolled into the Test Lab for climate controlled storage, as shown in Figure 6. We are making plans for testing the magnet with a new power supply and in-situ mapping.



Figure 6: CLEO II magnet at JLab.

#### 1.4.2 Acceptance, Efficiency and Systematics

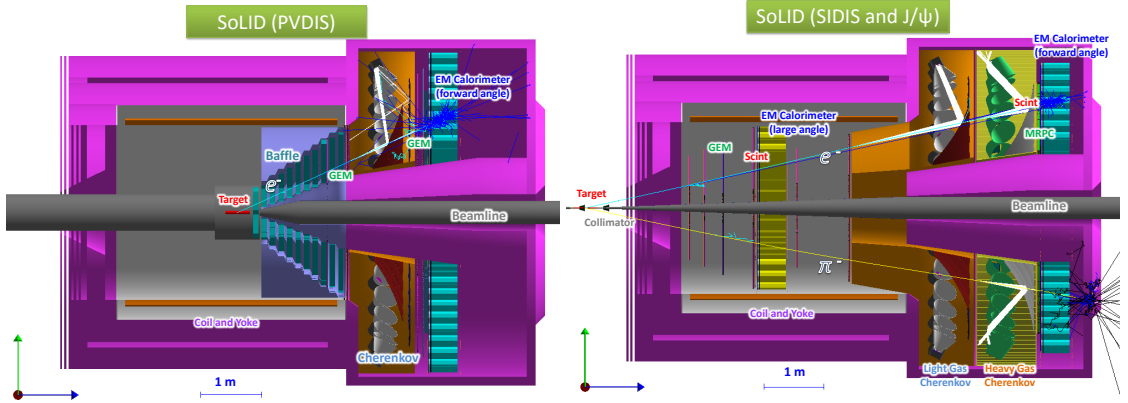


Figure 7: Left: SoLID PVDIS setup. Right: SoLID SIDIS and  $J/\psi$  setup.

The SoLID setups for the PVDIS and the SIDIS and  $J/\psi$  configurations are shown in Figure 7. Substantial progress has been made in developing a SoLID simulation package with realistic sub-system responses that includes all elements of the apparatus: EM showers in the electromagnetic calorimeter, optical processes in the two Cherenkov detectors, energy deposition in the GEMs and MRPC and their digitizations. A new event generator has been used for the estimation of hadron background rates. The simulation package allowed detailed simulations of the performance and feasibility of all core measurements, namely the PVDIS, SIDIS and  $J/\psi$  measurements.

A Kalman Filter based track finding and fitting algorithm is being developed and tested with digitized GEM simulation data. Tracking resolution from the simulated tracking fitting results including all material effects was studied. With background taken into account, tracking efficiency

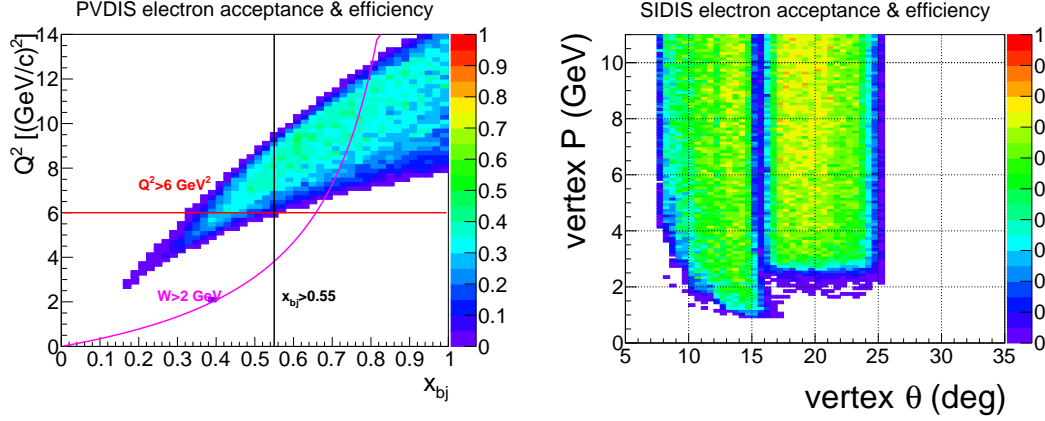


Figure 8: Left panel: electron acceptance and efficiency (except tracking) of SoLID PVDIS with the 40 cm LD2 target and the baffle. Curves show bounds of the kinematic range with  $Q^2 > 6 \text{ GeV}^2$ ,  $W > 2 \text{ GeV}$ , and  $x_{bj} > 0.55$ . Right panel: electron acceptance and efficiency (except tracking) of SoLID SIDIS with the 40 cm  $^3\text{He}$  target and two target window collimators. The result for  $J/\psi$  has a similar shape, but higher values because it has a 15 cm long target and no collimator.

Table 1: Average electron detection efficiencies of all SoLID sub-detectors and the total SoLID efficiency.

Detector	EC	Cerenkov	Scintillator pad and MRPC	GEM tracking	Total
average efficiency	95%	95%	98%	90%	80%

was obtained with the simulation. We have good electron detection efficiency from all sub-detectors. They vary slightly across the phase space and the average efficiency values are shown in Table 1. The PVDIS setup with its 40 cm long LD2 target has an  $\approx 0.35$  acceptance due to the baffle and the SIDIS setup with its 40 cm long  $^3\text{He}$  target has an  $\approx 0.7$  acceptance due to the two target window collimators. Figure 8 shows the combined effect of acceptance and efficiency (except tracking) for the two configurations. Systematic uncertainties for PVDIS and SIDIS are summarized in Table 2. The total systematic uncertainty for  $J/\psi$  is about 11%, dominated by acceptance, and the bin-migration effect is expected to be small. These results were used as inputs to the physics projections.

Table 2: The systematic uncertainties on the asymmetry measurements of PVDIS and SIDIS.

PVDIS Systematic (rel.)		SIDIS Systematic (abs.)		SIDIS Systematic (rel.)	
Polarimetry	0.4%	Raw asymmetry	0.0014	Target polarization	3%
$Q^2$	0.2%	Detector resolution	$< 0.0001$	Nuclear effect	(4 – 5)%
Radiative corrections	0.2%			Random coincidence	0.2%
Reconstruction errors	0.2%			Radiative correction	(2 – 3)%
				Diffraction meson	3%
Total	0.6%	Total	0.0014	Total	(6 – 7)%

### 1.4.3 Rates and Data Acquisition

The trigger rates were simulated with the full background, see Table 3. The SIDIS configuration, with an expected trigger rate of 100 kHz and total data rate of over 3 GB/s, represents the greatest challenge for SoLID data acquisition. Recent performance of GlueX and HPS DAQs with extrapolations by the JLab data acquisition and fast electronics groups give confidence that trigger rates of 100 kHz and above are achievable. Data for each of the 30 sectors of SoLID will pass through two readout controllers (ROCs), a PC based ROC for GEM data, and a VME ROC for all other detectors. The portion of the total data rate for non-GEM detectors, about 400 MB/s, is less than 15 MB/s per VME crate, so will not limit the trigger rate at 100 kHz. GEM detector trigger rates of 50 kHz have been achieved by HPS using an APV25 sample size of six. With a planned sample size of one for SIDIS, the GEM readout will not be limited to 100 kHz. The overall data rate required by SIDIS, which exceeds the rate currently achieved by GlueX, can be recorded by multiplexing data from the readout controllers to multiple event-building computers. Designing a DAQ system with 60 ROCs that can handle data rates of several GB/s will require some R&D, including firmware and software improvements, but is feasible using technology currently in use at JLab.

Table 3: Rates, run times and data total estimates for PVDIS, SIDIS and  $J/\psi$  experiments. For PVDIS, there are 30 sectors each of which has a separate DAQ.

Experiment	PVDIS	SIDIS $^3\text{He}$	$J/\psi$
Trigger rate (expected) (kHz)	$15 \times 30$	100	30
Data rate (GB/s)	$0.2 \times 30$	3.2	2.5
Running time (days)	169	125	60
Total data (PB)	175	70	25

## 1.5 Summary

The strong and unique physics program of SoLID, consisting of PVDIS, SIDIS and  $J/\psi$  production, was presented in the context of the worldwide effort. The science related recommendations from the Director's Review committee have been addressed. The scientific reach, unique strength and feasibility of the SoLID program demonstrate that we are ready for the next step: the anticipated Science Review by DOE.

## **2 Introduction and Overview of SoLID Experimental Programs**

### **2.1 SoLID Project Introduction/Overview**

#### **2.1.1 Base Equipment Description**

The SoLID (Solenoidal Large Intensity Device) project will develop a large acceptance spectrometer/detector system capable of handling very high rates. It is designed to satisfy the requirements of five approved high-scientific rated experiments, four A and one A-, as well as to become base equipment for a continued program of physics in the 12 GeV era at Jefferson Lab that requires both high luminosity and large acceptance. The base equipment composing the SoLID project includes two configurations: the “SIDIS” (Semi-Inclusive Deep Inelastic Scattering) configuration and the “PVDIS” (Parity-Violating Deep Inelastic Scattering) configuration. Although the geometrical layouts for the detectors are not the same in the two configurations, most of the following items are common:

1. A solenoidal magnet with a power supply and cryogenic system, identified as the CLEO-II magnet. With some modifications as described in the magnet section, this magnet meets the experimental requirements. The coils and cryostat of the CLEO-II magnet have arrived at JLab in 2016 and the exterior steel is arranged to be shipped to JLab in the summer of 2017.
2. An electromagnetic calorimeter for electron identification. (In the SIDIS configuration, it is separated into two sectors, a forward sector and a large-angle sector).
3. A light gas Cherenkov detector for electron identification.
4. A heavy gas Cherenkov detector for pion (hadron) identification. This is for the SIDIS configuration only.
5. A forward-angle and a large-angle scintillator-pad detectors for time-of-flight and for photon rejection. These are for the SIDIS configuration only.
6. A set of baffles. This is for the PVDIS configuration only.
7. A data acquisition system (DAQ). Part of the DAQ electronics, mainly FADCs, will be from the JLab Physics Division Shared Electronics Pool (see next section on Dependencies to Base Equipment).
8. Supporting structures for the magnet and the detectors.
9. Requisite Hall A infrastructure to accommodate the functioning of the above — cooling, cabling, and the like.

#### **2.1.2 Dependencies to Base Equipment**

The following items are requisite outside contributions to the SoLID base equipment:

1. GEM detectors for tracking: These are planned to be provided by a SoLID Chinese Collaboration. Five Chinese institutions (USTC, CIAE, Tsinghua, Lanzhou and IMP), in collaboration with UVa (Nilanga Liyanage group), have committed to perform R&D and apply for full funding from the Chinese funding agencies to construct the full set of GEMs for the SoLID project.

2. A MRPC (Multi-Gap Resistive Plate Chamber) detector serving as a time-of-flight (TOF) detector for pion (hadron) identification: Two Chinese groups (Tsinghua University and USTC) have committed to perform R&D and apply for full funding to construct the required MRPC detector for the SoLID project. The Chinese groups, in collaboration with US institutions, will also apply for separate funding for MRPC electronics.
3. DAQ electronics: JLab intends to have an electronics pool to share basic DAQ electronics among the four experimental halls. Some of these electronics, mainly FADCs, will be utilized by SoLID.
4. Magnet: JLab formally requested the CLEO-II magnet and received a positive response from Cornell University. JLab, in coordination with Cornell, had the magnet coils and cryostat be transported to JLab in the fall of 2016 and plans to have the steels be shipped to JLab in the Summer of 2017.
5. Beamline: The Hall A beam line with standard instrumentation is assumed to be in operational condition and is not included in the SoLID base equipment.

### 2.1.3 Experiment-specific Dependencies

The five approved experiments in the SoLID research program would require the SoLID base equipment, as well as the development of components outside the base equipment of the SoLID project. The following lists such additional equipment that is either standard and existing at JLab or that will be available for experiments planned before the SoLID experiments:

1. For SIDIS transverse  $^3\text{He}$  and longitudinal  $^3\text{He}$ : The existing polarized  $^3\text{He}$  target with performance already achieved from the 6 GeV transversity (E06-010) experiment is required. However, modifications to the stand, supports, and service may be required to accommodate integration into SoLID.
2. For  $J/\Psi$  the standard cryogenic LH2 target system is assumed. This is standard Hall A equipment, however the SoLID SIDIS configuration will require re-arrangement of the detector system for the target and there may be significant modifications required for both to accommodate integration into SoLID.
3. For PVDIS: A Compton polarimeter and a super-conducting Moller polarimeter (both also required by MOLLER and to be employed for PREX also) are assumed to be available.

For completeness, though not as general dependencies for SoLID base equipment, the following experiment-specific items which will require additional resource/funding are listed:

1. For PVDIS: a custom, high-power cryotarget is required. ESR2 is assumed to be available (required by the Moller project).
2. For SIDIS transverse proton: a transversely polarized proton target will need development. An initial study has been performed by Oxford which concluded that such a target is feasible.

### 2.1.4 Research Program

The five currently-approved, high-impact experiments approved for the SoLID project are as follows:

1. SIDIS-transverse  $^3\text{He}$ : Semi-inclusive deep-inelastic-scattering of electron beam on a transversely polarized  $^3\text{He}$  target. It is focusing on charged pion production to study transverse spin (transversity) and other transverse momentum dependent parton distributions (TMDs). It will provide a 4-d  $(x, z, P_T, Q^2)$  mapping of the Collins, Sivers and pretzelosity asymmetries of the neutron in the valance quark region with high precision. Combined with the SIDIS measurement on the proton and the world  $e^+e^-$  data, the Collins asymmetries will allow for an extraction of one of the fundamental properties of the nucleon, the tensor charge of the u and d quarks to better than 10%, providing a benchmark test of lattice QCD. The Sivers and Pretzelosity asymmetries will allow an extraction of the Sivers function and pretzelosity function, providing crucial information on the quark orbital motion.
2. SIDIS-longitudinal  $^3\text{He}$ : Semi-inclusive deep-inelastic-scattering of electron beam on a longitudinally polarized  $^3\text{He}$  target. It is focusing on charged pion production to study TMDs. Combined with transversely polarized  $^3\text{He}$  target experiment, it will provide a precision 4-d  $(x, z, P_T, Q^2)$  mapping of the two worm-gear asymmetries of the neutron in the valence quark region, allowing an extraction of the two so-called worm-gear TMDs ( $g_{1T}$ , longi-transversity and  $h_{1L}^\perp$ , trans-helicity) with high precision, providing crucial information on the quark orbital motion and the spin-orbital correlations.
3. SIDIS-transverse proton: Same as in 1) but on the proton.
4. PVDIS on the deuteron and the proton: PVDIS on the deuteron will provide a precision test of the Standard Model. It provides the best measurement of the  $C_2$  coupling and also provides a precision measurement of  $\sin^2 \theta_W$  at an intermediate value of  $Q^2$ . The broad kinematical range enables the separation of the testing of the Standard Model and the study of fundamental hadron properties, including a precision measurement of possible charge symmetry violation at the partonic level and a unique measurement of the higher-twist effect (twist-4 term). The proton measurement provides a clean measurement of the d-quark over u-quark ratio in the high- $x$  region without nuclear effects.
5.  $J/\Psi$  production near threshold: This fully exclusive measurement of the electroproduction of  $J/\Psi$  mesons from protons near threshold will be sensitive to the non-perturbative gluonic interaction between the  $J/\psi$  and nucleon, and might reveal an enhancement of the cross section just above the production threshold. This in turn could be a manifestation of the important role of the conformal anomaly. A further consequence is whether or not  $J/\psi$ -nuclear bound states would exist in nature. This experiment could open a new window to study QCD in the non-perturbative region using charmonium in a multi-phase program.

All proposals are available at

[http://www.jlab.org/exp\\_prog/generated/12GeV/halla.html](http://www.jlab.org/exp_prog/generated/12GeV/halla.html)

## 2.2 SIDIS Program

### 2.2.1 Introduction

Deep inelastic lepton-nucleon scattering (DIS) experiments have played a fundamental role in describing the partonic momentum structure of hadrons. The unpolarized parton distribution functions (PDF) have been extracted with excellent precision over a large range of  $x$  and  $Q^2$  from DIS, Drell-Yan and other processes after several decades of experimental and theoretical efforts. The comparison of the structure functions in the large  $Q^2$  range with QCD evolution equations has provided one of the best tests of QCD.



When the target and/or beam are polarized the essential properties of spin-angular momentum structure of hadrons is probed. Three decades of intensive experimental and theoretical investigation have resulted in a great deal of knowledge on the partonic origin of the nucleon spin structure. Motivated by the “spin crisis” from the European Muon Collaboration experiment in the 1980s [11], the longitudinal polarized parton distribution functions have been determined with significantly improved precision over a large region of  $x$  and  $Q^2$  from polarized deep-inelastic (DIS) experiments carried out at CERN, SLAC, DESY in the last two decades, and more recently at JLab and at RHIC from polarized proton-proton scattering (see [12, 13] for reviews and compilation of references). In particular, considerable knowledge has been gained from inclusive DIS experiments on the longitudinal structure – the  $x$ -dependence and the helicity distributions – in terms of the unpolarized (denoted  $q^a(x)$  or  $f_1^a(x)$ ) and helicity (denoted  $\Delta q^a(x)$  or  $g_1^a(x)$ ) parton distribution functions for the various flavors (indicated by  $a$ ).



In more recent experimental and theoretical studies, it has become evident that precise knowledge of the transverse structure of partons is essential to unfold the full momentum and spin structure of the nucleon. This concerns in particular the investigations of the chiral-odd transversely polarized quark distribution function or transversity [14] (denoted as  $\delta q(x)$ ,  $h_1(x)$  or also  $\Delta_T q(x)$ ) which is probed in transverse spin polarization experiments. Like the axial charge  $\Delta q^a = \int_0^1 dx (g_1^a(x) + g_1^{\bar{a}}(x))$ , the tensor charge  $\delta q^a = \int_0^1 dx (h_1^a(x) - h_1^{\bar{a}}(x))$  is a basic property of the nucleon. The essential role of the transversity distribution function emerges from a systematic extension of the QCD parton model to include transverse momentum and spin degrees of freedom. In this context, semi-inclusive deep-inelastic lepton nucleon scattering (SIDIS) has emerged as an essential tool to probe both the longitudinal and transverse momentum and spin structure of the nucleon. The azimuthal dependence in the scattering of leptons off transversely polarized nucleons is explored through the analysis of transverse single spin asymmetries (TSSAs). Recent work [15–17] predicts that these observables are factorized convolutions of leading-twist transverse momentum dependent parton distributions (TMDs) and fragmentation functions (FFs) at low transverse momentum. These functions provide *essential non-perturbative* information on the partonic sub-structure of the nucleon; they offer a rich understanding of the motion of partons inside the nucleon, of the quark orbital properties, and of spin-orbit correlations. They also provide essential information on multi-parton correlations at leading-twist, allowing us to explore and uncover the dynamics of the quark-gluon structure of the nucleon.

At leading twist if we integrate over the transverse momenta of quarks, the three quark distribution functions remain: the unpolarized parton distribution  $f_1$ , the longitudinal polarized parton distribution  $g_1$ , and the quark transversity distribution  $h_1$ . Besides  $f_1$ ,  $g_1$  and  $h_1$ , there are five more transverse momentum dependent distribution functions [15, 16]. Fig. 9 tabulates all these eight TMDs according to the polarizations of the quark (f, g, h) and nucleon (U, L, T). Since these TMDs provide the description of the parton distributions beyond the collinear approximation, they depend not only on the longitudinal momentum fraction  $x$ , but also on the transverse momentum,  $k_T$ . An intuitive interpretation of the  $k_T$  dependent transversity distribution,  $h_1$ , is that it gives the probability of finding a transversely polarized parton inside a transversely polarized nucleon with certain longitudinal momentum fraction  $x$  and transverse momentum  $k_T$ . The JLab 12 GeV upgrade provides a unique opportunity to extend our understanding of nucleon spin and momentum structure by carrying out multi-dimensional precision studies of longitudinal and transverse spin and momentum degrees of freedom from SIDIS experiments with high luminosity in combination with large acceptance detectors. Such a program will provide the much needed kinematic reach to unfold the momentum and flavor structure of the nucleon. In the next section, we summarize the essential role that transverse polarization studies play in unfolding this structure in SIDIS.



### 2.2.2 Transverse Structure and Semi-Inclusive Deep Inelastic Scattering

The transverse spin and momentum structure of the nucleon was first discussed in 1970s [18, 19] followed by renewed interest in late 1980s [14, 20]. The transversity function is a chirally odd quark distribution function, and the least known among the three leading twist parton distribution functions. It describes the net quark transverse polarization in a transversely polarized nucleon [20]. In the non-relativistic limit, the transversity distribution function  $h_1(x, Q^2)$  is the same as the longitudinal quark polarization distribution function,  $g_1(x, Q^2)$ . Therefore, the transversity distribution function probes the relativistic nature of the quarks inside the nucleon.

**Leading Twist TMDs**       : Nucleon Spin       : Quark Spin

		Quark polarization		
		Un-Polarized (U)	Longitudinally Polarized (L)	Transversely Polarized (T)
Nucleon Polarization	U	$f_1 = \text{circle with dot}$		$h_1^\perp = \text{circle with dot} - \text{circle with dot}$ Boer-Mulder
	L		$g_1 = \text{circle with arrow} - \text{circle with arrow}$ Helicity	$h_{1L}^\perp = \text{circle with arrow} - \text{circle with arrow}$
	T	$f_{1T}^\perp = \text{circle with dot} - \text{circle with dot}$ Sivers	$g_{1T}^\perp = \text{circle with arrow} - \text{circle with arrow}$	$h_{1T}^\perp = \text{circle with dot} - \text{circle with dot}$ Transversity $h_{1T}^\perp = \text{circle with arrow} - \text{circle with arrow}$

Figure 9: Leading twist TMDs classified according to the polarizations of the quark (f, g, h) and nucleon (U, L, T).

There are several interesting properties of the quark transversity distribution. First it does not mix with gluons; that is, it evolves as a non-singlet distribution [21] and doesn't mix with gluons under evolution and thus has valence-like behavior [22]. Secondly in the context of the parton model it satisfies the Soffer bound [23], which is an inequality among the three leading twist distributions,  $|h_1^q| \leq \frac{1}{2}(f_1^q + g_1^q)$ , based on unitarity and parity conservation. QCD evolution of transversity was studied in Ref. [24], where it was shown that Soffer's inequality holds up to next to leading order (NLO) QCD corrections. In the past [25] and more recently [26], studies have been performed that consider the violation of this bound. Therefore, it is interesting to experimentally test the Soffer's inequality as a function of  $Q^2$ . Lastly, the lowest moment of  $h_1^q$  is the tensor charge, which has been calculated from lattice QCD [27] and various models [28–33]. Due to the valence-like nature of the transversity distribution, measuring transversity in the high- $x$  region (JLab kinematics) is crucial to determine tensor charge of quarks. The experimental determination of the transversity function is challenging - it is not accessible in polarized inclusive DIS measurements when neglecting quark masses -  $h_1$  decouples at leading twist in an expansion of inverse powers of the hard scale in inclusive deep-inelastic scattering due to the helicity conserving property of the QCD interactions. However, paired with another hadron in the initial state *e.g.* double polarized Drell-Yan processes

(two transversity distributions) [19], or in the final state, *e.g.* semi-inclusive deep-inelastic [34] scattering (transversity and Collins fragmentation function), leading twist  $h_1$  can be accessed without suppression by a hard scale.

The most feasible way to access the transversity distribution function is via an azimuthal single spin asymmetry, in semi-inclusive deep-inelastic lepto-production of mesons on a transversely polarized nucleon target,  $e N^\uparrow \rightarrow e \pi X$ . In this case the chiral-odd partner is the Collins fragmentation function,  $H_1^\perp$  [34], which has been extracted from charged pion pair production from  $e^+e^-$  annihilation [35]. Assuming factorization, schematically this transverse single spin asymmetry (TSSA) contains  $h_1$  and  $H_1^\perp$ ,  $A_{UT} \sim h_1 \otimes H_1^\perp$  ( $U \equiv$  unpolarized lepton beam,  $T \equiv$  transversely polarized target) [16].

The first evidence of non-trivial transverse spin effects in SIDIS has been observed in the transverse single spin asymmetries measured by the HERMES [36–38], and the COMPASS [39, 40] experiments from a transversely polarized proton or deuteron target, where an unpolarized lepton beam is scattered off  $l p^\uparrow \rightarrow l' h X$ . Besides the non-zero Collins asymmetry, which contains  $h_1$  and  $H_1^\perp$  discussed previously, another non-zero asymmetry (Sivers asymmetry), was also observed. The Sivers asymmetry is associated with a naive T-odd transverse momentum dependent (TMD) parton distribution function [41]. More recently, results on Collins and Sivers asymmetries on neutron were reported for the first time using a polarized  $^3\text{He}$  target at Jefferson Lab [42]. In contrast to inclusive deep-inelastic lepton-nucleon scattering where transverse momentum is integrated out, these processes are sensitive to the transverse-momentum scale,  $P_T$ , which is on the order of the intrinsic quark momentum,  $k_T$ ; that is  $P_T \sim k_T$ . This is evident by considering the generic structure of the TSSA for a transversely polarized nucleon target which is characterized by interference between helicity flip and helicity non-flip amplitudes  $A_{UT} \sim \text{Im}(f^{*+} f^-)$ . In the collinear limit of QCD, partonic processes conserve helicity and Born amplitudes are real [43]. For this structure to be non-zero at leading twist we must go beyond the collinear limit where such a reaction mechanism requires a recoil scale sensitive to the intrinsic quark transverse momentum. This is roughly set by the confinement scale  $k_T \sim \Lambda_{\text{QCD}}$  [44]. Because strongly interacting processes conserve parity transverse spin asymmetries are described by T-odd correlations between transverse spin  $\mathbf{S}_T$ , longitudinal momentum  $\mathbf{P}$  and intrinsic quark momentum  $\mathbf{k}_T$  [34, 41], which are depicted by the generic vector product  $i\mathbf{S}_T \cdot (\mathbf{P} \times \mathbf{k}_\perp)$ . These correlations imply a leading twist reaction mechanism which is associated with a naive T-odd transverse momentum dependent (TMD) parton distribution [41] and fragmentation [34] function (PDF & FF).

A crucial theoretical breakthrough [45–47] was that the reaction mechanism is due to non-trivial phases arising from the color gauge invariant property of QCD. This leads to the picture that TSSAs arise from initial and final state interactions [48–50] (ISI/FSI) of the active quark with the soft distribution or fragmentation remnant in SIDIS, which manifests itself as a gauge link that links the bilocal quark configuration. This gauge link gives rise to the final state gluonic interactions between the active quark and target remnant. Thus, T-odd TMDs are of crucial importance because they possess transverse spin polarization structure as well as the necessary phases to account for TSSAs at leading twist. Further work on factorization theorems for SIDIS indicate that there are two leading twist T-odd TMDs; the Sivers function, denoted as  $f_{1T}^\perp$ , describing the probability density of finding unpolarized partons inside a transversely polarized proton, is one of these functions. All these aforementioned ingredients (TMD, FF, gauge link) enter the factorized [17] hadronic tensor for semi-inclusive deep-inelastic scattering.

Exploring the transverse spin structure of the TMD PDFs reveals evidence of a rich spin-orbit structure of the nucleon. When the transverse spin and momentum correlations are associated with the nucleon, where the quark remains *unpolarized*, the Sivers function [41] describes the helicity flip of the nucleon target in a helicity basis. Since the quark is unpolarized in the Sivers func-

tion, the orbital angular momentum of the quarks must come into play to conserve overall angular momentum in the process [51, 52]. Indeed a partonic description of the Sivers and Boer-Mulders functions requires wave function components with nonzero orbital angular momentum and thus provides information about the correlation between the quark orbital angular momentum (OAM) and the nucleon/quark spin, respectively [48, 53].

Unlike the Sivers function, which provides a clean probe of the QCD FSI, the functions  $g_{1T}$  and  $h_{1L}^\perp$  are (naive) T-even, and thus do not require FSI to be nonzero. Nevertheless, they also require interference between wave function components that differ by one unit of OAM and thus require OAM to be nonzero. Recently, a first ever determination of  $g_{1T}$  was reported [54] using a polarized  $^3\text{He}$  target at Jefferson Lab, in which a positive azimuthal asymmetry for  $\pi^-$  production on  $^3\text{He}$  and the neutron was observed, while the  $\pi^+$  asymmetries are consistent with zero. Finally, the pretzelosity  $h_{1T}^\perp$  requires interference between wave function components that differ by two units of OAM (e.g. p-p or s-d interference). Combining the wealth of information from all these functions could be invaluable for disentangling the spin orbit correlations in the nucleon wave function, thus providing important information about the quark orbital angular momentum.

Complementary to Generalized Parton distributions (or Impact Parameter Dependent distributions), which describe the probability of finding a parton with certain longitudinal momentum fraction and at certain transverse position  $b$  (1-D momentum space and 2-D coordinate space), TMDs give a description of the nucleon structure in 3-D momentum space. Furthermore, by including the transverse momentum of the quark, the TMDs reveal important information about the nucleon/parton spin-orbital angular momentum correlations.

### 2.2.3 The Phenomenology TSSAs and TMDs

All eight leading twist TMDs can be accessed in SIDIS. The transversity, Sivers, and pretzelosity TMDs can be accessed through a transversely polarized target. There are three mechanisms which can lead to the single (transversely polarized target) spin azimuthal asymmetries, which are the Collins asymmetry, the Sivers asymmetry, and the pretzelosity asymmetry. As mentioned previously, the quark transversity function in combination with the chiral-odd Collins fragmentation function [34] gives rise to an azimuthal (Collins) asymmetry in  $\sin(\phi_h + \phi_S)$ , where azimuthal angles of both the hadron (pion) ( $\phi_h$ ) and the target spin ( $\phi_S$ ) are with respect to the virtual photon axis and relative to the lepton scattering plane. The Sivers asymmetry [41, 55, 56] refers to the azimuthal asymmetry in  $\sin(\phi_h - \phi_S)$  due to the correlation between the transverse target polarization of the nucleon and the transverse momentum of the quarks, which involves the orbital angular momentum of the unpolarized quarks [48, 51]. The pretzelosity asymmetry is similar to Collins asymmetry except it is due to quarks polarized perpendicularly to the nucleon spin direction in the transverse plane in a transversely polarized nucleon. It has an azimuthal angular dependence of  $\sin(3\phi_h - \phi_S)$ . One can disentangle these angular distributions by taking the azimuthal moments of the asymmetries as has been done by the HERMES Collaboration [38], the COMPASS Collaboration [40], and most recently by the Jefferson Lab E06-010 collaboration [42]. With a longitudinally polarized lepton beam, and a transversely polarized target, the double spin asymmetry from SIDIS has an azimuthal angular dependence of  $\cos(\phi_h - \phi_S)$  that allows for the determination of the  $g_{1T}$  TMD as was done in [54]. With a longitudinally polarized target, the single target spin asymmetry with an azimuthal angular dependence of  $\sin(2\phi_h)$  is sensitive to  $h_{1L}^\perp$ , while the double spin asymmetry allows for the determination of the helicity TMD,  $g_1$ .

In recent years a great deal of understanding of transverse spin effects, final state interactions, and the spin orbit structure of partonic-hadronic interactions has been gained from model calculations of the TMDs and fragmentation functions. In particular the final state interactions in TSSAs

through the Sivers function has been studied in spectator models and the light-cone wave function approach [48–50, 57–61] as well as the bag model [62] and the NJL jet model [66]. The Collins function has been calculated in [63–65] while studies of the universality of T-odd fragmentation functions have been carried out in [67–69]. The Boer-Mulders function has been calculated in [50, 59, 61, 70, 71] and the spin orbit effects of the pretzelosity function have been studied in both light-cone constituent quarks models [72–75], while model predictions of azimuthal and transverse spin asymmetries have been predicted in [59, 76, 77].

The first model dependent extractions of the transversity distribution have been carried out [78] by combining SIDIS [37, 38, 79, 80] data with  $e^+e^-$  data [35] on the Collins function. Within the uncertainties, the Soffer bound is respected. In addition, the extraction of the Sivers function [81–85] has been performed by combining SIDIS data from the HERMES [38] on the proton and COMPASS data [40] on the deuteron. Complementing the data from the HERMES [37, 38], COMPASS [80], and BELLE [35] experiments, the recent results from the Jefferson Lab Hall A experiment E06-010 [42] on the neutron (with polarized  $^3\text{He}$ ) will facilitate a flavor decomposition of the transversity distribution function,  $h_1$  [20, 86] and the Sivers distribution function  $f_{1T}^\perp$  [41] in the overlapping kinematic regime. However a model-independent determination of these leading twist functions requires data in a wider kinematic range with high precision in *four dimensions* of  $(Q^2, x, z, P_T)$ .

#### 2.2.4 Overview of SIDIS program

The 12-GeV energy upgrade at CEBAF together with the newly proposed SoLID opens a great new window to perform precision studies of the transverse spin and transverse-momentum-dependent structure in the valence quark region for both the proton and the neutron. The experimental program on TMDs is one of the main thrusts of the 12-GeV physics program at Jefferson Lab.

Currently, there are three A rated SoLID experiments (E12-10-006 [87], E12-11-007 [88], and E12-11-108 [89]) on TMD physics with two involving a transversely (longitudinally) polarized  $^3\text{He}$  (neutron) target, and one employing a transversely polarized  $\text{NH}_3$  (proton) target. To extract TMDs with precisions from single and double spin asymmetry measurements, the detection system should have the capability to handle large luminosities, a full azimuthal angular coverage, good kinematic coverage in terms of  $Q^2, x, z, P_T$  for SIDIS, and good particle identification for electrons and charged pions. Further, the influence due to the residual magnetic field of the spectrometer magnet needs to be negligible for polarized targets. SoLID is such a device that has been proposed and designed for these newly approved SIDIS experiments.

These new SIDIS experiments employ a superconducting solenoid magnet, a detector system consisting of forward-angle detectors and large-angle detectors, and a high-pressure polarized  $^3\text{He}$  target or a polarized  $\text{NH}_3$  target positioned upstream of the magnet. The polarized  $^3\text{He}$  target is based on the technique of spin-exchange optical pumping of hybrid Rb-K alkali atoms. Such a target was used successfully in the recently completed SSA experiment [42, 54] with a 6-GeV electron beam at JLab and an in-beam polarization of 55-60% was achieved. For the polarized proton experiment E12-11-108, an upgraded version of the JLab/UVa/SLAC polarized  $\text{NH}_3$  target will be used. The main upgrade will involve using a new magnet to replace the aging Helmholtz-coil magnet and to have fast spin-flip capability with the Adiabatic Fast Passage (AFP) technique. Preliminary design study has been carried out for such a magnet with a vertical opening angle of  $\pm 25^\circ$  to satisfy the requirement of the experiment. The target is based on the principle of dynamic nuclear polarization (DNP) by using microwave pumping to reach high proton polarizations [90, 91]. The CLEO-II magnet with new end caps and modification of the yolks has been identified as the magnet of the choice for SoLID based on both the requirements of the experiments and the

availability of the magnet. Six layers of GEM detectors will be placed inside the coils as tracking detectors. A combination of an electromagnetic calorimeter, gas Cherenkov counters, a layer of Multi-gap Resistive Plate Chamber (MRPC) and a thin layer of scintillator will be used for particle identification in the forward-angle region. As only electrons will be identified in the large-angle region, a shashlyk-type [92, 93] electromagnetic calorimeter will be sufficient to provide the pion rejection. More details about SoLID experimental setup, kinematic coverage, particle identification, and other important considerations for SIDIS can be found in Section 3.2 and 3.3.

### 2.2.5 Beam Time and Projections

**E12-10-006** Experiment E12-10-006 was approved 90 days of total beam time with 15  $\mu\text{A}$ , 11/8.8 GeV electron beams on a 40-cm long, 10 amgs transversely polarized  $^3\text{He}$  target. 69 days is for beam on the polarized  $^3\text{He}$  target, and 10 days for a dedicated study of the  $x - z$  factorization with Hydrogen and Deuterium gas using a reference target cell. Additional 3.0 days is requested with a longitudinal target polarization to study the systematics of potential  $A_{UL}$  contamination, where  $U$  stands for an unpolarized beam and  $L$  for a longitudinally polarized target. A total overhead time of 8 days is requested. This overhead time will be shared among activities such as unpolarized target runs, target spin flip and target polarization measurements, as has been done in the past during other Hall A polarized  $^3\text{He}$  target experiments. Although beam polarization is not required for the proposed SSA measurements, polarized beam with polarization of 85% or higher will be used for parasitic measurements of  $A_{LT}$ , which can be used to access,  $g_{1T}$  as demonstrated in [54].

Projected data from E12-10-006 are binned into 4-dimensional  $(x, P_h, z, Q^2)$  bins. For a typical  $z$  and  $Q^2$  bin ( $0.40 < z < 0.45$ ,  $2 \text{ GeV}^2 < Q^2 < 3 \text{ GeV}^2$ ), data projections for Sivers asymmetry measurements, left panel for  $\pi^+$  and right panel for  $\pi^-$ , are shown in Fig. 10 as examples. Also shown are results from the 6-GeV experiment E06-010 [42], and predictions of Sivers asymmetries from Anselmino *et al.* [94] with model uncertainties. For complete projections which consist of 1400 data points, we refer to the proposal [87].

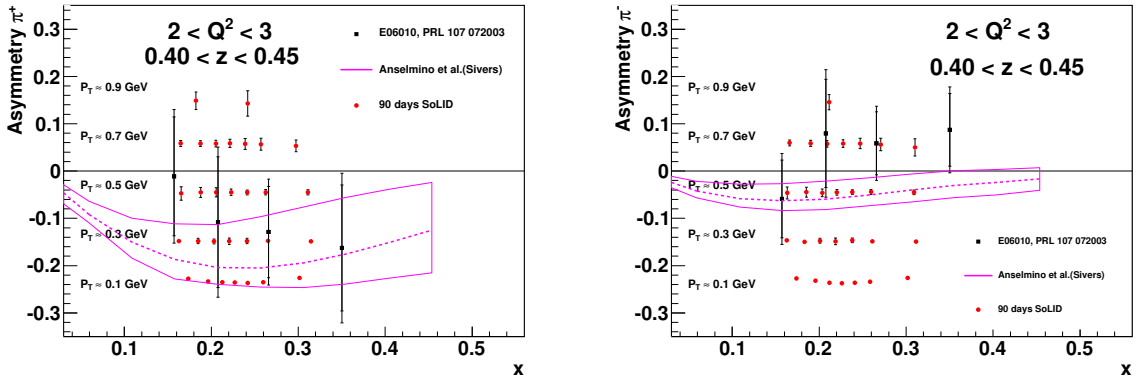


Figure 10: The left panel shows the projected Sivers asymmetry measurement for  $\pi^+$  for a typical  $z$  and  $Q^2$  bin ( $0.40 < z < 0.45$ ,  $2 \text{ GeV}^2 < Q^2 < 3 \text{ GeV}^2$ ) as a function of  $x$  with different ranges of the hadron transverse momentum labeled. The right panel shows the projection for the corresponding  $\pi^-$  Sivers asymmetry measurement. Also shown are the results from the 6-GeV experiment E06-010 [42].

**E12-11-007** Experiment E12-11-007 was approved 35 days of total beam time with 15  $\mu\text{A}$ , 11/8.8 GeV electron beams on a 40-cm long, 10 amgs longitudinally polarized  $^3\text{He}$  target to match about

50% statistics of experiment E12-10-006. When combined with experiment E12-10-006, this experiment will not require any beam time for calibration data, including reference cell runs and detector calibrations.

A maximum likelihood method [95] was used to extract angular modulations with combined, projected data sets from both E12-11-007 and E12-10-006. Projected data are binned into 4-dimensional  $(x, P_h, z, Q^2)$  bins. For a typical  $z$  and  $Q^2$  bin ( $0.40 < z < 0.45$ ,  $2 \text{ GeV}^2 < Q^2 < 3 \text{ GeV}^2$ , one of the total 48  $z - Q^2$  bins), data projections are shown in Fig. 11 as examples. For complete projections, we refer to the proposal [88].

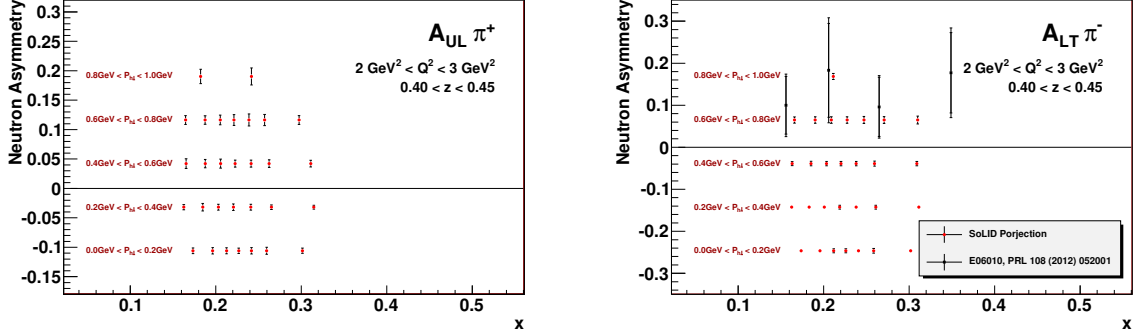


Figure 11: The left panel shows the projection for a typical  $z$  and  $Q^2$  bin ( $0.40 < z < 0.45$ ,  $2 \text{ GeV}^2 < Q^2 < 3 \text{ GeV}^2$ , one of the total 48  $z - Q^2$  bins) for the  $\pi^+$  single target spin asymmetry  $A_{UL}^{\sin(2\Phi_h)}$  measurement as a function of  $x$  with different ranges of the hadron transverse momentum labeled. The right panel shows the projection for the corresponding  $z - Q^2$  bin for the  $\pi^-$  double spin asymmetry  $A_{LT}^{\cos(\Phi_h - \Phi_S)}$  measurement. Also shown are the results from the 6-GeV experiment E06-010 [54].

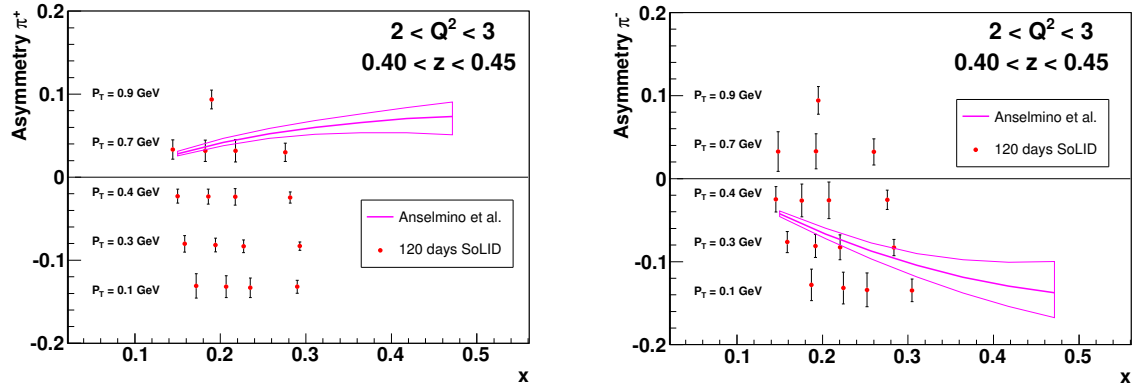


Figure 12: The left panel shows the projection for a typical  $z$  and  $Q^2$  bin ( $0.40 < z < 0.45$ ,  $2 \text{ GeV}^2 < Q^2 < 3 \text{ GeV}^2$ ) for the  $\pi^+$  Collins asymmetry measurement as a function of  $x$  with different ranges of the hadron transverse momentum labeled. The right panel shows the projection for the corresponding  $z - Q^2$  bin for the  $\pi^-$  measurement. Also shown are predictions of Collins asymmetries from Anselmino *et al.* [94] with model uncertainties.

**E12-11-108** Experiment E12-11-108 was approved 94 days of total beam time with 100 nA, 11/8.8 GeV electron beams on a 3-cm long, polarized  $\text{NH}_3$  target. The 8.8 GeV beam energy will



provide precision data on the radiative corrections along with the increased  $Q^2$  coverage. 90 days are for beam on a transversely polarized  $\text{NH}_3$  target including 7.5 days for dilution measurements, optics, and detector calibrations. Also 4 days are requested with a longitudinal target polarization to study the systematics of potential  $A_{UL}$  contamination. Although beam polarization is not required for the proposed SSA measurements, a longitudinally polarized beam will be used for a parasitic measurement of the  $A_{LT}$ , which can be used to access  $g_{1T}$ . In addition, there will be an overhead time of 26 days for regular target annealing which does not need an electron beam.

Projected data from E12-11-108 are binned into 4-dimensional  $(x, P_h, z, Q^2)$  bins. For a typical  $z$  and  $Q^2$  bin ( $0.40 < z < 0.45$ ,  $2 \text{ GeV}^2 < Q^2 < 3 \text{ GeV}^2$ ), data projections for Collins asymmetry measurements, left panel for  $\pi^+$  and right panel for  $\pi^-$ , are shown in Fig. 12 as examples. Also shown are predictions of Collins asymmetries from Anselmino *et al.* [94] with model uncertainties. For complete projections of E12-11-108, we refer to the proposal [89].

The combination of these three experiments will allow for accessing important information about TMDs from proton and neutron, and the flavor separation of the TMDs (transversity, Sivers, pretzelosity, and  $g_{1T}$ ) for u and d quark. A good example based on a study in Ref. [96] to demonstrate the impact of this program is shown in Fig. 13 in which the projected transversity distributions for u and d quarks are shown at a typical  $Q^2 = 2.4 \text{ GeV}^2$  based on the up-to-date knowledge of evolution of the transverse momentum dependent distribution and fragmentation functions. The expected improvement in the knowledge of the transversity distribution is enormous: from the wide error bands based on the current knowledge to the narrow bands from the SoLID program, and the access to the valence quark region, which has been essentially unexplored as of now. In fact the proposed SoLID SIDIS program will allow for studies of the  $k_T$  dependence, and the  $Q^2$  evolution of the TMDs also. Furthermore, the SoLID SIDIS program will provide precise information on the tensor charge of the nucleon, an important property of the nucleon like spin or magnetic moment, and is determined by the valence quarks inside the nucleon. A quantitative study [96] demonstrates that the SoLID SIDIS program will improve the accuracy of the tensor charge determination by one order of magnitude, and allows for benchmark tests of lattice QCD predictions. The high impact of these data on the extraction of the tensor charge of the u and d quark is shown in Fig. 14.

### 2.2.6 Comparisons with SBS and CLAS12 SIDIS programs

In Table 4, we compare the experimental conditions of the SIDIS experiments with SoLID, SBS and CLAS12. The values of solid angle coverage in the table are simplified descriptions. A more realistic acceptance from GEMC is used for the estimation of the physics impact. Compared with SBS, the statistics of SIDIS events with SoLID are much better due to the large acceptance. This will allow us to have 4-dimensional bins with SoLID, while SBS will only have 3-dimensional bins.

A comparison of the Figure of Merit (FOM), which is calculated by the sum of the inverse square of the statistical uncertainties of the SSA, is shown in Figure 15 and Figure 16. In these comparisons, we applied the same kinematic cuts of  $W > 2.3 \text{ GeV}$  and  $0.3 < z < 0.7$ . Compared with CLAS12, SoLID has higher statistics in smaller  $x$  region and has comparable (or slightly lower) statistics in larger  $x$  region. Compared with SBS, SoLID has higher statistics up to about  $x \sim 0.55$ , while SBS has more coverage in large  $x$  region.

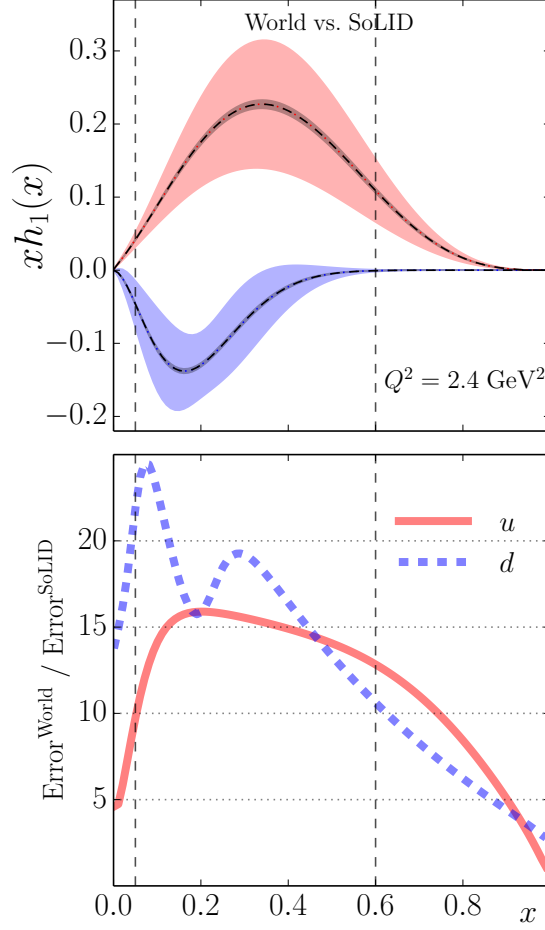


Figure 13: The impact on  $u$  and  $d$  quark transversity distributions by the SIDIS program using SoLID. The wide error bands show the current knowledge from the global analysis of the world data, and the narrow error bands show the SoLID projections. The lower panel shows the improvements, which are the ratios between the current errors and the projected errors.

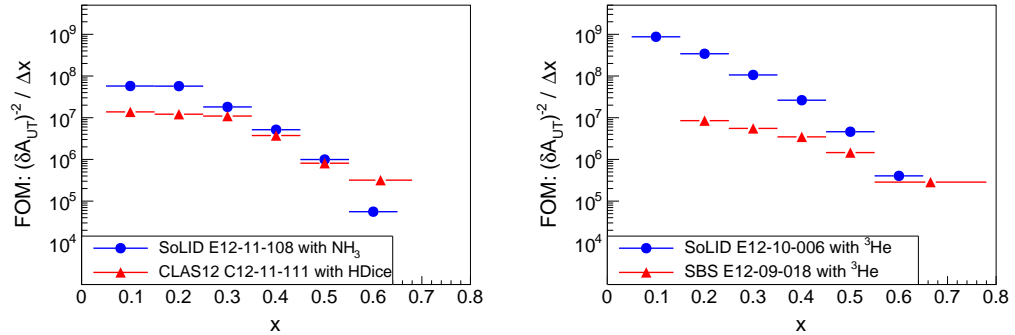


Figure 15: Comparison of the FOM at different  $x$  regions. SoLID SIDIS experiment with the proton target is compared with CLAS12 in the left panel. SoLID SIDIS experiments with the neutron target are compared to the SBS experiment in the right panel. In both comparisons, the same kinematic cuts of  $W > 2.3 \text{ GeV}$  and  $0.3 < z < 0.7$  are applied.



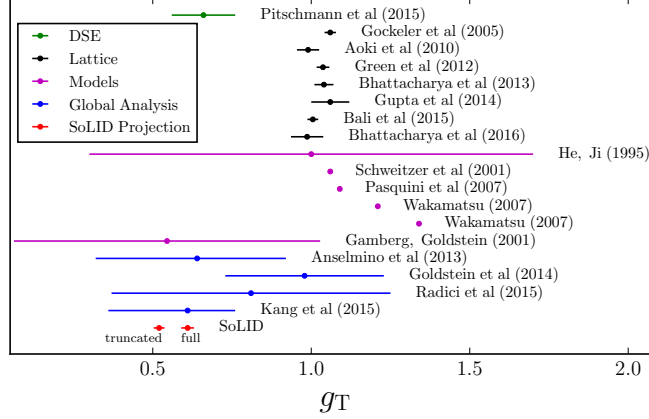


Figure 14: The impact of the projected SoLID measurement of the tensor charge together with current knowledge from models, Dyson-Schwinger equations, global analyses, and lattice QCD simulations.

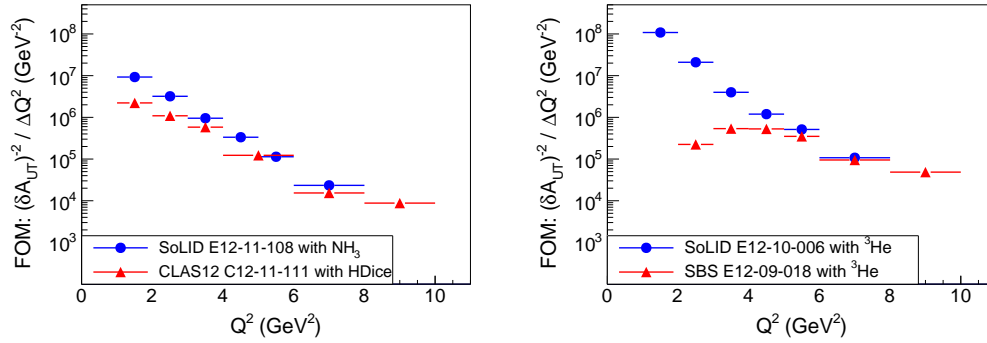


Figure 16: Comparison of the FOM at different  $Q^2$  regions. SoLID SIDIS experiment with the proton target is compared with CLAS12 in the left panel. SoLID SIDIS experiments with the neutron target are compared to the SBS experiment in the right panel. In both comparisons, the same kinematic cuts of  $W > 2.3$  GeV and  $0.3 < z < 0.7$  are applied.

The physics impact of SoLID is the precise measurement of the TMDs in the valence region. One highlight is the Collins SSA, which is related to the transversity distribution, which in turn is dominated by the valence quark distribution. It is related to quark transversity distribution, which is valence quark dominant. To compare the improvement on the determination of transversity, we model the transversity distributions with the recent global fit of [1], which includes the TMD evolution effect. We estimate the errors with the standard Hessian method [286]. The Hessian is the second derivatives of the  $\chi^2$  with respect to the parameters at the least  $\chi^2$  point. It reflects not only the uncertainties of the parameters but also the correlations of the parameters. The Hessian of the world data is obtained from the covariant matrix of the global fit [1]. The Hessians of SoLID, CLAS12, and SBS are calculated with the simulated data. To ensure that the SIDIS events are in the current fragmentation region, which can be described by TMD factorization, we adopt the recent theoretical study on the criteria of the current fragmentation kinematics [10] and only use the bins in the current fragmentation region to study the physics impact. The impacts on the transversity extrac-

	SoLID	SBS	SoLID	CLAS12
Experiment	E12-10-006 Approved (A)	E12-09-018 Approved (A-)	E12-11-108 Approved (A)	C12-11-111 Conditional
Targets	$^3\text{He}$ (“n”)	$^3\text{He}$ (“n”)	$\text{NH}_3$ (“p”)	HDice (“p”)
Polarization ( $P$ )	65% (60% in beam)	65% (<60% in beam)	70%	60%
Dilution ( $f$ )	0.15~0.3	0.15~0.3	0.13	0.33 $\times$ 80%
Luminosity ( $L \text{ cm}^{-2}\text{s}^{-1}$ )	$1.0 \times 10^{36}$	$2.7 \times 10^{36}$	$1.0 \times 10^{35}$	$1.4 \times 10^{33}$
Solid angle ( $\Omega_e \times \Omega_h \text{ sr}^2$ )	$0.482 \times 0.139$	$0.044 \times 0.063$	$0.482 \times 0.139$	$1.14 \times 1.16$

Table 4: Comparison of the experimental conditions of SoLID, SBS, and CLAS12.

tions are compared in Figure 17 and Figure 18. In the comparison, only statistical uncertainties are used to compare with CLAS12 and SBS. The improvement from SoLID data including systematic errors is also shown in Figure 18. To remove the model dependence as much as possible, we take the ratio between the prior uncertainties and the post uncertainties to show the improvements from the SoLID, CLAS12, and SBS SIDIS experiments. SoLID can improve the transversity uncertainty for  $u$  ( $d$ ) quark by a factor of 3 (7) over CLAS12, and by a factor of 5 (10) compared to SBS.

The tensor charge, which is the integral of transversity distributions, is a fundamental quantity in QCD. It describes the coupling between a nucleon and a tensor current. Note that in QCD, this correlation is different from the correlation between the longitudinal quark spin with the longitudinal spin of the nucleon which is measured by the structure function  $g_1$ . The impact of the determination of the tensor charge from SoLID, CLAS12, and SBS are compared in Table 5. The improvements are shown in two ways, the typical measured  $x$  region by JLab-12 experiments and the full  $x$  region.

	World vs. SBS+CLAS12	World vs. SoLID	SBS+CLAS12 vs. SoLID	World vs. SoLID including systematics
$\delta u^{\text{measured}}$	6.1	16	2.8	6.7
$\delta d^{\text{measured}}$	1.9	17	9.3	11
$\delta u^{\text{full}}$	5.4	16	3.0	5.9
$\delta d^{\text{full}}$	1.8	17	10	10

Table 5: Comparison of improvements to tensor charge extractions. “World” represents all world available data by 2015. In the first three comparisons, only statistical errors are used, while in the last comparison both statistical and systematic errors are included. The values in the table give the ratio between the prior error and the post error. The measured region is the integral over  $x$  from 0.05 to 0.6, and the full region is the integral over  $x$  from 0 to 1.

One of the advantages of SoLID SIDIS experiments is that the high statistics allows us to have four-dimensional bins. This will help study TMDs, which are three dimensional distributions. To show the impact of SoLID on TMD measurements, we take the Sivers function as an example. In the analysis, we do a global fit with both unpolarized multiplicity data and Sivers asymmetry data.

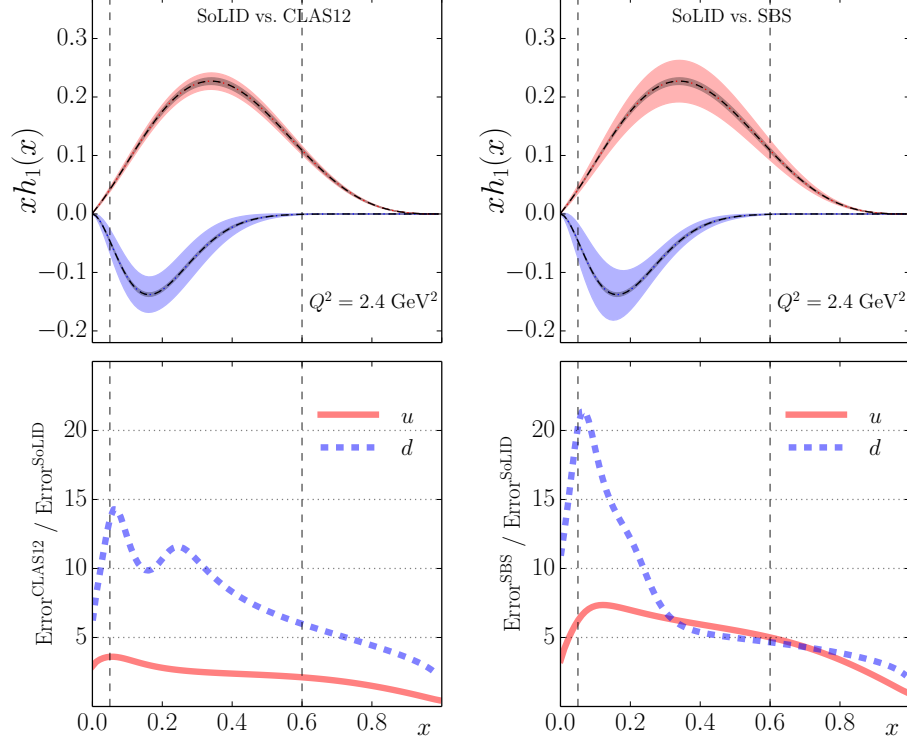


Figure 17: Comparisons of the impact on transversity extractions for up (red) and the down (blue) quarks, as the extension of published works [1, 2]. The left column shows the comparison between SoLID and CLAS12, and the right column shows the comparison between SoLID and SBS. In the upper panels, the light shaded bands show the uncertainties of the transversity function  $h_1(x)$  expected from SBS or CLAS12, and the dark shaded bands show the uncertainties expected from SoLID. The ratio of CLAS12 or SBS expected results to those from SoLID are shown in the lower panels. All results are plotted at a typical JLab12 scale  $Q^2 = 2.4 \text{ GeV}^2$ .

The fitting result is used as the input model for future SoLID, CLAS12, and SBS pseudo-data. The uncertainties from the world data and from inclusion of SoLID, CLAS12, and SBS are estimated in the same framework. Similar to the case of transversity extraction, we only select the bins that pass the kinematic cuts of the current fragmentation criteria. In Figure 19, we show the improvement from SoLID on the extraction of the Sivers function, and compare it with CLAS12 and SBS.

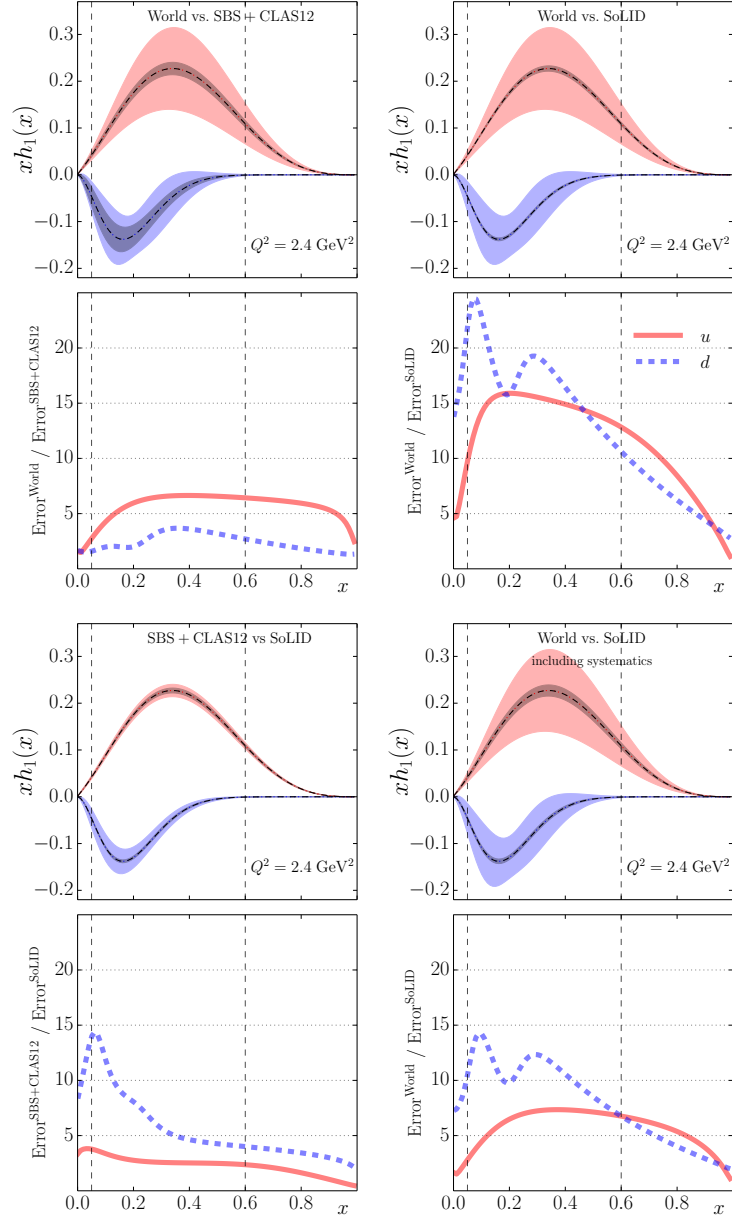


Figure 18: Comparison of the impact on the transversity extractions. The “World” represents all world available data by 2015. The upper left panel shows the improvement from future JLab12 data, i.e. SBS and CLAS12, before SoLID on the base of world available data by 2015. The upper right panel shows the improvements from SoLID data. The lower left panel shows the further improvement from SoLID data after the expected SBS and CLAS12 data. The lower right panel shows the improvements from SoLID data including the systematic uncertainties. The current uncertainties are from the global fit [1], and the future uncertainties are obtained by including the pseudo-data from these experiments with only statistical errors for the first three, and with both statistical and systematic errors for the last one. The curves in the lower panels show the improvement, which is the ratio between the prior uncertainties and the post uncertainties. The  $x$ -range between the two vertical dashed lines is directly measured by SoLID.

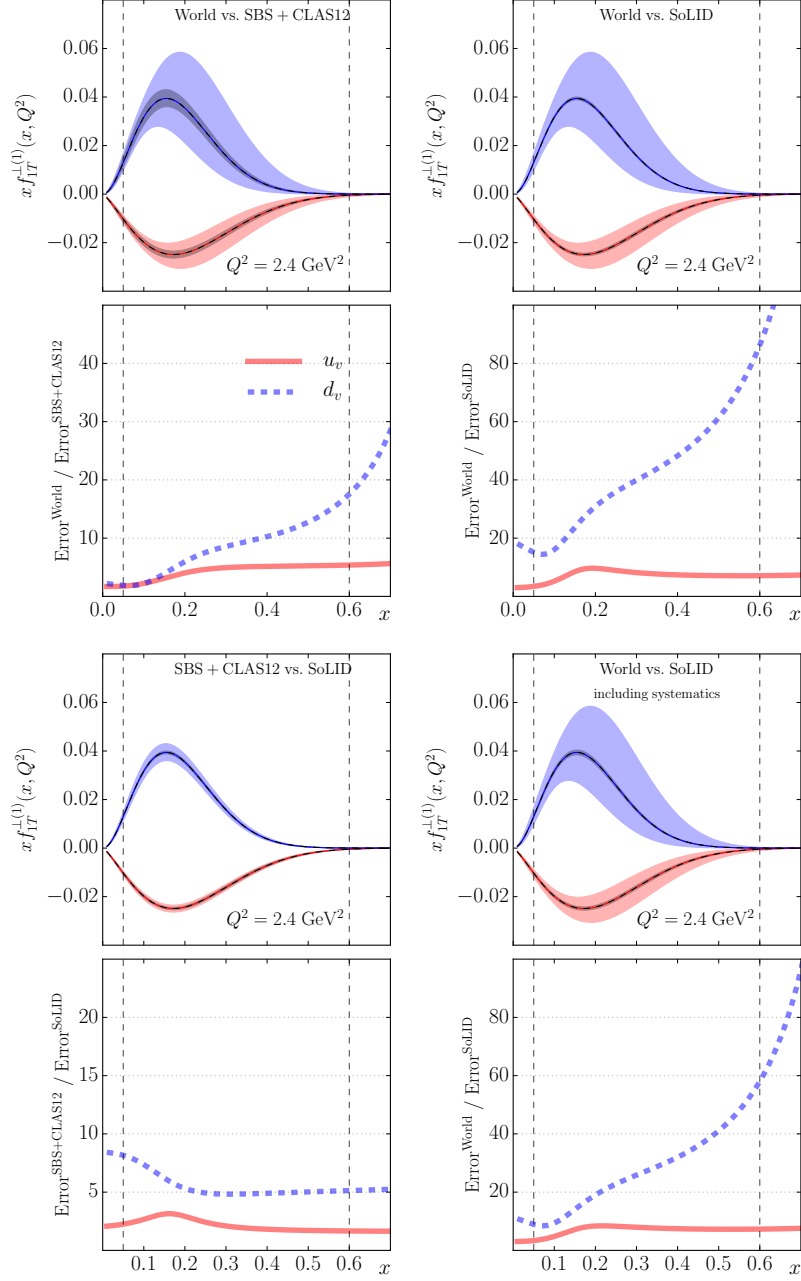


Figure 19: Comparison of the impact on the first transverse moment of the Siverson function. Labels are the same as those in Figure 18.

## 2.3 PVDIS Program

### 2.3.1 Motivation for PVDIS

The unique opportunities for experiments on parity violation at JLab with the 12 GeV upgrade were recognized in the NSAC long-range planning exercises. The experiment was approved by PAC 35. Quoting the PAC 35 report, “the PAC believes the mission of this and future experiments using SoLID are sufficiently important that the Laboratory should make every effort to assist in securing the necessary funding.”

We reiterate here the physics topics that become accessible with the advent of a longitudinally polarized 11 GeV electron beam via measurements of the parity-violating asymmetry  $A_{PV}$  in deep inelastic scattering (DIS) in the kinematic region of large Bjorken  $x = Q^2/2M\nu$ .  $A_{PV}$  is defined to be:

$$A_{PV} = \frac{\sigma_R - \sigma_L}{\sigma_R + \sigma_L} \quad (1)$$

where  $\sigma_R(\sigma_L)$  is the cross section for incident right-(left-) handed electrons.

The primary motivation of PVDIS is to search for new interactions beyond the Standard Model (SM). PVDIS is unique in that it is sensitive to fundamental axial-hadronic currents but does not have large radiative corrections that involve soft hadronic physics and are impossible to make reliably.

We propose to obtain data over a broad kinematic range, with  $x > 0.2$ ,  $2 < Q^2 < 10$ . With a deuterium target, the asymmetry is approximately independent of kinematics and insensitive to the structure function. However, it is possible that the following physics could be observed in our data:

1. Charge Symmetry violation (CSV) at the quark level.
2. Higher-twist effects in the parity-violating asymmetry. Significant higher-twist effects are observed in DIS cross sections, but in PVDIS large higher-twist contributions can only be due to quark-quark correlations.

If these effects are large, they will constitute an important discovery. If they are small, our test of the SM will be quite reliable.

It has been suggested that there is additional CSV in heavier nuclei. By obtaining data with a lead target, we could test this hypothesis. Such an effect would have profound implications for our understanding of the EMC effect.

By switching the target to hydrogen, we can also measure the  $d/u$  ratio in the proton, without requiring any nuclear corrections.

### 2.3.2 Review of the Theory

The general expression for  $A_{PV}$  for  $Q^2 \ll M_Z^2$  is [97]

$$A^{PV} = - \left( \frac{G_F Q^2}{4\sqrt{2}\pi\alpha} \right) \left[ g_A^e Y_1 \frac{F_1^{\gamma Z}}{F_1^\gamma} + \frac{g_V^e}{2} Y_3 \frac{F_3^{\gamma Z}}{F_1^\gamma} \right] = - \left( \frac{G_F Q^2}{4\sqrt{2}\pi\alpha} \right) (Y_1 a_1 + Y_3 a_3). \quad (2)$$

Here the  $F_i^\gamma$  are the electromagnetic structure functions and the  $F_i^{\gamma Z}$  are structure functions for the parity-violating interference term. The  $Y_i$  are functions of the kinematic variable  $y = \nu/E$  and the ratios of structure functions  $R^j(x, Q^2)$ :

$$Y_1(x, y, Q^2) = \frac{1 + (1-y)^2 - y^2(1-r^2/(1+R^{\gamma Z})) - 2xyM/E}{1 + (1-y)^2 - y^2(1-r^2/(1+R^\gamma)) - 2xyM/E} \left( \frac{1+R^{\gamma Z}}{1+R^\gamma} \right) \quad (3)$$

$$Y_3(x, y, Q^2) = \frac{1 - (1 - y)^2}{1 + (1 - y)^2 - y^2(1 - r^2/(1 + R^\gamma)) - 2xyM/E} \left( \frac{r^2}{1 + R^\gamma} \right) \quad (4)$$

The above expressions are quite general.

In order to account for possible violations of the Standard Model, it is essential to express the parity-violating part of the electron-hadron interaction in terms of general phenomenological four-fermion contact interactions

$$\mathcal{L}^{PV} = \frac{G_F}{\sqrt{2}} [\bar{e}\gamma^\mu\gamma_5 e (C_{1u}\bar{u}\gamma_\mu u + C_{1d}\bar{d}\gamma_\mu d) + \bar{e}\gamma^\mu e (C_{2u}\bar{u}\gamma_\mu\gamma_5 u + C_{2d}\bar{d}\gamma_\mu\gamma_5 d)]$$

with additional terms as required for the heavy quarks. Here  $C_{1j}$  ( $C_{2j}$ ) gives the vector (axial-vector) coupling to the  $j^{th}$  quark. For the Standard Model:

$$C_{1u} = g_A^e g_V^u \approx -\frac{1}{2} + \frac{4}{3} \sin^2 \theta_W \approx -0.19 \quad (5)$$

$$C_{1d} = g_A^e g_V^d \approx \frac{1}{2} - \frac{2}{3} \sin^2 \theta_W \approx 0.34 \quad (6)$$

$$C_{2u} = g_V^e g_A^u \approx -\frac{1}{2} + 2 \sin^2 \theta_W \approx -0.030 \quad (7)$$

$$C_{2d} = g_V^e g_A^d \approx \frac{1}{2} - 2 \sin^2 \theta_W \approx 0.025 \quad (8)$$

The numerical values include electroweak radiative corrections. The key point is that the  $C_{1i}$  are about an order of magnitude larger than the  $C_{2i}$ , which makes the  $a_1$  term dominant. Recently, the JLab PVDIS collaboration published in the journal Nature[98] the result that the  $C_{2i}$ 's are indeed nonzero. The results are shown in Figure 20.

As recently pointed out by Mantry, et al., [99] for the deuteron where  $I = 0$ ,  $Y_1 = 1$  and

$$a_1^D(x) = g_A^e \frac{F_1^{D\gamma Z}}{F_1^{D\gamma}} = a_1^D(x) = \frac{6}{5} (2C_{1u} - C_{1d}) \left( 1 + \frac{2s^+}{u^+ + d^+} \right)$$

The only corrections to these formulae are physics beyond the Standard Model, CSV and quark-quark correlations, which form the motivation for the experiment, and known corrections including strange quarks and target mass corrections.

For the  $a_3$  term, we use the quark-parton model (QPM), which describes the structure functions in terms of parton distribution functions (PDF's) functions  $f_i(x)$  ( $\bar{f}_i(x)$ ), which are the probabilities that the  $i^{th}$  quark (antiquark) carries a fraction  $x$  of the nucleon momentum. With the definitions  $f_i^\pm = f_i \pm \bar{f}_i$ ,  $y = \nu/E$ , the structure functions are given by

$$F_1^\gamma = \frac{1}{2} \sum_i e_i^2 (f_i(x) + \bar{f}_i(x))$$

$$F_1^{\gamma Z} = \sum_i e_i g_V^i (f_i(x) + \bar{f}_i(x))$$

$$F_3^{\gamma Z} = 2 \sum_i e_i g_A^i (f_i(x) - \bar{f}_i(x)),$$

where  $e_i$  is the electromagnetic charge of the  $i^{th}$  quark. Then

$$a_3^D(x) = \frac{g_V^e}{2} \frac{F_3^{\gamma Z}}{F_1^\gamma} = 2 \frac{\sum_i C_{2i} e_i f_i^-(x)}{\sum_i e_i^2 f_i^+(x)} = \frac{6}{5} (2C_{2u} - C_{2d}) \left( \frac{u^+ - d^+}{u^+ + d^+} \right) + \dots$$

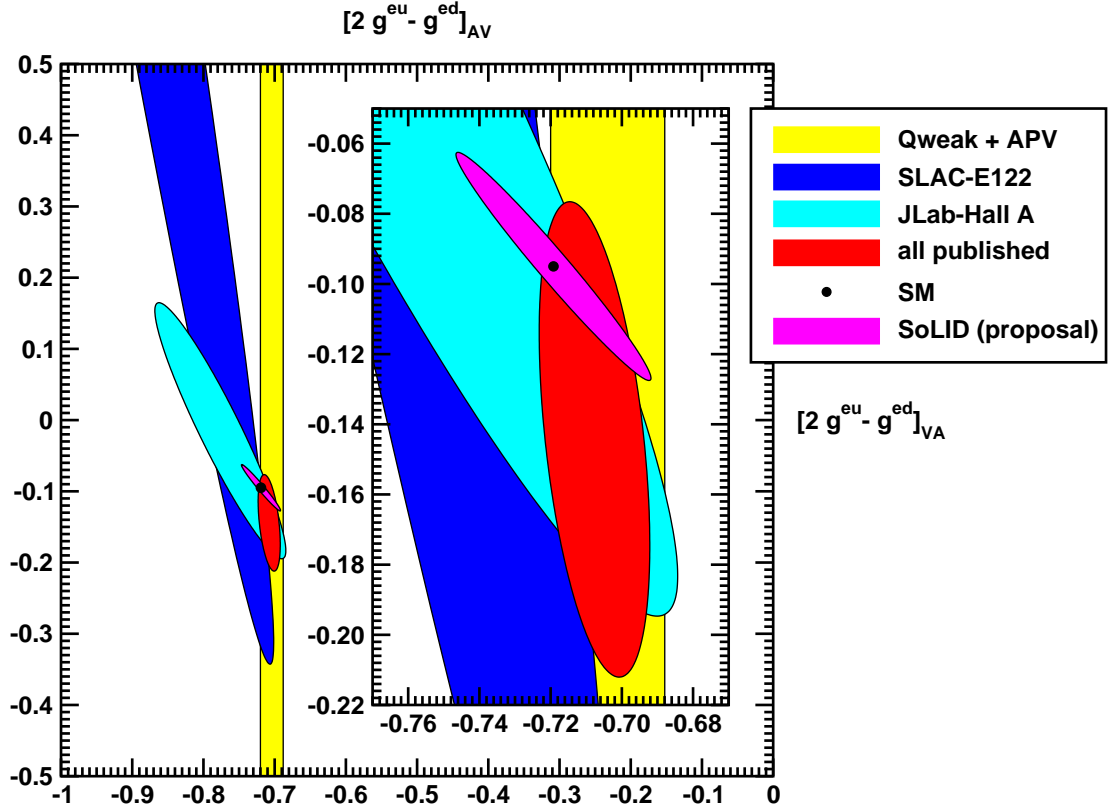


Figure 20: Results from the JLab PVDIS collaboration together with the projected results from the SoLID PVDIS experiment.

Contributions due to higher twist to this term can be obtained from neutrino scattering. The contribution of  $R^\gamma$  to  $A_{PV}$  is given in the  $Y_3$  factor.

The key is that since  $(2C_{2u} - C_{2d})$  is small, there is less sensitivity to the hadronic physics, whereas  $(u^+ - d^-)(u^+ + d^+) \sim 1$  so that we are sensitive to new physics contributions to the  $C_{2i}$ .

The main goal of the experiment is to place a narrow error band on the  $C_{2i}$  plots of Figures 21 and 20. An example of new physics that can contribute to the  $C_{2i}$  but not to the  $C_{1i}$  that have been precisely measured by Qweak and atomic parity violation in Cs, is a leptophobic  $Z'$  [100] as illustrated in Fig. 22. At the LHC, such a particle would be swamped by background. The proposed data will also improve the mass limits for generic models for composite for quarks and leptons [101] as shown in Figure 23.

### 2.3.3 Charge Symmetry Violation

The subtle violation of fundamental symmetries in hadronic systems can often provide important insights into the dynamics at work in those systems. The famous Nolen-Schiffer anomaly has played a significant role in nuclear structure for decades. When it comes to hadron structure charge symmetry violation is of great interest because of its link to the role of di-quarks in non-perturbative parton distribution functions [102–104].

The NuTeV experiment published a discrepancy with the Standard Model [105] with a significance of about three sigma. The result stirred a lot of controversy, resulting in a serious re-evaluation



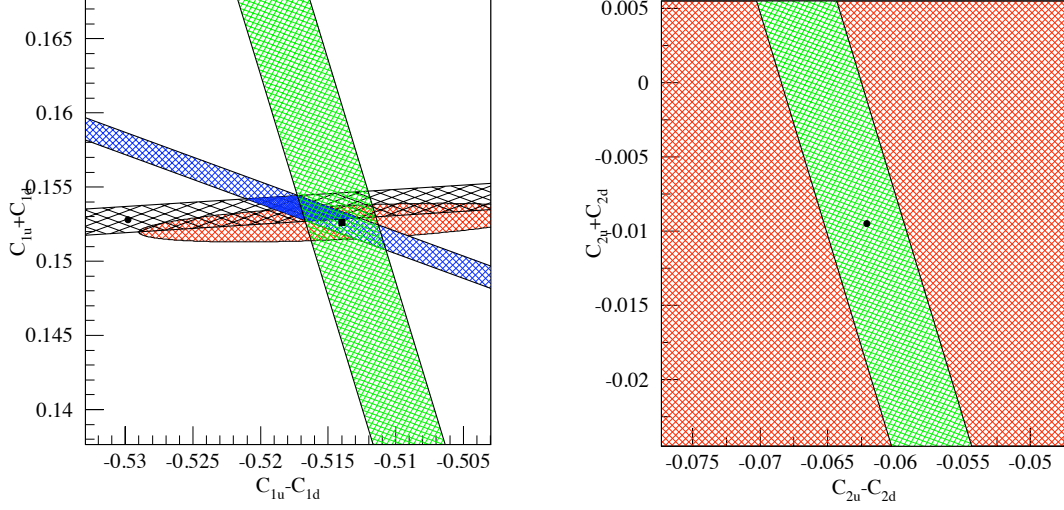


Figure 21: Green band: limits projected for this experiment. The blue band is the Qweak experiment and the black is the Cs APV.

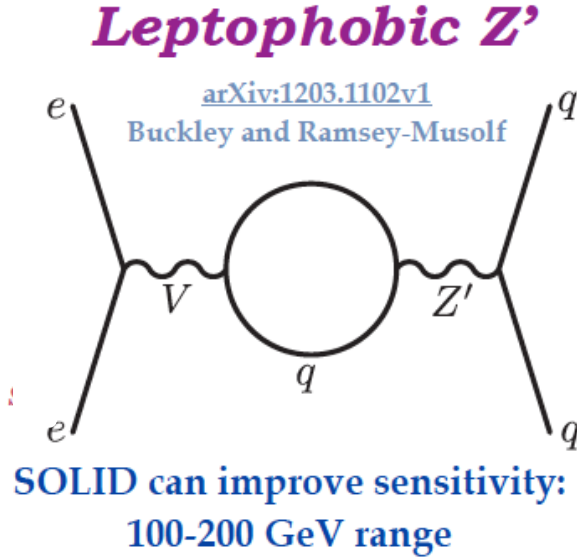


Figure 22: Diagram of a leptophobic  $Z'$  that can contribute to the  $C_{2i}$  and few other observables.

of the work. Additional corrections, including changes in the Cabibbo angle, strange sea, and improved radiative corrections, have recently been made, but have changed the result very little.

One possible explanation of the NuTeV result is charge symmetry violation (CSV) in the PDF's. This was overlooked in the NuTeV analysis, even though estimates which suggested how important it could be had existed in the literature for almost a decade [103, 104]. Various authors [106–108] have also presented the case that this is a reasonable explanation.

Our experiment is also sensitive to CSV. If the  $x$ -dependence of the CSV falls slower than the

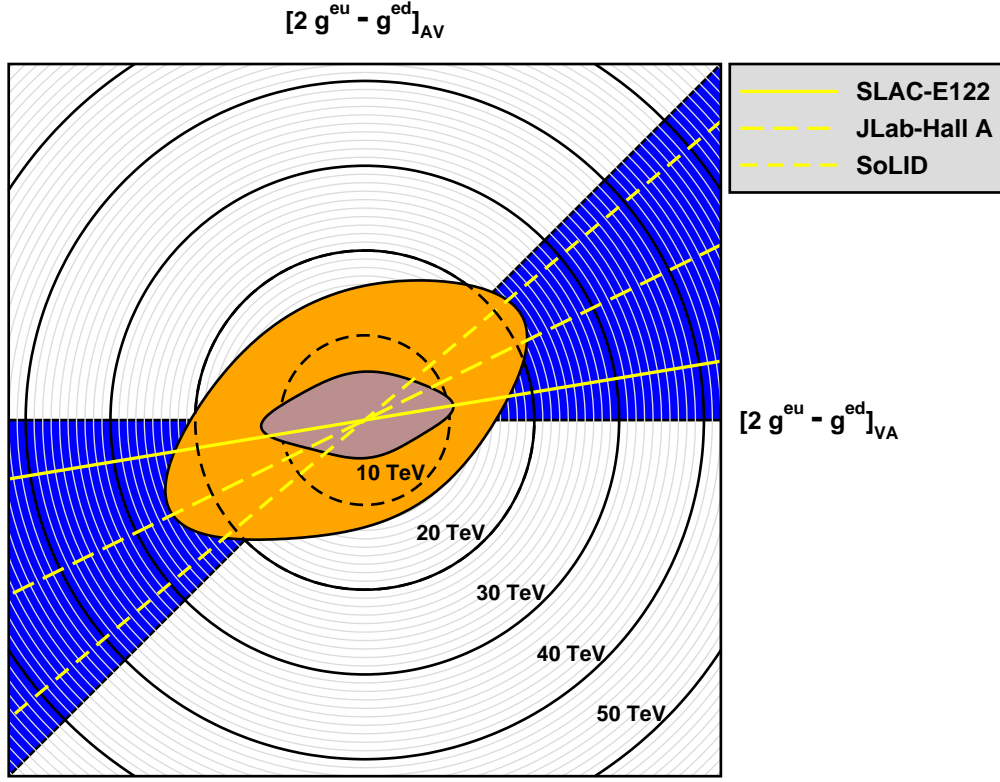


Figure 23: Polar plot for limits on composite models. The gray ellipse includes the published results from the PVDIS and Qweak collaborations. The orange ellipse gives the projected limits with the full Qweak statistics and the SoLID data.

PDF's as suggested by the curves in Figure 24 our asymmetry should display a clear  $x$ -dependence. Moreover, these results will provide an important test of the CSV explanation for NuTeV.

Another interesting possible contribution to the NuTeV anomaly is the isovector EMC effect [109], which occurs for heavy nuclei. Measuring PVDIS in a target such as Pb would be able to demonstrate this effect.

### 2.3.4 Higher Twist

A recent paper has examined the contribution of higher twist (HT) effects to the dominant  $Y_1 a_1$  term in  $A_{PV}$ . [99] The correction can be parameterized as a fractional contribution  $R_1(HT)$  by

$$Y_1 a_1 \approx Y_1 a_1 (1 + R_1(HT) + \dots)$$

where the ellipsis refers to other corrections including CSV. It turns out that the only contribution comes from the operator

$$\mathcal{O}_{ud}^{\mu\nu} = \frac{1}{2} [\bar{u}(x) \gamma^\mu u(x) d(0) \gamma^\nu d(0) + (u \leftrightarrow d)]$$

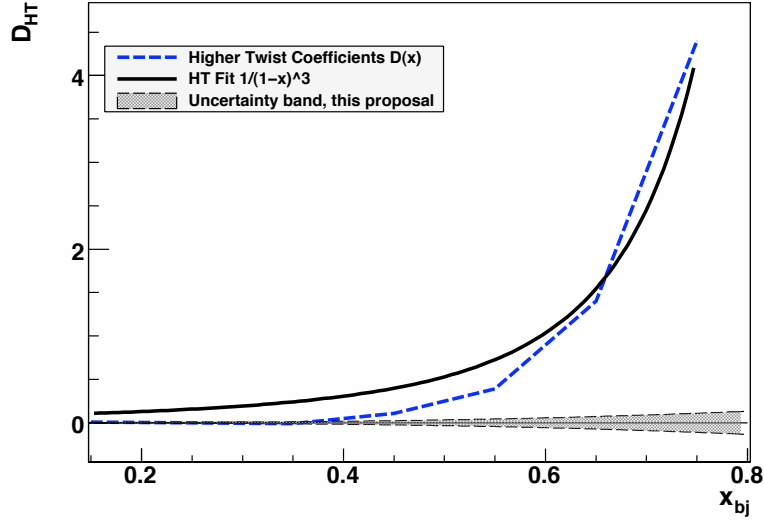


Figure 24: Possible contribution to  $A_{PV}$  due to CSV

which arises only from quark-quark correlations, or in other words, di-quarks in the nucleon. Higher twist contributions involving gluons cancel in the ratio. The special feature of  $A_{PV}$  is that it is the only practical experiment that can isolate higher twist due to four quarks.

The result is

$$R_1(HT) = -\frac{4}{5} \frac{[(9 - 20 \sin^2 \theta_W) F_1^{\gamma;4q} - 5 F_1^{\gamma Z;4q}]}{(1 - \frac{20}{9} \sin^2 \theta_W)[u_p(x) + d_p(x)]}$$

where  $F_1^{\gamma;4q}$  and  $F_1^{\gamma Z;4q}$  are the four-quark higher twist contributions to the structure functions.

### 2.3.5 Data Sample and analysis

The observation of CSV is possible with our apparatus only if the effect varies with  $x$ . An  $x$ -independent CSV effect would be indistinguishable from a change in the  $C_{1q}$ 's. It is quite natural, however, to expect that the  $x$ -dependence is similar to that shown in Figure 24, and we will make that assumption in our further discussion. From observations of higher-twist contributions to DIS cross sections, it is also natural to assume that  $Q^2$ -dependent effects will also increase with increasing  $x$ .

If indeed either higher twist effects or CSV are clearly seen, the experiment will be a success. If they are absent, we plan to untangle the effects of hadronic and electroweak physics by fitting the asymmetries to a function of the form

$$A_{PV}^D = A_{PV}^{EW} \left( 1 + \beta_{HT} \frac{1}{(1-x)^3 Q^2} + \beta_{CSV} x^2 \right) \quad (9)$$

Since the size of the hadronic effects is small, the sensitivity to the exact form is not important. The resulting statistical errors on the fit parameters are:

$$\delta A_{PV}^{EW} / A_{PV}^{EW} = 0.3\%; \quad \delta \beta_{HT} = 0.0026; \quad \delta \beta_{CSV} = 0.017$$

With this method, we use the full statistical power of the data set. However, the result has some sensitivity to the exact form of the chosen fitting functions. Under the scenario where the hadronic

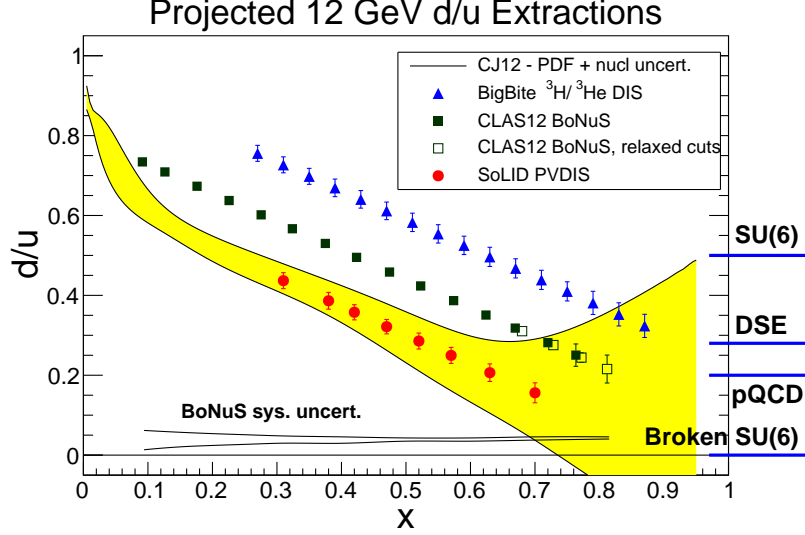


Figure 25: Anticipated precision for  $d/u$  measurement with SoLID as well as other proposed experiments.

effects are small, these errors are negligible as long as we assume that CSV and higher twist effects depend strongly on  $x$ , as expected. The one-sigma band for the CSV term is plotted in Figure 24.

If the pattern of higher twist effects is the same for  $A_{PV}$  as it is for the cross sections, then at  $x = 0.6$  the asymmetries at the different  $Q^2$  values will differ by 15%. In that scenario, the rapid  $x$ -dependence of the higher-twist coefficients for the cross section would imply that higher twist effects would still be negligible at  $x = 0.4$ . With a comparable  $x$ -dependence, a  $Q^2$ -dependent effect as small as  $\sim 3\%$  of the effect seen in cross-section measurements would be easily identifiable given our statistical precision.

**Measuring  $d/u$  at high  $x$**  Hydrogen is another useful target. Since it is not isoscalar, the structure functions do not cancel in the expression for  $a(x)$ . In particular,

$$a(x) \approx \frac{3}{4} \left[ \frac{6C_{1u}u(x) - 3C_{1d}d(x)}{u(x) + \frac{1}{4}d(x)} \right] \sim \left[ \frac{u(x) + 0.912d(x)}{u(x) + 0.25d(x)} \right]$$

and we see that  $a(x)$  is sensitive to the ratio  $d/u$ . The determination of this for the proton is a topic of considerable interest at large values of  $x$  [110–113]. The ratio is difficult to determine from cross section data because at large  $x$  complicated nuclear physics effects become important for deuterium targets. Alternative methods include comparing  $^3\text{He}$  and tritium or detecting the recoil proton from deuteron. Projected errors for all three approaches are shown in Fig. 25.

### 2.3.6 Beam Time and Projections

For the deuterium data, we have based our sensitivity on 180 days of production running at  $50 \mu\text{A}$ , with 1/3 of the data at 6.6 GeV and the rest at 11 GeV. Approximately 27 additional days, run at various currents, will be required for checkout and calibrations. An additional 18 days will be required at 4.4 GeV and  $50 \mu\text{A}$  for radiative correction measurements. The total beam request at

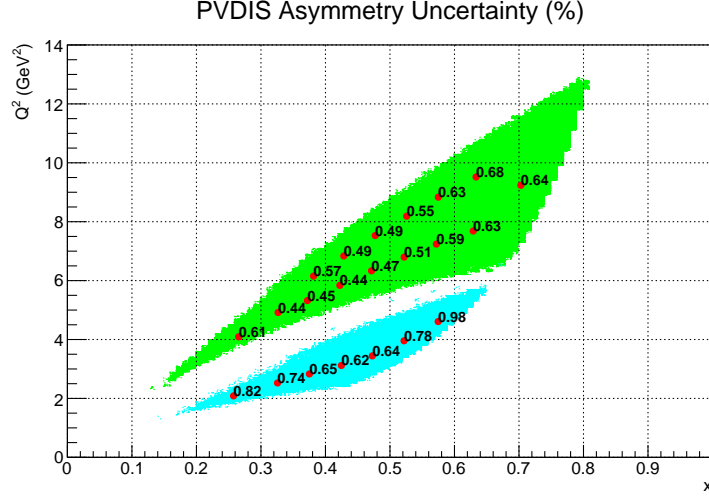


Figure 26: Anticipated statistical precision for  $A_{PV}$  in percent versus  $Q^2$  and  $x$ . 11 GeV data (green region) are based on a simulation including the electron calorimeter trigger. For the 6.6 GeV data the effect of the trigger is estimated.

all energies for the deuterium measurement is 225 days, with about 25 of those days run mostly at reduced beam currents. Projected statistical uncertainties in  $A_{PV}$  are shown in Fig. 26.

For the hydrogen measurement, 90 days are needed for production data at 11 GeV, about 9 days are required at 4.4 GeV to control radiative corrections and another 14 days will be required for calibration. The running time requested for hydrogen totals to 113 days. We have been approved for 180 days total. The plan is to first take half the deuterium data. If nothing exciting appears, we will switch to hydrogen.

In the future, we would also anticipate requesting an additional comparable run for a heavy nucleus such as Pb.

## 2.4 $J/\psi$ Program

### 2.4.1 Motivation

One of the fundamental goals of modern nuclear physics is to understand hadrons and nuclei starting with the basic ingredients of QCD namely quarks and gluons and their interactions. While significant progress has been made in exploring the theory in its perturbative region much remains to be understood in the strong region, particularly where gluonic exchanges dominate. Strong gluonic field configurations and interactions are responsible for most of the mass of nucleons and nuclei. Fundamental approaches such as lattice QCD, effective field theories or dual string theories (that would match QCD) could in principle shed light on confinement of hadrons and perhaps make predictions of novel phenomena of strong interactions.

We plan to explore this strong interaction using a particular system that emphasizes the multi-gluon exchange between two color neutral particles which do not share a common valence quark, namely nucleons/nuclei and charmonia. It has long been argued that the force acting between nucleon/nucleus and  $J/\psi$  is an attractive force, which has negligible mesonic ( $D\bar{D}$ ) or multi-mesonic ( $\rho\pi$ ) exchange contribution at low energies [114]. Since the nucleon/nucleus and  $J/\psi$  are color neutral, this force is dubbed as color Van der Waals force in analogy with the atomic-molecular physics case. This situation is unique in nuclear physics where a force exchanged between nucleons or hadrons is purely gluonic especially at low energy. A direct consequence of such an attractive force is the possible existence of a nuclear bound quarkonium state which was proposed more than 20 years ago by Brodsky, Schmidt and de Teramond [115] but has yet to be observed. A calculation using the operator product expansion (OPE) [116] to describe the low energy interaction of quarkonium with nuclei, in the limit where the mass of the charm quark is infinite, found that the  $J/\psi$  binds in nuclear matter with about 10 MeV but the authors caution about possible large corrections due to confinement effects.

Due to the lack of experimental data, a timid but sustained theoretical activity on the subject followed over the past twenty years. For example, Kaidalov and Volkovitsky [117] argued that S-wave quarkonia can be found in nuclei with  $A \geq 10$  and with binding energy of few MeV, while de Teramond et al. [118] in an update to his original paper with Brodsky [115] estimated a binding energy of 2 MeV in  $^{12}\text{C}$  and 10 MeV in  $^{208}\text{Pb}$ , while Shevchenko [119] pointed in a later work that the interaction of charmonium-nucleon is so small that the potential depth for nuclear bound state may only be possible for nuclei with  $A > 200$ . Applying QCD sum rules Hayashigaki [120] finds a 4 to 7 MeV binding of the  $J/\psi$  in nuclear matter. Yokokawa, Sasaki, Hatsuda and Hayashigaki [121] performed a first lattice study in the quenched approximation of low energy charmonium-hadron interaction to determine the scattering length. But more recently Kawanai and Sasaki [122] calculated the charmonium-nucleon potential from the equal-time Bethe-Salpeter amplitude through the effective Schrödinger equation and found that the charmonium-nucleon potential is weakly attractive at short distances and exponentially screened at large distances. Finally, Tsushima, Lu, Krein and Thomas [123, 124] have recently explored the  $J/\psi$ -nuclear bound states and found that the attractive potential that originate from the  $D$  and  $D^*$  meson loops in the  $J/\psi$  in nuclear medium should produce bound states.

Many of the  $J/\psi$  photoproduction experiments that have been performed at high photon energies and low  $t$  or in the case of electroproduction at large center of mass energy  $s$  and low  $t$  (see Refs. [125–132]) are usually considered as a diffractive production. Experiments in the threshold region are few and were performed soon after the discovery of the  $J/\psi$  particle more than 35 years ago [133–136]. In particular, the measurements of Cornell [134] and SLAC [136] show large discrepancies at photon energy around 10 GeV.

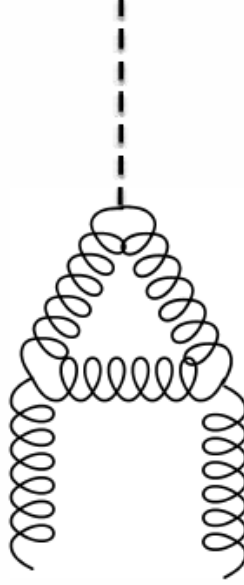


Figure 27: Anomaly diagram which dominate the cross section interaction at threshold.

It is fair to say that not much is known in the region where the energy of the photon is just above 8.2 GeV and where  $t$  is about 2 GeV, namely the threshold region. With Jefferson Lab at 12 GeV, we enter a new kinematic domain where the electro/photo-production of charmed hadrons near threshold becomes possible. It is precisely a region well suited for the investigation of the QCD Van der Waals interaction, since as we approach the threshold and due to the conformal scale anomaly of the low energy  $J/\psi$ -nucleon interaction [137, 138] the non-perturbative part of the interaction vanishes more slowly than the perturbative part. In his paper of 1998 [138], Kharzeev considered explicitly the possible enhancement of the threshold cross section due to this conformal scale anomaly which corresponds to a diagram where the coupling of the quarkonium to the nucleon occurs through triangle gluonic lines (see Fig. 27). As shown in Fig. 28, the scattering amplitude in the threshold region is also dominated by its real part in contrast to the case of high energy.

Later Brodsky, Chudakov, Hoyer and Laget [139] discussed the photoproduction of charm near threshold and invoked the two-gluon exchange mechanism in the production. These authors also considered the possible enhancement of the cross section at threshold due to a strong interaction beyond two-gluon exchanges as shown in Fig. 29. Whereas Sibirtsev, Krewald and Thomas [140] attributed the mechanism of the  $J/\psi$  photoproduction at low energies and large  $t$  to a mechanism different from pomeron or two-gluon exchange. They considered the possibility of the exchange of an axial vector trajectory that couples with the axial form factor of the nucleon in this case also enhancing the cross section at threshold.

At first, the charmonium production near the threshold region would not seem to lend itself to calculations using pQCD similar to the case of deep inelastic scattering at large  $Q^2$ . However, a closer look reveals a new scale at play, namely the mass of heavy quarks, which when compared to  $\Lambda_{QCD}$  enables a perturbative approach to evaluate the scattering amplitude of the process. This fact was used a while ago to derive charm photoproduction sum rules in a way similar to deep inelastic scattering [141–143].

In the reaction  $\gamma^* + N \rightarrow J/\psi + N$ , the production mechanism at threshold can be viewed in a

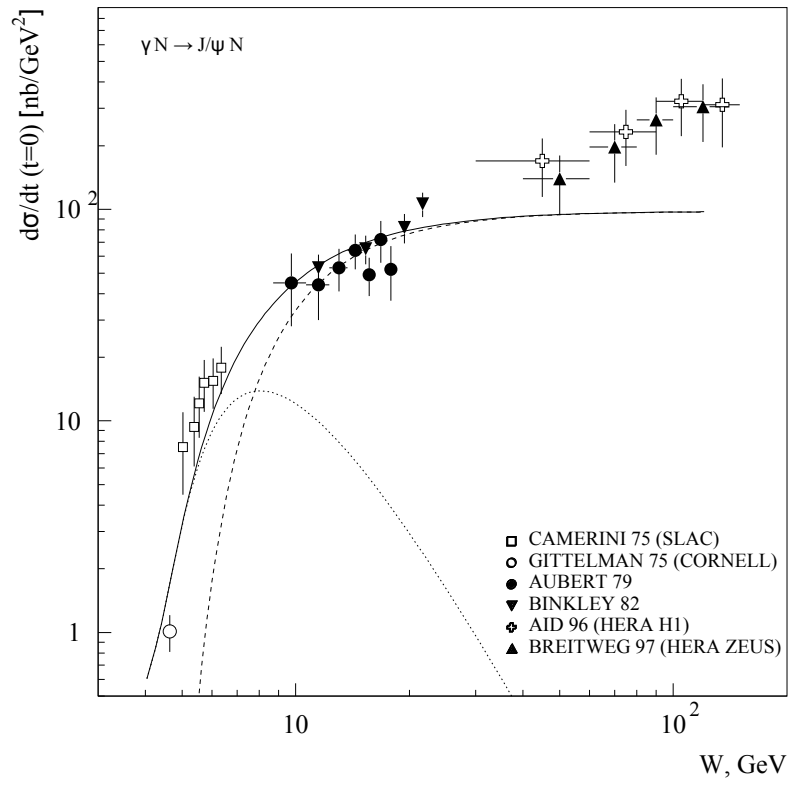


Figure 28: Forward  $J/\psi$  photoproduction data compared to the results of [138] with (solid line) and without (dashed line) the real part of the amplitude.



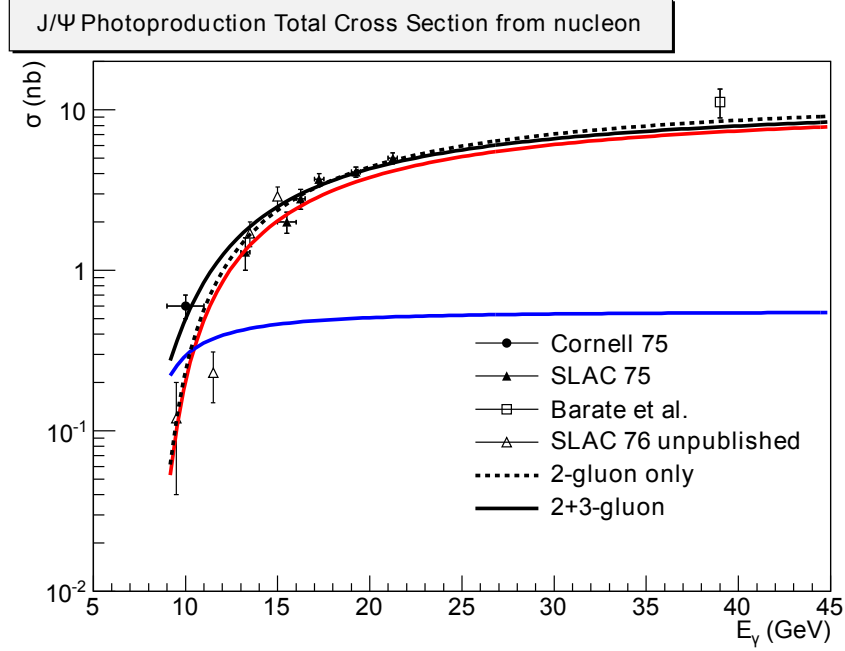


Figure 29: The 2-gluon model is shown as dotted black line. The (2+3)-gluon model is shown as solid black line. Furthermore, the 2-gluon contribution and 3-gluon contribution in the (2+3)-gluon model are shown as red and blue lines as well. Data are from “Cornell 75” [134], “SLAC 75” [133], “SLAC 76” [136] and “Barate et al.” [128].

way similar to the  $J/\psi$  elastic scattering off a nucleon at small relative velocity. The coupling of the soft gluonic fields to the nucleon, at low  $Q^2$  is determined by the low-energy theorem in QCD based on the anomaly in the trace of the energy-momentum tensor. The  $J/\psi$ -nucleon scattering amplitude is proportional to the nucleon matrix element of the following gluon operator [144]:

$$\langle N | \frac{1}{2} \vec{E}^a \cdot \vec{E}^a | N \rangle = \frac{4\pi^2}{b} \langle N | \theta_\mu^\mu | N \rangle + 2\pi\alpha_s \langle N | \theta_G^{00} | N \rangle, \quad (10)$$

where  $\vec{E}^a$  represents the chromo-electric field,  $\theta_G^{\mu\nu}$  is the energy-momentum tensor of the gluon field,  $\theta_\mu^\mu$  is the anomalous trace of the full energy-momentum tensor in QCD in the chiral limit,  $b$  is the coefficient in the QCD beta function with three light (massless in the chiral limit) quarks and  $\alpha_s$  is the QCD coupling.

It is argued [144] that this matrix element is bound by

$$\langle N | \frac{1}{2} \vec{E}^a \cdot \vec{E}^a | N \rangle \geq \frac{4\pi^2}{b} 2m_N^2 \quad (11)$$

In a measurement of electroproduction close to the threshold region, and unlike at high energy, the real part of the scattering amplitude contribution dominates compared to the imaginary part even though the allowed exchanges are purely gluonic. This contribution probes the matrix element represented by  $\langle N | \theta_\mu^\mu | N \rangle = 2m_N^2$ . Hence, in a threshold measurement we probe the conformal anomaly contribution to the low energy  $J/\psi - N$  interaction comparable to a Higgs-like coupling<sup>1</sup>.

<sup>1</sup>The coupling of the contact term is sensitive to the entire mass of nucleon, and as such is similar to the Higgs coupling.

Furthermore, the determination of an upper limit of the strength of this interaction will help determine whether or not a nucleon- $J/\psi$  bound state due to the Van der Waals color forces would exist.

#### 2.4.2 Program Overview

The high luminosity and large solid angle offered by the Jefferson Lab 12 GeV energy upgrade combined with the SoLID detector in Hall A is a unique tool to start an investigation program of the  $J/\psi$ -nucleon interaction.

In a first phase, measurements of the cross section of electro- and photo-production of  $J/\psi$  on a nucleon near threshold will take place with experiment E12-12-006[151] using SoLID. These measurements at threshold have not been revisited since the 70s. The precision and energy range close to threshold of the proposed measurements will best probe the possible enhancement of the cross section due to the contribution of the conformal anomaly very close to the threshold photon energy of  $J/\psi$  production. Threshold enhancements due to on-shell rescattering or quasi-bound states around threshold have been observed in several processes such as  $e^+e^- \rightarrow p\bar{p}, \Lambda\bar{\Lambda}, \Sigma^0\bar{\Sigma}_0, \Lambda\bar{\Sigma}_0$  [145] as well as in the  $J/\psi$  radiative decays, e.g.  $J/\psi \rightarrow p\bar{p}\gamma$  [146]. The experiment E12-12-006 aims at observing such enhancement in the  $J/\psi$ -proton system and offers the capability to explore the region below threshold if there are hints of an enhancement of the cross section just above threshold. Furthermore, the proposed cross section measurement could also shed light on the existence of predicted super-heavy  $N^*$  with hidden charm with a mass around 4.3 GeV [148].

In a second phase we shall explore the interference of the Bethe-Heitler amplitude with that of the  $J/\psi$  electroproduction to attempt a determination of the relative contribution of the real and the imaginary part of the scattering amplitude. Moreover, a study of the angular distribution of the  $J/\psi$  decay can reveal whether the  $J/\psi$  was originally produced from an octet or singlet state. Recently a phenomenological analysis of the forward  $J/\psi - p$  scattering amplitude within a dispersive framework [147] resulted in a  $\psi$  binding energy in nuclear matter of  $2.7 \pm 0.3$  MeV. The latter number uncertainty would be dramatically improved with more accurate cross section data in the threshold region. Furthermore, in the same reference a path towards unraveling the ratio of real to imaginary part of the  $J/\psi$ -nucleon scattering amplitude is described through the measurement of the  $\gamma p \rightarrow e^+e^-p$  forward-backward asymmetry in the vicinity of the  $J/\psi$  resonant amplitude. This forward-backward asymmetry is sizable due to the interference of the Bethe-Heitler amplitude with the  $J/\psi$  production amplitude.

Finally, studies of  $J/\psi$  production and propagation in the nuclear medium is the natural extension of the proposed measurements on a nucleon. The study of multi-gluon QCD Van der Waals forces in nuclei is believed to shed new light on their possible role in  $J/\psi$ -nuclear bound states [115, 115–122]. Another related challenge is the in-medium properties of charmonia as well as the possible restoration of the chiral symmetry in the nuclear medium, which is closely connected to the modifications of masses and widths of mesons when embedded in the nuclear environment [123]. For these studies, it is important to find the appropriate kinematical conditions to produce  $J/\psi$  near rest, or with small momentum relative to the nucleus. Therefore, measurements near threshold and even sub-threshold look promising [149].

At JLab Hall C, a photoproduction experiment (E03-008) was performed in the *subthreshold* regime using the CEBAF at 6 GeV. Unfortunately no signal was observed after one week of beam on a  $^{12}\text{C}$  target [149]. This experiment allowed to set a limit on the cross section, which was found to be consistent with the quasi-free production. The experiment used a bremsstrahlung beam produced on a copper radiator by the 6 GeV incident electron beam. The pair of spectrometers (HMS and SOS) of Hall C were used to detect the pair of leptons resulting from the decay of the  $J/\psi$ . A

proposal "A-dependence of  $J/\psi$  photoproduction near threshold" [150] for the 12 GeV upgrade of Hall C was also considered by the PAC32 and conditionally approved. The authors proposed the use of bremsstrahlung photon beam created in a radiator to look at the photoproduction near threshold in a series of nuclei. The physics goal was to measure the photoproduction cross section on hydrogen and then investigate the A dependence of the propagation of the  $J/\psi$  in the nuclear medium. In this proposal, only the  $J/\psi$  is detected through the detection of the decay leptonic pair.

The experiment E12-12-006[151] as the first phase of the program, will utilize the SoLID spectrometer to measure the cross section of the full exclusive electro- and photo-production of  $J/\psi$  near threshold ( $4.05 \text{ GeV} < W < 4.45 \text{ GeV}$  and  $|t - t_{min}| < 2.5 \text{ GeV}^2$ ) to study QCD in the non-perturbative regime with luminosity of  $10^{37} \text{ cm}^{-2} \text{ s}^{-1}$ .

### 2.4.3 Beam Time and Projection

The experiment E12-12-006 was approved by Jefferson Lab PAC39 with total 60 PAC days[151]. Among them, 50 days will be used for production run with  $3 \mu\text{A}$ , and 11 GeV electron beam on a 15 cm long liquid hydrogen target. The other 10 days will be shared among activities, such as detector calibration, data taking with Al dummy target, and special low luminosity running for understanding the trigger efficiency and normalization for the cross section measurement.

Our projections for the total elastic cross sections of electro- and photo-production are plotted against the effective photon energy in Fig. 30. Together, we have also plotted the world data of  $J/\psi$  photoproduction near threshold. The fit of 2-gluon exchange only model is shown as well with a solid line. In our projections we also included the possible photoproduction of the LHCb "pentaquark" [160]. It is clear that the proposed measurements will significantly advance our knowledge of electroproduction of  $J/\psi$  near the threshold region.

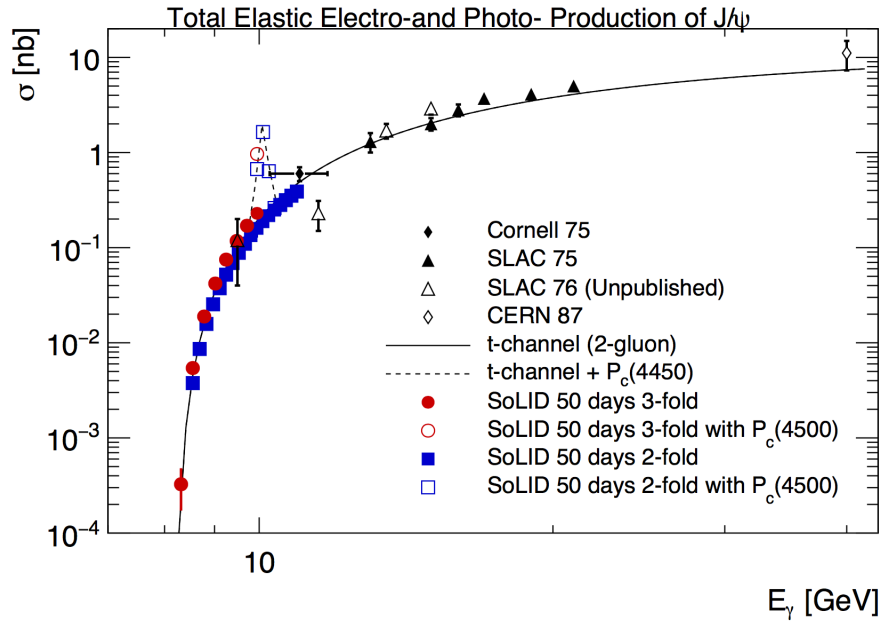


Figure 30: Projected uncertainties on the total elastic  $J/\psi$  electro-and photo-production cross sections. Our projections are based on the 2-gluon exchange model. The central values of our projections are positioned at 1.2 times or 0.8 times of the predicted total cross section of the 2-gluon exchange model in order to differentiate our projections from SLAC76 [136] points. The electro-production data is plotted against effective photon energy. We have also included the projection of the LHCb pentaquark photoproduction with a 5% coupling according to [7]

## 2.5 Possible Expansion in Physics Reach

### 2.5.1 GPD Program

There are several GPD experiments in different stages of study/approval. As has been remarked elsewhere, a variety of hard exclusive measurements are needed to disentangle the contributions of the different GPDs, with the general Compton processes (DVCS, TCS, DDVCS) sensitive to various real and imaginary combinations of all four leading twist GPDs (Fig. 31), vector-meson Deep Exclusive Meson Production (DEMP) sensitive to the spin-average  $H$  and  $E$  GPDs and pseudoscalar-meson DEMF sensitive to the spin-difference  $\tilde{H}$  and  $\tilde{E}$  GPDs. The SoLID GPD program under investigation includes many of these reactions, and has the potential to improve greatly our understanding of nucleon structure.

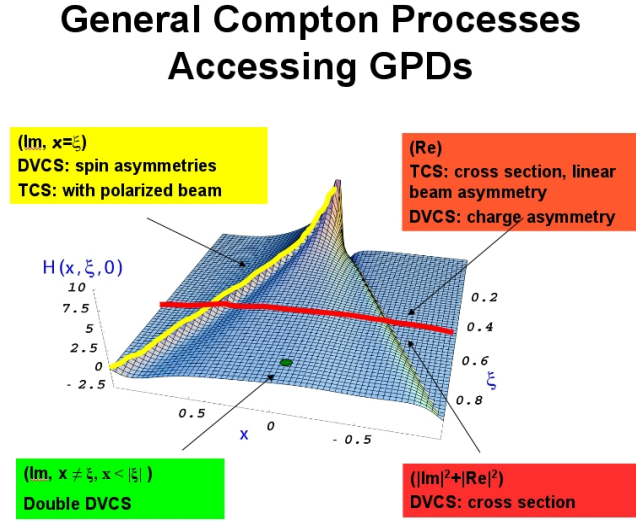


Figure 31: General Compton processes accessing GPDs.

Timelike Compton Scattering (TCS) from an unpolarized  $\text{LH}_2$  target can provide information on the real (imaginary) parts of the Compton amplitude using unpolarized (circularly polarized) photons. In this case, the produced lepton pair sets the hard scale ( $Q^2 > 4 \text{ GeV}^2$ ) and the azimuthal asymmetry of the  $\ell^+\ell^-$  plane with respect to the  $q$ -vector allows the separation of the GPD and Bethe-Heitler contributions. This has been approved as a run group experiment with the  $J/\psi$  experiment (E12-12-006A).

Double Deeply Virtual Compton Scattering (DDVCS) in the di-lepton channel on an unpolarized  $\text{LH}_2$  target has been reviewed by PAC43 as LOI12-12-005. The solenoidal configuration is ideal for high luminosity, with a fully parasitic proposal (as part of the  $J/\psi$  run group) for the  $e^+e^-$  channel under preparation. Once this experiment has run, a later phase of measurements might include the  $\mu^+\mu^-$  channel. A workshop at ECT Trento to refine the TCS and DDVCS physics program was held for October 24-28, 2016.

A possible Deeply Virtual Compton Scattering (DVCS) experiment on polarized  $^3\text{He}$  is also under study. The 12 GeV polarized DVCS experiments to date utilize longitudinally (E12-06-119) and transversely (C12-12-010) polarized proton targets. No polarized neutron-DVCS experiment has been proposed at JLab to date, and SoLID could make a unique contribution here once the

reaction exclusivity requirements and possible backgrounds are better understood. A complete set of SoLID DVCS data with both proton and neutron targets at varied polarization would be essential to control systematic uncertainties, perform flavor decomposition, and disentangle the different GPDs.

Deep Exclusive Meson ( $\pi^-$ ) Production (DEMP) using a transversely polarized  $^3\text{He}$  (neutron) target looks very promising. The transverse single-spin asymmetry in exclusive charged  $\pi$  production has been identified as the most sensitive observable to probe  $\tilde{E}$ . In this case, one fits the  $\sin(\phi - \phi_S)$  dependence, where  $(\phi - \phi_S)$  is the azimuthal difference between the  $\pi^-$  reaction plane and the polarized target. Theoretical calculations suggest higher twist corrections likely cancel in the asymmetry, allowing access to GPDs at much lower value of  $Q^2$  than typically required in DEMP reactions. This measurement has been proposed as a run group experiment with the transversely polarized  $^3\text{He}$  SIDIS experiment (PR12-10-006B), and detailed studies on the expected uncertainties are underway.

This summary makes clear that the SoLID-SIDIS setup is indeed very attractive in terms of acceptance and luminosity, and will allow a Phase 1 GPD program to be initiated with minimal impact on the approved SoLID program. Once this has been executed, one could envision a later Phase 2 suite of GPD experiments with additional recoil detectors near the target (such as low momentum proton tagging for DEMP), dedicated configurations (for DDVCS), or improved EC resolution (to allow exclusive vector meson and  $\pi^0$  measurements). These would require much more study, and are clearly beyond the scope of the present proposals.

### 2.5.2 SIDIS Production of Charged Kaons

The extension of the SIDIS production of charged pion to the SIDIS production of charged kaons is under study. Because the kaon contains a valence strange/antistrange quark, the SIDIS production of charged kaons is more sensitive to the strange distributions. Compared to the pion data, the kaon data are very limited. Lacking the knowledge of the strange quark distributions will prevent us from fully understanding the spin structures of the nucleon. Taking advantage of high luminosities and large acceptance, SoLID could be ideal to measure the SIDIS production of charged kaons with high statistics. The combination of the proton and the neutron ( $^3\text{He}$ ) targets, and the detection of charged pions and charged kaons in a similar kinematic region helps us to have flavor separations of all light quark distributions, *i.e.*,  $u$ ,  $\bar{u}$ ,  $d$ ,  $\bar{d}$ ,  $s$ , and  $\bar{s}$ . As kaon is heavier than pion, the SoLID kinematics covers a intermediate region from target-fragmentation to current-fragmentation. A precise measurement in this region will allow us to understand how the factorization breaks down.

A full RICH detector for kaon detection is likely to be too costly to consider. A high resolution TOF is a more practical solution. SoLID needs to do kaon identification over a momentum range of 1 GeV/c to 7 GeV/c. Given the 8 m flight distance, a TOF time resolution of 20 ps is required to obtain a 3-sigma separation between pions and kaons, as shown in Figure 32. Two detector technologies that could give high resolution TOF are being investigated.

The Large Area Picosecond Photodetector (LAPPD) collaboration [178] is developing large area detectors capable of time resolutions in the picosecond range. Such detectors use Micro Channel Plate photomultipliers, which have small paths for electrons, achieving better timing resolution than traditional PMTs. Resolutions of 20 ps for a single photoelectron have been achieved and resolutions of under 10 ps could be obtained for multiple photoelectrons. The main drawback of Micro Channel Plate PMTs is the high cost per area. The LAPPD project is aiming to producing large area MCP PMTs with a cheaper microchannel plate, significantly reducing the cost for large area of detectors. Depending on the ultimate costs, this could be an option for SoLID.

A second TOF option is improving the timing performance of the MRPC detector in SoLID. The baseline MRPC is designed to reach 80 ps. Improvement of the MRPC timing resolution would

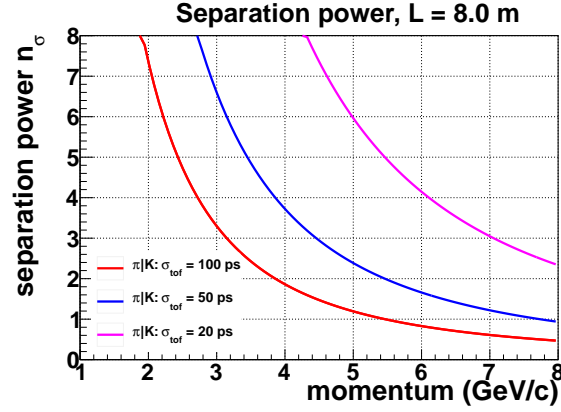


Figure 32: Kaon identification by TOF.

extend the momentum range of  $\pi/K$  identification to the full momentum range. Beam tests showed that current MRPC designs can reach 50 ps with test beam and 80 ps in high background area. There is ongoing EIC R&D [179] on Multi Gap Resistive Plate to improve the timing resolution. A thin gap MRPC prototype has been built and tested by BNL and University of Illinois, achieving a resolution of 20 ps. The R&D plan is described in the MRPC section.

### 3 Technical Requirements and Experimental Setup

#### 3.1 Summary of Requirements

The minimum requirements of the base equipment for SoLID are summarized below and also listed in Table 6,

- Magnet: Outer diameter is 3 meters (to fit in Hall A), inner diameter is 1 meter and length is greater than 3 meters. Field strength is greater than 1.35 tesla and integrated BdL is 5 tesla-meters. Acceptance in azimuthal angle ( $\phi$ ) is  $2\pi$ , in polar angle ( $\theta$ ) is  $8^\circ$  to  $24^\circ$  for the SIDIS configuration and  $22^\circ$  to  $35^\circ$  for the PVDIS configuration. Momentum range is 1–7 GeV, and momentum resolution (combined with 100-micron tracking resolution) is 2%. Fringe field at the front end after endcap (shielding) is less than 5 gauss (for polarized target operation).
- GEM Tracking Chambers: Six planes for SIDIS and five for PVDIS. Total area is  $37 \text{ m}^2$ , total number of channels 165K. Tracking efficiency is greater than 90%. Radial position resolution reaches 0.1 mm. Works in high rate environment.
- EM Calorimeter: Shashlyk sampling (lead-scintillator/fiber) calorimeter. Total 1800 modules of shower (18 radiation length) and 1800 pre-shower (2 radiation length), with an area of  $100 \text{ cm}^2$  for each module. Energy resolution is  $10\%/\sqrt{E}$ . Reaches  $50 : 1$   $\pi$  suppression with electron efficiency better than 90%. Reaches  $5 : 1$  photon suppression. Radiation hard (gain decreasing less than 20% after 400 KRad). Combined EC and Cherenkov for PVDIS trigger rate to be below 600 KHz (20 KHz/sector). In front of the EM Calorimeter, there are 300 pieces of scintillator pad detectors (SPDs) with thickness of 5 mm or 20 mm to help with photon rejection.
- Light Gas Cherenkov: 2 meters long with 1 atm  $\text{CO}_2$  gas for SIDIS and 1 meter long with 1 atm  $\text{CO}_2$  for PVDIS. Contains 60 mirrors and 270 PMTs. The total area is  $20 \text{ m}^2$ . Provides number of photo-electrons larger than 10 and electron efficiency greater than 90%.  $\pi$  suppression is greater than 500 for momentum less than 4 GeV (SIDIS) or less than 3.2 GeV (PVDIS). Works in moderate field up to 200 gauss ( $< 100$  gauss after mu-metal shielding). Combined EC and Cherenkov for PVDIS trigger rate to be below 600 kHz (20 KHz/sector).
- Heavy Gas Cherenkov: 1 meter long 1.5-atm  $\text{C}_4\text{F}_8\text{O}/\text{C}_4\text{F}_{10}$  gas, with 30 mirrors and 480 PMTs. Total area is  $20 \text{ m}^2$  (active  $8.5 \text{ m}^2$ ) and the number of photo-electrons is greater than 10. With an efficiency for  $\pi$  better than 90%, kaon suppression is greater than 10:1. Works in moderate field up to 200 gauss ( $< 100$  gauss after mu-metal shielding).
- MRPC: 50 super-modules, each of which contains 3 MRPC modules. There are totally 1650 strips and 3300 readout channels, covering an area of  $10 \text{ m}^2$ . Timing resolution is better than 100 ps. Kaon suppression is about 20:1 for momentum from 2.5 to 7 GeV and photon suppression is as high as 10:1. Works at a high rate up to  $10 \text{ KHz/cm}^2$ .
- DAQ: 282 FADC sampling at 250 MHz. 32 high-speed pipeline VME switched Series (VXS) system. 30 GEM Scalable-read-out system (SRS). Can handle trigger rate of 100 KHz for SIDIS with event size of 2.6 KBytes and trigger rate of 600 KHz (20 KHz per sector) for PVDIS with event size of 48 KBytes
- Baffles: Eleven planes of lead blocks, 30 sectors in each plane, thickness of 9 cm, with azimuthal angle opening for each block to be more than  $4^\circ$  out of  $12^\circ$  ( $360^\circ/30$ ). One additional



plane of lead blocks with thickness of 5 cm is placed in front of the EM Calorimeter at the small radius region ( $110 \text{ cm} < r < 200 \text{ cm}$ ). The design is optimized to block low energy particle, photon and hadron backgrounds to an acceptable level (total trigger rate below 600 kHz (20 KHz/sector) for the PVDIS configuration).

A summary of the detector requirements of all approved experimental programs is given in Table 7. The key parameters of the approved programs are in Table 8. The experimental setup of PVDIS, SIDIS- $^3\text{He}$ , SIDIS-proton and  $J/\psi$  are shown in the next few subsections.

Table 6: Summary of Minimum Requirements of SoLID Base Equipment. Items listed in brackets are particularly for SoLID-PVDIS requirements.

Equipment	dimension/description	description	performance, eff	performance, rej	conditions
Magnet	OD 3m, ID 1m, L > 3m	B > 1.35 T, BDL > 5 T-m	$2\pi$ , 8 to $24^\circ$ (22 to $35^\circ$ )	P: 1-7 GeV, Res 2%	Fringe field < 5 G
GEMs	6 planes (5 planes)	Total 37 m <sup>2</sup> , Chan 165K	Track Eff > 90%	Posi res 100 $\mu$ m	high rate
EM Calorimeter	1800 $\times$ 100 cm <sup>2</sup>	18 RL + 2 RL + 5 mm SPD	E res 10%, eff > 90%	50:1 $\pi$ , 5:1 $\gamma$	rad hard
Light Cherenkov	2m CO2 (1m C4F8O/N2)	60 mirr, 270 PMTs, 20 m <sup>2</sup>	$\gamma$ -e > 10, Eff > 90%	$\pi$ 500:1 < 4.5/3.2 GeV	100 G field
Heavy Cherenkov	1m 1.5 atm C4F8O	30 mirr, 480 PMTs, 20 m <sup>2</sup>	$\gamma$ -e > 10, Eff > 90%	K 10:1 2.5-7 GeV	100 G field
MRPC	50 $\times$ 3 modules, 10 m <sup>2</sup>	1650 strips, 3300 chan.	Time res < 100 ps	K 20:1 < 2.5 GeV, $\gamma$ 10:1	high rate
DAQ	282 FADC @ 250 MHz	32 pipeline VXS, 30 SRS	Trig 100 KHz $\times$ 2.6 KB	Trig 30 $\times$ 20 KHz $\times$ 48 KB	high noise
Baffle	11 $\times$ 30 blocks, 9 cm	5 cm, r 110-200 cm	area open $\phi$ > $4^\circ$ / $12^\circ$	reduce background	

Table 7: Detector Summary for Approved Experiments

Experiments	PVDIS	SIDIS- $^3\text{He}$	SIDIS-Proton	$J/\psi$
Target Length	$\text{LH}_2/\text{LD}_2$ 40 cm	$^3\text{He}$ 40 cm	$\text{NH}_3$ 3 cm	$\text{LH}_2$ 15 cm
Target Polarization	N/A	$\sim 60\%$	$\sim 70\%$	N/A
Target Spin Flip	N/A	$\leq 20$ mins	$\leq 4$ hours	N/A
GEM Tracking Chambers	5 chambers	6 chambers	6 chambers	6 chambers
E&M Calorimeter	Forward angle	Forward + Large angle	Forward + Large angle	Forward + Large angle
Light Gas Cherenkov	1 m long	2 m long	2 m long	2 m long
Baffles	Yes	N/A	N/A	N/A
Heavy Gas Cherenkov	N/A	1 m long	1 m long	N/A
MRPC (TOF)	N/A	100 ps resolution	100 ps resolution	100 ps resolution
Beam Polarimetry	0.4% determination	$< 3\%$	$< 3\%$	N/A
Target Polarimetry	N/A	$\sim 3\%$	$\sim 3\%$	N/A
DAQ	Single trigger	Coincidence trigger	Coincidence trigger	Coincidence trigger

Table 8: Summary of Key Parameters for Approved Programs

Experiments	PVDIS	SIDIS- <sup>3</sup> He	SIDIS-Proton	$J/\psi$
Reaction channel	$p(\vec{e}, e')X$	$(e, e'\pi^\pm)$	$(e, e'\pi^\pm)$	$e + p \rightarrow e' + J/\psi(e^-, e^+) + p$
Approved number of days	169	125	120	60
Target	LH <sub>2</sub> /LD <sub>2</sub>	<sup>3</sup> He	NH <sub>3</sub>	LH <sub>2</sub>
Unpolarized luminosity (cm <sup>-2</sup> s <sup>-1</sup> )	$0.5 \times 10^{39}/1.3 \times 10^{39}$	$\sim 10^{37}$	$\sim 10^{36}$	$\sim 10^{37}$
Momentum coverage (GeV/c)	2.3-5.0	0.8-7.0	0.8-7.0	0.6-7.0
Momentum resolution	$\sim 2\%$	$\sim 2\%$	$\sim 2\%$	$\sim 2\%$
Polar angle coverage (degrees)	22-35	8-24	8-24	8-24
Polar angle resolution	1 mr	0.6 mr	0.6 mr	0.6 mr
Azimuthal angle resolution	-	5 mr	5 mr	5 mr
Trigger type	Single $e^-$	Coincidence $e^- + \pi^\pm$	Coincidence $e^- + \pi^\pm$	Triple coincidence $e^- e^- e^+$
Expected DAQ rates	$\sim 20 \text{ kHz} \times 30$	$< 100 \text{ kHz}$	$< 100 \text{ kHz}$	$< 10 \text{ kHz}$
Backgrounds	Negative pions, photons	$(e, \pi^- \pi^\pm)$ $(e, e' K^\pm)$	$(e, \pi^- \pi^\pm)$ $(e, e' K^\pm)$	BH process Random coincidence
Major requirements	Radiation hardness 0.4% Polarimetry $\pi^-$ contamination $Q^2$ calibration	Radiation hardness Detector resolution Kaon contamination DAQ	Shielding of <i>sheet-of-flame</i> Target spin flip Kaon contamination	Radiation hardness Detector resolution

### 3.2 SIDIS- $^3\text{He}$ Experiments

The E12-10-006 [181] (E12-11-007 [182]) is designed to measure the single/double spin asymmetries through the semi-inclusive deep-inelastic scattering (SIDIS) ( $e, e'\pi^\pm$ ) with the SoLID spectrometer and the transversely (longitudinally) polarized  $^3\text{He}$  target. The layout of the experiment is shown in Fig. 33 and Fig. 34. The entire detector system consists of two parts: the forward-angle detectors and the large-angle detectors.

At forward angle, there are five layers of GEM detectors inside the coils to provide the forward-angle tracking, and the first three of them are shared with the large-angle detectors. A 2 m long light gas Cherenkov counter is installed after the GEM detectors to discriminate the scattered electrons from the produced pions. A 1 m long heavy gas Cherenkov counter right after the light gas Cherenkov counter can separate kaons and protons from the pions at momenta larger than 2.5 GeV/c. One layer of Multi-gap Resistive Plate Chamber (MRPC) is placed after the heavy gas Cherenkov counter to provide timing information and particle identification of hadrons at low momentum ( $< 2.5$  GeV/c), as well as to suppress photon background. A “Shashlyk”-type forward-angle Electromagnetic calorimeter (FAEC) will be used for electron/pion separation. One layer of scintillator pad detector (SPD) is placed in front of the FAEC to reject photons and reduce the calorimeter-based trigger rates. The polar angular coverage for the forward-angle detectors ranges from  $8^\circ$  to  $14.8^\circ$  and the momentum coverage extends from 0.8 GeV/c to 7.0 GeV/c. A combination of the FAEC, the gas Cherenkov counter, and the MRPC will be used for electron and pion identifications.

To cover the large electron scattering angles, there are four layers of GEM detectors placed inside the coils, with the last three layers shared with the forward angle detectors. Following a layer of SPD, another “Shashlyk”-type large-angle Electromagnetic calorimeter (LAEC) will be placed inside the coils to separate electrons and hadrons. The large-angle detectors are mainly used for electron detection in a momentum range of 3.5-6.0 GeV/c where the expected  $\pi^-/e$  ratio smaller than 1.5. The polar angle coverage ranges from  $15.7^\circ$  to  $24^\circ$ .

The standard Hall A polarized  $^3\text{He}$  target will be used in its transverse mode. A higher than 60% target polarization with a faster than 20 minutes target spin flip is expected at the full polarized luminosity of  $10^{36}$  N cm $^{-2}$  s $^{-1}$ , which is corresponding to the unpolarized luminosity of  $10^{37}$  N cm $^{-2}$  s $^{-1}$ . The target polarization is expected to be limited by the magnetic field gradient in the target region, which is dominated by the leakage field from the SoLID magnet. Therefore, the design of the magnet yokes is important to achieve the required target polarization. As shown in Fig. 33 and Fig. 34, the target will be located about 70 cm upstream of the front yoke. Two target collimators will be placed close to two windows of the 40 cm long target in order to reduce backgrounds generated from both windows. The expected kinematic coverage includes: i)  $0.05 < x < 0.6$  which comprises the majority of the valence quark region; ii)  $0.3 < z < 0.7$  in which the leading order  $x - z$  factorization is expected to hold; iii) maximum pion transverse momentum  $P_T$  up to 1 GeV/c, where the TMD framework is valid; and iv)  $1 \text{ GeV}^2 < Q^2 < 8 \text{ GeV}^2$  with about 2 GeV $^2$  coverage in  $\Delta Q^2$  at fixed  $x$ . These kinematic coverages can be achieved by combining data with incident electron energies of 11 and 8.8 GeV.

In order to achieve the proposed precision in asymmetries, the negative pion contamination in the electron sample needs to be controlled to below 1%. At forward angle, it is achieved by a combination of the FAEC and the light gas Cherenkov detector. At large angle, the LAEC alone will be enough to provide the required pion rejection, since the expected pion to electron ratio is small. Furthermore, the coincidence detection of electron and leading pion in the SIDIS kinematics would further reduce the pion contamination in the electron sample.

The particle identification of the leading pion (forward angle detector only) will be achieved by a combination of time-of-flight (TOF) from the MRPC and the heavy gas Cherenkov detector. The

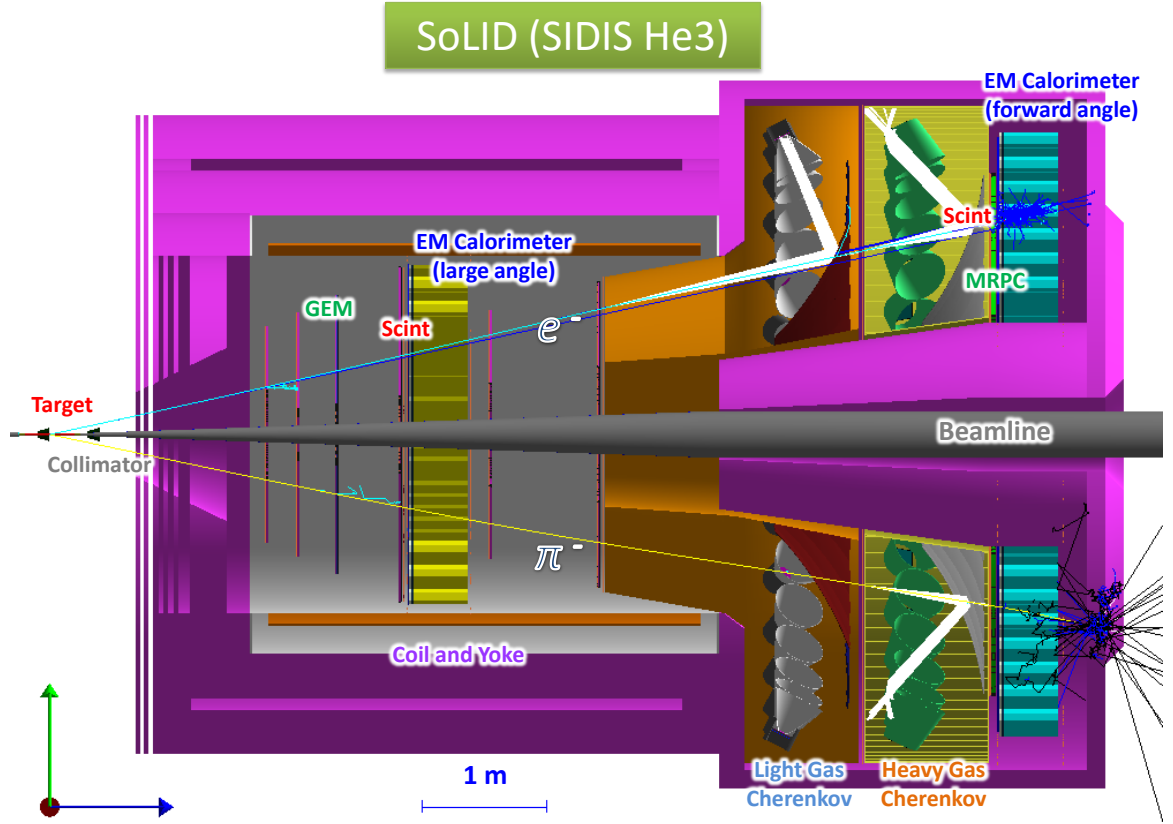


Figure 33: The experimental layout of the SoLID SIDIS- $^3\text{He}$  setup based on the CLEO magnet. The scattered electrons are detected by both forward-angle and large-angle detectors. The leading pions are detected by the forward-angle detector only. The polarized  $^3\text{He}$  target will be placed upstream in front of the spectrometer entrance.

electron, kaon, and proton contaminations in the pion samples are all required to be kept below the 1% level. The electron rejection will be achieved by the combination of the FAEC and the light gas Cherenkov counter. With the expected  $100\text{ps}$  TOF resolution from the MRPC, a separation of 3 standard deviations (6 standard deviations from peak to peak) between pions and protons can be achieved for momenta up to  $4\text{ GeV}/c$ . Pions with momenta higher than  $2.5\text{ GeV}/c$  will trigger the heavy gas Cherenkov detector, while the momentum threshold for kaons to trigger the same detector is  $7.6\text{ GeV}/c$ . Therefore, the heavy gas Cherenkov detector would provide additional rejection of protons when the pion momenta are larger than  $2.5\text{ GeV}/c$ . For pions with momenta below  $2.5\text{ GeV}/c$ , the TOF would provide a separation better than 2 standard deviations (4 standard deviations from peak to peak) between pions and kaons. Since the kaon to pion ratio is expected to be about 0.1, a combination of the TOF and the heavy gas Cherenkov detector would easily satisfy the requirement of below 1% kaons contamination.

The extraction of various TMD asymmetries relies on the  $\phi_S$  and  $\phi_h$  angular dependence of the measured single/double spin azimuthal asymmetries in each kinematic bin of the 4-D ( $x$ ,  $Q^2$ ,  $z$ , and  $P_T$ ) phase space. Since the kinematics of interests are in the deep-inelastic-scattering (DIS) region, the requirements on the resolution of the reconstructed kinematic variables are modest. For

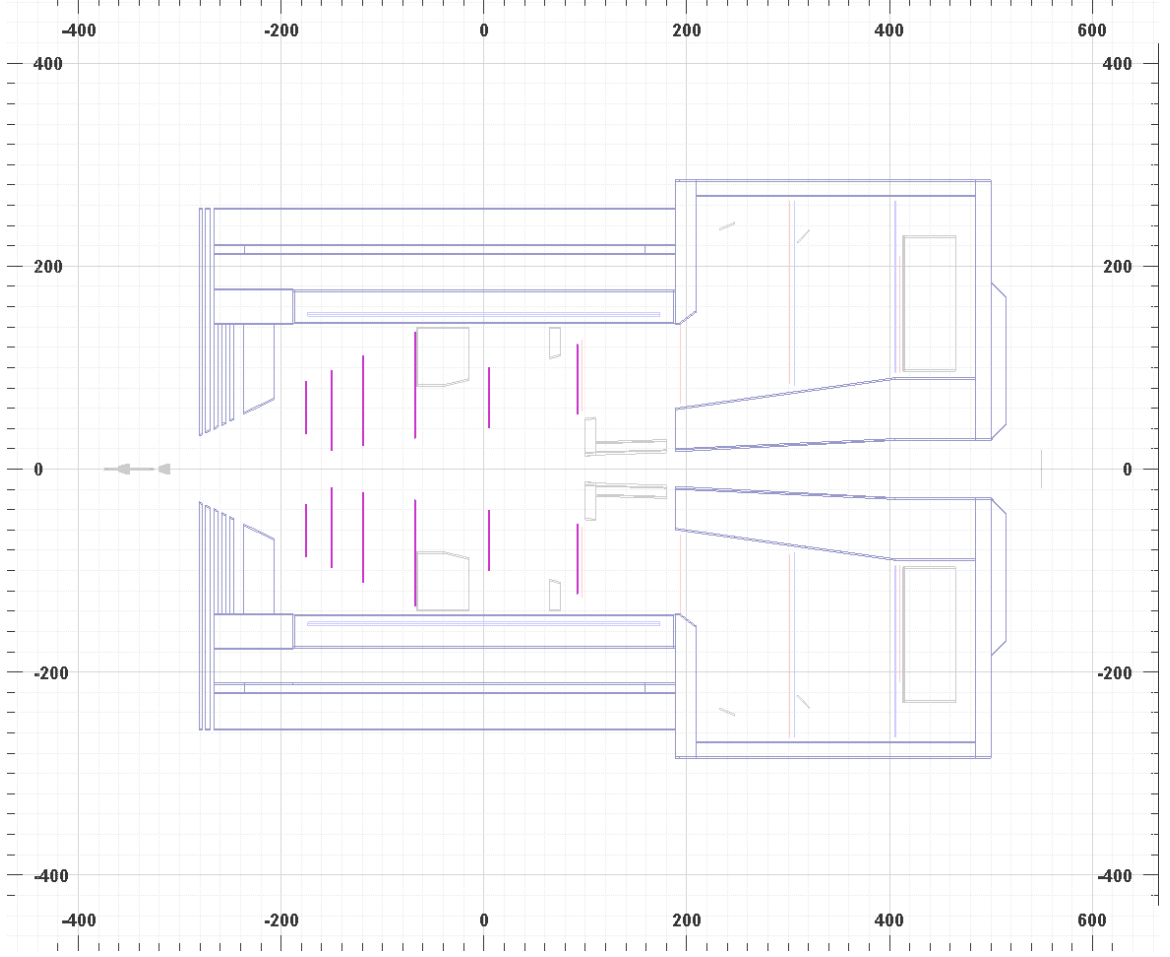


Figure 34: A 2D representation of the experimental layout of SoLID SIDIS- $^3\text{He}$  setup based on the CLEO magnet.

example, a better than a few percent momentum resolution, a better than a few mrad polar angular resolution, a better than 10 mrad azimuthal angular resolution, and a 1-2 cm reconstructed vertex resolution would satisfy the needs of these experiments.

With similar reaction channels, E12-10-006 [181], E12-11-007 [182], and E12-11-108 [183] (see next section) will share the same design of the DAQ system. The required overall luminosity of E12-10-006 and E12-11-007 is  $10^{37} \text{ N/cm}^2\text{s}^{-1}$ , which is an order of magnitude higher than that of E12-11-108. The goal of the SIDIS DAQ is to satisfy the requirement of  $\sim 100 \text{ kHz}$  trigger rate.

The SIDIS process requires the detection of both the scattered electron and the leading pion. Therefore, a single electron trigger or a coincidence trigger of electron and hadron would satisfy this need. The electron trigger at the large-angle detectors will be provided by the LAEC at an energy threshold of about 3 GeV. Such a trigger would be sensitive to both high energy electrons and high energy photons (mostly from the  $\pi^0$  decay). With the large angle SPD being incorporated into the trigger, the electron-like triggers can be significantly suppressed. The electron trigger at the forward angle detector will be formed by a coincidence between the light gas Cherenkov detector, the FAEC, the SPD and the MRPC. Considering the kinematic information of the scattered electrons from the DIS process (e.g.  $Q^2 > 1 \text{ GeV}^2$ ), a position dependent energy threshold with a low limit

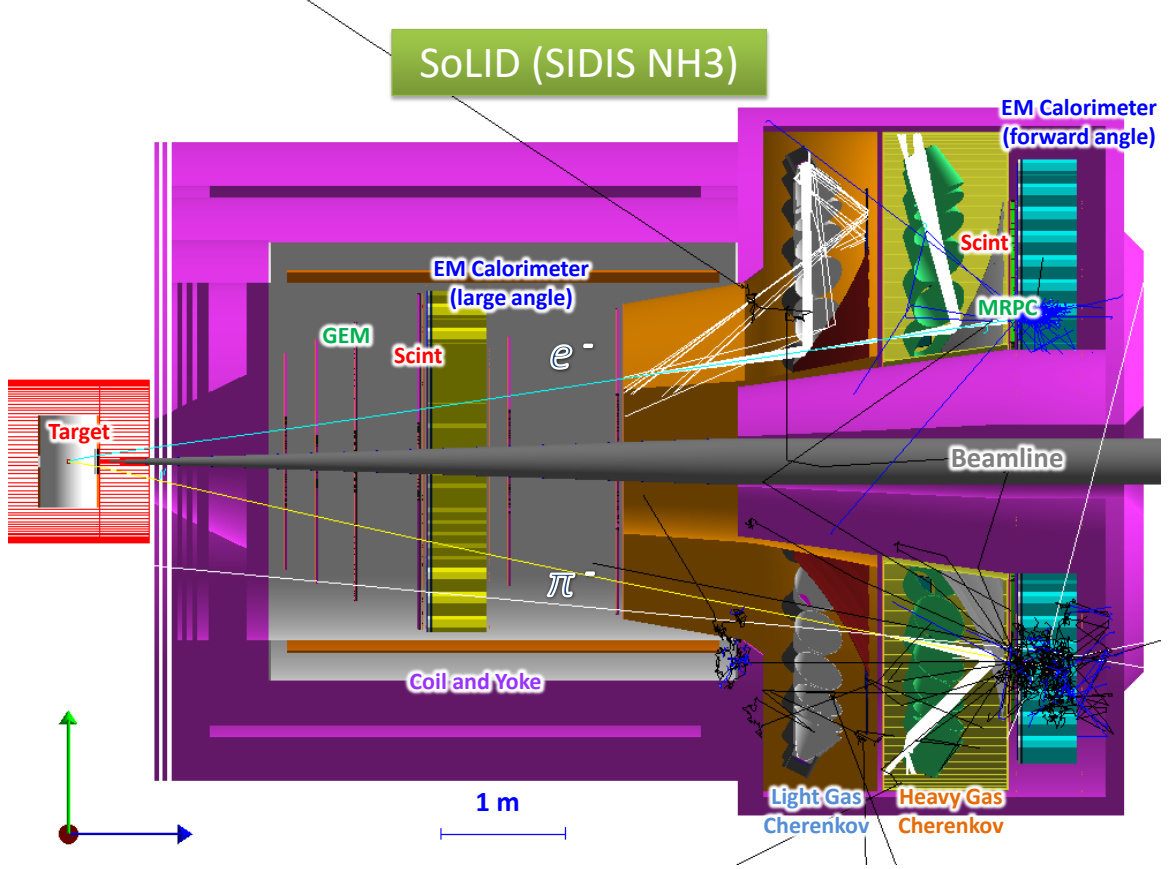


Figure 35: The experimental layout of the SoLID SIDIS-proton setup based on the CLEO magnet. It's the same like SIDIS- $^3\text{He}$  setup, except the  $^3\text{He}$  target is replaced by transversely polarized  $\text{NH}_3$  target upstream in front of the spectrometer entrance. The scattered electrons are detected by both forward-angle and large-angle detectors. The leading pions are detected by the forward-angle detector only.

at 0.8 GeV in FAEC could significantly reduce the trigger rate. The charged hadron trigger at the forward angle will be formed with a coincidence between the FAEC, the SPD and the MRPC. The coincidence trigger is given by overlapping the electron trigger and the hadron trigger within a narrow time window. If the single electron trigger can not satisfy the requirement of  $\sim 100$  kHz trigger rate, the coincidence trigger could retain more SIDIS events. Therefore, it is important to include the coincidence trigger in the baseline design of the SIDIS DAQ system.

### 3.3 SIDIS-proton Experiment

The E12-11-108 [293] is designed to measure the single/double spin asymmetries through the semi-inclusive deep-inelastic scattering (SIDIS) ( $e, e'\pi^\pm$ ) with the SoLID spectrometer and a transversely polarized proton target. The layout of the experiment is same as  $^3\text{He}$  program except the target as shown in Fig. 35. The entire detector system consists of two parts: the forward-angle detectors and the large-angle detectors. The overall luminosity in this case is smaller compared to that of using the polarized  $^3\text{He}$  target.

An improved version of JLab/UVa/SLAC polarized  $\text{NH}_3$  target (shown in Fig. 36) will be used.



The main upgrade is to replace the aging Helmholtz-coil magnet with a new magnet and to have a fast spin-flip capability with the AFP technique to minimize the systematic uncertainty in the single spin asymmetry measurement. In order to satisfy the requirements of phase space coverage, the new design will further allow both transverse and longitudinal direction to have a nominal forward opening of more than  $\pm 25^\circ$ , while maintaining the same maximum field (5 Tesla) and a uniform field region in the center. The target polarization is required to be higher than 70% with the spin flip every few hours.

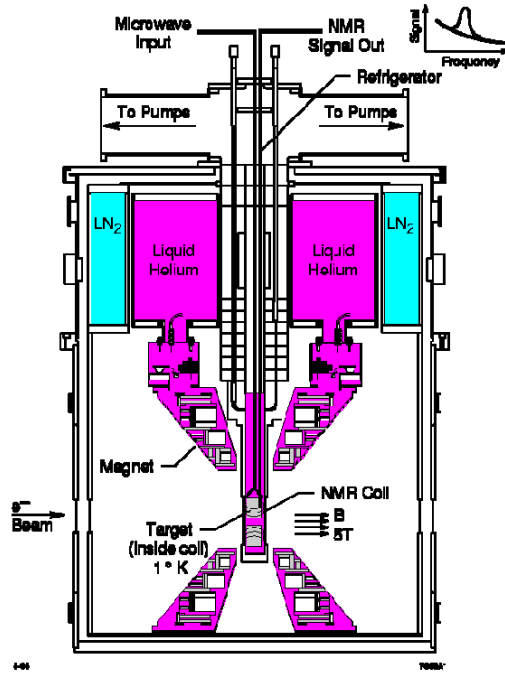


Figure 36: Polarized target system.

Due to the large magnetic field in the transverse direction, this experiment suffers from a different kind of background compared to the low field polarized  $^3\text{He}$  experiment, known as *sheet-of-flame*. The main feature of such a background is that a very high rate of charged particles with momentum range between 1-2 GeV will be localized in a very narrow region of the acceptance. Fig 37 shows this background on all six GEM planes in the SoLID. The GEM chambers in regions outside of the *sheet-of-flame* location see a background rate of less than 1.0 KHz/mm<sup>2</sup> on, whereas the regions inside have much higher rates. In order to handle this background and avoid damage to the apparatus, detector sectors in the direct line-of-sight of this *sheet of flame* will be removed or turned off during the proton experiment.

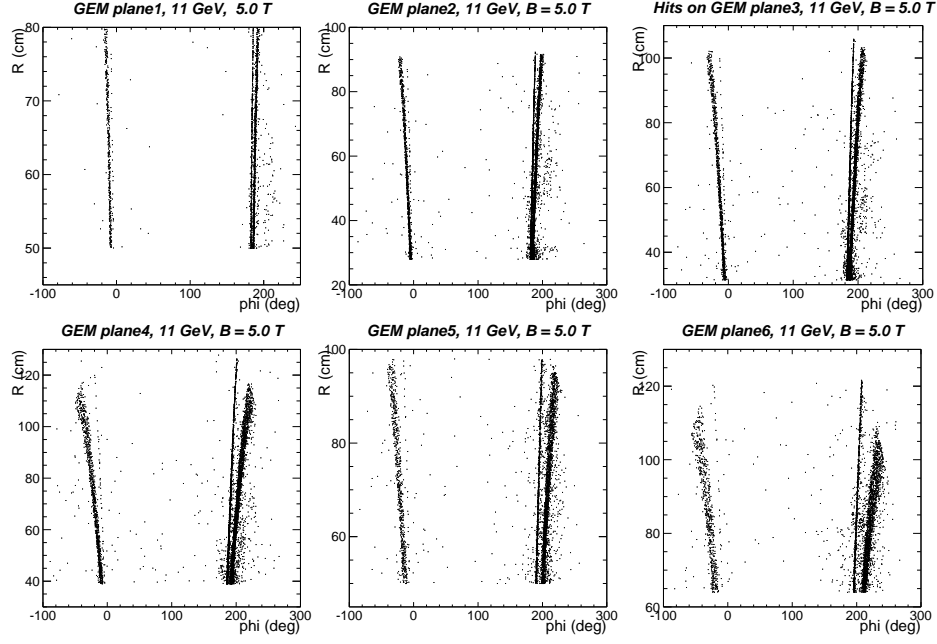


Figure 37: GEANT3 simulation results of background with  $\text{NH}_3$  target field ON. The  $x$ -axis is the azimuthal angle in lab frame. The  $y$ -axis is the radius of GEM chambers (1-6). Narrow regions of high rate (compared to rest of the acceptance) are clearly seen as a function of azimuthal angle  $\phi$ .

### 3.4 PVDIS Experiment

Experiment E12-10-007 [180] is designed to measure the parity violating asymmetries ( $A_{PV}$ ) through the inclusive deep-inelastic scattering (DIS)  $p(\bar{e}, e')X$  with the SoLID spectrometer. The layout of the experiment is shown in Fig. 38 and Fig. 39. In order to eliminate high energy ( $\sim \text{GeV}$ ) photons, a lead baffle will be placed downstream of the target to block direct lines of sight to the detector system. The detector system consists of four layers of GEM chambers for particle tracking, a 107 cm long light gas Cherenkov counter for electron/pion separation, and a “shashlyk”-type electromagnetic calorimeter system for the trigger and additional electron/pion separation. The GEM chambers will be divided into two groups, with one group placed in front of the gas Cherenkov counter and the other group behind it. This configuration will maximize the detector resolution, leading to about 2% momentum and 1 mr polar angle resolutions. The entire detector system will be divided into 30 independent sectors in the azimuthal angle.

The polar angle and momentum coverages of the detector system are from  $22^\circ$  to  $35^\circ$  on an extended (40 cm) target and from 1.5 GeV/c to 5 GeV/c, respectively. These coverages transform into kinematic coverages of  $0.2 < x < 0.8$  and  $2 (\text{GeV}/c)^2 < Q^2 < 12 (\text{GeV}/c)^2$ . The overall luminosity is required to be larger than  $5 \times 10^{38} \text{ N cm}^{-2} \text{ s}^{-1}$  in order to reach about 0.5% relative statistical uncertainties on the parity violating asymmetries  $A_{PV}$  in each of the kinematic bins (see. Fig. 26). Such a high luminosity places specific requirements on the radiation hardness of the detector system.

To leading order, the physics asymmetry  $A_{PV}^{\text{phys}}$  is related to the measured asymmetry  $A_{PV}^{\text{measured}}$

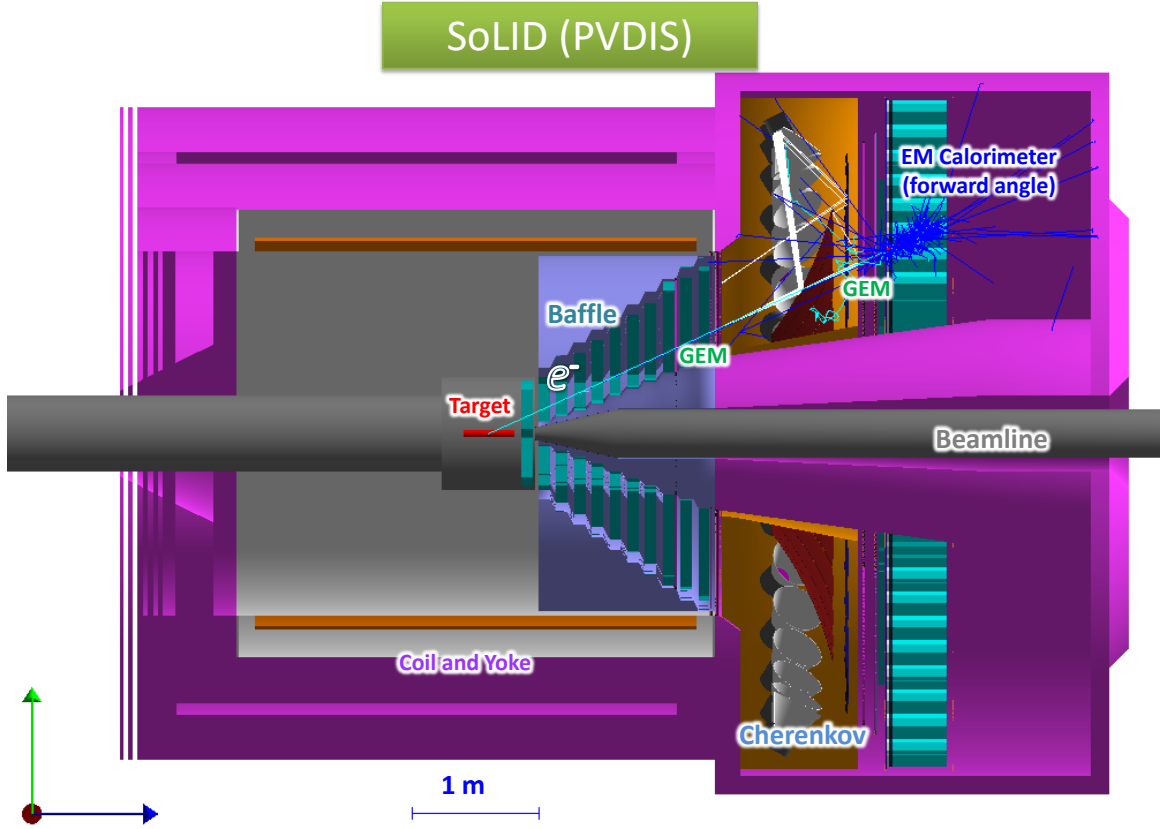


Figure 38: The experimental layout of SoLID PVDIS setup based on the CLEO magnet.

by

$$A_{PV}^{phys} \sim \frac{1}{Q^2 \cdot P_{beam}} \cdot \frac{A_{PV}^{measured} - f \cdot A_{PV}^{\pi^-}}{1 - f} \quad (12)$$

where  $P_{beam}$  is the polarization of the electron beam, and  $f$  and  $A_{PV}^{\pi^-}$  are the pion contamination and the parity violating asymmetry of pions, respectively. The proposed high precision measurement of  $A_{PV}$  (about 0.5% in each kinematic bin) requires high accuracy. The uncertainty of the electron beam polarization is required to be smaller than 0.4%. Since  $A_{PV}$  for produced pions is expected to be similar to that of scattered electrons, the contamination of negative pions in the electron sample needs to be determined to about a  $10^{-3}$  level. Furthermore, the uncertainty in  $Q^2$  also must be controlled to below 0.1% using a precise and comprehensive optics calibration program.

Since only the scattered electrons are detected in this experiment, each sector of the detector system can employ an independent DAQ system. Thus the requirement on the DAQ system for this experiment is modest. The average trigger rate for each sector is estimated to be less than 20 kHz, leading to a total trigger rate less than 600 kHz.

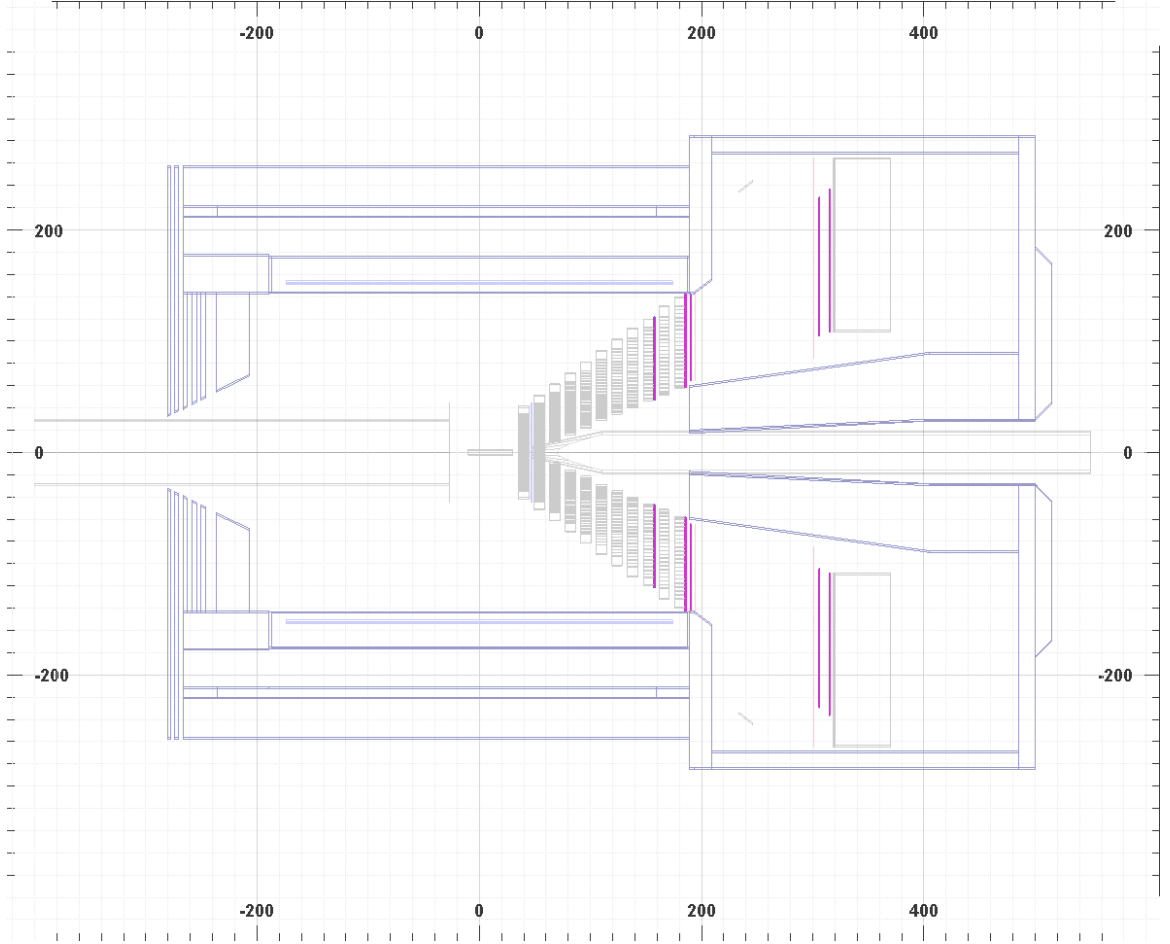


Figure 39: A 2D representation of the experimental layout of SoLID PVDIS.

### 3.5 $J/\psi$ Experiment

The E12-12-006 experiment [195] is designed to measure the cross section of  $J/\psi$  electroproduction near threshold. The reaction of interest is  $e + p \rightarrow e' + J/\psi(e^-, e^+) + p$  where  $J/\psi$  is detected through its decay in a lepton pair ( $e^+, e^-$ ) with 5.94% branching ratio. Primary detection channels include a 4-fold coincidence, which consists of a detection of the scattered electron, the recoil proton, and the leptonic pair ( $e^+e^-$ ) from the  $J/\psi$  decay, a 3-fold coincidence, which is similar to the 4-fold coincidence but without the either scattered electron or the proton detection, and a 2-fold coincidence of the leptonic pair ( $e^+e^-$ ) from the  $J/\psi$  decay only. In the 3-fold coincidence channel, the full kinematics of the recoil proton can be reconstructed through energy and momentum conservation. Since the recoil proton is not detected, the total number of events and the kinematic coverage are greatly enhanced compared to the 4-fold coincidence channel. Possible background in the 3-fold coincidence channel can be investigated fully with the 4-fold coincidence channel which offers a better signal to noise ratio. Because the electrons, positrons, as well as protons are required to be detected in coincidence, the configuration of SoLID will be similar to that of SIDIS. Fig. 40 and Fig. 41 illustrates the layout of the experiment. The scattered electron and the recoil proton will be detected mostly by the forward angle detector, while the electron-positron pair from  $J/\psi$  decay will be mostly detected by the large-angle detector. Compared to the SoLID-SIDIS setup,

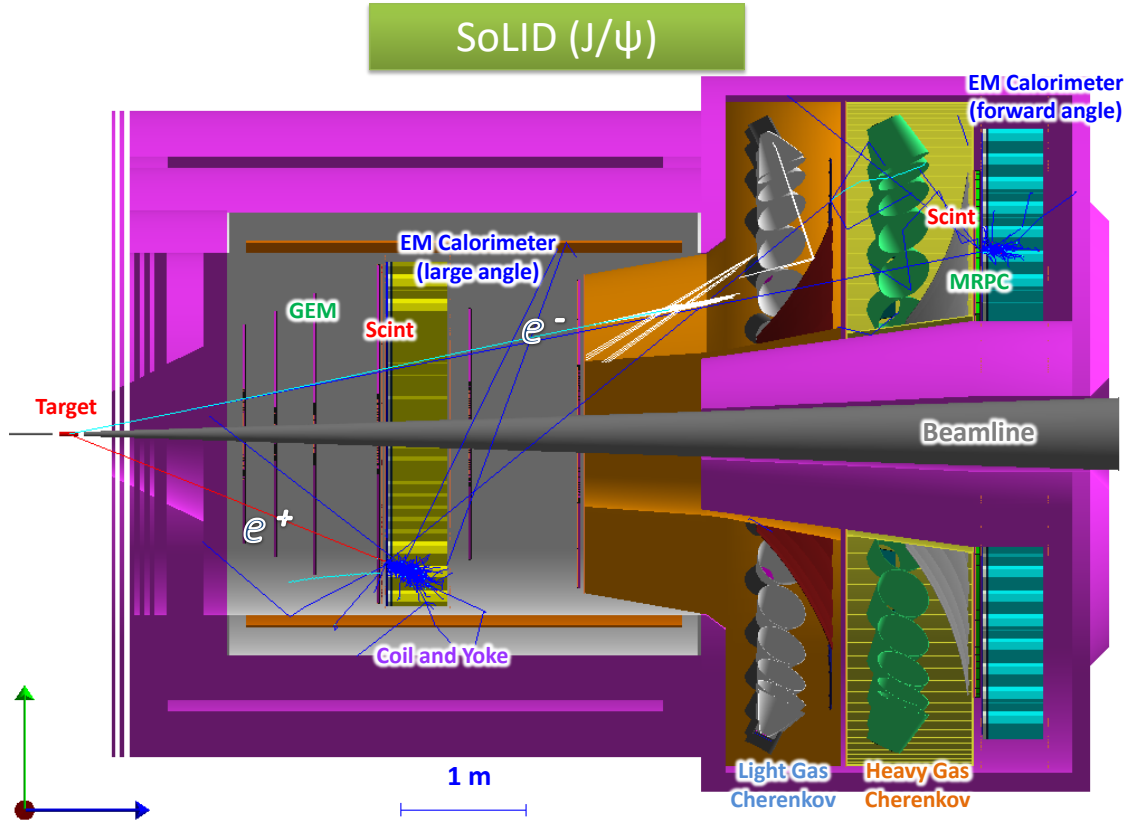


Figure 40: The experimental layout for the SoLID  $J/\psi$  setup based on the CLEO magnet. It's the same like SIDIS- $^3\text{He}$  setup, except the  $^3\text{He}$  target is replaced by the standard Hall A 15 cm liquid Hydrogen target upstream in front of the spectrometer entrance.

the polarized target will be replaced by the standard Hall A 15 cm liquid Hydrogen target, but its position will be located about 35 cm more downstream relative to the target center of the SIDIS setup to improve the acceptance.

The approved beam time for this experiment is 60 PAC days at an unpolarized luminosity of  $10^{37} \text{ N cm}^{-2} \text{ s}^{-1}$ . The kinematic coverage will be  $4.05 \text{ GeV} < W < 4.45 \text{ GeV}$  and  $|t - t_{\min}| < 2.5 \text{ GeV}^2$ . Depending on the cross section model, the expected physics counts with 50 days production data for 4-fold (3-fold) coincidence range from  $\sim 0.7\text{k}$  ( $2.1\text{k}$ ) to  $\sim 2.9\text{k}$  ( $8.1\text{k}$ ) at the proposed luminosity. Since this measurement is limited by statistics due to the rare nature of the  $J/\psi$  production near threshold process, a higher luminosity ( $> 10^{37} \text{ N cm}^{-2} \text{ s}^{-1}$ ) is strongly desired.

The primary trigger is a triple coincidence of scattered electron,  $J/\psi$  decay electron, and  $J/\psi$  decay positron. With a 100 ns coincidence window, the trigger rate would be dominated by the random coincidence events with a rate of about 3 kHz, which is far below the required  $\sim 100 \text{ kHz}$  trigger rate of SoLID-SIDIS. Therefore, the main requirement of SoLID- $J/\psi$  is the capability of forming hardware coincidence trigger.

Since we are interested in the exclusive electroproduction of  $J/\psi$ , the resolution of the  $J/\psi$  setup is important in rejecting different backgrounds. Currently the expected resolutions are similar between SIDIS and  $J/\psi$  setups and it would satisfy the requirement of this experiment. We are working on improving the  $J/\psi$  resolution further.

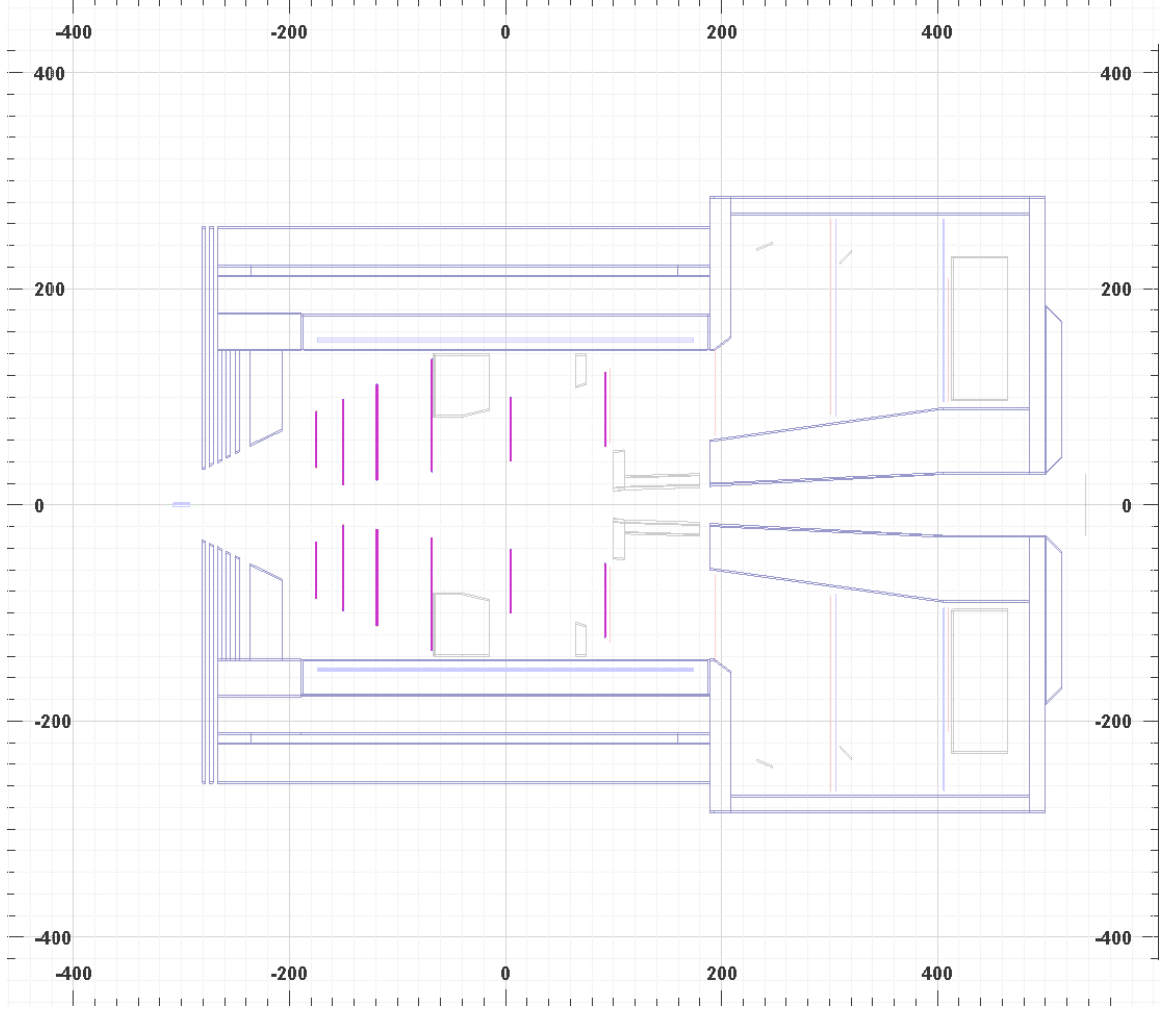


Figure 41: A 2D representation of the experimental layout of SoLID  $J/\psi$  setup.

The particle identification of the recoil proton for the 4-fold coincidence relies on the time-of-flight (TOF) from the MRPC. The highest momentum of the recoil proton is about 3 GeV/c. With the designed 100 ps resolution in TOF, protons can be separated from kaons at 2 standard deviations (4 standard deviations from peak to peak). In addition, protons can be separated from pions at 6 standard deviations (12 standard deviations from peak to peak). The requirement on the exclusive kinematics in the off-line data analysis would further strengthen the particle identification of protons.

There are two major types of backgrounds. The main physics background originates from the Bethe-Heitler (BH) process. At the proposed kinematics, the BH background is expected to be smaller than the physics  $J/\psi$  events by 1-2 order of magnitude in average <sup>2</sup>. The cross section associated with the BH background can be directly measured by choosing the invariant mass of the electron-positron pair to be away from the  $J/\psi$  peak. The other major background is the random coincidence of a  $J/\psi$  (normally photo-produced) and a scattered electron. The random coinci-

<sup>2</sup>Due to the rapid decrease of the cross section near threshold for the physics  $J/\psi$  events, the BH background becomes comparable at low W.

dence background is expected to be 1-2 orders of magnitude smaller than the physics events with the proposed setup. In addition, the random coincidence backgrounds can also be directly measured/subtracted through the commonly used off-window method.

## 4 Magnet

### 4.1 Requirements

The SoLID spectrometer is designed to have large acceptance in polar angle, azimuthal angle, and momentum acceptance, and also operate at high luminosity. A solenoid magnet is a natural choice in this case. The magnetic field is symmetric around the beamline, confining the copious low energy charged background particles to the beam pipe region. The detectors are placed symmetrically around the beamline, both within the solenoid and in the end cap region. The approved experiments all have some requirements on the magnet. They are summarized below:

- The PVDIS experiment requires polar angle coverage for the center of the target from  $22^\circ$  to  $35^\circ$ . Its hydrogen and deuterium targets can operate in the magnetic field. To operate the detectors at the design luminosity of  $10^{39}/\text{cm}^2/\text{s}$ , a set of baffles is required to block unwanted photons and hadrons originating in the target. The magnetic field must then be strong enough to spiral the several GeV DIS electrons through the gaps in the baffles and also provide sufficient curvature in the tracks so that their momentum can be reconstructed. Both requirements can be met with a field integral along the flight path on order of 2.5 T-m.

- Both SIDIS proton and neutron experiments need polar angle coverage from  $8^\circ$  to  $24^\circ$ . The  $^3\text{He}$  and  $\text{NH}_3$  targets must be located just upstream of the solenoid where the fringe fields before additional shielding are on the order of 5 G. The  $\text{NH}_3$  targets require a uniform 5 T field and the  $^3\text{He}$  targets require uniform fields on the order of a 25 Gauss. There are two sets of detectors. The forward detectors, located in the end cap, cover particles with angles below  $15^\circ$ . This requires the solenoid to be on the order of 3-4 m long. The large angle detectors are located near the center of the magnet, requiring a diameter on the order of 3 m. The field integral needs to be on the order of 5 T-m in order to provide sufficient momentum resolution from the GEM tracking system.

- The  $J/\psi$  experiment must detect the electron-positron pair from the  $J/\Psi$  decay as well as the scattered electron. With a liquid hydrogen target placed upstream of the magnet, the configuration for the SIDIS experiment meets the requirements.

Overall, the ideal SoLID solenoid needs to have an outer radius  $< 3$  m to fit in the experimental hall, an inner radius  $> 1$  m, a length of 3–4 m, and a field integral on the order of 5 T-m.

### 4.2 SoLID magnet

We have chosen the CLEO II magnet for the SoLID spectrometer. It is a solenoidal magnet with a uniform axial central field of 1.5 T, a large inner space with a clear bore diameter of 2.9 m and a coil of 3.1 m diameter. With a coil length of 3.5 m, its magnetic field uniformity is  $\pm 0.2\%$ . It was built in the 1980s by Oxford in England and installed for CLEO II in 1989 [197, 198].

The coil is made of  $5 \times 16 \text{ mm}^2$  aluminum stabilized superconductor and run at 3266 A with an average current density of 1.2 MA/m. The large conductor size provides simpler construction and ease of protection. A 3.8 m long cryostat encloses the coil and cools it with a thermosyphon system. The return yoke has 3 layers with 36 cm thickness each and is octagonally divided. There are 2 collars 60 cm thick supporting not only the return yokes, but also the coil with 4 rods. The magnet has good stability, low cryogenic heat load, passive cooling, and passive protection. This gave it the flexibility to be frequently de-energized for maintenance and accelerator studies. It has been kept in good condition since stopping beam. The coils and cryostat of the CLEO-II magnet have arrived at JLab in 2016 and the exterior steel is being shipped as of Spring 2017. To use the CLEO magnet for SoLID, we will reuse the coil and cryogenic system, but the downstream collar and return yoke will be modified to allow the PVDIS acceptance up to  $35^\circ$ . New endcap and front



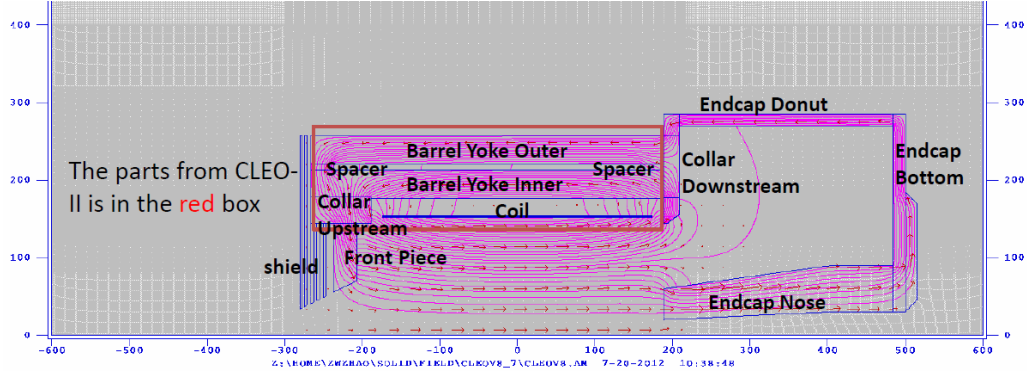


Figure 42: Design of the CLEO II magnet yoke for SoLID.

pieces will be fabricated.

The design of the yoke for SoLID with the CLEO II magnet is shown in Figure 42. There are two layers of barrel flux return and an upstream collar which are kept from the original CLEO-II magnet. The simulation has shown that the original third layer of barrel flux return is not needed for SoLID and the field in the rest of two layers is well below saturation. The downstream collar is either modified or a new part. All other parts including the endcap, the front piece and the target shielding need to be built.

The  $B$  field for the CLEO II magnet with the SoLID yoke is shown in Figure 43. The strongest field is within the solenoid and drops sharply in the endcap and upstream opening. The magnetic field was calculated using the 2D Poisson Superfish program.

The  $B_z$  and  $B_r$  fields along the beamline are shown in Figure 44. The  $B_z$  field at the center is about 1.4 T, dropping to 0.8 T at the exit of the coil.

The axial force for the 3 section of coils and all parts of yoke are shown in Figure 45. There are two strong forces compressing the coil. These forces can be balanced so that the net force on the coil is small. It can be adjusted by moving the location of the front piece, where the force varies by 3–5 t/cm.

### 4.3 Planned Modifications

The CLEO magnet will require some modifications to its design for use in the SoLID experiments. Much of the CLEO magnet will be reused in its original condition. However, SoLID will not use the outermost muon ring. It will use the inner two rings, each consisting of 8 slabs of iron to make up the 8-sided ring. Each of these slabs will have to be shortened to allow the proper position of the endcap. The original upstream coil collar will be reused. Spacers between the slabs will also be reused. The downstream coil collar will be modified if an economical way of reducing its thickness can be found without wasting a majority of its unwanted material. If a solution is not found then a new downstream coil collar will be created. Additional pieces of iron will need to be fabricated to allow for the proper mating of the endcap with the barrel yoke. The existing outer and inner shower counters that mount inside of the coil collars do not appear to be reusable as the upstream coil cup that will reside inside the upstream coil collar. All supporting structure for the magnet barrel yoke and detector endcap will be new fabrications. Please refer to the study in Ref. [196].

The endcap, which consists of the outer cylindrical ring, the backplate, and endcap nose, will all be made from new material. The endcap is designed to be part of the magnetic flux return yoke and house the downstream forward angle detector package. The endcap will be split vertically into

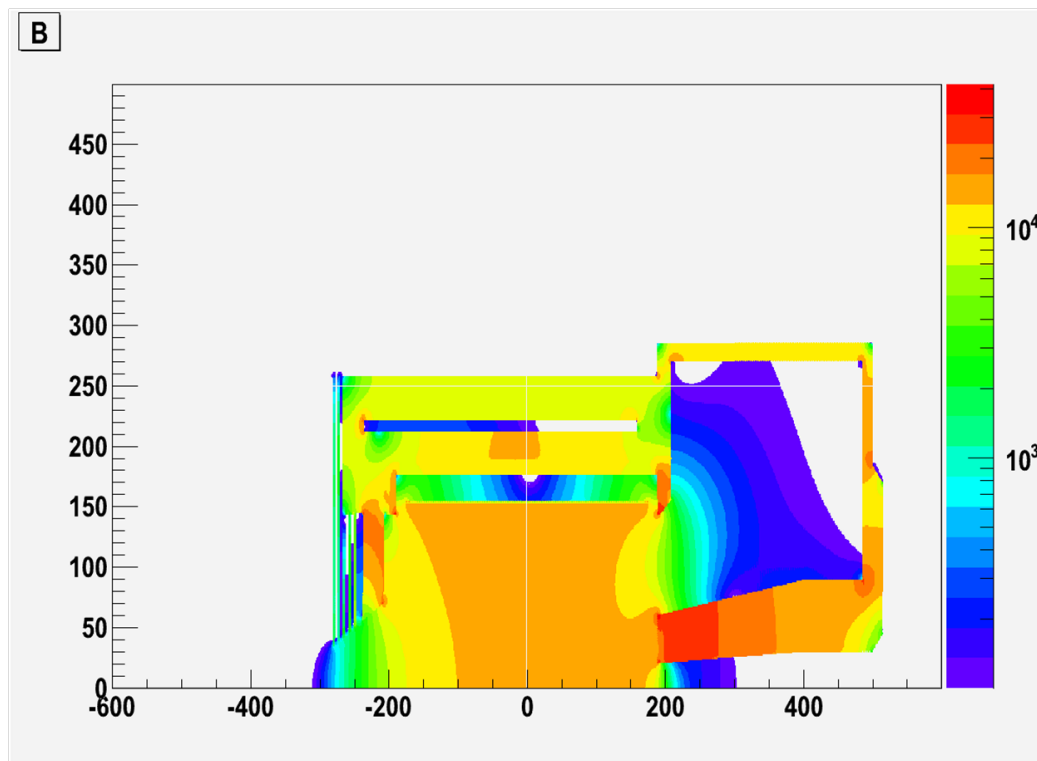


Figure 43: SoLID CLEO magnet field  $B > 100\text{G}$ .

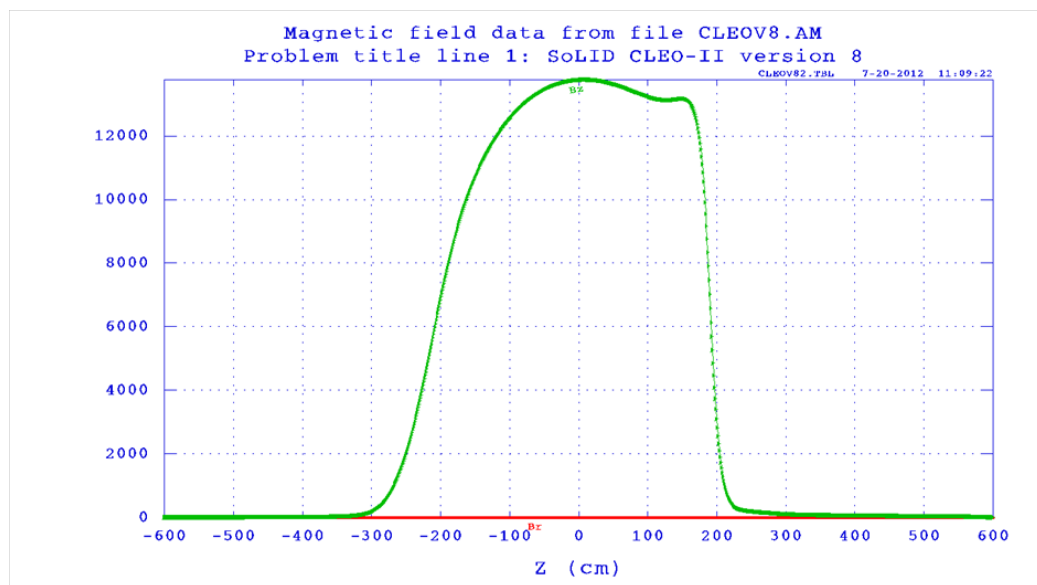


Figure 44: SoLID CLEO magnet field along beamline.

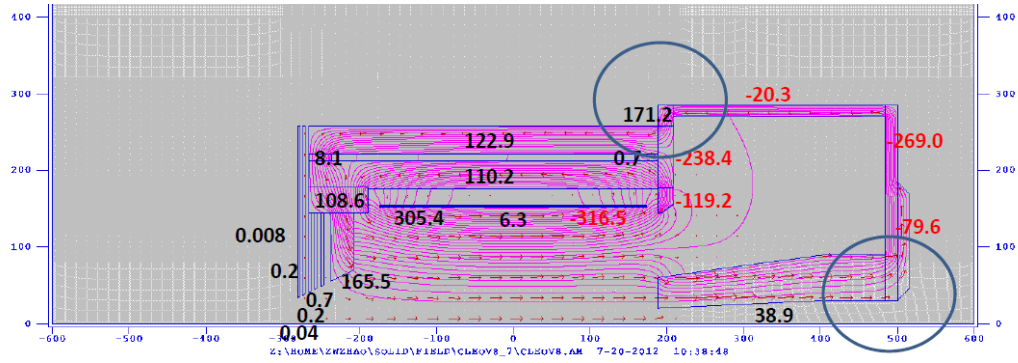


Figure 45: SoLID CLEO axial force in metric t. The two circles show where the force changes direction.

halves and capable of separation to allow for access to the detector package, see Figure 46. The endcap nose with a secondary backing plate will be a cast two piece design to allow for separation. Each section of the nose will bolt to the main backplate which consists of a two piece round disk. The two halves of the cylindrical outer ring will bolt to the corresponding backplate. The structural support and motion mechanism for the endcap will be discussed in Section 18.

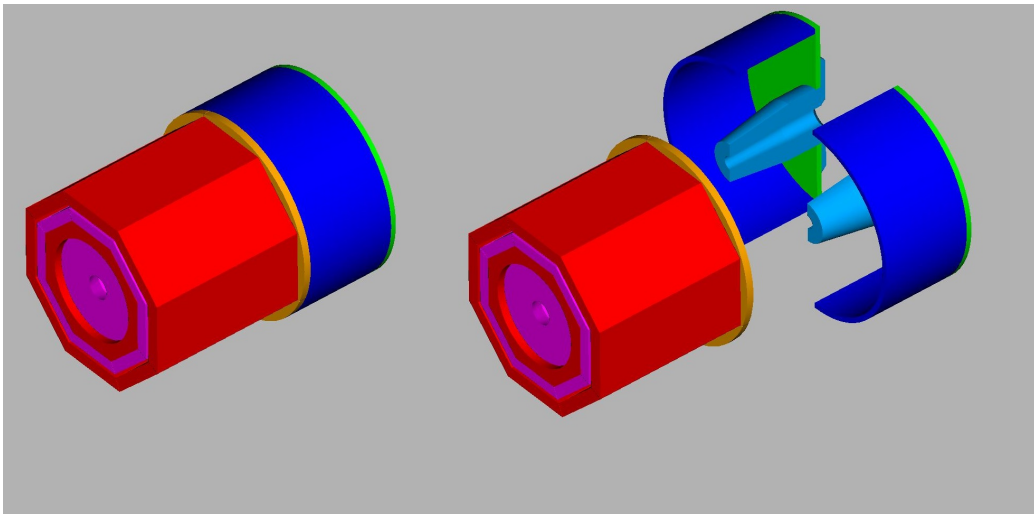


Figure 46: The endcap will be split vertically and also have the capability of separating in the lateral direction

#### 4.4 Current Status and Planned Test

Jefferson Lab will develop a cold test requirements document and implementation plan prior to installing the magnet in Hall A. The cold test will be done without the iron yoke and thus at reduced operating parameters.

A new magnet power supply cost has been added to the SoLID costs. Cost basis is from recent purchases.

Mapping the magnetic field and evaluating the data will require an additional 4–6 weeks in

schedule with use of 2 technicians and 1 scientist/engineer for the duration. Additional funding will be required for the mapping apparatus, \$200k.

Scheduling of the SoLID experiments will allow 1 year prior to installation for testing of the magnet.

We have included the cost for new power supply, controls, transfer lines and supports. The only reuse will be some magnet yoke steel and the cryostat.

Work on the dismantling of the CLEO II magnet was started by Cornell University in the summer of 2015 with the disconnection of power, cryogen and control lines for the magnet from the building infrastructure. Several of the large return iron blocks were also removed to provide practical experience for the Cornell rigging crew and the project management team to develop a comprehensive schedule for the 2016 removal.

The 2016 summer down period started with the removal of the 700 liter helium dewar and outer steel cladding. The leads, cooling supply and return lines as well as instrumentation cables needed to be severed at the top of the service turret to allow the dewar to be lifted away. Next, the beamline and detectors that resided in the bore of the magnet were uninstalled and the return iron was removed layer by layer.

Upon completion of the iron removal, including the coil collars, the axial transport brackets were installed to protect the coils during movement. The cryostat housing the coils could then be moved to the transport frame. The service turret and neck could then be removed from the top of the cryostat. The neck required disassembly to separate the continuous leads from the thermal shielding and cooling lines. The above mentioned disassembly steps adhered to the recommendations of the Oxford Operating Manual for the CLEO II Magnet. The leads were packaged for protection and secured to the side of the cryostat for safe transport. A stainless steel cover was fabricated and attached to the flange on the top of the cryostat providing protection for the ends and the cryo lines and leads. Any remaining openings were sealed to prevent contaminants from entering the vacuum space. Prior to loading on a flatbed truck the entire cryostat was wrapped in fire retardant marine grade shrink wrap to keep the unit weathertight for the trip to JLAB.

After arrival at JLAB the cryostat was rolled into the high bay area of the Test Lab for climate controlled storage until future use. Inspection indicated the cryostat remained sealed through transport. Loads on the magnet were monitored during transport using (2) three-axis accelerometers and remained under the maximum safe threshold indicated in the Oxford Manual. The two coil collars accompanied the cryostat in the November 2016 delivery and were stored in the Test Lab, as shown in Figure 47. The remaining return iron was stored at Cornell and will be shipped in fiscal year 2017. The Test Plan for characterizing the magnet and integrating it into the JLAB systems remains to be developed.



Figure 47: CLEO II magnet at JLab.

## 5 Targets

There are five approved SoLID experiments. Two semi-inclusive DIS experiments (E12-10-006 and E12-11-007) use a polarized  $^3\text{He}$  target with the achieved performance. One SIDIS experiment (E12-11-108) uses a transversely polarized proton ( $\text{NH}_3$ ) target. The parity-violating DIS experiment (E12-10-007) uses a 40-cm cryogenic liquid deuterium (hydrogen) target system. The J/Psi experiment uses the standard cryogenic liquid hydrogen target. The following subsections will describe the polarized  $^3\text{He}$  target, the polarized proton ( $\text{NH}_3$ ) target and the PVDIS cryotargets.

### 5.1 Polarized $^3\text{He}$ Target

The polarized  $^3\text{He}$  target is based on the technique of spin-exchange optical pumping of hybrid Rb-K alkali atoms. Such a target was used successfully in the recently completed SIDIS experiment [199] with a 6-GeV electron beam at JLab. Three sets of Helmholtz coils provide a 25 Gauss holding field for any direction, supporting polarization in transverse (for E12-10-006) or longitudinal (for E12-11-007) direction. Target cells were 40-cm long with density of about 10 amg (10 atm at  $0^\circ$ ). The luminosity was about  $10^{36}$  nuclei/s/cm with a beam current of 15  $\mu\text{A}$ . An in-beam polarization of up to 60% was achieved. Both achieved luminosity and figure-of-merit are the world-best so far. Two kinds of polarimetry, NMR and EPR (paramagnetic-Resonance), were used to measure the polarization of the target. The precision for each method was about 5% (relative) and the methods agreed well within uncertainties. It is expected to be able to reach 3% with the planned improvements.

Frequent target polarization direction reversal is needed to minimize target-spin-correlated systematic uncertainties. The fast target spin reversal was achieved in a few seconds for the 6 GeV SIDIS experiment by using RF AFP technique. The frequency of the spin reversal was kept to 20 minutes to minimize the polarization loss due to AFP. The additional polarization loss due to frequent spin reversal was kept at  $< 10\%$  (relative). The above quoted maximum in-beam polarization achieved for the 6 GeV experiment (up to 60%) included the loss due to spin reversal. A new method using field rotation for spin reversal was tested and a nearly no polarization-loss result was achieved and will result in an improved performance. It will allow to have more frequent (a few minutes instead of 20 minutes) spin reversal to help further improve the target-spin-correlated systematics.

The upstream endcap plate will keep the magnetic field and its gradients under control in the target region. In this design, the absolute magnetic field strength in the target region is about a few Gauss with field gradients 50 mG/cm. Correction coils around the target will further reduce field gradients to the desired level of 30 mG/cm.

A collimator, similar to the one used in 6 GeV experiment, will be placed next to the target cell window to minimize the target cell contribution to the total events.

In addition to the polarized  $^3\text{He}$  target, the current target system has a multi-foil  $^{12}\text{C}$  target for spectrometer optics study, a BeO target for beam tuning and a reference target cell system, which allows to have different target gases, hydrogen, deuterium,  $^3\text{He}$  and nitrogen, be used to measure unpolarized cross sections, for calibration and dilution study.

Upgrades are planned for other polarized  $^3\text{He}$  experiments before the SoLID experiments. These upgrades are not required for the SoLID experiments but will benefit them.

### 5.2 Transversely Polarized Proton Target

The SoLID collaboration proposes to measure single spin asymmetries in the semi-inclusive, deep-inelastic ( $e, e'\pi^\pm$ ) reaction using a transversely polarized proton target. The target to be used is the

dynamically polarized ammonia target that has been used at SLAC and at Jefferson on numerous occasions [200]. Its last use was in 2012 for the g2p/Gep experiments, which took place in Hall A [201]. Proton luminosities of  $10^{35} \text{ cm}^{-2}\text{s}^{-1}$  have been achieved with this target, in conjunction with electron beam currents up to 100 nA. In order to meet requirements of the SoLID measurements however, a new superconducting magnet must be procured, as discussed below.

Dynamic nuclear polarization (DNP) has been used to polarize solid targets for nuclear and particle experiments for more than four decades. To realize DNP, a paramagnetic species is implanted into the target material, either by dissolving a stable radical into the material (if the latter is liquid at room temperature), or by producing radicals directly within the material using ionizing radiation. The unpaired electrons are highly polarized by cooling the sample to a low temperature and exposing it to a high magnetic field. For example, at the 1 K and 5 T operating conditions of the JLab target, the electron polarization is -99.8%. Off-center microwave saturation of the radicals Electron Spin Resonance (ESR) frequency is used to transfer this polarization to nearby nuclear spins, with one or more mechanisms, such as the solid effect, thermal mixing or the cross effect, being responsible for the polarization transfer. Spin diffusion then transports the nuclear polarization throughout the bulk of the sample. The polarization may be positive or negative, depending upon whether the microwave frequency is below or above the ESR frequency. In well-designed systems, proton polarizations exceeding 95% [202] and deuteron polarizations approaching 90% [203] have been achieved.

Frozen ammonia ( $\text{NH}_3$ ) has been the target material of choice for electron beam experiments at Jefferson Lab. Proton polarizations in excess of 90% are routinely achieved in ammonia, and it has a relatively high ratio of polarizable-to-nonpolarizable nucleons (17.6%). Additionally, ammonia displays a very high resistance to radiation damage, and simply warming the material to about 100 K for a few minutes can largely repair the damage that does occur. Prior to the experiment, paramagnetic radicals (chiefly  $\text{NH}_2$ ) are created within the ammonia by irradiating the material (under liquid argon) with an electron beam. For convenience, this irradiation is typically done off site, and the material is then stored under liquid nitrogen until required for the experiment. The JLab target system, as utilized in Hall A, is shown in Fig 48. It consists of a 5 T split-coil superconducting magnet, a  $^4\text{He}$  evaporation refrigerator with a cooling power of about 1 W at 1 K, and a target insert containing two samples of frozen ammonia along with additional targets for background and dilution studies. These reside in a purpose-built, evacuated scattering chamber with thin windows around its perimeter for beam entrance and exit. Equipment outside the chamber includes a large set of vacuum pumps for the evaporation refrigerator, microwave electronics for polarizing the target sample, and a NMR system for measuring its polarization. Liquid helium is provided to the target from a nearby 500 L dewar.

Before its use in the g2p/Gep experiments, numerous upgrades were made to the polarized target in order to improve its performance, reliability, and safety:

- An entirely new refrigerator was constructed at JLab according to the safety regulations dictated by 10 CFR 851;
- The quench-relief piping system for the superconducting magnet was upgraded to replace leaking rubber seals with copper gaskets, and also made compliant to 10 CFR 851;
- The pumping system and controls were overhauled;
- A more robust sample insert and motion mechanism were constructed to address problems that were encountered in previous experiments;

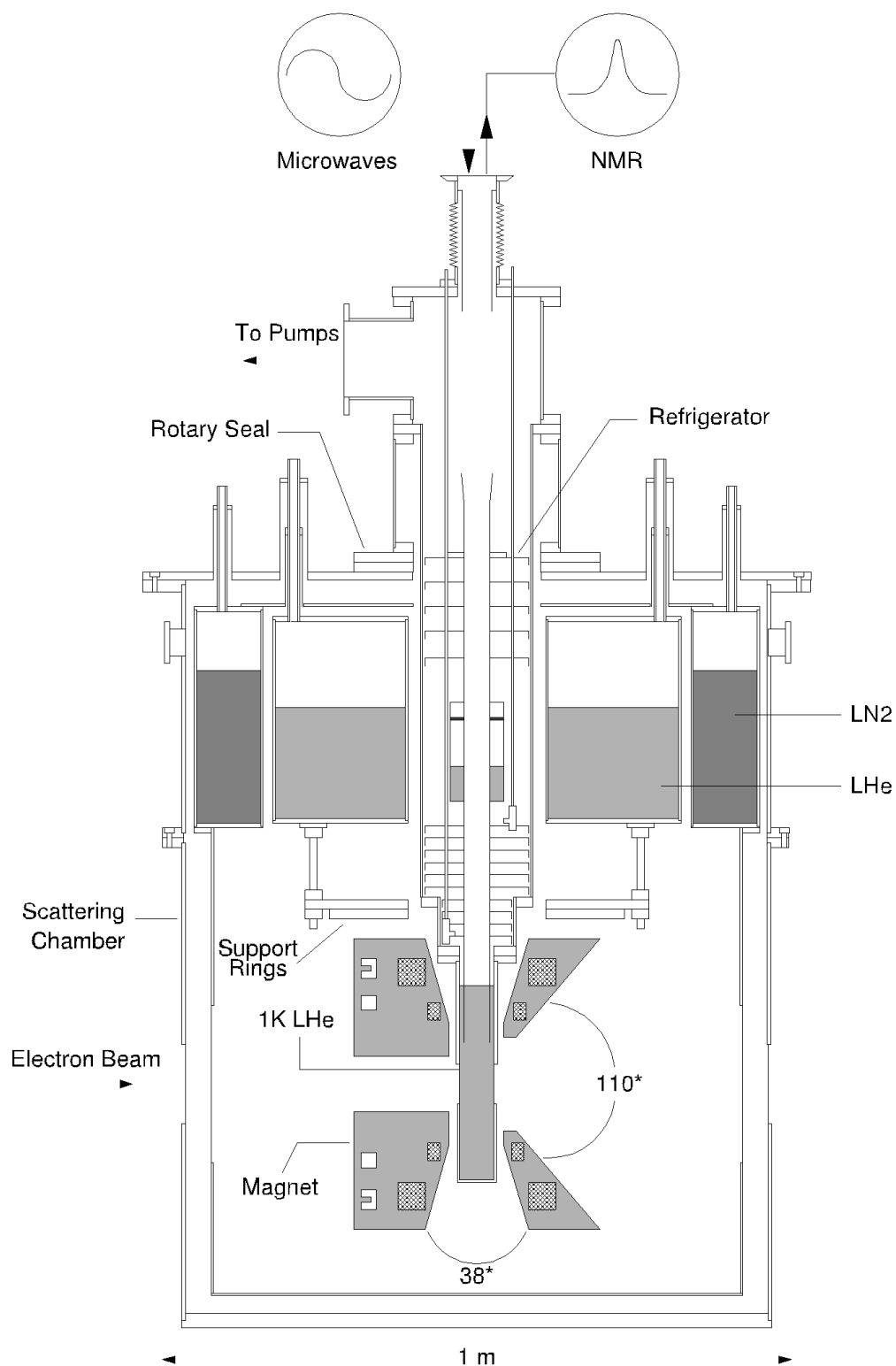


Figure 48: The dynamically polarized target, as utilized in Hall A. The cryostat can rotate  $90^\circ$  about the vertical axis, thus providing either longitudinal or transverse polarization with respect to the electron beam. The longitudinal orientation is shown.



- A new rotary vacuum seal was implemented that significantly reduces the time required to rotate the magnet between its longitudinal and transverse orientations. With the new seal, there is no longer a need to disconnect the refrigerator pumping line, nor remove and replace the sample insert;
- The 5 T magnet suffered irreparable damage during the final systems tests, and was replaced with a similar magnet removed from the Hall B polarized target [204].

It should be noted that both the original and Hall B magnets were primarily designed to provide longitudinal polarization, while still permitting limited use for transverse polarization. As such, each magnet possesses an opening angle of  $110^\circ$  ( $\pm 55^\circ$ ) in the direction parallel to the magnetic field, compared to only  $\pm 17^\circ$  perpendicular to it (see Fig. 48). Because the SoLID proposal requests transverse polarization with an opening angle  $\pm 25^\circ$  or greater, a new magnet will be necessary.

Oxford Instruments (manufacturer of both the Hall B and original magnet) has performed a detailed feasibility study and concludes that they can build a 5 T split-coil magnet with both a  $\pm 25^\circ$  split angle and the homogeneity required for DNP [205]. The SoLID collaboration and JLab Target Group will work alongside the eventual vendor to ensure the magnet can be easily incorporated into the existing JLab cryostat. This will greatly reduce the time and cost required to field a transversely polarized target for SoLID.

### 5.3 Cryogenic Target for PVDIS

The proposed target consists of 40 cm liquid hydrogen/deuterium cell. This cell will be filled with either hydrogen or deuterium as needed. The heat load on this target will be much more modest than the Qweak target that was employed from 2010 to 2012 at JLAB. A conceptual design of the target is shown in the figure. The current concept allows for remote placement of a single cryogenic cell and a dummy cell with several solid targets necessary for calibrations. Such a target has the following basic elements:

1. Heat exchanger (HX)
2. Insulating vacuum chamber (IVC)
3. Target stack
  - (a) Cell
  - (b) Dummy target
  - (c) Solid targets
4. Recirculating pump
5. Cryostat
6. Temperature stabilizing heater
7. Positioning system
8. Gas handling system and gas storage
9. Instrumentation
10. Depolarizer

All components in the system must comply with 10 CFR 851 with regard to pressure, electrical, and fire safety. The majority of these components will remain outside the high magnetic field of the solenoid. The cell and connecting piping together with the rest of the target stack are necessarily placed in the magnetic field of the solenoid. Selection of materials for these components shall consider this.

The insulating vacuum chamber will consist of two main sections. One section will be inside the bore of the solenoid and a section similar to the IVC for the standard Hall A cryogenic target will be upstream of the magnet. This latter section will contain the motion system, heat exchanger, etc. The section in the magnet will only contain the target stack and connecting piping. Materials for the chamber section inside the solenoid must be compatible with the magnetic field inside the solenoid. The exit of the chamber will be compatible with the acceptance of the detector.

Careful attention must be given to the design of the cell. While the requirements of this target regarding density fluctuations are much less stringent than those imposed on either the Qweak or G0 targets, it is of some concern. Analysis of the cell design using computational fluid dynamics (CFD) will be employed to ensure an acceptable cell design. Based on experience with previous targets at JLAB, noise associated with density fluctuations is not expected to be significant compared to counting statistics. To reduce the background from Al-e- asymmetries, the sections of the cell upon which the beam impinges will be thin. Thicknesses of 120  $\mu\text{m}$  are commonly available and are adequate for the needs of the experiment. The remainder of the cell will be designed to optimize boiling performance, detector acceptance, and pressure safety. High strength aluminum alloys such as AL-7075 and AL-2219 (used on welded components) shall be used on critical parts of the cell. Through extensive experience it has been shown that cell and cell block assemblies are much more reliable when welds and mechanical joints such as conflat (CF) are employed. This avoids the issues with solder and other sealing techniques. This approach also accelerates the design and prototyping phase and simplifies testing and assembly.

To avoid interference between the exiting particles at maximum scattering angle of  $35^\circ$  and the upper and lower target components, the cell and dummy target must be separated by a minimum of 28 cm plus half the width of the cell and dummy target. Similarly the dummy and the solid targets (positioned at  $Z = 0$ ) will require 14 cm of separation plus half the width of the dummy target and first solid target frame. A total stack height of more than 70 cm is expected. The motion system must accommodate this height and allow for some alignment adjustments. The standard Hall A cryogenic target has over 70 cm of travel, thus a similar mechanism will be suitable.

Dummy and solid targets can be selected and installed as needed. The thickness of the dummy target will be chosen to match the radiation length of the liquid cell. Solid targets required for optics studies, background measurements and alignment checks will also be installed.

The cryogenic liquid hydrogen and deuterium target must accommodate a beam current of 50  $\mu\text{A}$  on a 40 cm long cell. The estimated beam heat load for this is  $\sim 800\text{W}$ . The pump, heater overhead, transfer line and other losses require an additional estimated  $\sim 250\text{W}$ . During the Qweak experiment, more than 3 kW of power at 20K was dissipated by the heat exchanger. This design made use of both 15K and 4K refrigerant from the End Station Refrigerator (ESR) and the Central Helium Liquefier (CHL). A careful study of the target heat load and ESR/CHL refrigerators will be necessary to design the heat exchanger. However, it is expected that the heat exchanger will not need to dissipate more than 1500 W which includes a comfortable operating margin. Operationally, only  $\sim 1\text{kW}$  of refrigeration will be required by one or more refrigerator.

The hydrogen and deuterium target fluids may become slightly polarized in the magnetic field of the solenoid. This would result in an asymmetry unrelated to the physics of interest. This effect can be mitigated in the case of deuterium with an RF-depolarizer. In the case of hydrogen, pure para-hydrogen would reduce this effect. A catalyst (such as an iron oxide bed) would enhance the

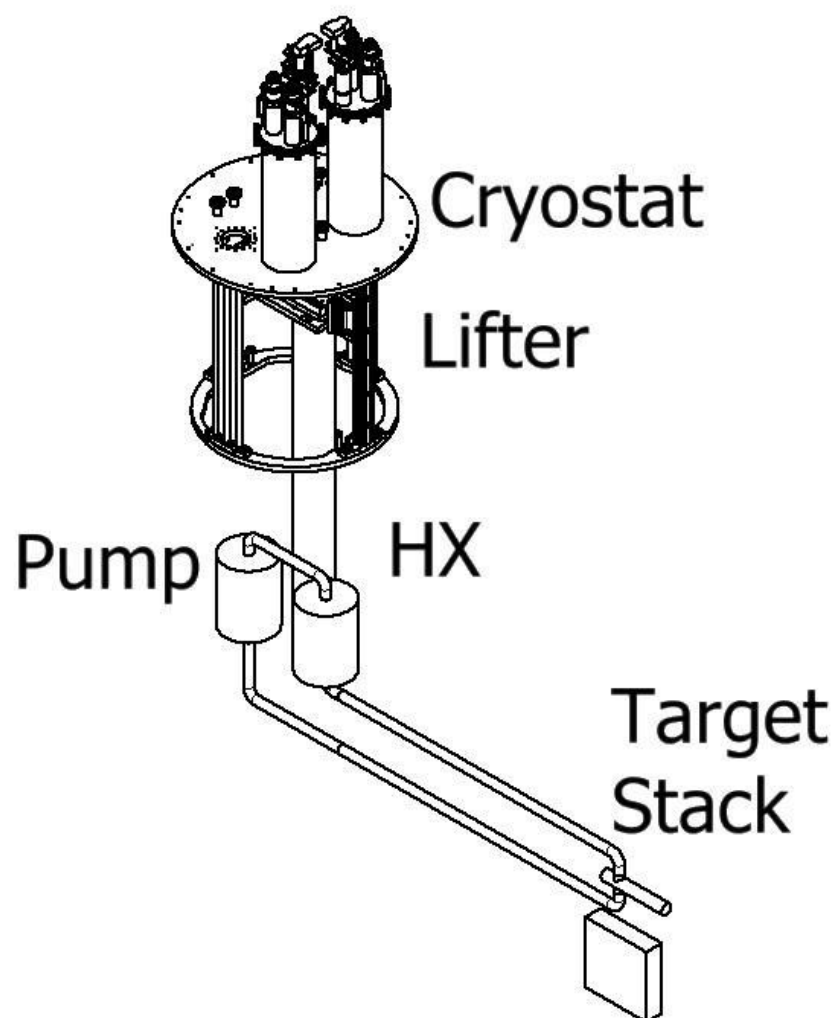


Figure 49: Cryogenic Target for PVDIS

para to ortho fraction.

## 6 Baffles

In order for the detectors in the PVDIS experiment to operate at the design luminosity, a set of baffles is required that passes a reasonable fraction of the DIS electrons while blocking as much of the background as possible. The baffles provide curved channels through which only the spiraling high energy negative particles can pass. Most line-of sight photons and positively charged hadrons are blocked.

The design of the baffles requires careful optimization since there are many sources of background and the different detectors respond differently to the different backgrounds. The dominant background in the GEM's is soft photons, especially those between 1 and 2 MeV. The GEM's are relatively inefficient for lower energy photons. Sources of these photons include beam bremsstrahlung, forward radiation from wide-angle 30-100 MeV Møller electrons generated in the target, and photons from showers in the baffles induced by neutral pions. The light gas Cerenkov is sensitive to pair production from photons above 20 MeV or so which can come from neutral pions produced in the target to bremsstrahlung from the wide-angle Møller electrons. The ECal is sensitive the positive hadron punch-through and high energy photons from neutral pion decay.

To design the baffles for a specific magnetic field and detector configuration, ray-tracing of simulated DIS electrons is performed for the desired momentum range. For a uniform solenoidal field, high momentum electrons have a trajectory in  $\phi - z$  space that is linear and the  $\theta - z$  trajectory is independent of the field. The design process takes simulated electrons in a realistic field and exploits this approximate behavior to define pathways for ranges of electron momenta. This allows for a relatively simple design process involving an extended target where one considers radial rings of restricted scattering angle and places blocking material to only allow these trajectories. The number of sectors to be used for this experiment is driven by the azimuthal angle  $\phi$  traversed by the minimum momentum particles, which for these kinematics is about  $12^\circ$ , hence 30 sectors.

To block line-of-sight photons, there must be sufficient material to block line particles that have a constant trajectory in  $\phi$ . Due to the fact that the target is extended, the simple model does not completely hold, allowing some fraction to leak through.

We recently have undertaken studies of our baffle design including evaluation of materials, acceptance, and background reduction. While our baseline baffle design uses lead, other possibilities include copper or tungsten. These materials vary by a factor of four in radiation length. The variation in nuclear interaction length is smaller, as shown in Table 9. Tungsten's high density and short interaction length is advantageous, however its cost is higher, and solid tungsten is difficult to machine. An easier approach to construction would be to use powdered tungsten which can be easily molded and glued.

We have performed studies of trigger rates in the EC, rates of neutrons entering the EC, and rates of photons striking the last GEM with baffles constructed of different materials, but with the same geometry. All show fairly small differences, seen in Table 9. Lead provides a slightly lower photon rate than copper, while copper's hadron rates are slightly better. Powdered tungsten has a density only about 60% of solid tungsten, and consequently provides little or no performance advantage over lead.

An important background is photons from  $\pi^0$  decay interacting in the baffles. When photons strike the baffles close to the "hot" edge of a slit, shower products can escape into the slit and from there thread through the slits in the remaining baffle plates. A modification we have considered is to remove material amounting to  $0.6^\circ$  in angular width from the hot edges on baffle plates 2, 4, 6, 8 and 10, allowing photons that would have hit near these slits to strike instead further from the hot edges on the next plate. Our simulations show a 16% reduction in photon rates above  $p = 1$  GeV/c, and 26% reduction for  $p > 10$  GeV/c. Removal of this material would increase the pion background,

	Copper	Lead	Tungsten powder	Solid tungsten
Radiation length (cm)	1.436	0.5612	0.583	0.3504
Nuclear interaction length (cm)	15.32	17.59	16.58	9.946
Machinability	Easy	Soft, needs support	Easy to mold and glue	Hard
Cost	Low	Low	High	High
EC trigger rate (kHz)	$4.78 \times 10^3$	$5.45 \times 10^3$	$5.25 \times 10^3$	$4.59 \times 10^3$
Neutron rate in EC (kHz)	$3.35 \times 10^7$	$4.7 \times 10^7$	$4.0 \times 10^7$	$2.9 \times 10^7$
Photon rate in last GEM (GHz/sector)	2.98	2.59	—	—

Table 9: Properties and performance of copper, lead, tungsten powder and solid tungsten as baffle materials.

but by less than 10%.

We have performed detailed studies of track trajectories through the baffles to identify places where improvements in the baffle geometry can be made. One finding was that, for the upstream baffle plates, the solid ring at the inner radius and an angular constriction at small radius interfere with the acceptance for electrons produced at the downstream end of the target. For vertices at the upstream end of the target, acceptance was being lost due to the too-small outer radii of the upstream baffle plates.

Based on these studies we have developed an improved baffle design, shown in in Fig. 50. Inner rings and angular constrictions on the first few plates have been removed, and outer radii of these plates have been increased. Shapes of the slits in all the plates were optimized, keeping the overall aperture in polar angle unchanged, but tightening up slits that were slightly too wide. The outcome of this program was a geometrical design, having modest acceptance improvements over our previous baffles while not significantly affecting photon rejection, which we believe to be optimal; see Figures 51 and 52.

A detailed study of the activation of different materials suitable for the baffle has been carried out. Radiation levels for each material were studied for three different durations of beam exposure, and possible shielding configurations were evaluated. The final selection of the baffle material will likely be driven less by performance and more by activation and ease of construction.

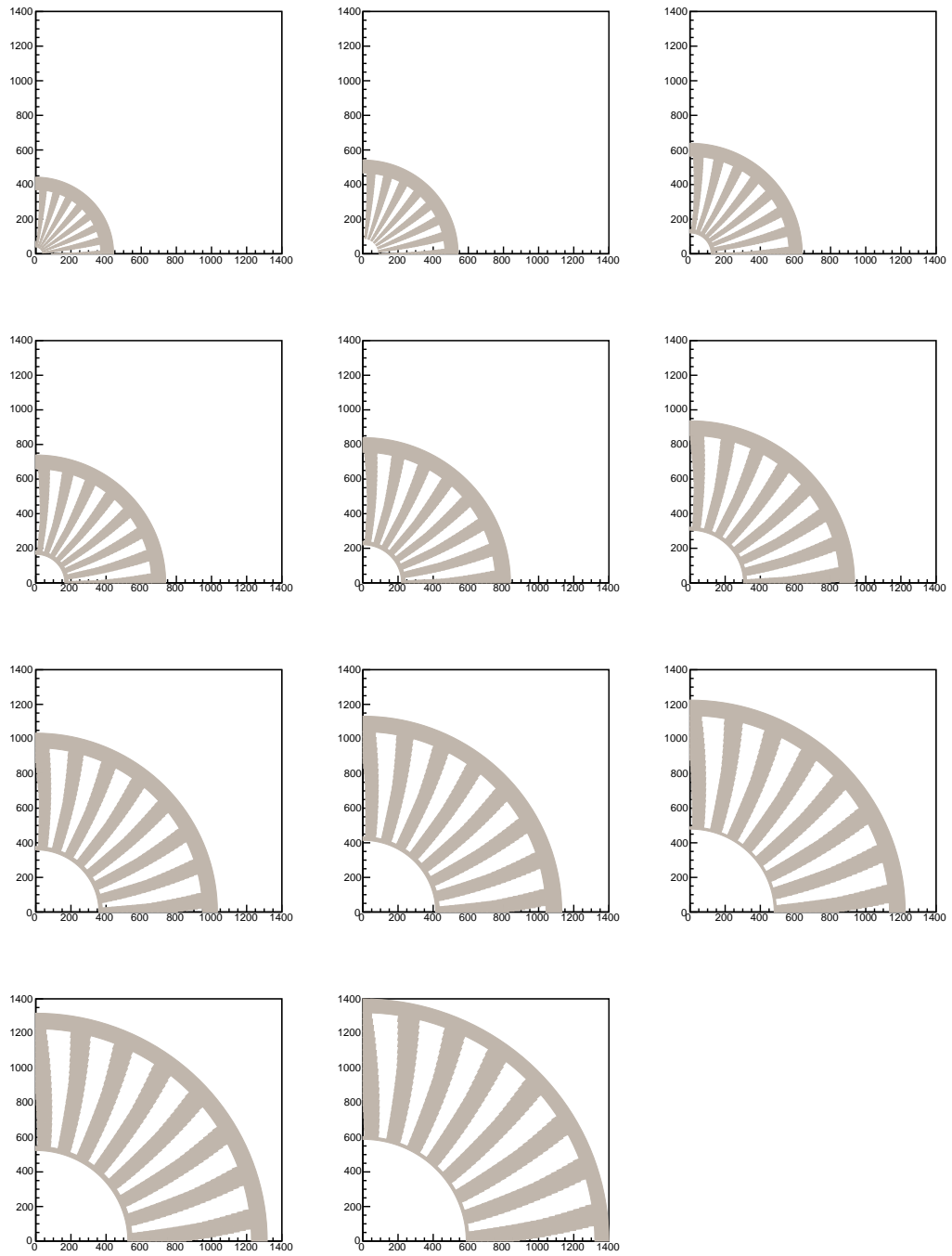


Figure 50: Face on views (first quadrant only) of the 11 plates in the PVDIS baffle system.

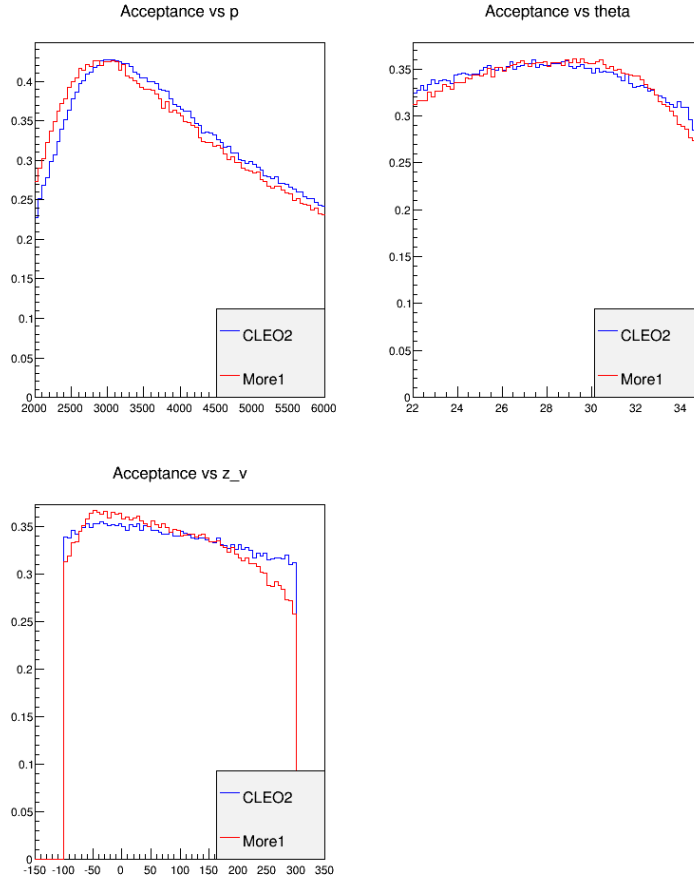


Figure 51: Geometric acceptance of the PVDIS baffles for DIS electrons with  $Q^2 > 6 \text{ GeV}^2$ ,  $W > 2 \text{ GeV}$ , and  $x_{bj} > 0.55$  versus momentum (top left), scattering angle (top right), and vertex position (bottom left). Blue (red) lines are acceptance for the optimized (previous) baffle design.



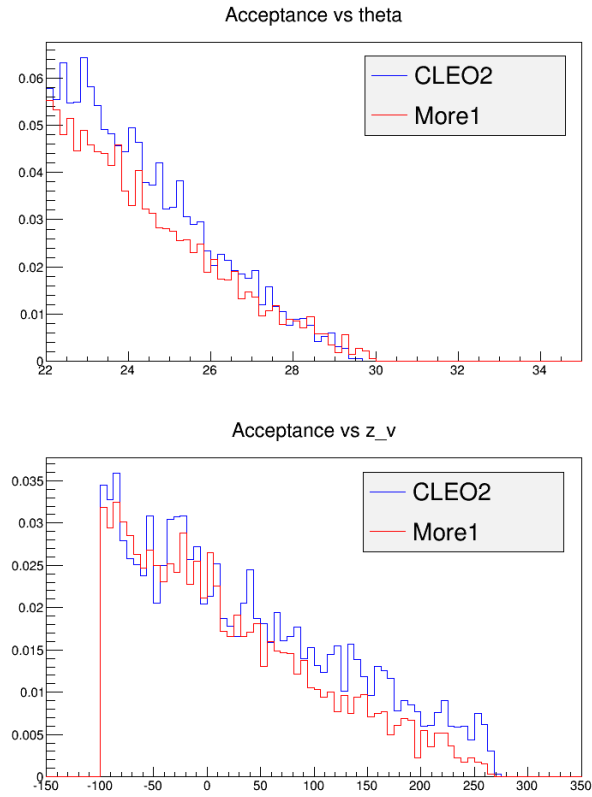


Figure 52: Geometric acceptance of the PVDIS baffles for photons versus scattering angle (top), and vertex position (bottom). Blue (red) lines are acceptance for the optimized (previous) baffle design.

## 7 GEM Tracker

### 7.1 Design

The SoLID spectrometer requires high resolution track reconstruction under high rate conditions over a large area. A cost effective solution for such requirements is provided by the Gas Electron Multiplier (GEM) technology invented by F. Sauli [206] in 1997. The GEM is based on gas avalanche multiplication within small holes (on a scale of  $100\ \mu\text{m}$ ), etched in a Kapton foil with a thin layer of copper on both sides. The avalanche is confined in the hole resulting in fast (about 10 ns rise time) signals. Several GEM foils (amplification stages) can be cascaded to achieve high gain and stability in operation. The relatively small transparency of GEM foils reduces the occurrence of secondary avalanches in cascaded GEM chambers. All these properties result in very high rate capabilities of up to 100 MHz per  $\text{cm}^2$  and an excellent position resolution of  $70\ \mu\text{m}$ . Fig. 54 illustrates the principle of operation of a triple (three foil) GEM chamber. Triple GEM chambers were successfully used in the COMPASS experiment at CERN [207].

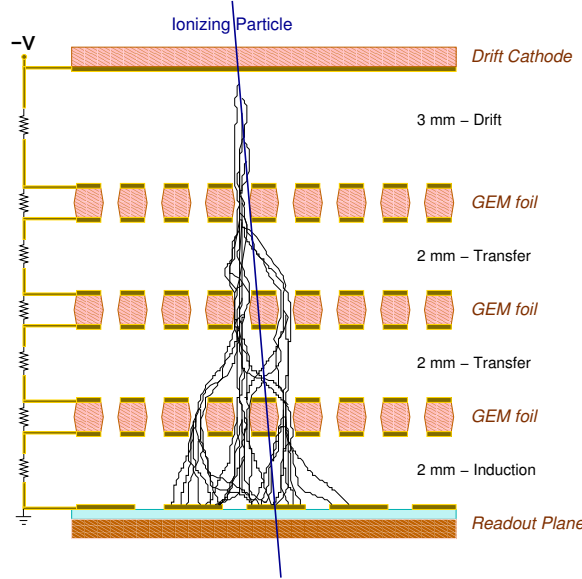


Figure 53: Principle of triple GEM operation.

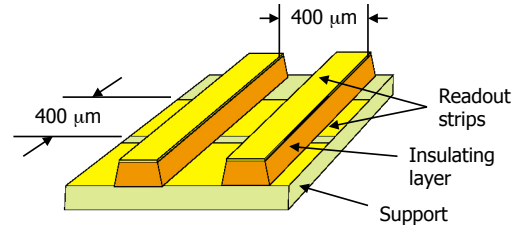


Figure 54: 3D view of the readout board.

For the PVDIS configuration of SoLID, detector locations 1, 2, 3, 4, and 5 will be instrumented with GEM chambers. Table 10 summarizes the parameters of the SoLID PVDIS GEM chambers. At each detector location there will be 30 trapezoidal GEM chamber modules, one for each sector defined by the baffles. The GEM modules will have an angular width of  $12^\circ$  with the readout stripes parallel to the two edges of the sector, so that the stripes from the two readout layers are at a  $12^\circ$  stereo angle. The readout pitch for locations 1, 2 and 3 will be 0.4 mm while the pitch for locations 4 and 5 will be 0.6 mm. Figure 55 shows the GEM module arrangement for one of the detector locations of the PVDIS configuration. Figures 56 and 57 show the details of the GEM module edges and mounting at the inner and outer radii of the SoLID detector wheel.

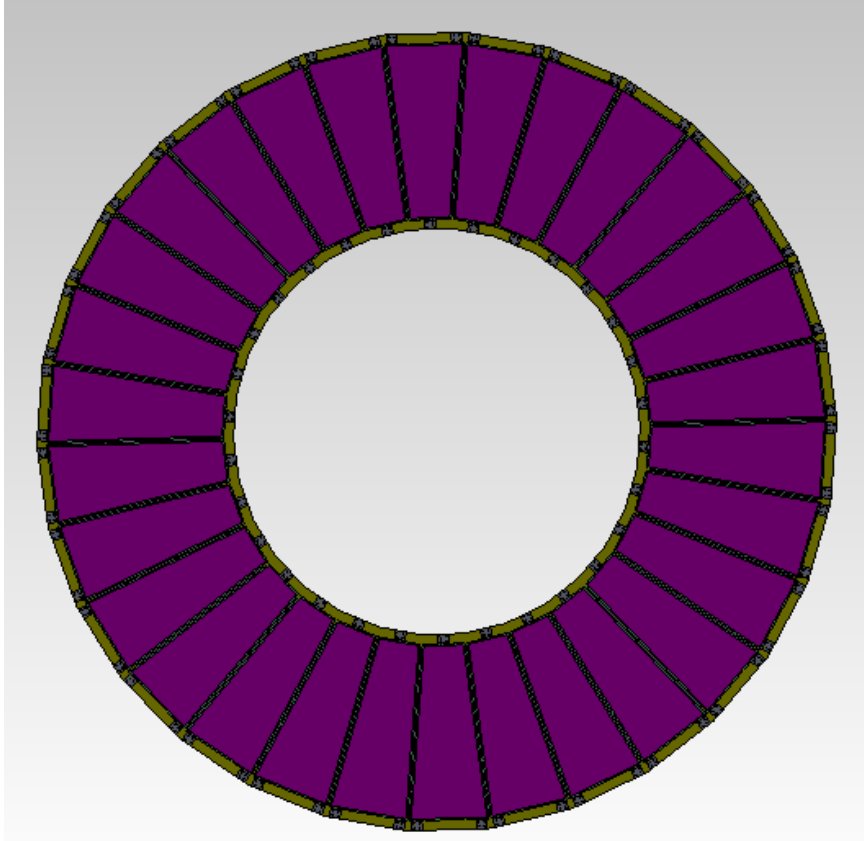


Figure 55: The GEM module arrangement at one of the detector locations of the SoLID PVDIS configuration

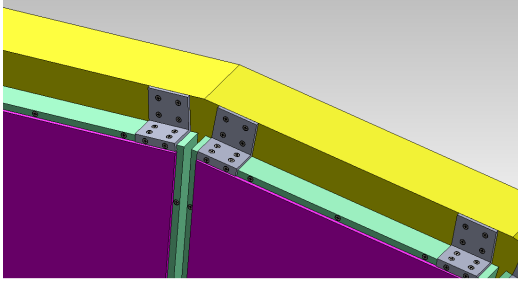


Figure 56: GEM module mounting at the outer edge of a GEM ring in the PVDIS configuration.

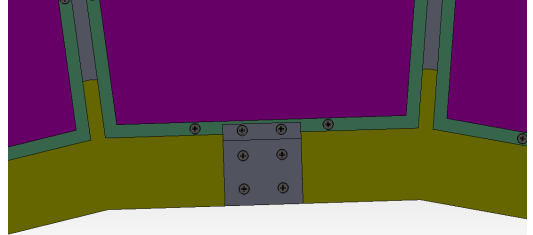


Figure 57: GEM module mounting at the inner edge.

Location	$Z$ (cm)	$R_{min}$ (cm)	$R_{max}$ (cm)	Surface (m <sup>2</sup> )	# chan
1	157.5	51	118	3.6	24 k
2	185.5	62	136	4.6	30 k
3	190	65	140	4.8	36 k
4	306	111	221	11.5	35 k
5	315	115	228	12.2	38 k
Total				$\approx 36.6$	$\approx 164$ k

Table 10: The locations, sizes and number of readout channels of GEM detectors for the SoLID PVDIS configuration

The SIDIS configuration of SoLID calls for detector locations 1, 2, 3, 4, 5, and 6 instrumented with GEM modules. Table 11 summarizes the parameters of the SIDIS GEM chambers. While the number of detector stations is higher in the SIDIS configuration, the inner and outer radii of the detector wheels are significantly smaller compared to the PVDIS configuration. Furthermore, since there are no baffles in the SIDIS configuration, the active detection area has to cover the entire surface area of each detector wheel. In order to meet these requirements, the SIDIS detector configuration will be set up by arranging the GEM modules from the PVDIS configuration in an overlapping two-wheel arrangement at each detector station as indicated in Figure 58. In this arrangement, 20 modules cover the entire active area of each detector station.

Location	$Z$ (cm)	$R_{min}$ (cm)	$R_{max}$ (cm)	Surface (m <sup>2</sup> )	# chan
1	-175	36	87	2.0	24 k
2	-150	21	98	2.9	30 k
3	-119	25	112	3.7	33 k
4	-68	32	135	5.4	28 k
5	5	42	100	2.6	20 k
6	92	55	123	3.8	26 k
Total				$\approx 20.4$	$\approx 161$ k

Table 11: The locations, sizes and number of readout channels of GEM detectors for the SoLID SIDIS configuration

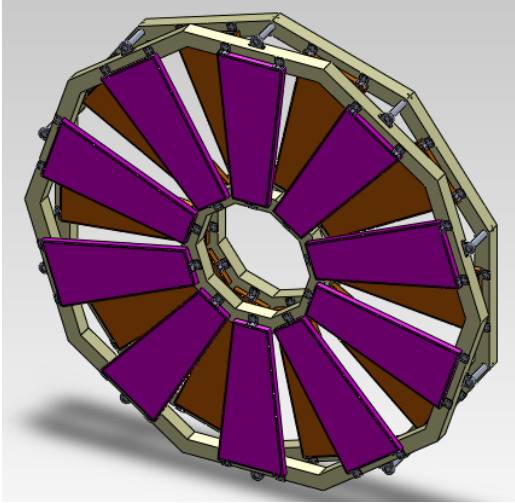


Figure 58: The GEM module arrangement at one of the detector locations of the SoLID SIDIS configuration

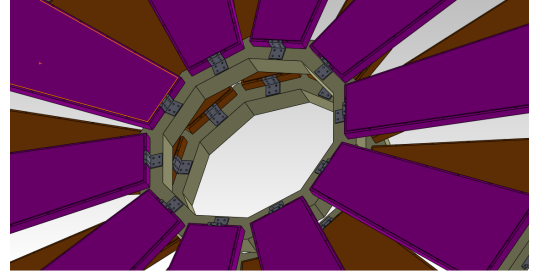


Figure 59: GEM module mounting at the inner edge of the ring in the SIDIS configuration

Figure 60 shows the detailed design for a GEM module of the size proposed for SoLID. The “wings” shown in the frames are to support the frames during chamber assembly; they will be removed once the chamber is completed. The 2D readout plane will be glued on the bottom plate (shown in cyan). This plate, made out of a 3 mm thick honeycomb structure material, also provides

structural rigidity to the GEM chamber. All other frames are made out of Permaglass<sup>3</sup> with 8 mm wide sides. The spacers shown within the active area are for keeping the GEM foils from touching each other; these spacers are approximately 300  $\mu\text{m}$  wide and contribute only about 1% reduction to the active area of the chamber. The GEM foils are mounted on the 3 light green frames, while the drift cathode is glued on the red frame. A thin gas window is glued on the orange frame.

Figure 61 shows the concept for the 2D readout frame. Strips for one direction (shown in blue) continue across the readout plane, while the short segments of the strips for the other direction (shown in red) are connected via through holes to readout lines running along the back of the plane. Large area readout planes of similar design have been tested in prototype GEM chambers for KLOE2 at Frascati.

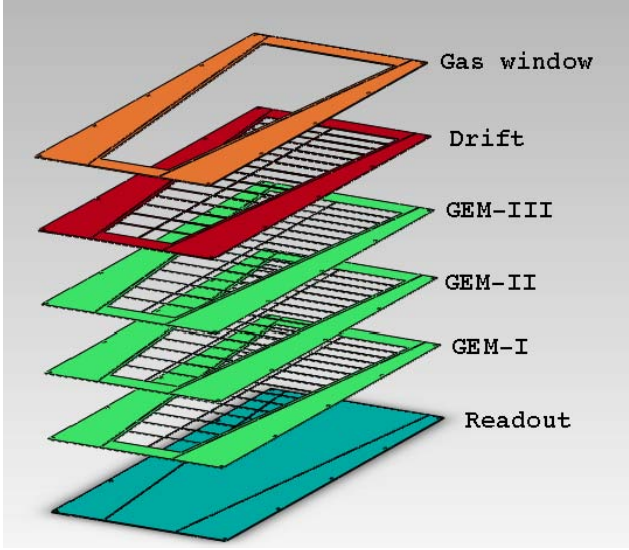


Figure 60: The frame assembly for a GEM module prototype of the size proposed for the largest SoLID GEMs

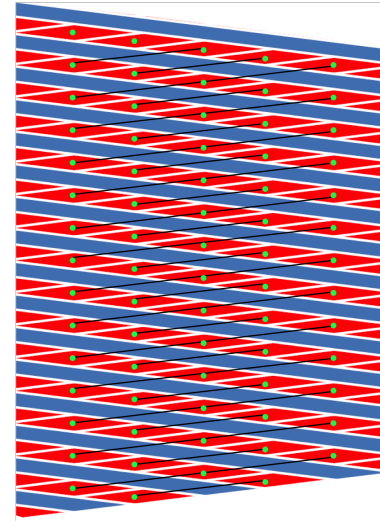


Figure 61: The schematics of the 2D readout plane proposed for SoLID

One challenge we are facing for the GEM trackers of SoLID is the large active area required; the active area of the largest GEM modules needed will be approximately  $113 \times (21-44) \text{ cm}^2$ . Until recently, the maximum GEM foil area had been limited to  $45 \times 50 \text{ cm}^2$ . However, over the last few years the Micro Pattern Gas Detector (MPGD) group at CERN, in collaboration with INFN, has perfected two techniques to produce large area GEM foils: single mask GEM etching and GEM splicing [208, 209]. The single mask technique allows for the fabrication of foils as large as  $100 \times 200 \text{ cm}^2$ . The splicing technique allows for two such foils to be combined with only a 3 mm wide dead zone between the two foils. Recently several large prototype GEM chambers were constructed and tested at CERN using the large area GEM foils fabricated using the new techniques [210]. These new prototype chambers, constructed under the CMS upgrade GEM project, have trapezoidal shapes with an active areas of  $99 \times (25-45.5) \text{ cm}^2$ ; these dimensions are close to the dimensions of the largest GEM chamber modules planned for SoLID.

Furthermore, there have been significant advances in the GEM chamber readout systems in the recent years. The RD-51 collaboration funded Scalable Readout System (SRS) project at CERN

<sup>3</sup>Permaglass is a glass fiber material with randomly oriented fibers that can be machined with very high precision.

has already developed and tested a low cost APV-25 based readout. The APV25-S1 analog readout chip [211] is currently in use for the COMPASS GEM trackers and the CMS silicon strip detectors. A mid-size prototype system consisting of 15,000 channels was successfully tested and was shown to work very well. The SRS group is continuing the development and is also working with a commercial vendor to fabricate the SRS modules. The cost of the APV-25 based SRS readout is expected to be approximately \$ 3 per channel.

## 7.2 GEM tracker R&D

Research and development towards the SoLID GEM tracker is currently being conducted in the United States at the University of Virginia (UVa) and in China at five institutions: China Institute of Atomic Energy (CIAE), Lanzhou University (LZU), Tsinghua University (THU), the University of Science and Technology of China (USTC) and the Institute of Modern Physics (IMP). According to the current plan, the UVa group, which has an ongoing large area GEM module production program, will do the initial designs and prototyping of the SoLID GEM chambers, while the Chinese institutions get their large area GEM production programs set up. At the same time CIAE has been working with CERN and Chinese manufacturers to develop large area GEM foil production capabilities in China.

### 7.2.1 GEM chamber R&D program in UVa

The Istituto Nazionale di Fisica Nucleare (INFN)-Roma group and the University of Virginia group are currently leading an aggressive R&D program to develop large area GEM chambers for the Hall A Super Bigbite apparatus (SBS). The active area of large tracking chambers of SBS will be  $50 \times 200 \text{ cm}^2$ . These large GEM trackers will be assembled by combining  $40 \times 50 \text{ cm}^2$  and  $50 \times 50 \text{ cm}^2$  “chamber modules” with narrow edges. The UVa group has already constructed several  $40 \times 50 \text{ cm}^2$  and  $50 \times 50 \text{ cm}^2$  GEM chamber modules. The expertise gained with these GEM modules will be applied to the design of GEM modules for SoLID.

The UVa group operates a well-equipped GEM R&D facility that includes the following:

- **UVa Detector development lab:** This  $10 \times 10 \text{ m}^2$ , well-equipped nuclear physics detector lab has been used for the development, construction and testing of many large detector systems. The detector lab consists of two  $3 \times 3 \text{ m}^2$  level 1,000 clean rooms located within a  $4 \times 10 \text{ m}^2$  semi-clean area. So far seven large area GEM chambers have been successfully constructed in this clean room. The specialized GEM construction equipment in the lab includes large area GEM foil stretchers, GEM foil testing high-voltage boxes, a large volume ultra-sonic cleaner for GEM frame cleaning, a Keithley 6485 picoammeter for GEM foil testing, and a GEM foil storage dry  $\text{N}_2$  box.
- **GEM readout systems based on APV25-S1 electronics:** The UVa group has two APV25 based readout systems: a 10,000 channel SRS system from CERN and a 3,500 channel system developed by the INFN group. Both systems are fully operational and are used for testing prototype GEM chambers.
- **Wiener-Iseg multi-channel high voltage system** The UVa detector group owns a brand new Wiener-Iseg multi-channel high voltage system that is especially suited to provide high voltage to sensitive tracking chambers. This system currently has 24 channels and can be expanded to 160 channels.

The  $50 \times 50 \text{ cm}^2$  GEM chambers built at UVa are currently being tested with radioactive sources and cosmic rays. Figures 62 and 63 show results obtained from these test data. Figure 62 is the absolute efficiency measured at several locations using electrons from a beta source, as a function of the high voltage. An efficiency of  $\approx 97\%$  is achieved. Figure 63 is the ratio of cluster charge for x and y hits.

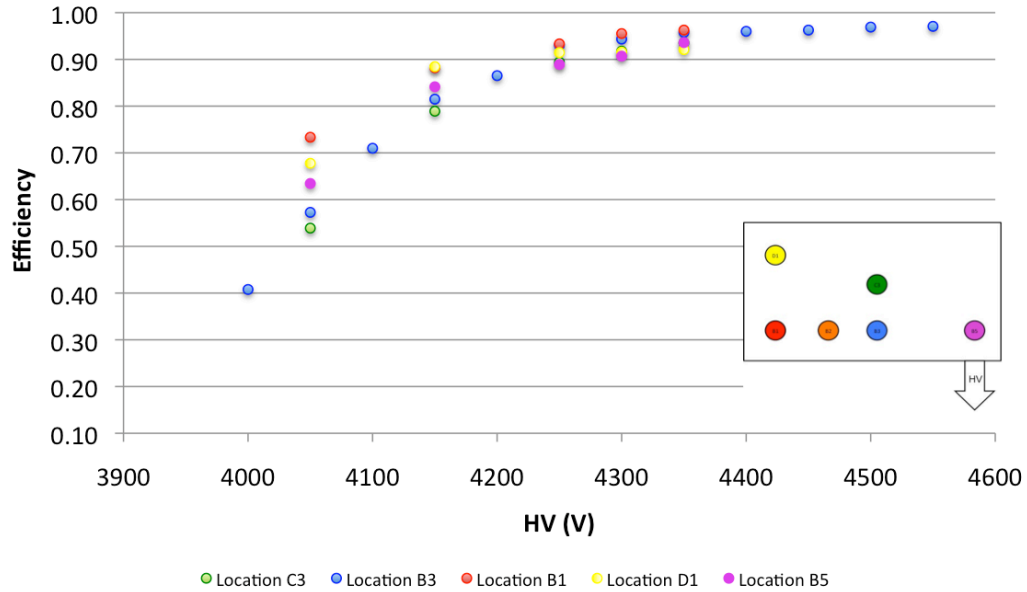


Figure 62: Efficiency of the  $40 \times 50 \text{ cm}^2$  GEM chamber

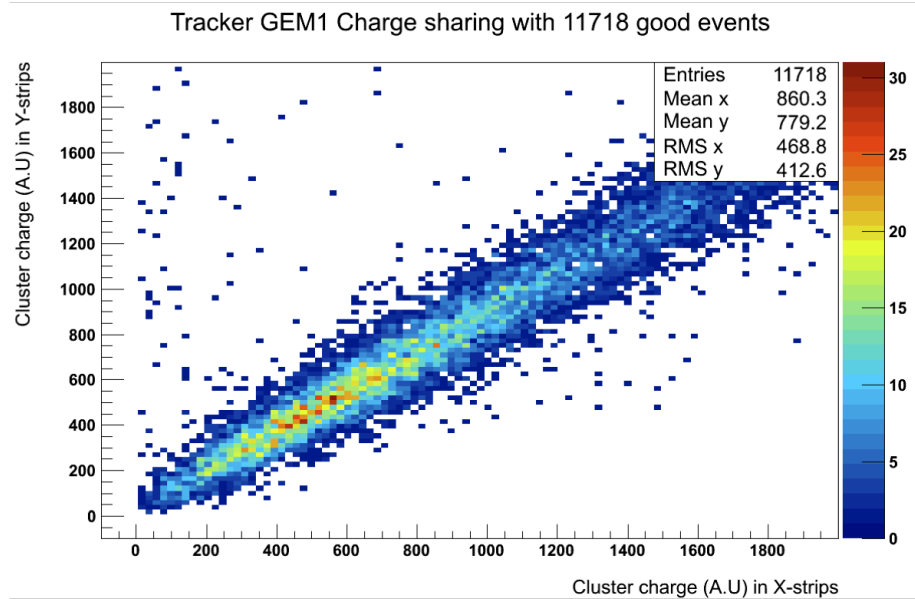


Figure 63: The charge division between x and y strips for the  $40 \times 50 \text{ cm}^2$  GEM chamber.



The UVa group recently completed the fabrication of a large prototype GEM module with dimensions of  $100 \times (21-38)$  cm<sup>2</sup>, approaching the proposed size of the largest SoLID GEM sectors (Figure 64). This prototype was constructed under the Electron Ion Collider (EIC) detector R&D program. This chamber is the largest GEM chamber ever built with a 2-D readout. Its readout consists of stripes from the two readout layers at a 12° stereo angle. The chamber is currently prepared for a beam test at Fermilab scheduled for October 2013. The development and testing of this large prototype is used to gain expertise and understand the mechanical, electrical and electronic properties of very large area GEM chambers.

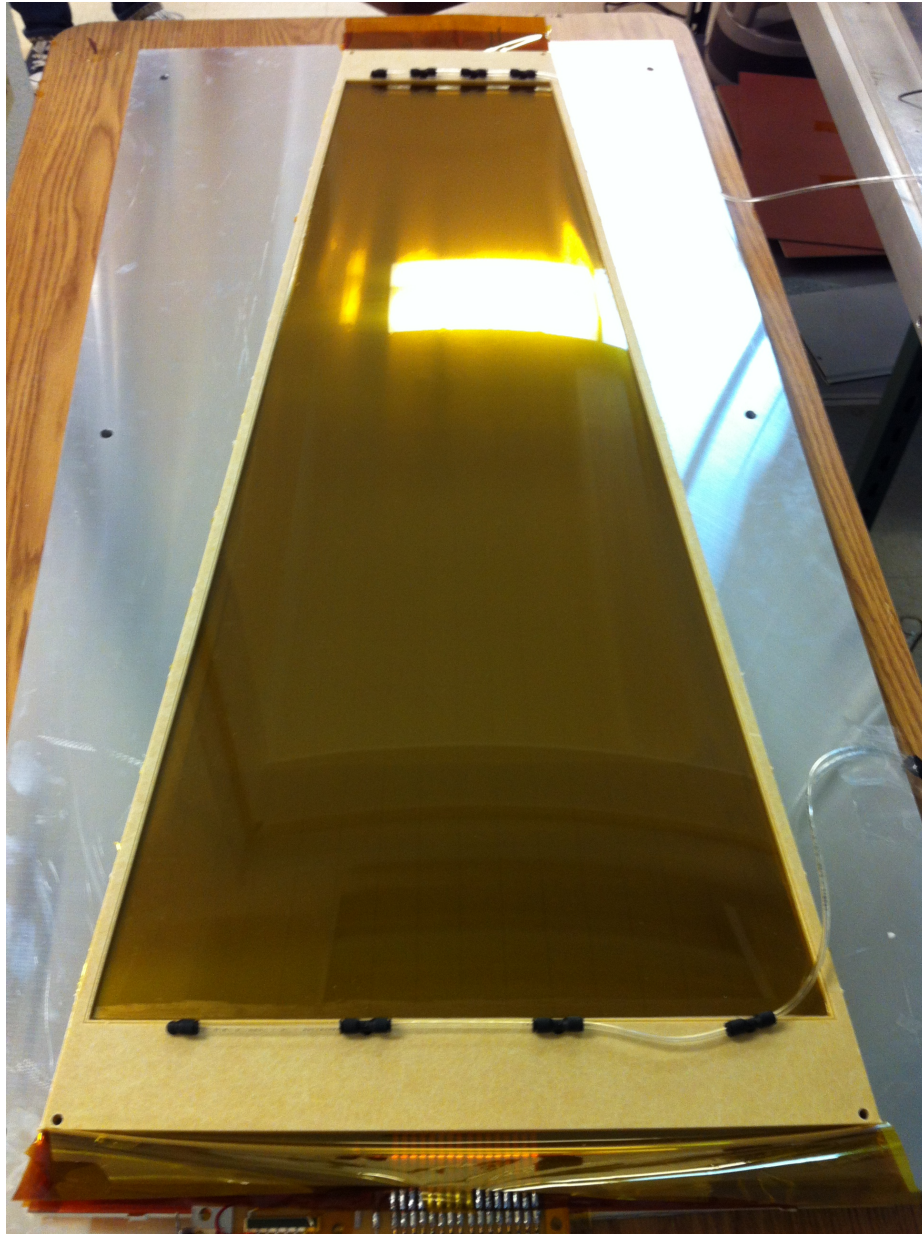


Figure 64: The 100 cm x (21 - 38) cm prototype GEM chamber at UVa being prepared for a beam test.



### 7.2.2 GEM chamber R&D programs in China

The five institutions of the Chinese collaboration for SoLID GEM detectors all have worked on gas detectors for many years, including R&D work on MWPC, MRPC, GEM, Micromegas, THGEM, and TPC, and applications of these detectors. These institutions have well-equipped GEM R&D facilities that include:

- Clean rooms for GEM detector assembling
- Front-end readout electronics based on APV25-S1 (developed by the INFN group)
- Multi-channel HV power supply systems and DAQ systems

CIAE, which has over 20 years of experience in nuclear pore foil production and Kapton etching, just signed a license agreement for manufacturing and commercialization of GEM foils and GEM based products with CERN, and received technical assistance from CERN. The base material of GEM foil is ultrathin, non-adhesive copper on a polyimide substrate, which can be purchased from CERN and other vendors. Several printed circuit board (PCB) technologies are applied during the manufacture of GEM foil. Recently, CIAE has started working on:

- Production of photo-masks, a component for the manufacturing of PCBs which is transferred onto a light-sensitive chemical resist covering the surface of copper layer in the production of GEMs.
- Lamination and exposure of dry film photoresist: Using a hot roll lamination (HRL) machine, both sides of the GEM substrate are laminated simultaneously by photoresist. The exposure system consists of an exposure unit, vacuum exposure frame, light source cooling, and an exposure control unit. This treatment transfers the photo-mask pattern onto the photoresist, forming an exact copy.
- Copper etching.
- Polyimide film etching.
- Final cleaning and chrome coating.

Figure 65 shows the film etching device at CIAE. In the beginning of 2013, a physicist from CIAE completed a training in GEM foil manufacturing at CERN.

LZU has been building a Micromegas+AFTER chip system for fast neutron (14 MeV) imaging in the past few years. The experience gained from this R&D work is useful to their GEM project. For instance, several designs of neutron converters with different parameters were tried in a simulation based on MCNP4 and GEANT4 (for both Micromegas and GEM), and different conversion efficiencies were compared. Other studies based on Garfield to improve the spatial and time resolution (as shown in Figure 66) were also performed and were proved to be helpful for the experimental study. The first version of the detector frame was designed and manufactured. 4 sets of GEM foils with the standard frame were purchased from CERN. Currently, a PhD student and a staff member are working together on the APV25-VME system. In the summer of 2013, an engineer visited JLab to gain experience about the SoLID DAQ.

THU has experience with GEM detectors by developing the electronics, such as a GEM-based TPC readout, a 16-channel CSA and shaping amplifier for GEM. Recently, a planar GEM tracking detector prototype was assembled for a spatial resolution test. In this test, THU used the event rate



Figure 65: Film etching device at China Institute of Atomic Energy

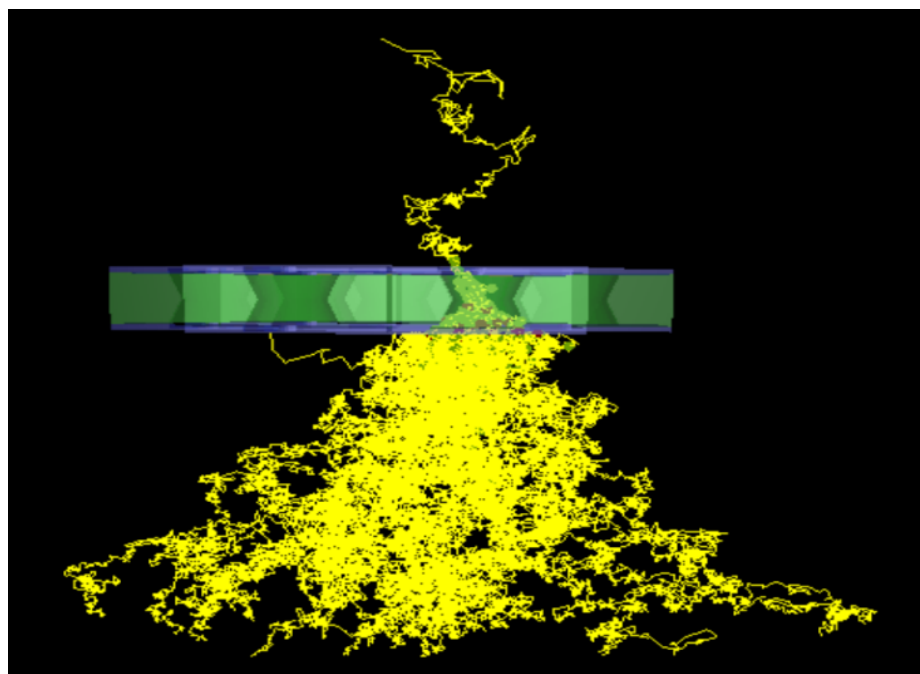


Figure 66: Avalanche process of an electron in a hole of GEM

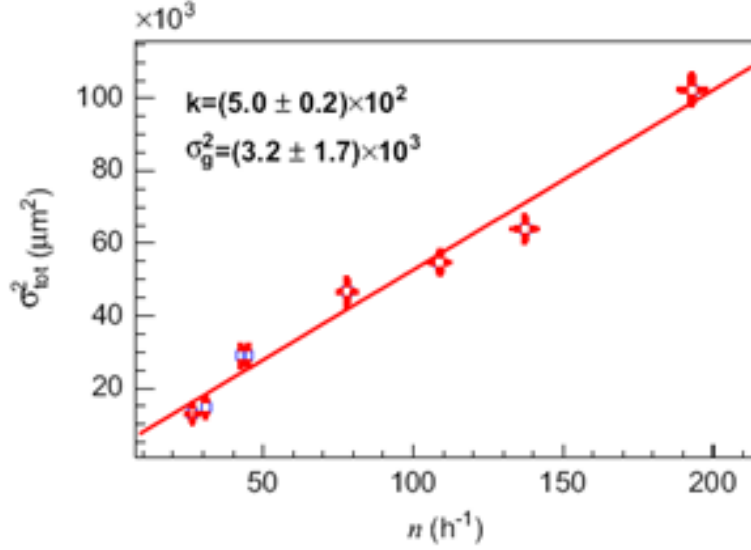


Figure 67: Linear fit of  $\sigma_{tot}^2$  versus  $n$

to substitute for the square of the slit width to overcome the magnified uncertainty of the spatial resolution which arises from the uncertainty of the slit width. The test demonstrated that the total position variance of the incident particles exhibits a linear dependence on the event rate or square of the slit width. The next step was to extend the measurement to zero slit width which is not directly achievable, and it was practically implemented by a linear fit to data points on the  $\sigma_{tot}^2 - n$  plane. Figure 67 shows the linear fitting of  $\sigma_{tot}^2$  versus  $n$  and the spatial resolution of the prototype is  $56 \pm 14 \mu m$ . Currently, THU is focusing on the inter-foil and inter-strip distance effects of the GEM detector. An APV based DAQ system will be built in the near future.

USTC started the GEM R&D work in 2000. After working on the 3D electric field simulation of GEM, USTC carried out a detailed gain performance test for the  $10 \times 10 \text{ cm}^2$  triple GEM detector, then made a GEM X-ray imaging prototype. Both Center-of-Gravity (COG) and delay-line readout methods were used on this imaging prototype and a very good spatial resolution ( $\sim 80 \mu m$ ) was obtained. Currently, USTC is focusing on the R&D of the large area GEM detector. Due to the fact that large area GEMs built by the glue technology have some disadvantages (e.g. very long assembling period; parts of GEM detector are not replaceable; dead regions in the effective area; aging problems of the glue and so on), USTC decided to use the NS2 (No Stretch, No Stress) technology for the construction of a  $30 \times 30 \text{ cm}^2$  GEM detector. NS2, which was developed at CERN recently, is a totally new technology especially used for large area GEM detectors. The idea of NS2 is to use screws and a stable main frame to achieve self-stretching of the GEM foils. The advantages of NS2 are:

- The whole construction process involves mainly tightening the screws, so it is easy and fast and we can assemble a detector in half a day.
- Because all the GEM foils are self-stretched, the detector does not need support frames. There is no glue aging problem or dead area inside the detector.
- All the screws can be loosened and tightened again, so that any part of the detector is replaceable. This also means that the cost of the project can be greatly reduced.

USTC just finished the design of the new  $30 \times 30 \text{ cm}^2$  NS2 GEM and purchased six  $30 \times 30 \text{ cm}^2$  GEM foils from CERN. The HV dividers and screws are ready. The frames, drift electrode and readout PCB are in manufacturing. The readout electronics and instruments are ready. Figure 68 shows a model of the  $30 \text{ cm} \times 30 \text{ cm}$  NS2 GEM detector (without readout PCB). This detector has been assembled and tested in Summer 2013.

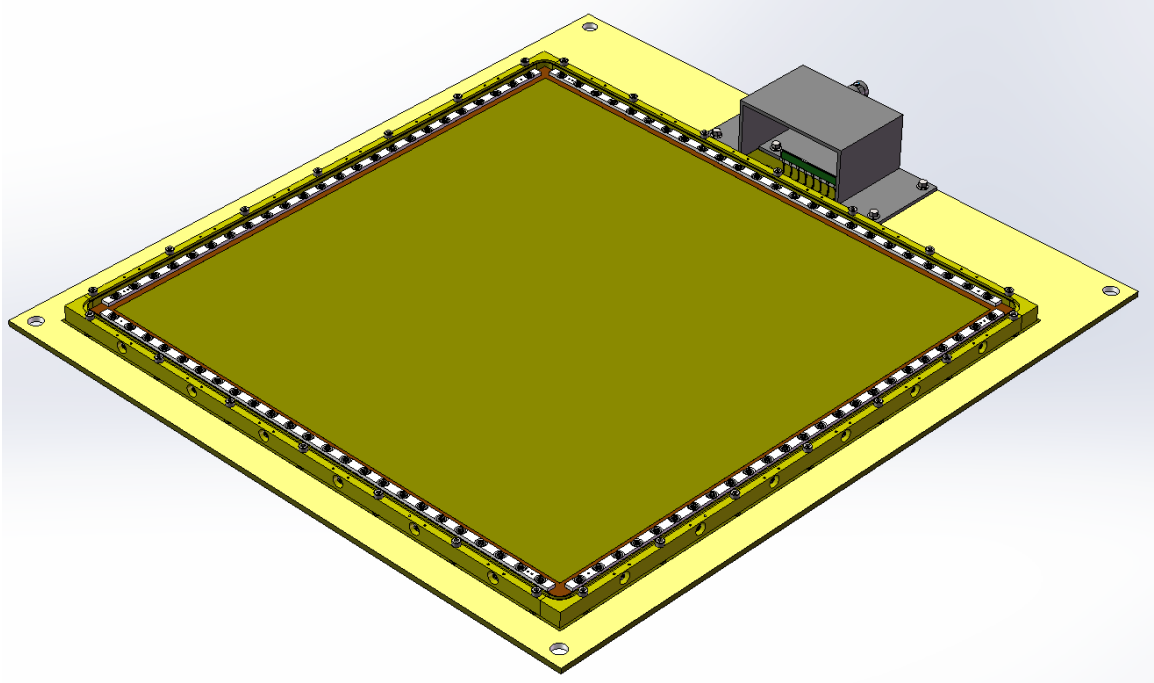


Figure 68: Design of the  $30 \times 30 \text{ cm}^2$  NS2 GEM detector

### 7.3 Collaboration Status and Construction Outlook

The close collaboration between the CIAE group in China developing GEM foil fabrication capabilities and the US groups (UVa and Temple) is essential as the project moves forward. The ongoing China-USA SoLID GEM collaboration activities have included monthly phone meetings, discussion during SoLID collaboration meetings and hosting of Chinese visiting researchers at the GEM lab at UVa.

A timetable is worked out with the CIAE group to lay out milestones for the fabrication of GEM foils with increasing active areas up to the full size of the largest SoLID modules. This timetable will also include goals for providing specific numbers of GEM foils produced in China to the Temple group for hole inspections and to the UVa and Temple groups for construction of test modules with these foils. The Chinese foils will be subjected to all acceptance criteria used for CERN GEM foils. The test modules will be evaluated under high luminosity conditions at the UVa x-ray test-stand as well as in beam tests at Jefferson lab. The two US groups will be closely interacting with the Chinese groups and giving them feedback during these evaluations. As part of the proposed SoLID pre-R&D program, funds have been requested for covering the cost of these Chinese GEM foils as well as for the fabrication of test modules.

The current plan for SoLID calls for approximately 400 GEM foils. In the event the CIAE group is unable to meet the GEM foil production goals, the backup option is purchasing the required

number of foils from CERN. The estimated cost of purchasing all 400 SoLID GEM foils from CERN will be approximately \$ 650 k

The CERN workshop has demonstrated the capability to produce the largest size GEM foils (113 cm x 44 cm) needed for SoLID. In fact, the UVa group recently used 123 cm x 55 cm GEM foils produced at CERN to build two large area GEM detectors; these detectors were successfully used for Jefferson Lab PRad experiment. Furthermore, CERN has the production capacity to deliver large orders of GEM foils in a timely manner. Over the last two years the CERN workshop produced and delivered approximately 140 large area GEM foils to UVa for SBS and PRad GEM modules; these foils were of high quality with about 90% of the foils passing the acceptance criteria. The manager of the CERN GEM workshop, Rui De Oliveira, has indicated that they have the capacity to deliver the required number of GEM foils for SoLID and with an order to produce the required number of foils they will hire the needed technicians to deliver the order in a timely manner.

While the R&D to produce large area single mask GEM foils has been suspended for the moment at Tech-Etch due to lack of large orders for such foils, Tech-Etch has indicated that in the event they receive a firm order for a large GEM production, they will be able to commit the resources for the required R&D and production.

Given these two backup options, the schedule risk due to a delay in Chinese GEM foils fabrication schedule will be rather low.

## 8 Light Gas Cherenkov

### 8.1 Design

The light gas Cherenkov detector for SoLID is divided into 30 identical sectors to match the 30 sector symmetry of the PVDIS baffle system. Many elements of the light gas Cherenkov remain identical between the PVDIS and SIDIS /  $J/\Psi$  experimental configurations, but some elements are adjusted or added / removed. Beyond the criteria dictated by the experimental physics requirements, the design of the Cherenkov detector was optimized with the goal of reducing the costs of construction and maintenance over the detector's lifetime including the switch over between experiments. The specifications of the tank and each major element per sector for each configuration are described below:

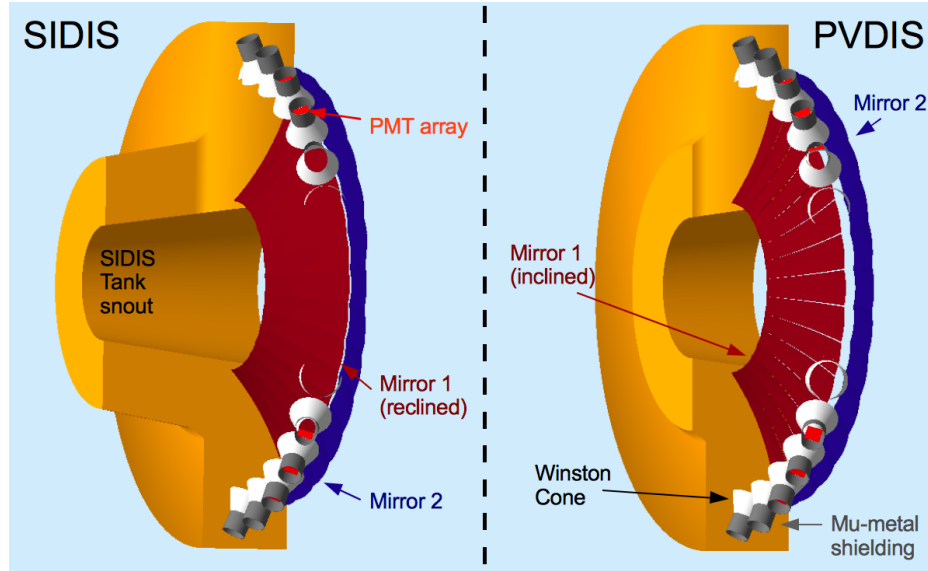


Figure 69: A side by side cross-section comparison of the light gas Cherenkov detector for both the SIDIS and PVDIS configuration with all major components labeled.

#### 8.1.1 Tank and Cherenkov Gas

The main body of the tank remains identical between PVDIS and SIDIS configurations, and has a length roughly 105 cm with an inner radius of 71 to 85 cm, and an outer radius of 265 cm. With the PVDIS baffles removed for SIDIS, an additional tank ‘snout’ is attached upstream of the main tank inside the additional space evacuated by the baffle system. This tank snout adds an additional 107 cm of length to the tank with an inner radius of 58 to 71 cm, and an outer radius of 127 to 144 cm. In both configurations, the windows will be constructed from polyvinyl fluoride (PVF or Tedlar) at a thickness of 0.05 mm and 0.1 mm for the entrance and exit windows respectively. PVF provides a strong and gas-tight seal at minimal density ( $1.45 \text{ g/cm}^3$ ). The radiator gas in both configurations will be  $\text{CO}_2$  pressurized at slightly over atmospheric pressure to maintain gas purity.

#### 8.1.2 Mirrors

Each sector will consist of two spherical mirror segments with dimensions listed in Tab. 12. Radially outward from the beam line, the inner most segment we will refer to as mirror 1 (red in Fig. 69) and

the outermost segment as mirror 2 (blue in Fig. 69). In order to accommodate two different incident particle angles between PVDIS ( $22^\circ$  to  $35^\circ$  from a central Z-vertex 270 cm away) and SIDIS ( $8.0^\circ$  to  $15.0^\circ$  from a vertex 520 cm away), mirror 1 must be adjusted between experiments such that the reflected Cherenkov light in both configurations falls into the PMT detector acceptance. This is achieved by rotating mirror 1 by an angle of approximately  $8^\circ$  inward about the mirror's inner-most edge (or edge closest to the beam-line). In Fig. 69 we see a cross section of the light gas Cherenkov, sliced along the beam or Z-direction, with the mirrors in both the reclined and inclined positions. Mirror 2 is fixed in position and rotation and non-contributing to the SIDIS configuration; however, mirror 2 is necessary to cover the larger angular range in the PVDIS configuration. The mirrors will be crafted from carbon-fiber-reinforced polymer (CFRP) by Composite Mirror Applications (CMA) [219] with an areal density no larger than  $6 \text{ kg/m}^2$ . The surface smoothness and uniformity will achieve a D0 spot size of  $<2 \text{ mm}$  and be of similar quality to the mirror blanks CMA manufactured for the RICH detectors at LHCb [220]. Mirror coating will be performed by our collaborators at Stony Brook, and will consist of high reflectance ( $\geq 85\%$  for  $\lambda = 200 \text{ nm}$  to  $620 \text{ nm}$ ) aluminum with a protective coating of  $\text{MgF}_2$ .

Mirror	inner-edge W (cm)	outer-edge W (cm)	L (cm)	R of curv. (cm)
Mirror 1	16.26	36.03	114.53	277.51
Mirror 2	37.06	45.95	59.26	157.99

Table 12: The dimensions of the two mirror segments in the light gas Cherenkov.

### 8.1.3 PMTs

The light gas Cherenkov will use Hamamatsu flat panel multianode photomultiplier tube assemblies: H12700C [221]. These PMT assemblies are an  $8 \times 8$  pixel square array with a total active surface area of  $49 \text{ mm} \times 49 \text{ mm}$  with a UV-glass window, Bialkali photocathode material producing an average quantum efficiency around 15%, and a 12-stage dynode structure allowing resolution down to a single photoelectron. A  $3 \times 3$  array of these PMT assemblies will be mounted in each sector, as shown in the PMT mounting prototype in Fig. 70. The position and orientation of the PMT array will remain fixed between PVDIS and SIDIS configurations. The PMTs will be coated with a wave-length shifting p-Terphenyl coating. This coating is a cost effective method to boost the PMT response of Cherenkov radiation in the UV range. The expected effective increase in photoelectron gain is shown in Fig. 71. Every pixel in the H12700C will be wired together to produce one signal per PMT; a trigger will then be constructed by requiring two PMT assemblies in the same array to fire in the same time window, with a minimum photoelectron discrimination. Simulations show a  $>90\%$  average electron detection efficiency, integrated over all angles and momenta, when requiring 2 separate PMTs assemblies in an array to each generate 2 or more photoelectrons in either the PVDIS or SIDIS configurations. This trigger configuration would result in 36 possible coincidences per sector, consequently reducing the single photoelectron rate due to dark current or other backgrounds by at least a factor of 10. Specific filtering of the PMT signals will be tested while prototyping the PMT array and electronics. Additionally, we plan on improving the resolution of the PMT sum signal through matrix gain balancing of the PMT pixel-array patented by Vladimir Popov to Jefferson Lab.



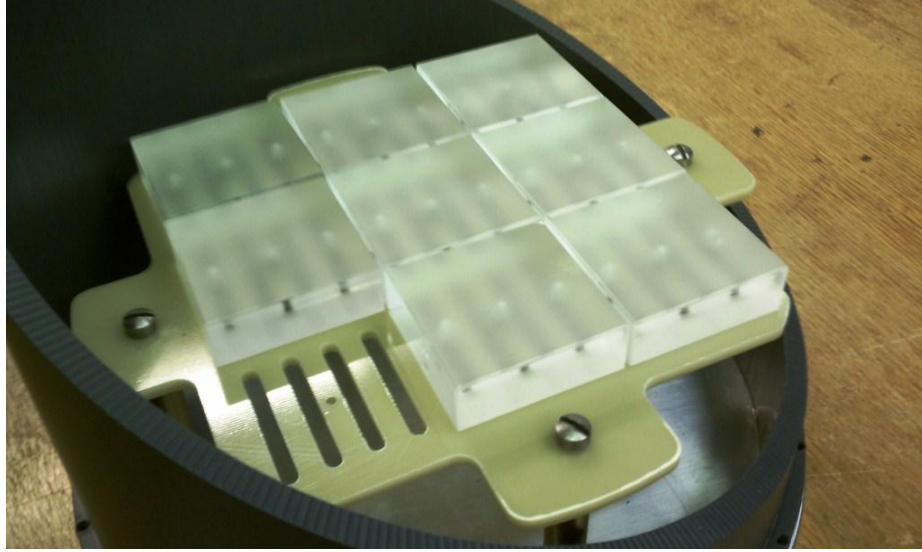


Figure 70: PMT assembly mounting prototype showing  $3 \times 3$  array of dummy PMTs inside the space restricted by magnetic shielding.

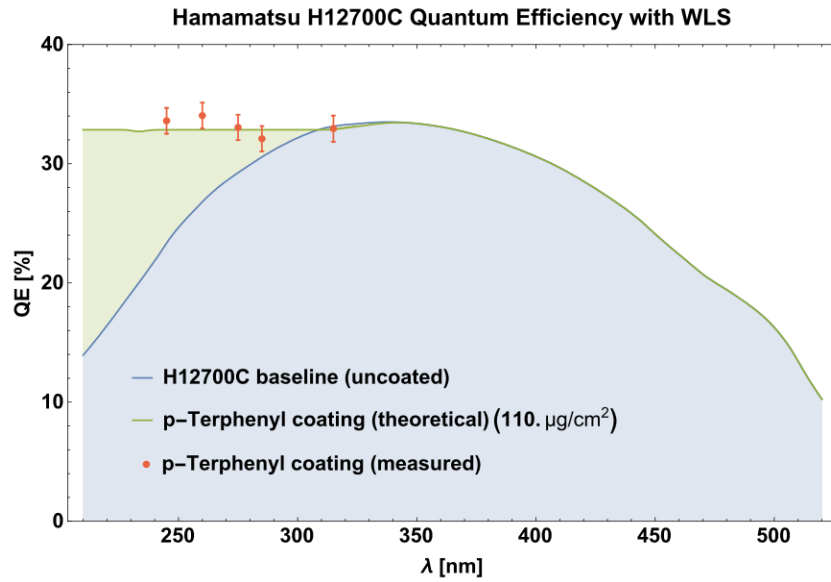


Figure 71: The increase in effective gain resulting from p-Terphenyl coating on H12700C PMTs. Red points are measurements done at Temple University. The curves show the current H12700C quantum efficiency, and the expected effective gain in the quantum efficiency from p-Terphenyl coating as a function of optical photon wavelength.

#### 8.1.4 Magnetic Shielding and Winston Cones

The PMTs will be shielded by a mu-metal cylinder / cone construction that doubles as support for a reflective aluminum inner glass cone to direct light onto the PMT array. The cylinders will measure 30 cm in length with an inner radius of 11.28 cm, the cone will have a height of 30 cm with an inner radius of 7.8 cm at the narrow end and an inner radius of 21 cm at the wide end. The mu-metal



shielding will be 0.04 inch thick reinforced by 0.125 inch thick 1008 carbon steel and manufactured by Amuneal Manufacturing Corp [222]. The PMTs are most sensitive to the magnitude of the magnetic field parallel to the photon collection face (transverse direction). We require a reduction of 95 gauss to <50 gauss in the transverse direction, and a reduction of 135 gauss to <50 gauss in the longitudinal direction, to where we expect an output loss <10% as seen in Figure 83

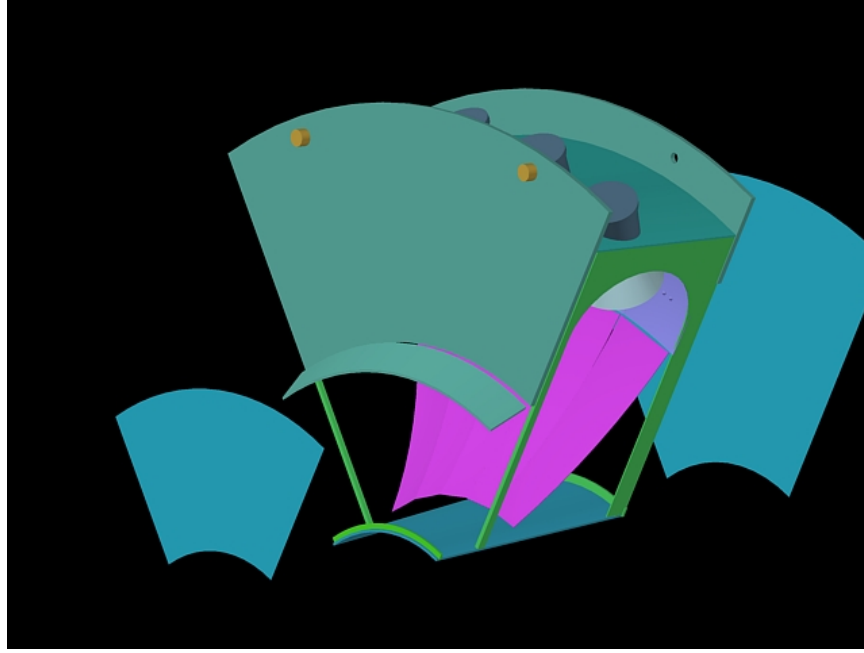


Figure 72: The support frame for one subsection of the light gas Cherenkov. The front and back acceptance windows (blue) are exploded to show the mirrors (pink and purple) and the support frame (green). The mounting points of the tank to the magnet housing are shown in orange.

## 8.2 Tank Support

The Cherenkov tank front and back windows will be divided into six radial sections. Between each pair of sections will be two thin rectangular aluminum support spokes, one to support and frame the upstream side of the tank and another to support and frame the downstream side (see Fig. 72). Both spokes are positioned and aligned to minimize the probability of tracks passing through the support material. Additionally, both spokes are interconnected at the outer radius of the tank, outside of the desired physics acceptance, by a solid arc-shaped plane to increase the rigidity of the frame and provide additional support for mounting the focusing cones and PMT assemblies. The space between the upstream and downstream spokes will remain open to maximize Cherenkov light collection. The combined frame itself will be mounted to the back wall of the downstream magnet housing, to support the full weight of the Cherenkov detector. This alleviates placing additional stress on the end-cap nose, which other additional downstream detectors will use to support their weight. Each PMT array will be accessible from the outer radial wall of the tank for alignment or maintenance purposes.

### 8.3 Simulations

All simulations were done with a slightly modified version of the GEMC [223] software developed at Jefferson Lab. GEMC uses a GEANT4.95 [224] backend to simulate all particle tracking through and interaction with materials and geometries. All plots shown in the light gas Cherenkov section of this document use the same simulation dataset. Event generation was performed by the eicRate DIS event generation tool authored by Seamus Riordan. The simulations also have the following features:

- Acceptance through the PVDIS baffle system (PVDIS events only).
- Cherenkov radiation process for creation of optical photons.
- Expected delta ray and pair creation from  $e^-$  and  $\pi^-$  particles interacting with the Cherenkov front window using the standard and low energy EM packages for GEANT4.
- Expanded mirror reflection properties in GEMC to be more in line with the latest functionality from GEANT4.
- PMT photoelectron signal simulation which includes the PMT dead area, quantum efficiency pixel-by-pixel, and optical properties of the PMT UV glass window.

#### 8.3.1 Collection Efficiencies

The collection efficiencies for electrons in both the PVDIS and SIDIS configuration can be seen in Figs. 73 and 74. The slight jump in photoelectrons around  $32^\circ$  in the PVDIS figure is a result of the inclined inner mirror, which moderately reduces the number of optical photons produced by reducing the particle's path length through the gas before crossing the mirror.

#### 8.3.2 Background Rates

A low energy inclusive background simulation was performed using GEMC by generating an electron beam on target, including all expected materials between the beam entrance to the Cherenkov back window. Secondaries produced anywhere in the SoLID detector and above the Cherenkov radiation momentum threshold while passing through the Cherenkov gas were considered as a possible source of background. For the PVDIS configuration, lepton production from initial  $\pi^0$  production at small angle produced the majority of accidental backgrounds. This background was calculated using the same methodology as the modified Hall D generator, which uses a modified version of PYTHIA and SAID input to match known world data. More information on the pion generator can be found in Sec. 12.2.3. The combined background rate is estimated to be  $\approx 0.8$  MHz per sector for a trigger requiring at least 2 photoelectrons in 2 separate PMTs in the same sector. For the SIDIS configuration, the expected background rate is less than 100 KHz in the same trigger configuration above.

#### 8.3.3 Pion Rejection

The expected pion rejection is shown in Figs. 75 through 78. All pion signal below the pion Cherenkov radiation threshold (3.2 GeV/c for the PVDIS gas) is produced by knock-ons or ( $e^+$ ,  $e^-$ ) pair creation. The photoelectron signal itself is a poisson distribution convoluted with a gaussian to simulate the PMT 1 photoelectron resolution. The pion-electron photoelectron cut is determined by taking the intersection of the two signal distributions, simultaneously maximizing the electron

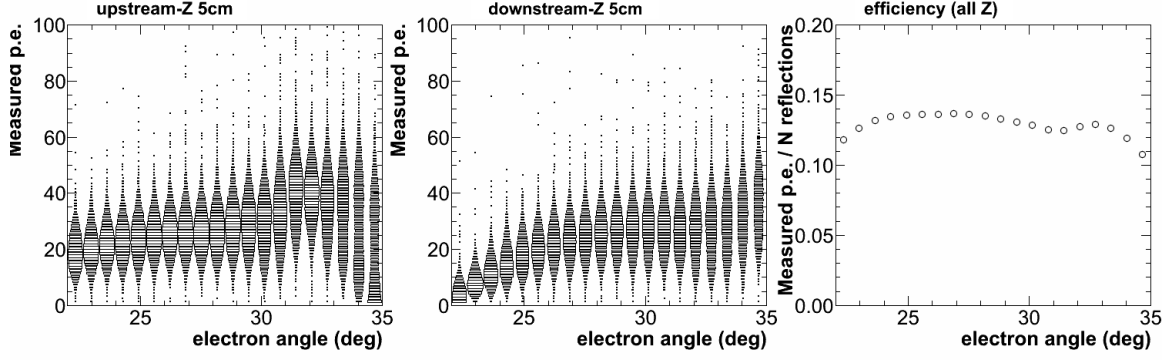


Figure 73: PVDIS configuration: The number of surviving photoelectrons versus theta after losses due to quantum efficiency of the PMTs, PMT dead area, or secondary reflections / absorptions off of the cones or PMT UV-glass window for events in the 5 cm of target most upstream (left) and 5 cm of target most downstream (middle). The right plot shows the corresponding collection efficiency versus theta for all 40 cm of the target Z-vertex.

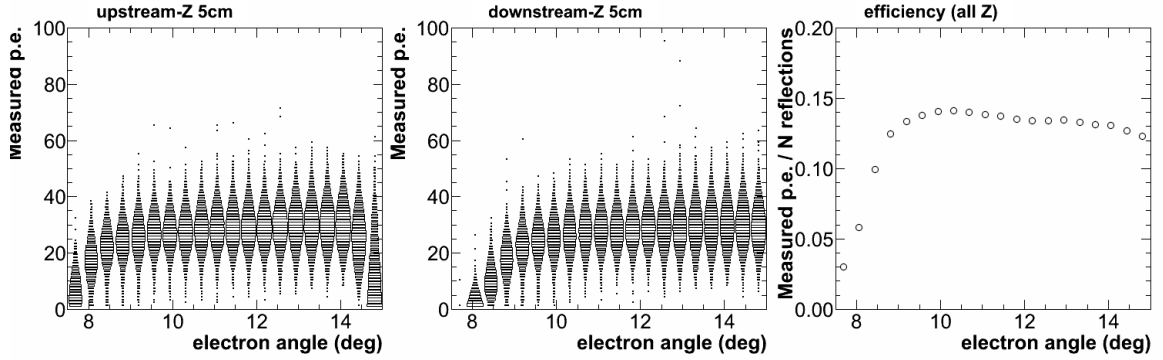


Figure 74: SIDIS configuration: Same as in Fig. 73 but with the SIDIS configuration.

selection probability while maximizing the pion rejection probability. Additional calculations are shown in Figs. 75 and 77 with a stricter cut on the pion signal, which consequently reduces the electron efficiency (by 10% for the red points and 20% for the blue points). An example of these photoelectron cuts are shown in table for one bin in momentum in the PVDIS configuration.

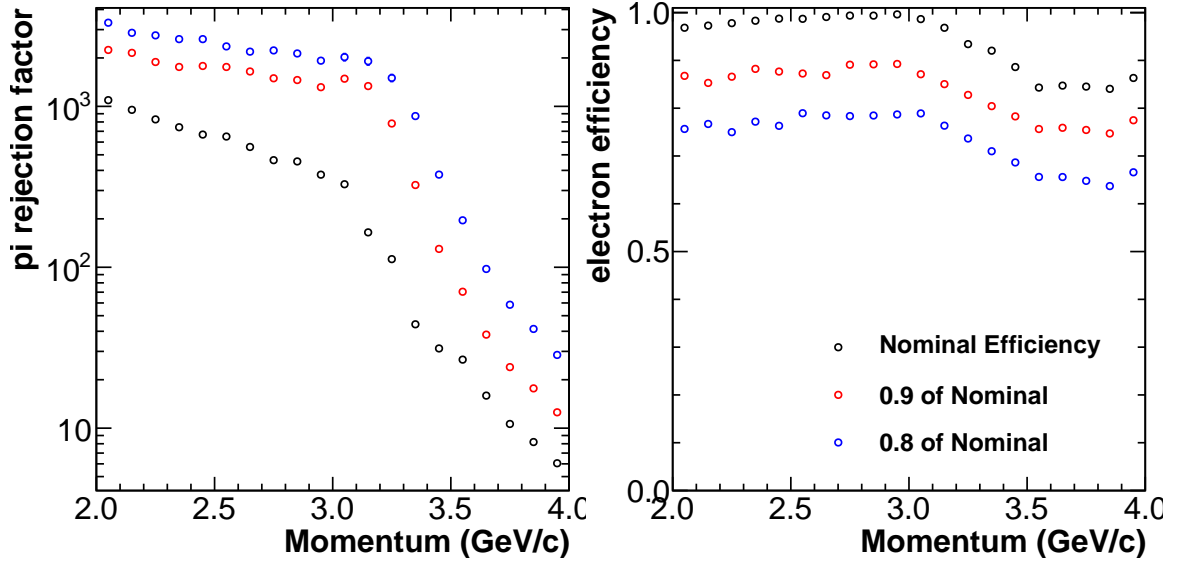


Figure 75: PVDIS configuration: The pion rejection factor versus momentum for 3 electron selection efficiencies: The nominal efficiency maximizes the pion rejection while minimizing loss of electrons, the red points correspond to a stricter pion cut with up to 10% additional loss of electrons, and the blue points allow an additional 20% loss of electrons.

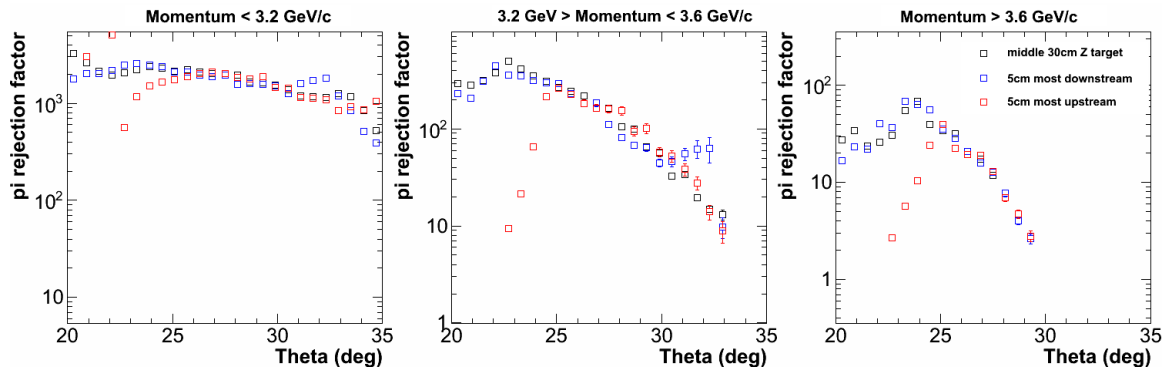


Figure 76: PVDIS configuration: The pion rejection factor versus the electron scattering angle theta over 3 momentum and Z-vertex ranges.

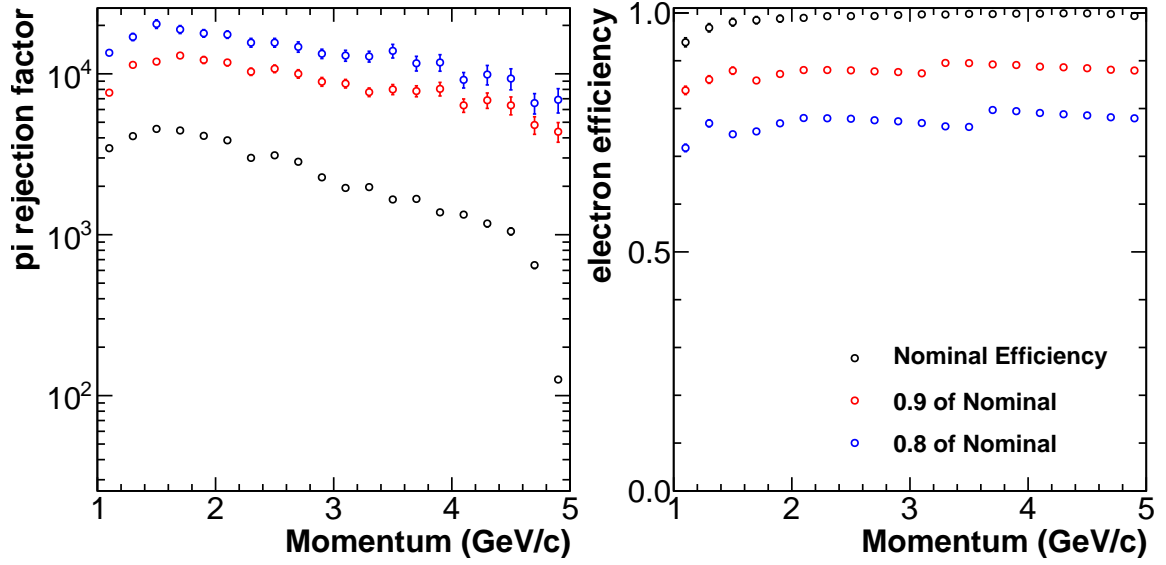


Figure 77: SIDIS configuration: Same as in Fig. 75 but with the SIDIS configuration.

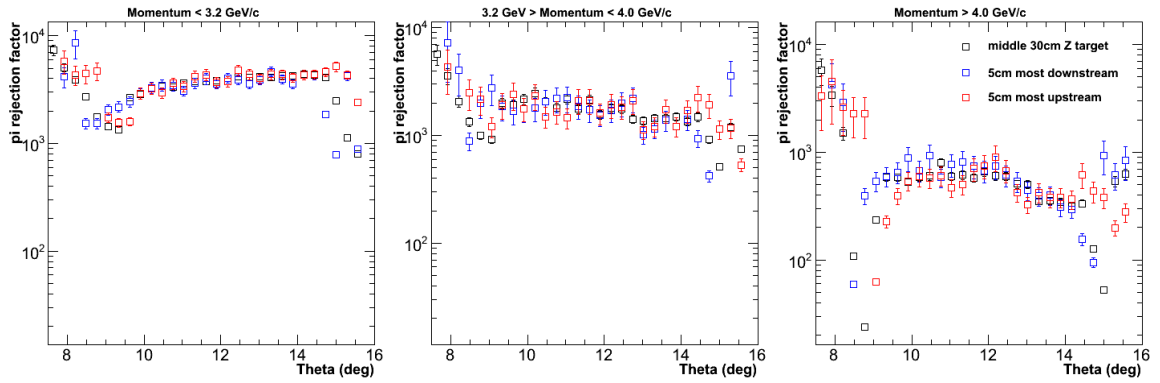


Figure 78: SIDIS configuration: Same as in Fig. 76 but with the SIDIS configuration.

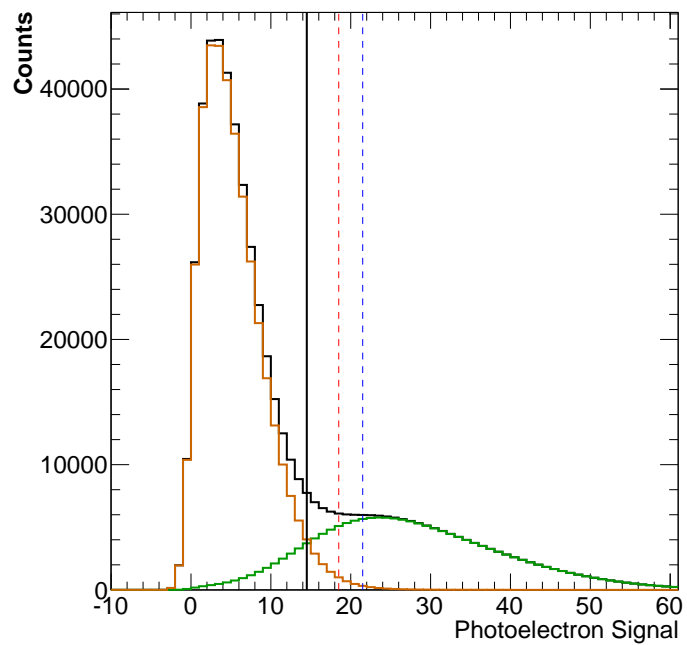


Figure 79: An example of the pion rejection cut made for one arbitrary bin in momentum for the PVDIS configuration. The pion signal is shown in orange and the electron signal is shown in green. The nominal efficiency cut is shown as a solid black line. The 90% and 80% electron efficiency cuts are shown as dashed red and blue lines respectively.

## 9 Heavy Gas Cherenkov

### 9.1 Optical System Design

A hadron Cherenkov detector is required to help with the identification of both positive and negative pions. A clear distinction between pion and kaon Cherenkov signals is mostly required in the mid to high momentum range, namely from 2.5 to 7.5 GeV. The  $C_4F_8O/C_4F_{10}$  gas at 1.5 atm and a temperature of 20°C gives a momentum threshold of 2.2 and 7.5 GeV for pions and kaons, respectively. Due to geometrical acceptance constraints the gas length available for Cherenkov light production is about 1 m. Requirements on the design are full azimuthal angular coverage and a good detector performance in a magnetic field with strength as high as 200 Gauss. The optical system for the Cherenkov light collection has been optimized using a GEANT4 simulation package taking into account the expected SoLID magnetic field configuration with the CLEO-II magnet. The system consists of a ring of 30 spherical mirrors of 1.2 m length each and inner and outer widths of 0.2 and 0.4 m, respectively. The mirrors will focus the light onto 30 photodetector as shown in Fig. 80. The size of each photodetector could be reduced to 8x8 inches (i.e. 16 of 2-inch PMTs per array) by use of straight cones as an additional optical element to mirrors. The PMTs of choice are similar to those used for the light gas Cherenkov namely the multi-anode 2 inch H8500-03/H12700-03 devices from Hamamatsu: they perform well in relatively high magnetic field, are square shaped, and have good photocathode coverage (89% of total area), making them ideal for tiling.

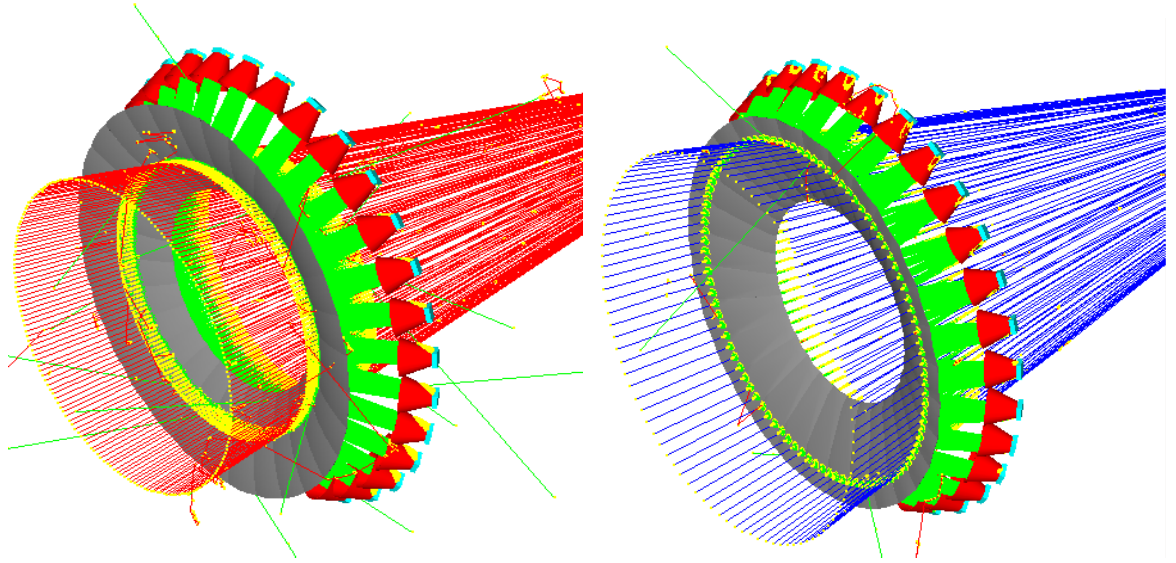


Figure 80: Optical system for the heavy-gas Cherenkov: a ring of 30 spherical mirrors (grey) will focus the Cherenkov photons created by the passage of negative (left panel) and positive (right panel) pions through the  $C_4F_8O$  radiator gas onto PMT (cyan) arrays with the aid of straight cones (red).

## 9.2 Simulation

### 9.2.1 Photoelectron Yield

Due to the SoLID geometrical acceptance with respect to the target and to the constraints on the photon detector positioning inside the Cherenkov tank, the particles with large polar angle entering the detector will travel a larger gas length compared to those with a low polar angle. Thus, the optimization was done favoring the low angle kinematics whenever possible and by keeping the number of maximum reflections to 2: one on the mirrors and one possibly on the cones (not all photons need the extra bounce on the cones to be collected by the PMT arrays). As a consequence, the loss of photons through absorption on the reflective surfaces is kept to a minimum.

Our simulation of the expected number of photoelectrons shown in Fig.81, takes into account realistic parameters for the gas index of refraction, gas transparency, mirror and cone reflectivities and the quantum efficiency of the H8500-03 PMTs to account for the photon to photoelectron conversion. We scaled down the number of photoelectrons obtained from the GEANT4 simulation by a conservative factor of 0.5 mostly to account for the dead zones on the PMT tiles due to incomplete photocathode coverage. The index of refraction of  $C_4F_8O$  has been measured at Syracuse University [225] between 400 and 650 nm, while below 400 nm we used an extrapolation based on a parametrization from HERA/DELPHI of this index[226]. We studied the impact on the expected number of photoelectrons on the large uncertainty in the  $C_4F_8O$  refractivity by assuming a refractivity 20% smaller than the nominal value extracted from the Syracuse and HERA/DELPHI measurements. We found that the yield of photoelectrons would still be sufficient, though marginal, at the lowest momentum of 2.5 GeV. The  $C_4F_8O$  transmittance has been measured at Jefferson Lab in Hall B with great accuracy in a photon wavelength range of 200 to 500 nm. We used these data in our simulation to account for Cherenkov photon absorption in the gas. For mirror, the Carbon Fiber Reinforced Polymer (CFRP) mirror base is preferred, which is a more rigid, lighter material as a suitable choice for large size mirrors. We contacted the USA company Composite Mirror Applications (CMA) that manufactured CFRP mirrors for the LHCb program at CERN [227] and we received a favorable response regarding the feasibility of such mirrors for our detector. CMA supplied us with data on CFRP mirror reflectivity as measured on the LHCb mirrors they manufactured. We used these parameters in our simulation to account for the Cherenkov photon absorption on the reflective surface of mirrors and cones. For the reflection cone, we plan to use the Aluminum coated Lexan film and attach it its base which sever as the magnetic fielding cone also. The film is also used by CLAS12 Low Threshold Cerenkov as their mirror reflection surface and has good performance.

The photoelectron yield dependence on polar angle and momentum is shown in Fig.81. For a fixed polar angle the number of photoelectrons increases with increasing momentum as we move away from the pion firing threshold of 2.2 GeV and then saturates. There is also an increase of yield with increasing polar angle due to the detector geometry which allows pions with larger angle to traverse more gas than those with low polar angle.

### 9.2.2 Pion Detection Efficiency and Kaon Rejection Factor

The expected performance of the detector has been further studied by estimating the pion detection efficiency and kaon rejection factor for a given cut on the number of photoelectrons with no input from other particle identification detectors. Background studies have shown [228] that the expected pion to kaon ratio is 10 to 1. The pion and kaon photoelectron distributions are simulated as convolutions of Poisson and Gauss distributions. The resolution of the PMT enters as the standard deviation of the Gauss distribution while the mean of the Poisson distribution is the output of the



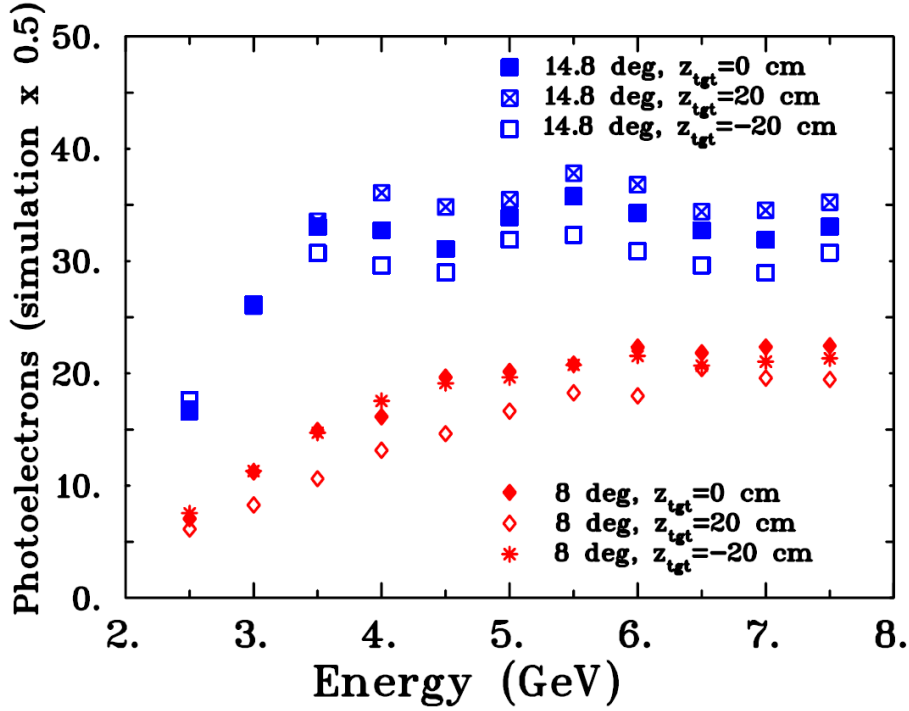


Figure 81: Simulated number of photoelectrons as a function of the pion polar angle and momentum. The results are shown for positive pions. A very similar output is obtained for negative pions.

GEANT4 simulation shown in Fig. 81. We measured the resolution of H8500C-03 to be 1 photoelectron. We mapped the pion detection efficiency and kaon rejection factor for few kinematics where we expect the smallest number of photoelectrons, namely at 8.0 degrees and momentum between 2.5 and 4.5 GeV and our results are shown in Fig. 82. Assuming that kaons would produce at most 1 photoelectron below the Cherenkov threshold, for a cut on the number of photoelectrons of 3, the pion detection efficiency is 99.0% (99.6%) at 2.7 GeV (3.0 GeV) with the same kaon contamination as small as 0.8%. At 8 degrees and below 2.7 GeV, the pion efficiency starts to drop below 99%. For larger momenta, a cut placed at 4 photoelectrons would result in a pion detection efficiency larger than 99.7% with a kaon contamination below 0.3%. This would meet the requirements of the approved experiments with SoLID.

### 9.3 Performance of the PMTs in Magnetic Field

We performed extensive bench tests of the H8500-03 and H12700-03 PMT at Jefferson Lab to map its performance in a magnetic field and assessed its capability of resolving single photoelectron signals[229]. The single photoelectron resolution was measured to be 1 photoelectron or better. The magnetic field test results are summarized in Fig. 83. The longitudinal field is perpendicular to the face of the PMT and is labeled as  $B_z$ . The transverse field orientations, perpendicular to the sides of the PMT are shown as  $B_x$  and  $B_y$ . The PMT relative output is reduced by at most 30% when exposed to a longitudinal magnetic field up to 400 Gauss. Our studies of the single photoelectron response in field indicated that these losses happen mostly at the amplification stage on the dynode chain making it possible to compensate for this effect with external amplification. These results are very encouraging as it suggests that the effect of the field component which is hardest to shield, the longitudinal one, could be compensated for by superficial shielding and additional external amplification. The degradation of the PMT output in transverse magnetic field is more pronounced,

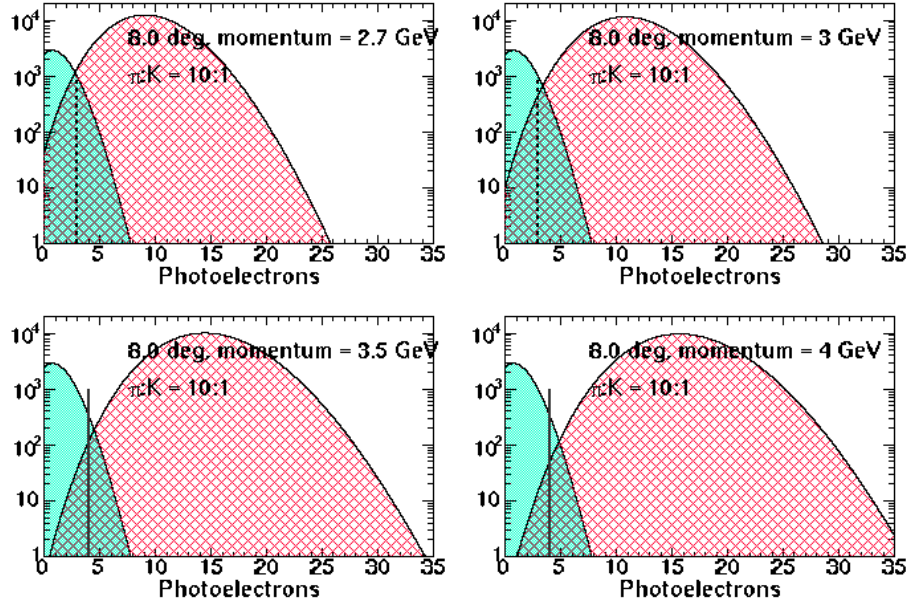


Figure 82: Simulated distributions of pions (red) and kaons (green) at with a polar angle of 8.0 degrees taking into account the photon detector resolution and the expected pion to kaon ratio.

up to 90% at 180 Gauss but this field component is easier to shield.

The magnetic field shield that would incorporate the cones used for focusing and that would reduce the SoLID field at the PMT location to a few tens Gauss in the longitudinal direction and to a few Gauss in the transverse one. Suggestion from the USA company Amuneal is that a 2-layer shield with a thin inner layer of Amumetal and a thin outer layer of carbon steel with mylar in between would meet our requirements.

## 9.4 Engineering Design

The detector is separated into two halves and total 10 (36 deg) segments to facilitate fabrication and handling. An engineering design of one half of the pressure tank is given in Fig.84. The structure is mostly made of Aluminum. The outer shell parts are formed into an arc, welded and then precision machined. One segment with PMTs, cones, and mirrors are shown in Fig.85. The PMT arrays are inserted from outside the tank, into tubes arrayed on the outer shell; they seal with an o-ring on a male gland. The cones are mounted inside the outer shell, with the possibility of fine position adjustment (from outside) through the PMT mount tube. The CFRP spherical mirrors are fixed with mounts at each end of the mirror and attached to the tank's outer shell and inner cone, respectively. The detector is positioned, in the magnet pole extension assembly, on large 1.5 inch diameter precision stainless steel rods (they could be shared with the adjacent detectors). The rods are mounted on the magnet extension black plate and insert into the magnet rear pole upon magnet assembly. Each detector segment will slide over them and are held in place (in Z) with shaft collars. The tank's inner cone is secured to the magnet inner cone.

## 9.5 Gas and Gas System

The detector uses  $C_4F_8O/C_4F_{10}$  gas as the radiator gas. The  $C_4F_8O$  gas is about 10 times heavier than air (9.19 g/L at 21°C), with a boiling point of  $-5^\circ\text{C}$  and a vapor pressure of 1.7 atm at 21°C. The gas is stable, non-toxic, non-explosive and non-reactive except with alkali metal halides.

However, due to its ability to pick up and transport oils, direct contact with organic materials needs to be avoided.  $C_4F_8O$  gas is not harmful to ozone but as being a perfluorocarbon compound, it is implicated as having a long atmospheric lifetime and high global warming potential. The  $C_4F_{10}$  gas has similar properties as the  $C_4F_8O$  gas, which is being considered as an alternative option for the radiator gas.

The total volume of the Cherenkov tank is  $\sim 20\text{ m}^3$  and it will be filled with  $\sim 300\text{ kg } C_4F_8O/C_4F_{10}$  gas. The detector is hermetically sealed to allow containment of the radiator gas near the 1.5 atm operation pressure at the temperature of  $20^\circ\text{C}$  which is the Hall A normal condition. The gas system is similar to the Hall B heavy gas system which has been operating for many years. During the filling process, the system will initially be purged using the nitrogen gas to avoid the contamination of the oxygen and water vapor in the air. Then the nitrogen gas will be purged by the radiator gas. The pressure of the gas will be monitored by pressure gauge and a regulation system will be incorporated to maintain the tank at the desired pressure. The gas will be collected back to the tank in the event of a refill situation and most of the inlet gas will be recovered with a separate molecular sieve filtration system. It may be necessary to continuously circulate the gas through the filters depending on the integrity of the seals in the PMT array.

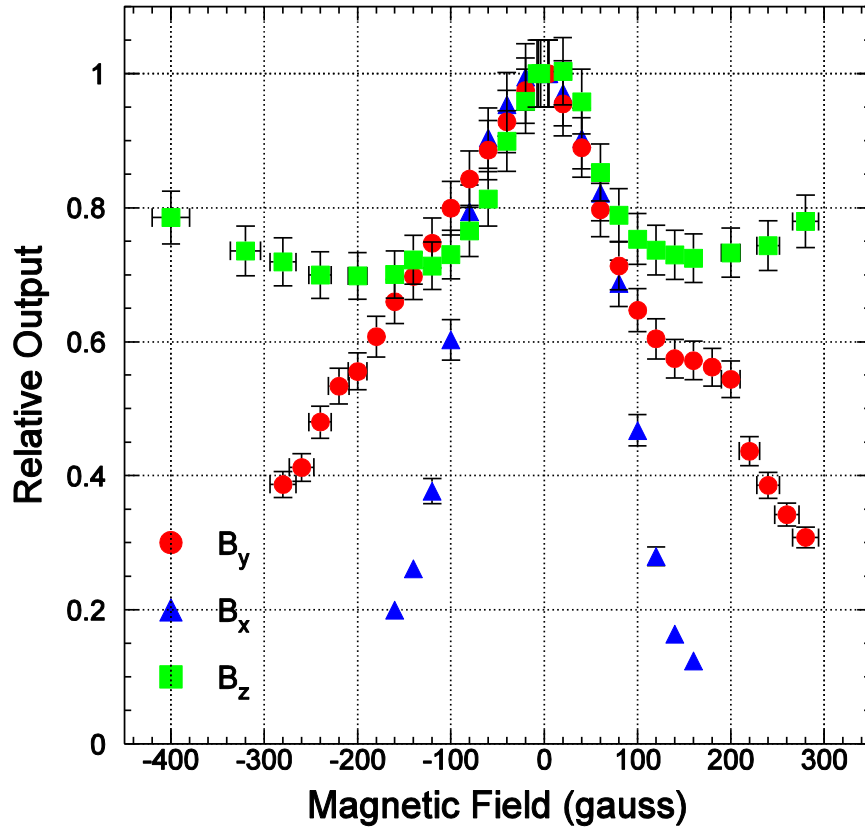


Figure 83: Relative output of the H8500-03 PMT in magnetic field. The PMT output normalized to the zero magnetic field configuration is shown for a longitudinal field orientation (i.e. perpendicular to the face of the PMT) in squares and for the transverse orientations (i.e. perpendicular to the sides of the PMT) in circles and triangles.

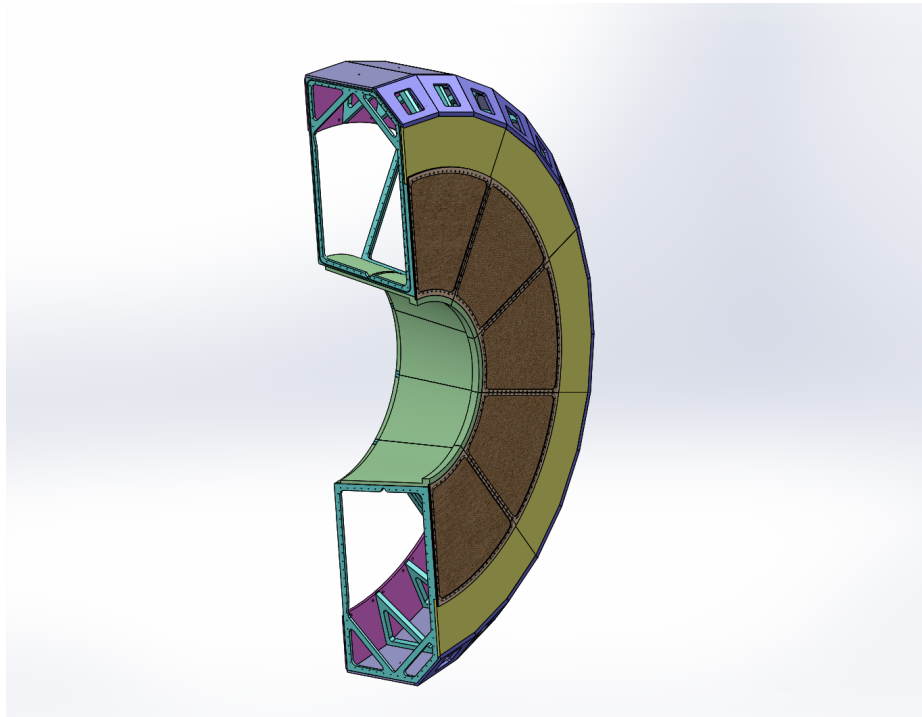


Figure 84: Conceptual design of the heavy gas Cherenkov detector

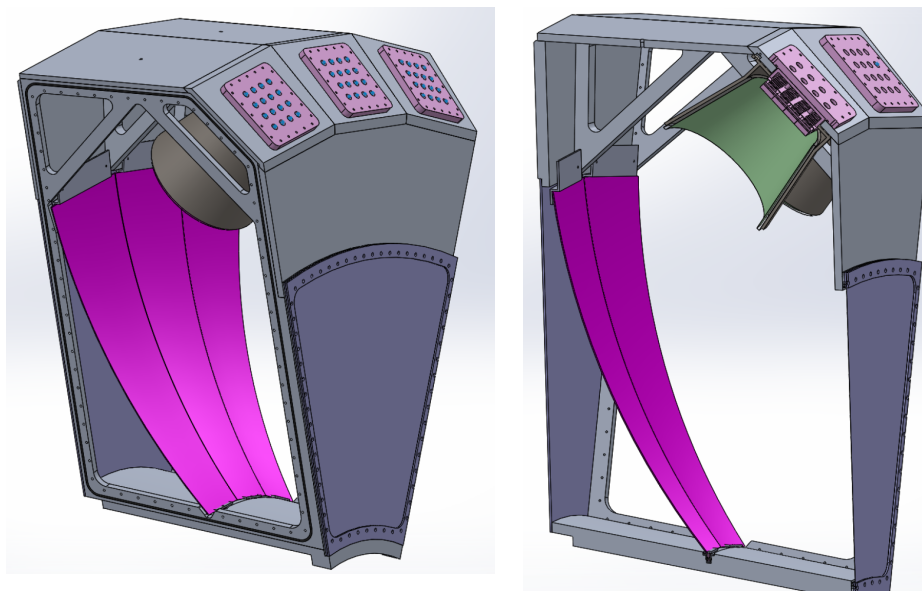


Figure 85: Conceptual design of the heavy gas Cherenkov detector (left) and PMT assembly (right)

## 10 Electromagnetic Calorimeter

### 10.1 Overview

Electromagnetic calorimeters (EC) are used in the PVDIS, SIDIS and  $J/\psi$  experiments to measure the energy deposition of electrons and hadrons, and to provide particle identification (PID). The SIDIS and  $J/\psi$  experiments share similar configurations and will be referred to as the SIDIS configuration hereafter. There are three calorimeters: the PVDIS experiment uses a forward angle calorimeter (FAEC) to detect the scattered electrons; the SIDIS experiments use a forward angle calorimeter (FAEC) and a large angle calorimeter (LAEC), both detect the scattered electrons while the FAEC also provides MIP triggers for pions. For electron detection, the dominant background comes from electro- and photo-produced pions. The desired performance is summarized in Table 13 and the EC geometry in Table 14. Please note that the EC geometrical coverage is slightly larger than other detectors because the edges of the EC are expected to have degraded performance due to shower spreading. The total coverage area of the SIDIS FAEC and LAEC is less than that of the PVDIS FAEC. The plan is to share modules between the two configurations, thus all modules need to be rearranged when switching between the PVDIS and SIDIS configurations.

	Desired performance
$\pi^-$ rejection	$\gtrsim[50:1]$
$e^-$ efficiency	$\gtrsim 95\%$
Energy resolution	$< 10\%/\sqrt{E}$
Radiation resistance	$\gtrsim 400$ kRad
Position resolution	$\lesssim 1$ cm

Table 13: Overview of the SoLID calorimeter desired performance.

	PVDIS FAEC	SIDIS FAEC	SIDIS LAEC
$z$ (cm)	(320, 380)	(415, 475)	(-65, -5)
Polar angle (degrees)	(22,35)	(7.5,14.85)	(16.3, 24)
Azimuthal angle	Full coverage		
Radius (cm)	(110, 265)	(98, 230)	(83, 140)
Coverage area (m <sup>2</sup> )	18.3	13.6	4.0

Table 14: Geometrical coverage for the SoLID electromagnetic calorimeters. The  $z$  direction is along the electron beam and the origin is at the solenoid center.

The design of the SoLID ECs is determined by both the physics goal and the expected running conditions. The design is challenging due to our unique constraints including high radiation background ( $\approx 400$  kRad, as in Table 13), strong magnetic field (1.5 T on SIDIS LAEC), large coverage area, and the budget. These factors prevent the use of many traditional calorimeter technologies, including NaI (TI), CSI, BGO and lead glass because of the low radiation resistance;  $\text{PbWO}_4$ , LSO and  $\text{PbF}_2$  because of their high cost; and lead/scintillator fiber calorimeter because of the high cost and the large amount of light readout required.

Due to the PID requirement, it is necessary to segment the EC longitudinally into a preshower and a shower detector. The following design that meets the experimental requirements was chosen: the shower calorimeter modules are based on the so-called Shashlyk design [230], a sampling-

type design consisting of alternating layers of scintillator and lead (as an absorber); the preshower detector is made of a layer of lead as a passive radiator followed by scintillator pads [231, 232]. Details of the design are summarized in Tables 15 and 16.

Type	passive radiator + sensitive layer
Passive radiator	$2X_0$ , Pb
Sensitive layer	2 cm, plastic scintillator 100 cm <sup>2</sup> hexagon tile
Light transportation	WLS fiber embedded in the scintillator

Table 15: SoLID electromagnetic calorimeter, preshower design.

Type	Shashlyk sampling calorimeter
Each layer	Absorber
	0.5 mm Pb
	Scintillator
	1.5 mm STYRON 637 plastic scintillator
Overall	Gap
	Paper, 0.12 mm $\times$ 2 sheets
	Radiation Length
	$0.093X_0$
	Radiation length ( $X_0$ )
	24 cm
	Molire radius
	5 cm
Overall	Length
	18 $X_0$ , 43.4 cm
	Total number of layers
	194
	Lateral granularity
	100 cm <sup>2</sup> hexagon
Overall	Light transportation
	WLS fiber, 100 per module, penetrating layers longitudinally

Table 16: SoLID electromagnetic calorimeter, shower design.

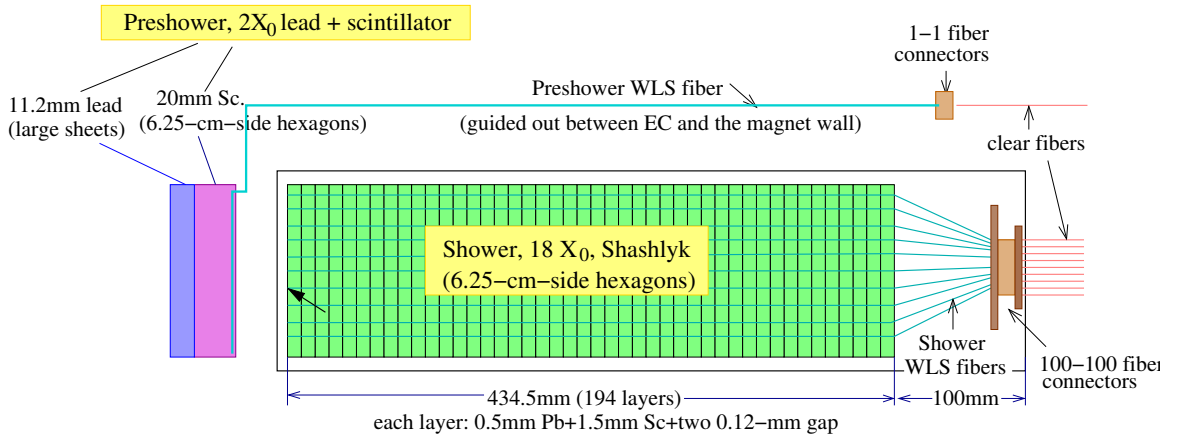


Figure 86: Design diagram of the SoLID electromagnetic calorimeter module. Spacing between the preshower and the shower detectors, and the spacing between the shower module and the 100-100 fiber connectors, need to be kept as small as possible yet still allow safe routing of the WLS fibers and positioning of the support structure.

The structure of both the preshower and the shower detector is illustrated in Fig. 86. In the experiment, particles are incident close to perpendicular to the scintillator-lead layers. Scintillation

light is absorbed, re-emitted and transported to the photon detector by wave-length shifting (WLS) optical fibers penetrating through the shower modules longitudinally, along the incident particle direction. The cross sectional area of the shower modules was optimized to be  $100 \text{ cm}^2$  (see Section 10.2.3), with a hexagon shape determined for the convenience of the support structure design. The scintillator tile of preshower modules has the same  $100 \text{ cm}^2$  hexagon shape to match the shower modules, which maximizes PID efficiencies, facilitates the design, and allows fast switch-over between SIDIS and PVDIS. The lead absorber of the preshower can be made of large sheets.

Geant4-based simulations are used to study the performance and optimize the design of the key specifications while minimizing the cost. Figure 87 shows the simulated shower of a 3 GeV electron incident on the PVDIS EC. In the following we will present details of the shower and the

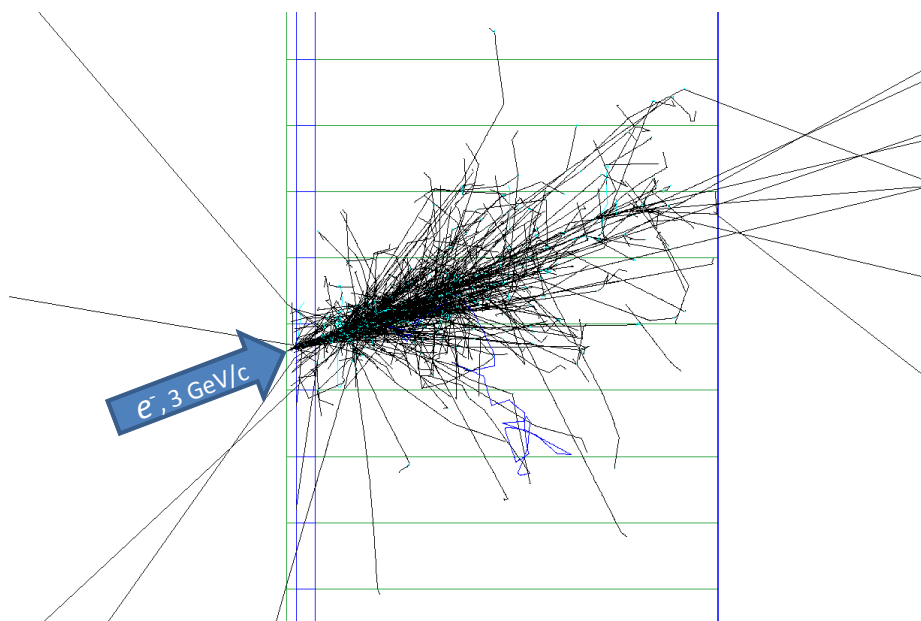


Figure 87: GEANT4 simulation of the shower generated by a 3-GeV electron incident on the PVDIS calorimeter. The black and green tracks are secondary photons and electrons respectively. The green horizontal lines are edges of calorimeter modules. The first two layers of materials are the preshower detector, consisting of  $2X_0$  of lead and 2 cm thick of scintillator.

preshower design, general layout and the support system, light readout, expected radiation dose, PID and trigger performance, and a cost estimate.

## 10.2 Shower Detector Design Considerations

### 10.2.1 Total Length of the Calorimeter

The overall length of calorimeter should be long enough to enclose most of the electromagnetic shower and short enough to maximize the difference in energy deposition between electrons and pions. The fraction of energy leak out for electron showers, averaged inside the acceptance of the SIDIS-Forward calorimeter, was studied for different total lengths of calorimeter. As shown in Fig.88, a total length of 20 radiation lengths was found to be a good balance. Considering the 2-radiation-length thickness of preshower, this leads to a shower detector length of 18 radiation lengths or 43.4 cm.



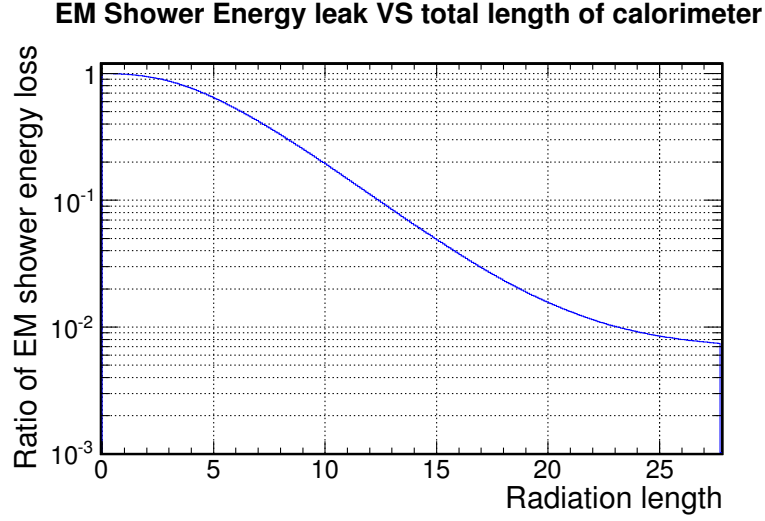


Figure 88: Fractional energy leak for an average SIDIS-Forward electron shower vs. different total length of the calorimeter.

### 10.2.2 Sampling Ratio of the Shower Detector

Each layer of the shower module consists of a 1.5 mm-thick scintillator plate and a 0.5-mm absorber plate made of lead. The Pb absorber thickness of 0.5 mm or less is favored to provide a fine sampling and therefore better energy resolution. The thickness of the scintillator plate should be thin enough to ensure fine longitudinal sampling, while thick enough to reduce light attenuation in the lateral direction. A thickness of 1.5 mm was chosen following the experience of previous Shashlyk designs used by the KOPIO experiment [230, 233], the PANDA experiment [234], and the COMPASS-II experiment. The COMPASS module is shown in Fig. 89. A gap of 120  $\mu\text{m}$  is kept between the lead and scintillator plates to accommodate a sheet of high-reflectivity paper, which reduces the loss of scintillation light.

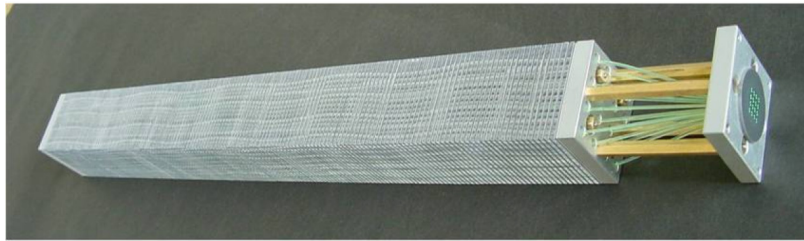


Figure 89: COMPASS-II Shashlyk calorimeter module. This illustrates the basic design of shashlyk modules: each module consists of alternating scintillator and lead (or other absorber material) layers, with WLS fibers penetrating across all layers to guide out the scintillation light signal. Four stainless steel rods are used to fix all layers together and support the whole module.

Figure 90 shows the simulated energy resolution using the chosen configuration of 1.5 mm scintillator and 0.5 mm lead. A resolution of about  $4\%/\sqrt{E}$  is achieved.

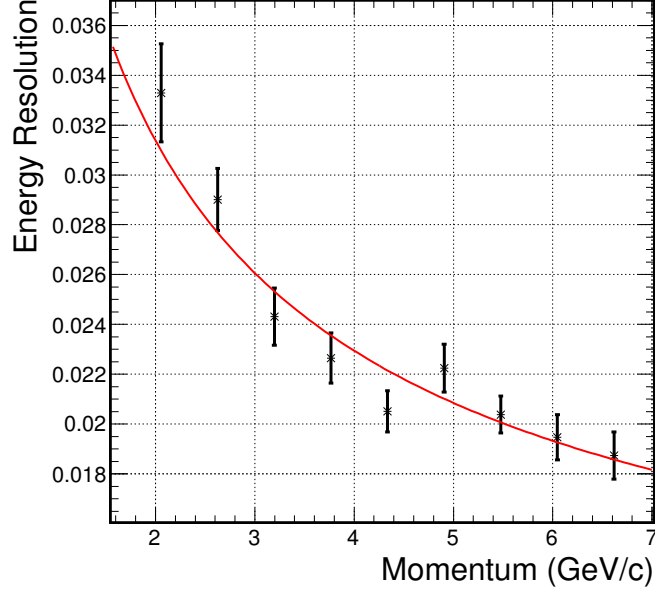


Figure 90: Simulated energy resolution of the SoLID calorimeter using both the Preshower and the Shower. The error bars are statistical error of the simulation. This simulation was performed without background to demonstrate the intrinsic PID performance of the EC. Simulation results including the background will be presented in section 10.7.

### 10.2.3 Lateral Size of the Calorimeter Module

A smaller lateral size for calorimeter modules leads to better position resolution and lower background. However, it will also increase the total number of modules and readout channels, leading to higher overall cost. The study shows that a lateral size of about  $100 \text{ cm}^2$  will provide a good balance between position resolution, background and the overall cost as shown in Fig. 91. A hexagon lateral shape is favored by the layout and the support design.

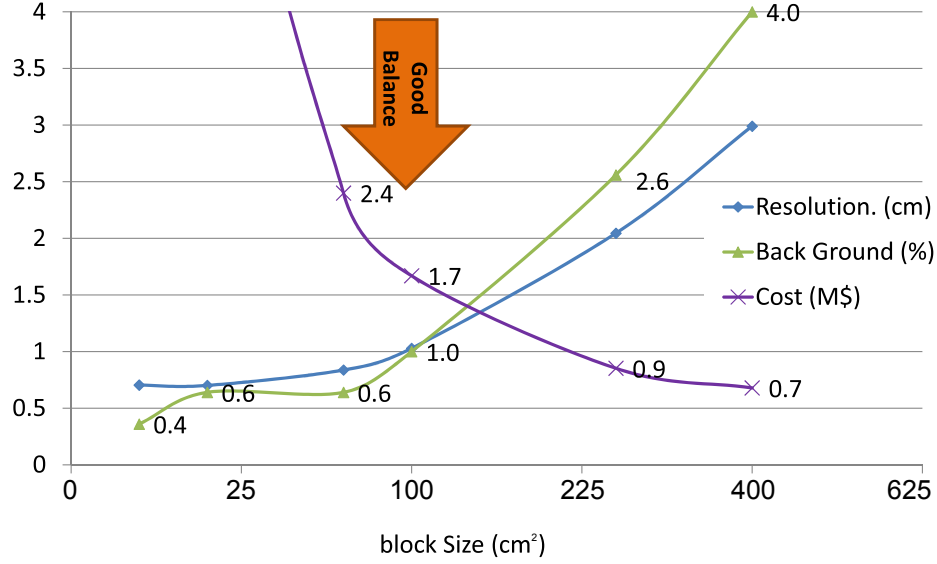


Figure 91: Position resolution and background level from simulation and the cost of the shower detector vs. lateral block size of the module.

### 10.3 Preshower Detector

Segmenting the EC longitudinally into a preshower and a shower part is essential to reaching the required pion rejection. Two designs were considered for the preshower detector: a full Shashlyk-type design that is optically isolated from the shower detector, and a passive radiator/scintillator pad design as used in the HERMES [231] and LHCb [232] experiments. Comparing to a Shashlyk-type preshower, the passive radiator/scintillator pad design has several advantages including increased radiation hardness, simplicity in construction, and fewer WLS fibers to read out. For a passive radiator of  $2X_0$ , the impact on overall energy resolution is less than  $0.5\%/\sqrt{E}$  for electrons with momentum larger than 2 GeV/c. Therefore, the passive radiator/scintillator pad design was adopted for the preshower detector. Details of the design are as follows:

- The thickness of the preshower radiator was determined by optimizing the overall pion rejection at the desired electron efficiency. As shown in Fig. 92 (top), the preshower-alone pion rejection improves as the radiator thickens up to  $3.5X_0$  due to immediate development of the electromagnetic shower. However, the impact on the overall energy resolution degrades with increased thickness of the absorber. A thickness of  $2X_0$  for the radiator was found to be an optimal choice for the SoLID application.
- The scintillator and readout design is similar to that of the LHCb experiment [232]: WLS fibers are embedded in one 2 cm-thick scintillator pad to absorb, re-emit and conduct the photons for readout.

With the above configuration and assuming a response of 100 photoelectrons per MIP (see next paragraph), the relation between pion rejection and electron efficiency for preshower alone can be plotted as a function of scintillator energy cuts, as shown in Fig. 92 (bottom right). One can see a pion rejection of better than 5 : 1 can be achieved at an electron efficiency of  $> 94\%$ .

Figure 93 shows pictures of the LHCb preshower tile (left) compared to a SoLID preshower prototype made by IHEP (right). Preliminary cosmic tests show that we can achieve up to 50 photoelectrons per MIP by embedding two 1.5-m long, 1-mm diameter Kuraray Y11(200)S WLS fibers

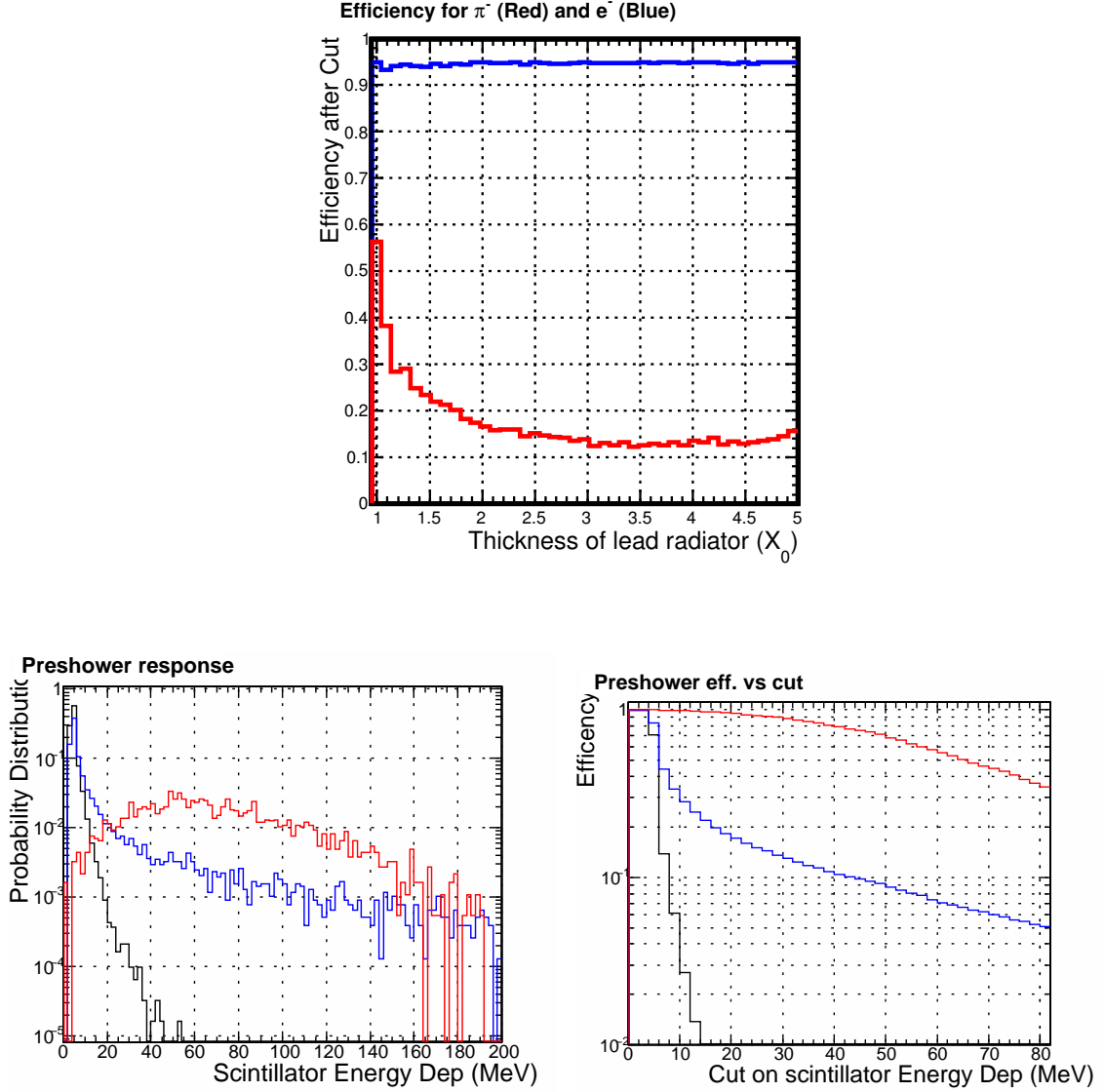


Figure 92: Simulated performance for the preshower detector. Top:  $1/(\pi^- \text{ rejection})$  (red curve) at a 95% electron efficiency (blue curve) vs. different thickness of the lead radiator. Bottom: Energy deposition in the scintillator (left) and detector efficiency vs. energy deposition cut (right), for electrons (red),  $\pi^-$  (blue) and  $\mu^-$  (black), for a preshower consisting of  $2X_0$  of lead radiator and 2 cm of scintillator.

in the circular groove on the preshower scintillator. The use of multiple fibers allows minimizing the attenuation due to WLS fiber length. The final number of photoelectrons that reaches the PMT will depend further on loss in the fiber connector and the attenuation in the clear fiber. Current simulation assumes a preshower response of 100 photoelectrons per MIP, and studies of how the number of photoelectrons affects the PID performance are ongoing.

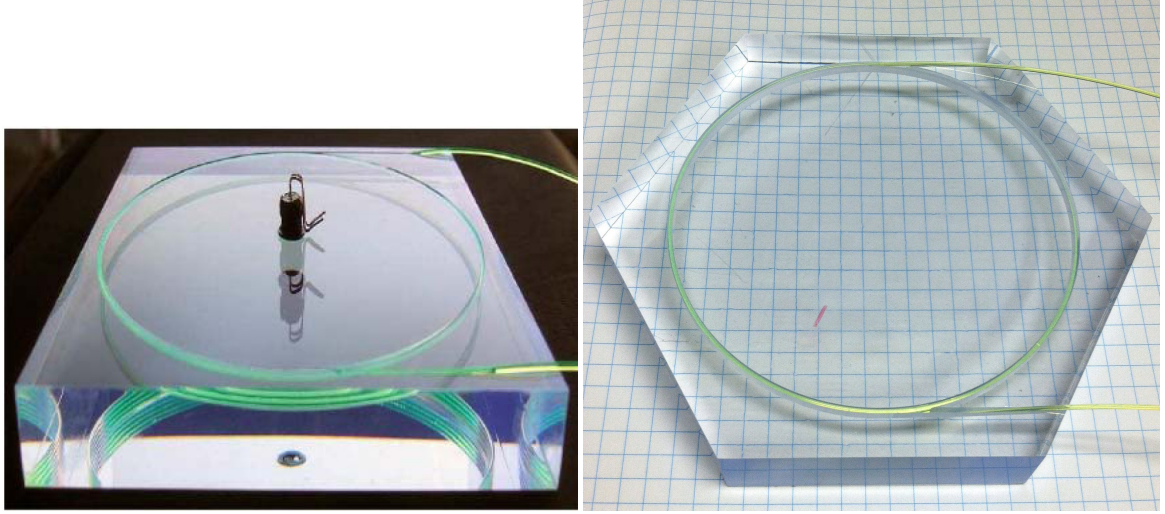


Figure 93: Preshower scintillators. Left: LHCb preshower tile ( $12 \times 12 \times 1.5$  cm) [232]. A single WLS fiber is embedded in a circular groove for 3.5 turns. In the middle of the tile is an LED for testing purposes. Right: SoLID preshower prototype made by IHEP. The SoLID prototype has a geometry of 6.25-cm-side hexagon and is 2 cm thick. Shown here are two 1-mm diameter WLS fibers embedded in a 9-cm diameter circular groove, each 2.5 turns.

## 10.4 Layout and Support

The total area of the PVDIS EC is slightly larger than that of the SIDIS ECs. The modules will be re-arranged between the two configurations, where modules from the PVDIS FAEC will be split and re-arranged into the SIDIS FAEC and LAEC. The SIDIS EC layout must preserve the 2-fold rotation symmetry in the spectrometer, and it is convenient to have the same symmetry for the PVDIS configuration as well. The design layout that meets these requirements is shown in Fig. 94 for the PVDIS configuration. The forward angle support system is shared by PVDIS and SIDIS FAEC, and the SIDIS LAEC will have a separate support system.

The scintillator tiles of the preshower modules will be mounted on an aluminum plate that simultaneously supports also the  $2X_0$  lead. For shower modules, the lead and the scintillator layers in each Shashlyk module are held together by six stainless steel rods penetrating longitudinally through the module. The modules are terminated by two aluminum endplates. The six rods protrude from the endplates and are supported by two aluminum support structures, one 2 cm thick plate between preshower and shower, and one 4 cm thick plate behind the shower. The support structure also holds the optical fiber connectors (see next section).

## 10.5 Light Readout

For both preshower and shower, the blue light from scintillators is converted into green light by WLS fibers embedded in or penetrating through the modules. Each preshower tile will use two WLS fibers with 1 mm diameter, each fiber arranged for two turns and embedded in a groove on the surface of the tile. The preshower WLS fibers will be routed using the space between preshower and shower to the space between EC and the solenoid wall. Each shower module will use 100 1 mm diameter WLS fibers arranged along the direction of the particle trajectory, and the fibers will be guided directly towards the back of EC. To avoid light loss over long distances, WLS fibers will be connected immediately to clear fibers using one-to-one connectors for readout by PMTs.

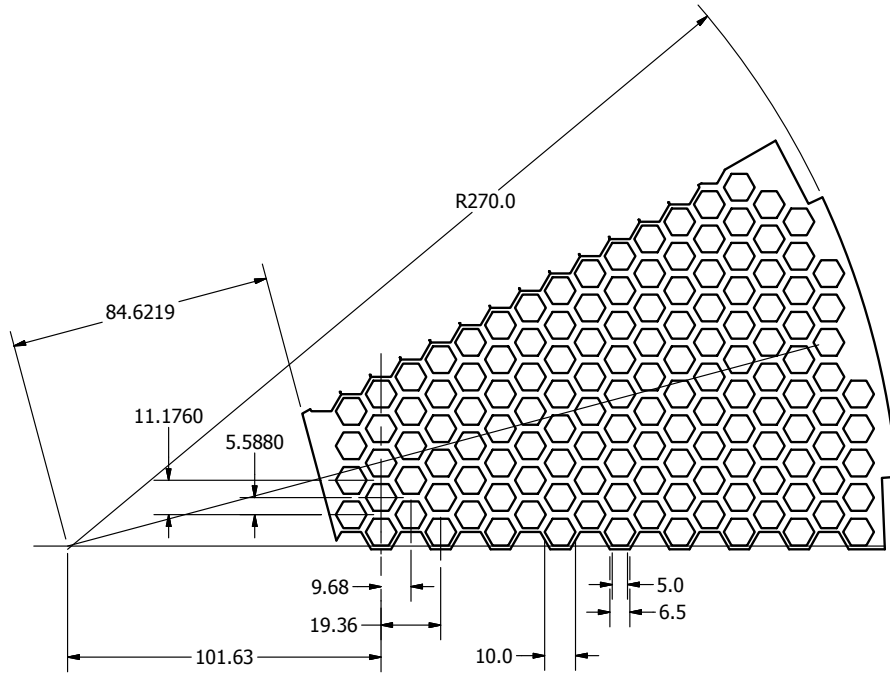


Figure 94: Layout of the hexagon-shaped modules with their support for a 30-degree wedge of the FAEC for the PVDIS configuration. The number of modules is 138 full modules plus 9 half-modules along the horizontal line. If counting 147 modules per 30-degree wedge, the total number of modules needed is 1764. We use 1800 modules for planning purposes at this stage.

LHCb used homemade fiber connectors. For SoLID, homemade connectors is an option but we have tested fiber connectors from the Japanese Fujikura company and found they work well. The Fujikura connectors were used by the Minerva experiment and their tests indicate the light loss in the connector is in an acceptable range of (10-20)% [236].

For the preshower it is essential to achieve a high photoelectron yield such that the best PID performance can be reached. We chose the Kuraray Y11(200) fiber because it has better mechanical properties and further a small minimal bending radius, as shown by the ATLAS Collaboration [235], which is crucial for us because our preshower fiber groove has a bending radius of 4.5cm. Our tests show the Bicron BCF91A fiber has similar light loss to Y11 but the light output is reduced by a factor of two when it is embedded in the preshower groove (compared to nearly zero loss for the Y11). The Y11 fiber has also been tested to higher radiation dose than Bicron BCF91A fibers by ATLAS [237]. For shower modules, the fibers are straight and hence the Bicron BCF91A WLS fiber becomes a more economical choice while still satisfying the requirement on radiation hardness. Bicron BCF92 fiber has faster decay time but gives less yield than BCF91A, and is not being considered for the SoLID ECs.

The magnetic field reaches about 1.5 T behind the SIDIS LAEC and a few hundred gauss behind both the PVDIS and SIDIS FAECs. For other experiments such as those at JLab Hall D or at LHC, silicon photomultipliers (SiPMs) are used. However, our simulation shows the radiation background behind the calorimeter is at the level of  $10^{13} \text{ cm}^{-2}$  1 MeV equivalent neutrons. Studies done by the LHCb on their tracker upgrade [238] reported cooling the SiPM can overcome the radiation damage from a high neutron background. Still, projecting from the LHCb study tells us for SiPM to work



for the shower detector, we need to cool to  $-70$  or  $-80$  °  $C$ . The space limitation alone imposed by the SoLID magnet makes such cooling nearly impossible, let alone the necessary electronics for temperature control. Therefore, our current default design is to use PMTs. Long clear fibers (about 1.5 m for the SIDIS FAEC and 3.5 m for the SIDIS LAEC) will be used to guide the light from the WLS fibers to PMTs located outside the solenoid region.

We will use one PMT per shower module to read out the 100 fibers. We plan to design custom PMT bases so that preamplifiers with a  $\times(2-5)$  gain can be used and to minimize the aging of the PMTs. For preshower modules we plan to use multi-anode PMT (MAPMTs), with all four fiber ends from each module read out by one pixel of the MAPMT. For MAPMT, the high background of the SoLID running condition constrains us to a relatively low gain in the range of  $5E3-2E4$ , due to the fact that the total anode current needs to be kept at only a fraction of the maximum specification to reduce the aging of the MAPMT. We plan to design pre-amplifiers with gain up to 50 and 16-channel MAPMTs. Pre-R&D of MAPMT and its preamplification board is currently underway. Note that LHCb used 64-ch MAPMTs at a gain of  $5E3$  combined with a front-end electronic board that provided an intrinsic gain of about 10, and our current design is based on and is consistent with the LHCb readout method.

## 10.6 Radiation Effects

The ECs for the SoLID spectrometer are designed for high luminosity experiments. The expected luminosity and run time are 169 PAC-days at  $10^{39} N \cdot \text{cm}^{-2} \text{s}^{-1}$  in the PVDIS configuration, 245 PAC-days at  $10^{37} N \cdot \text{cm}^{-2} \text{s}^{-1}$  for the SIDIS experiments and 60 PAC-days for the  $J/\Psi$  experiment. In the current design, the maximum radiation dose on the active material — scintillator and WLS fibers — in the calorimeter is significantly reduced by the use of the  $2X_0$  lead plate in the preshower, and the lead blocks described in section 6 for the PVDIS configuration. Because of the use of lead blocks, the PVDIS configuration has been divided into higher and lower photon flux regions; each consists of thirty 6-degree azimuthal regions.

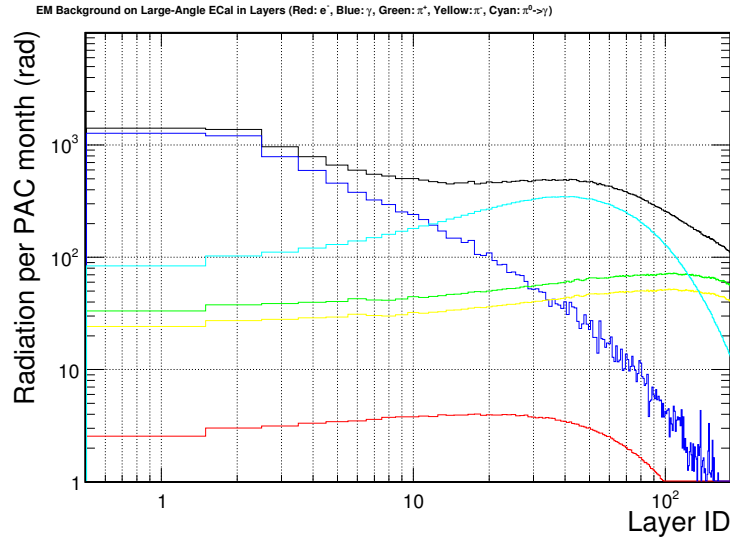
The radiation dose inside the calorimeter was simulated using GEANT4 based simulations considering a wide range of energy and species for the background particles. The dose rates for the active material (scintillators and fibers) are shown in Figs. 95 and 96. The highest radiation region is at the front part of the calorimeter, including the preshower scintillator pad and the front scintillators of the Shashlyk calorimeter modules. The maximum integrated radiation level for the active material reaches 100 kRad for the PVDIS experiment and 20 kRad in the SIDIS and  $J/\Psi$  experiments, which leads to a total radiation dose of less than 200 kRad for all approved experiments. This dose level can be safely handled by the choice of scintillator and WLS fibers.

## 10.7 Performance

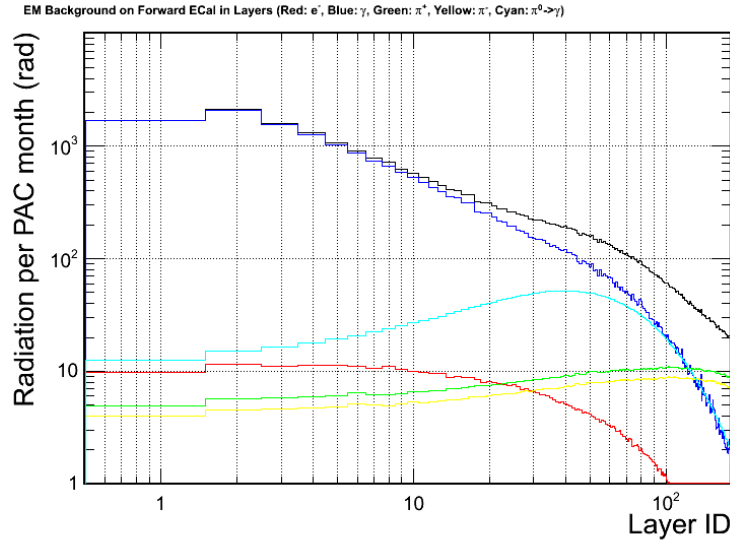
The EC system plays multiple roles in the SoLID spectrometer. Its performance was evaluated in the GEANT4 based simulation and discussed in this section, including PID performance, trigger capability and shower position resolution. A realistic background simulation was set up to evaluate the calorimeter considering a wide range of species and momenta of the background particles.

### 10.7.1 Intrinsic electron-pion separation

As a baseline, the PID performance was first evaluated without the background. The primary track is propagated through the SoLID magnetic field in GEANT4, then enters the calorimeter. A local cluster which consists of the central calorimeter module and six neighboring hexagon-shaped



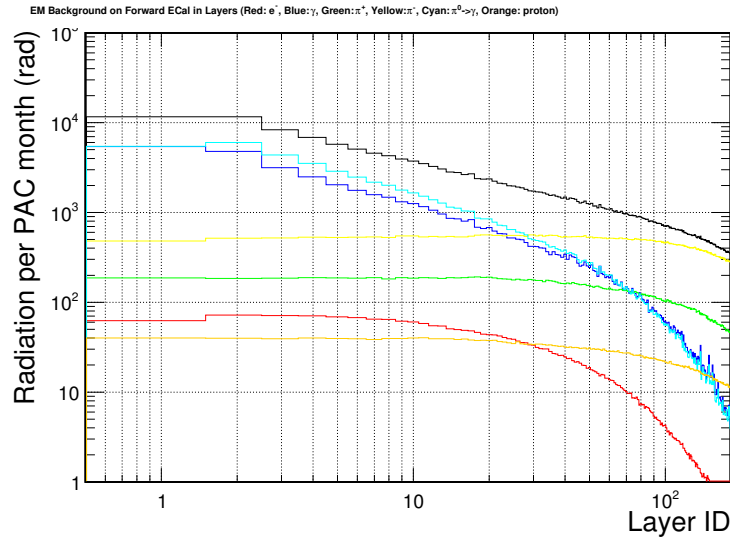
(a) SIDIS large-angle calorimeter



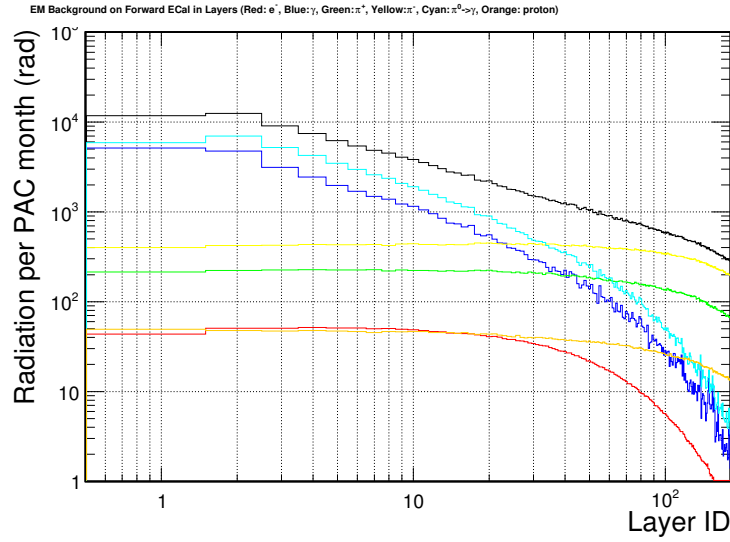
(b) SIDIS forward-angle calorimeter

Figure 95: SIDIS radiation dose rates per PAC month in each layer of the scintillator tiles in the calorimeter. Layer ID 1 is the preshower scintillator. The rest of IDs are assigned for each scintillator layer in the Shashlyk calorimeter in the order of increasing  $z$ . The color code stands for different contributions of various particle species at the front surface of the preshower: electrons (red), photons (blue), EM total (magenta),  $\pi^+$  (green),  $\pi^-$  (yellow). The overall dose is shown by the black curve.





(a) PVDIS calorimeter in higher-photon flux region



(b) PVDIS calorimeter in lower-photon flux region

Figure 96: PVDIS radiation dose rates per PAC month in each layer of the scintillator tiles in the calorimeter. Layer ID 1 is the preshower scintillator. The rest of IDs are assigned for each scintillator layer in the Shashlyk calorimeter in the order of increasing  $z$ . The color code stands for different contributions of various particle species at the front surface of the preshower: electrons (red), photons (blue), EM total (magenta),  $\pi^+$  (green),  $\pi^-$  (yellow), and protons (brown). The overall dose is shown by the black curve.

modules is formed. With a multidimensional cut of the preshower and shower response within the cluster (see Sec. 10.7.5), the overall pion rejection averaged over the acceptance of each calorimeter is shown in Fig. 97. A 100 : 1 pion rejection at 95% electron efficiency is achieved for momentum bins of  $p > 2 \text{ GeV}/c$ . For the lowest momentum bin  $1 < p < 2 \text{ GeV}/c$ , which is only needed for the SIDIS FAEC, a better than 50 : 1 pion rejection at 90% electron efficiency is obtained.

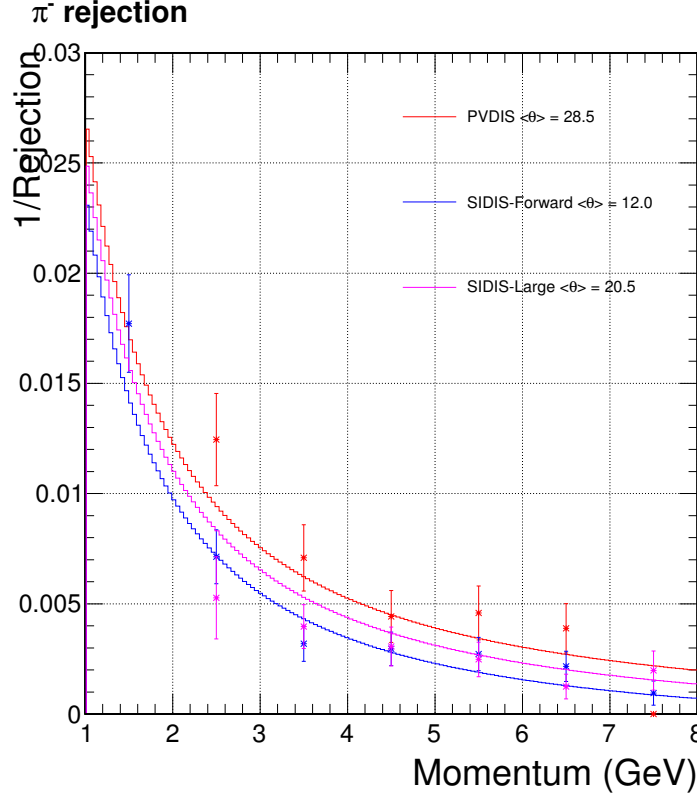


Figure 97: SoLID EC intrinsic (without background)  $\pi^-$  efficiency ( $1/\text{rejection}$ ). From top to bottom: PVDIS with average track polar angle  $\langle\theta\rangle = 28.5^\circ$  (red), SIDIS LAEC with  $\langle\theta\rangle = 20.5^\circ$  (magenta) and SIDIS FAEC with  $\langle\theta\rangle = 12.0^\circ$  (blue). A constant 95% electron detector efficiency is maintained for  $p > 2 \text{ GeV}/c$ . A 90% electron efficiency is maintained for the lowest momentum bin  $1 < p < 2 \text{ GeV}/c$ , which is only required for the SIDIS FAEC. The  $\langle\theta\rangle$  value is different for the three calorimeter configurations, which leads to slight differences in the pion rejection curves.

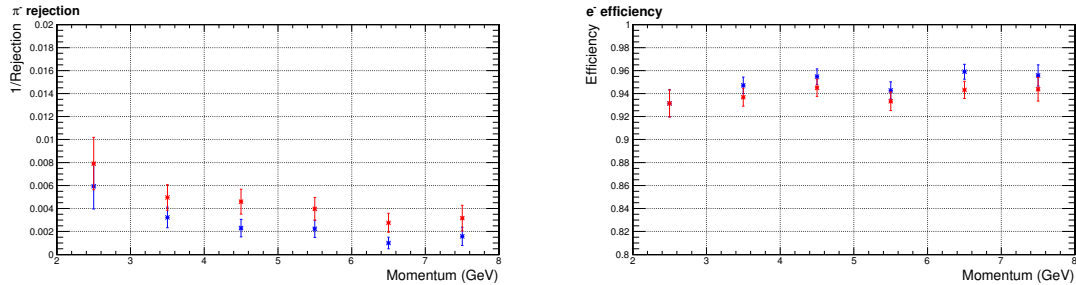
### 10.7.2 PID performance under realistic background simulation

For a large intensity device, background particles and their influence on the calorimeter performance have to be considered. A full background simulation was implemented to study calorimeter performance. The background simulation procedure is as follows:

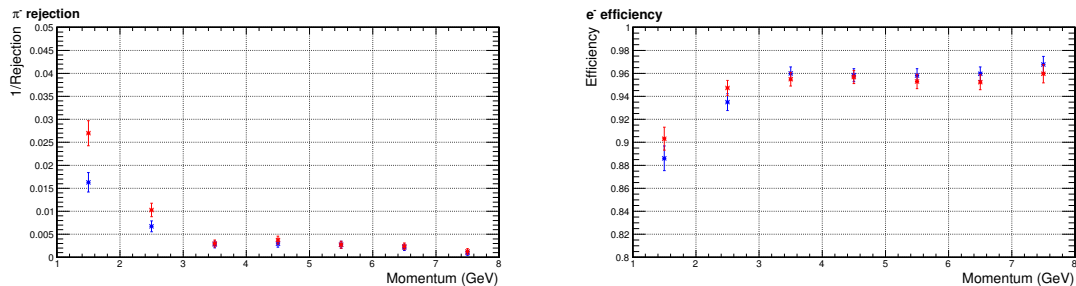
1. Particles are generated at the target including photons and electrons from the low energy EM processes (based on physics in GEANT4), DIS electrons (based on CTEQ6 PDF), and hadrons (based on the Wiser fit);

2. Particles are propagated through a SoLID GEANT4 simulation to the front surface of the calorimeter;
3. The EC response is simulated for a wide range of background particles — electrons, photons, pions, and protons — within the momentum range  $10 \text{ keV} < p < 11 \text{ GeV}$ . A statistical model is used for the correlation between preshower and shower responses;
4. The background contribution to each event is produced by combining the background rate at the EC front surface and the EC response described above for a region of interest on the calorimeter, usually defined by a radius-azimuthal angular bin. A conservative 30 ns coincidence window between background particles and the primary event is assumed.
5. The background contribution is embedded into the raw signal from the simulated primary particles (high energy electrons and pions). The background-embedded data are then analyzed as raw ADC signals. The energy response is calibrated and PID and trigger performance are analyzed.

Typically, background rate is the highest in the inner radius region and drops by approximately one order of magnitude in the outer radius region. Figure 98 shows the EC performance for the SIDIS configuration in the inner radius region. For SIDIS experiments, effects from background particles are visible but not significant: for large-angle EC, the pion rejection remains better than 100:1 for all momentum bins; for forward-angle EC, there is no noticeable change in the PID performance other than for the lowest momentum bin  $1 < p < 2 \text{ GeV}/c$  where the pion rejection is a half of the no-background case. However, the Cherenkov detector provides high PID performance in the low momentum range and the overall pion rejection is sufficient for the experiment.



(a) SIDIS large-angle calorimeter



(b) SIDIS forward calorimeter

Figure 98: Calorimeter pion and electron efficiency without (blue) and with (red) the consideration of background particles for the inner radius region (highest background) for the SIDIS configuration.

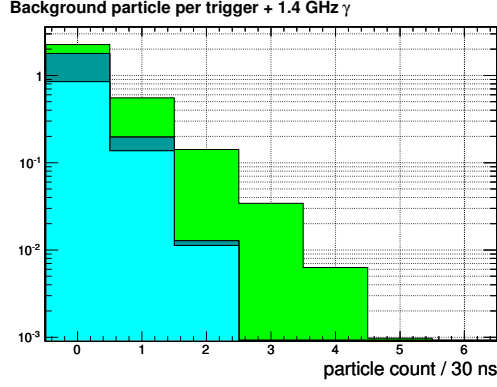
In the PVDIS configuration, the background rate is significantly higher and the performance is affected. The 30-fold structure of the baffle system for the PVDIS experiment causes the background to alternate between high- and low-rate 30 times in the azimuthal direction. Therefore, calorimeter performance is studied for the high- and the low-rate “slices” separately, with each fan-shaped slice covering 6 degrees. Background structure for the inner-radius, high-rate slice is shown in Fig. 99. The PID performance with the background is evaluated for different radius, see Fig. 100. Comparing to the intrinsic performance of Fig. 97, the pion rejection is up to 8 times worse: the pion rejection varies from 25–50 at  $p = 2.5 \text{ GeV}/c$  to 50–100 at  $p = 6 \text{ GeV}/c$ , while keeping the electron efficiency to be in the range (90–95)%. Particle identification for the experiment will need to rely on a full-waveform analysis of the EC, combined with information from the Cherenkov detector.

### 10.7.3 Trigger capability

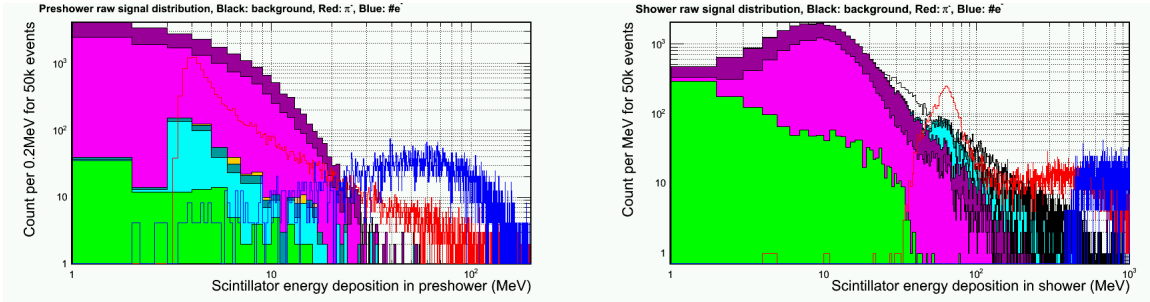
Trigger capability is an important function of the EC. The calorimeter shower energy deposition in all combinations of local 6+1 clusters (central block plus six neighboring hexagon blocks) is first summed after digitization, forming local shower sums. Triggers are then formed by passing the local shower sums through a threshold cut. Electron triggers are formed with a targeted electron threshold, and the efficiency curves for both pions and electrons are studied with the full-background simulation. The following triggering specifications have been studied:

- SIDIS large angle calorimeter: electron triggers of 3 GeV are formed by cutting on local shower sum larger than 2.6 GeV. The trigger turn-on curve is shown in Fig. 101. High electron efficiency is observed for electrons above the threshold. The rejection on few-GeV pion background is high, in the range (20-100):1, which satisfies requirement of the SIDIS experiments.
- SIDIS forward calorimeter: position dependent electron triggers provide high trigger efficiency for electrons of  $Q^2 > 1 \text{ GeV}^2$ . The pion rejections with 1 GeV threshold is shown on the left plot of Fig. 102. With higher thresholds, pion rejections are better.
- SIDIS forward calorimeter: MIP triggers allow the calorimeter to trigger on hadrons for the SIDIS measurement. The threshold is determined by MIP peak - two sigma of the Landau fit of the distribution, which lead to a calibrated local shower sum energy of 220 MeV. The trigger efficiency for pions is high, as shown on the right plot of Fig. 102.
- PVDIS forward calorimeter: electron triggers are formed with radius-dependent trigger thresholds. As shown in Fig. 103, the targeted electron threshold varies from 1.5 GeV at outer radius to 3.8 GeV at inner radius on the calorimeter, which produces high trigger efficiency for DIS electrons with  $x > 0.35$ . The trigger turn-on curves are evaluated for several regions on the calorimeter as shown in Fig. 103. The efficiency for both electrons and pions are lower for inner radius regions due to the use of high thresholds for background-suppression. Overall the pion rejection at the trigger level is  $> 2$  and varies with the radius.

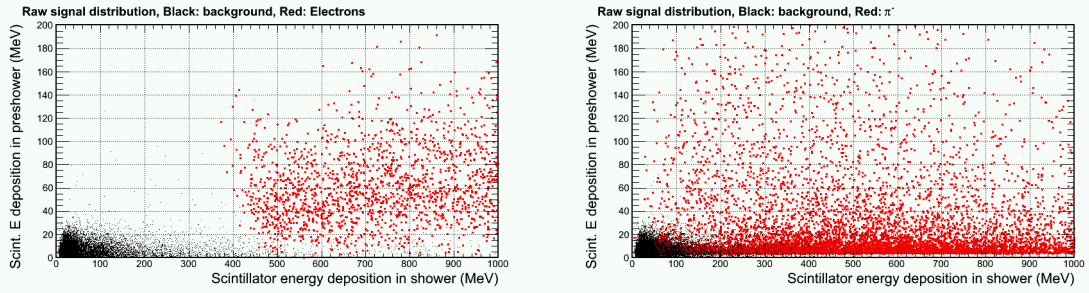
The PVDIS experiment will run with a luminosity up to  $10^{39} \text{ cm}^{-2}\text{s}^{-1}$ . A baffle system is used to reduce the very high background rate expected at this luminosity. To further reduce the rate from high energy photons from neutron pions and low energy backgrounds, fan-shape lead blocks, each covering 2.5 degrees azimuthally, will be placed in front of the EC. The trigger of PVDIS will be formed by taking the coincidence between the EC and the gas Cherenkov detector. Estimation of the trigger rate from EC can be performed using the realistic background simulation (described



(a) Stacked probability to find the number of background  $\pi^-$  (light blue),  $\pi^+$  (dark blue) and electrons (green) at the front of the preshower. The photon rate is as high as  $\sim 1.4$  GHz, thus the photon count is off-scale and not shown in this figure.

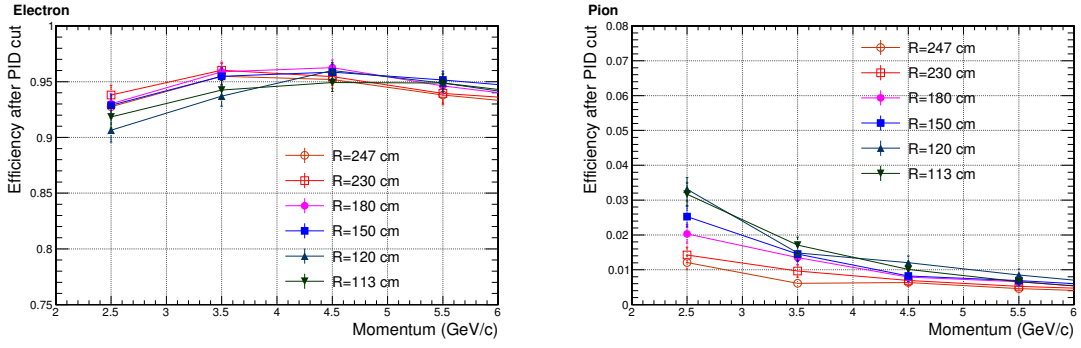


(b) Stacked probability (count per 50k events) vs. Preshower (left) and Shower (right) scintillator energy deposition for incoming background electrons (green),  $\pi^-$  (light blue),  $\pi^+$  (dark blue), protons (yellow), EM process-originated photons (magenta) and  $\pi^0$ -originated photons (dark magenta). For comparisons, energy deposition for high energy pion (red) and electrons (blue) are shown as non-filled curves.

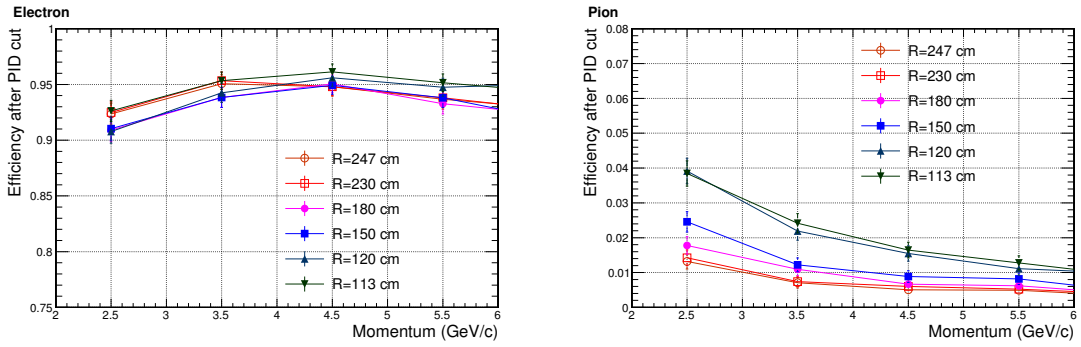


(c) Preshower-shower scintillator energy correlation for background particles (black), compared with high energy electrons (left, red) and pions (right, red)

Figure 99: Background distribution for the PVDIS forward calorimeter at the production luminosity of a liquid deuteron target. Background for the inner radius ( $R \sim 1.2$  m) and higher-radiation azimuthal region is shown. The energy deposition originated from background is compatible to that of high energy pions.

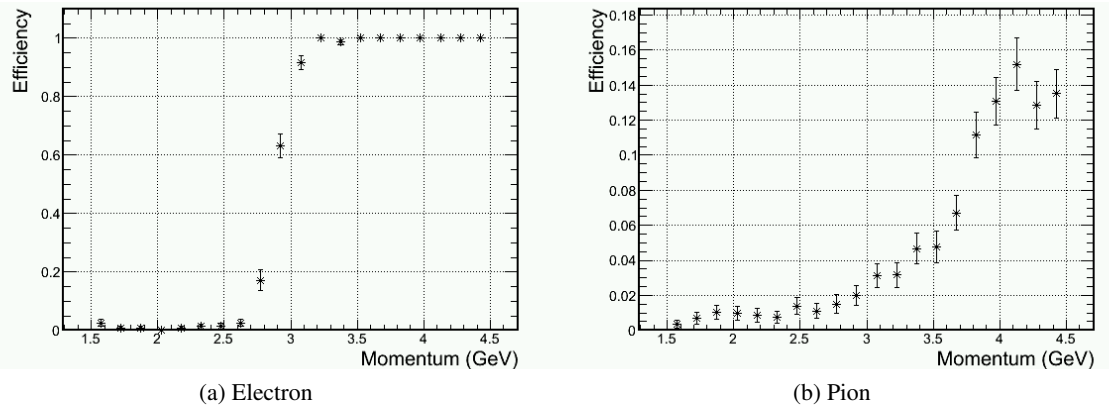


(a) lower-radiation azimuthal region



(b) higher-radiation azimuthal region

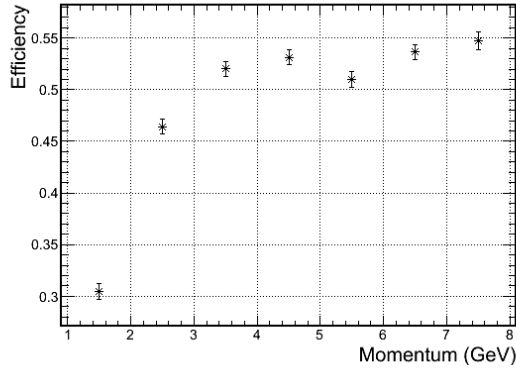
Figure 100: Calorimeter pion and electron efficiency for the PVDIS experiment, evaluated with the presence of background at eight typical regions on the calorimeter.



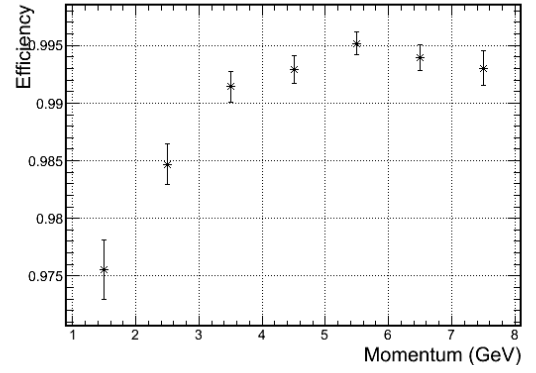
(a) Electron

(b) Pion

Figure 101: Trigger efficiency for electrons (a) and pions (b) for the SIDIS large angle calorimeter. The target trigger threshold is approximately  $P_e = 3 \text{ GeV}/c$ . Only the (high-background) inner-radius region is shown here.

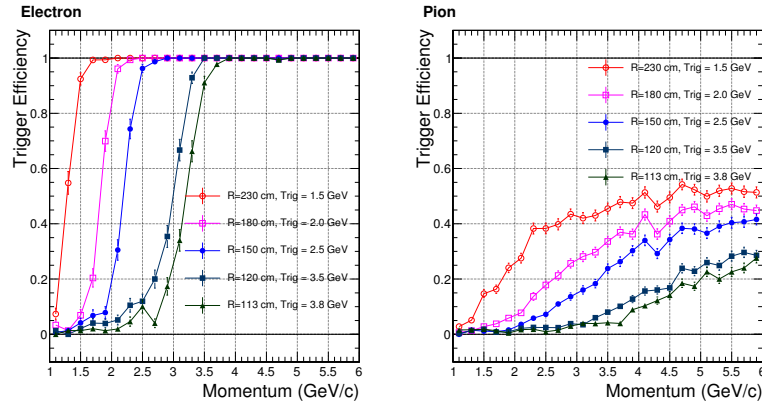


(a) Pion efficiency in electron trigger with a target trigger threshold of ( $P_e = 1 \text{ GeV}/c$ )

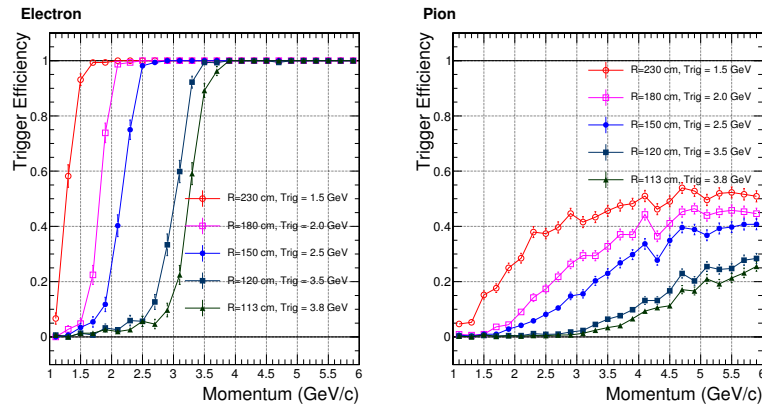


(b) Pion efficiency in the MIP trigger

Figure 102: Trigger efficiency for pions in the SIDIS forward calorimeter for electron triggers (a) and MIP triggers (b). Only the (high-background) inner-radius region is shown here.



(a) Higher-radiation azimuthal region



(b) Lower-radiation azimuthal region

Figure 103: Trigger efficiency curves for the PVDIS configuration.

previously in Section 10.7.2) combined with EC trigger capability results described above. The EC trigger rate will then be combined with gas Cherenkov trigger rate to obtain the expected DAQ trigger rates and to make sure they can be handled by the DAQ system. For SIDIS experiments on  $^3\text{He}$ , the luminosity will be up to  $3 \times 10^{36} \text{ cm}^{-2}\text{s}^{-1}$  on  $^3\text{He}$  target and additional about  $3.7 \times 10^{36} \text{ cm}^{-2}\text{s}^{-1}$  on target glass windows. Target collimators (described previously in Section 10.7.2) will be used to reduce backgrounds from the glass windows. The SIDIS triggers are formed from EC in combination with Cherenkov, MRPC and SPD. The FAEC will also provide MIP trigger for hadron detection. Trigger rate estimation for SIDIS is carried out similar to the PVDIS case. Results for both PVDIS and SIDIS trigger rates will be presented in Section 14.

#### 10.7.4 Shower Position Measurement

Position resolution of the shower center was studied for different lateral sizes of the calorimeter modules, as shown in Fig. 104. The radial resolution is in general worse than the azimuthal resolution because the tracks are not perpendicular to the radial direction. As can be seen from Fig. 104, with the use of proper algorithm, a position resolution of better than 1 cm is achieved for both directions at the designed lateral granularity of  $100 \text{ cm}^2$ .

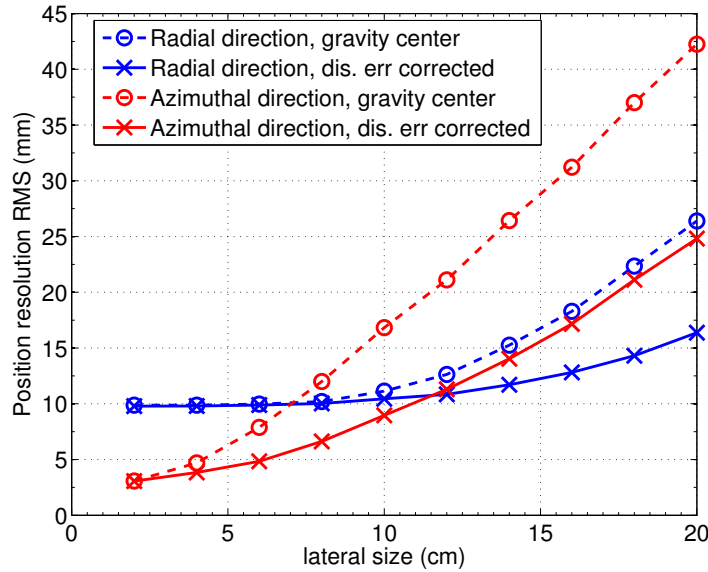


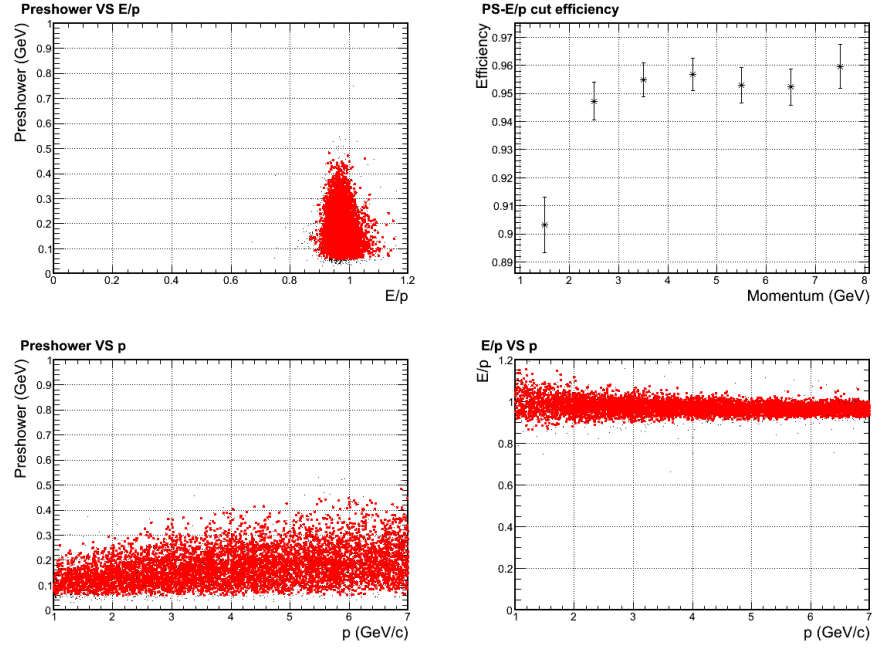
Figure 104: Position resolution for electron showers vs. different lateral size of the calorimeter module. Both azimuthal (red) and radial (blue) resolutions are shown, with the shower center calculated from a simple energy-weighted geometrical center (dashed curves), and those calculated with further corrections using the energy deposition distribution among neighboring modules (solid curves).

#### 10.7.5 Supplemental Information: PID Selection Cuts

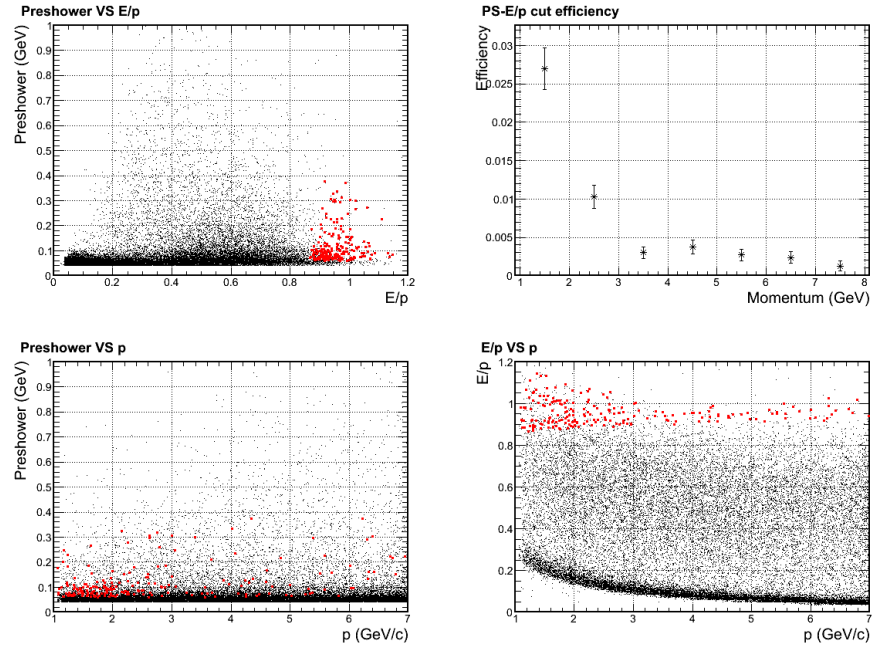
A three dimensional PID cut was used to select the best electron samples with maximal  $\pi^-$  rejection as illustrated in Fig. 105. For each given momentum bin, the cut on  $E/P$  and preshower energy roughly follows the contour lines of the ratio of  $\pi^-$  efficiency to  $e^-$  efficiency, which is the optimal cut for the  $\pi^-/e^-$  separation. A momentum dependence is then introduced to the cut to maintain a



constant 95% electron efficiency for most of the bins. Events passing the cut are highlighted in red in the plots.



(a)



(b)

Figure 105: Illustration of electron sample cuts as highlighted in red dots, in comparison to simulated electron (a) and  $\pi^-$  (b) samples. The SIDIS forward calorimeter in the high background (small radius) region is studied in these plots.

## 10.8 Scintillator Pad Detector for SIDIS Experiments

The main purpose of the scintillator pad detector (SPD) is to reduce calorimeter-based trigger rates for high-energy charged particles (see Section 10.7.3 for calorimeter trigger capability) by rejecting photons through the coincidence between the SPD and the calorimeter. Two SPDs will be used: one in the forward direction between the heavy gas Cherenkov detector and the MRPC, and the other in the large-angle direction immediately before the large-angle calorimeter. Both SPDs consist of fan-shaped scintillator pads arranged perpendicular to the beam direction. The LASPD will also provide time-of-flight for particle identification with a timing resolution goal of 150 ps.

The performance for the scintillator was studied in the GEANT4 simulation. For FASPD, we plan to use 5 mm thickness scintillators based on a balance between the light yield and the radiation length. The 5-mm thickness corresponds to a radiation length of  $\approx 0.013X_0$  which directly affect the photon conversion rate. Typical responses of the FASPD to photons and charged particles are shown in Fig. 106. Approximately 20% of the photon background leave energy in the scintillator due to back splashing from the calorimeter front face. The trigger threshold was set at two standard deviations below the MIP peak to ensure a high efficiency for charged particles. Pile up effects

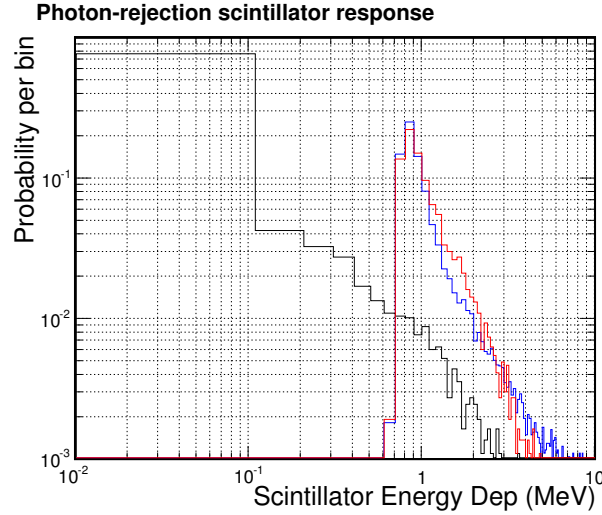


Figure 106: Typical probability for scintillator energy depositions in the SPD, for electron (blue), pion (red) and high energy photons (black).

were studied for fixed ADC timing windows of 30 and 50 ns. The photon rejection depends not only on the trigger rate per scintillator, but also the scintillator segmentation, see Fig. 107. In addition, photons attenuates significantly in long scintillators and thus the length of the individual segmentation needs to be minimized. The segmentation of FASPD is chosen to be 240 based on Fig. 107 and a desired 5:1 photon rejection at the large angle, and is further divided into 60 in the azimuthal direction and 4 in the radial direction. The readout of FASPD is by using WLS fibers embedded on the surface of the scintillator, then connected to clear fibers and are readout by MAPMTs. This is similar to the preshower. Because the threshold is below MIP and is much lower than for preshower, a higher combined gain of PMT and the preamplifier is needed. We currently plan to use preamplifiers with gain  $\approx 50$  because it's the maximum comfortable gain that can be achieved on a pre-amplifier board. This will allow us to place the threshold around 20 mV, the minimal threshold that is above the noise level.

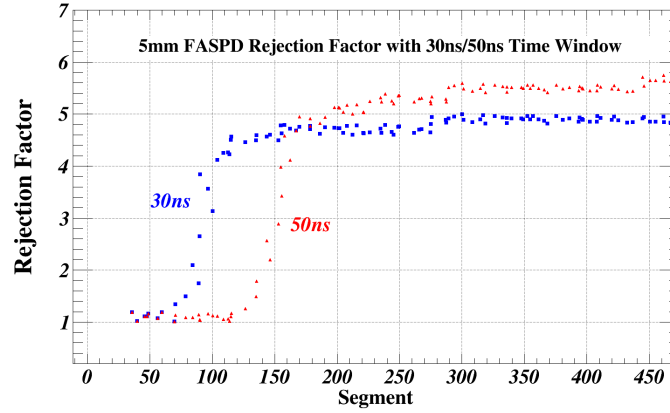


Figure 107: Photon rejection factor for 5-mm thick FASPD as a function of the segmentation, for DAQ windows of 30ns (blue) and 50ns (red), respectively. For the 30-ns timing window, a 240 segmentation is appropriate to reach a photon rejection of 5:1.

For the LASPD, a 10:1 photon rejection is desired to bring the photon-induced calorimeter trigger rate down to below the electron-induced rate. Figure 108 shows the simulated photon rejection factor vs. segmentation. The 10:1 rejection can be achieved by 60 azimuthal segments. Because the radial coverage of the LASPD is small and because of the requirement of high photoelectron statistics to reach the TOF requirement, the LASPD has only azimuthal segmentation, with each covering 6 degrees. For readout, the use of WLS fiber is impossible, again because of high photoelectron statistics. We plan to use field-resistant fine-mesh PMTs on the outer radial edge of the LASPD to readout the scintillating light.

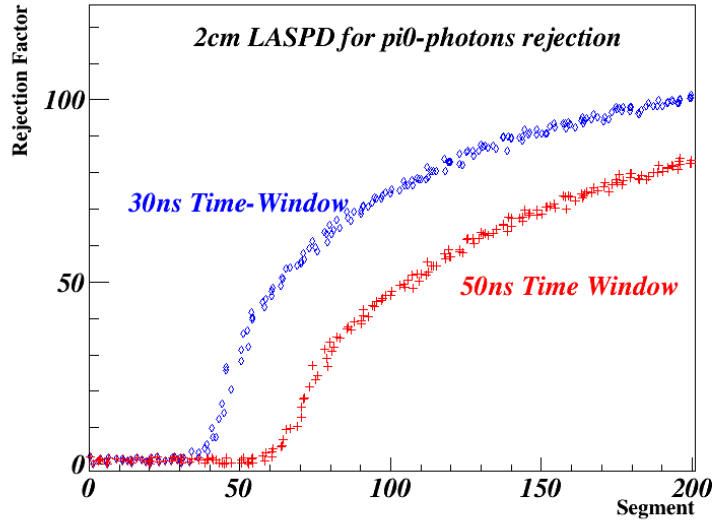


Figure 108: Photon rejection factor for 20-mm thick LASPD as a function of the segmentation, for DAQ windows of 30ns (blue) and 50ns (red), respectively. For the 30-ns timing window, a 60 segmentation is appropriate to reach a photon rejection above 10:1.

## 10.9 EC Collaboration Status and Construction Outlook

The shashlyk sampling technique used by the SoLID EC has been used by many experiments at the LHC, including LHCb, ALICE and ATLAS. The CMS experiment's calorimeter upgrade will use a similar technique. In the R&D for SoLID EC, we studied extensively the calorimeter design and technical details from these experiments. We also learned many useful facts from other experiments and/or collaborations, including for example Minerva, MINOS, and JLab Hall D.

Our general design for the SPD, the preshower, and the shashlyk shower modules is based heavily on the LHCb's SPD and ECal design. The LHCb and other LHC experiment's detector TDR and associated technical notes provide tremendous knowledge. This includes: readout design for the preshower and the SPD (WLS fiber embedding in grooves on the scintillator surface and the use of MAPMTs) (LHCb); wrapping of the scintillator (LHCb, ATLAS), relative light yield between different scintillator material and WLS fiber types (LHCb); the use of optical grease or glue (LHCb); side treatment and painting of shashlyk modules (LHCb); adding mirror ends to WLS fiber (LHCb); coupling between WLS fiber and MAPMTs (LHCb); Tests of light yield uniformity (LHCb); radiation hardness of the preshower and shashlyk modules (LHCb ECal and HCal) and plastic scintillating fibers (LHCb tracker upgrade, JLab Hall D GlueX barrel ECal); LED monitoring system (LHCb); WLS fiber bending light loss (simulation by LHCb; direct data from ATLAS Tile ECal TDR); performance of SiPM under high neutron radiation background (mainly LHCb tracker upgrade, but also JLab Hall D and CMS); EC commissioning and calibration procedure (LHCb ECal and HCal); tolerance/quality control for the scintillators and fibers (LHCb).

Once prototype modules are constructed, the light yield can be compared with that of LHCb, ALICE, KOPIO, PHENIX, COMPASS, and COMPASS-II.

For ECal construction, most of previous experiments that utilized the sampling-type design made use of the Russian IHEP for the scintillator production. On the other hand, assembling of the modules can be performed either by IHEP, or by other institutions. For example, Wayne State University (WSU) and China Central Normal University (CCNU) both assembled modules for the ALICE experiment (for CCNU, threading WLS fiber was done in Italy, separately from the initial assembling). The collaboration is in close contact with the WSU group but their module assembly lab has been dismantled a long time ago. We are also in contact with the U. of Iowa group (Prof. Onel) who is participating in the CMS ECal upgrade, but the CMS Ecal utilizes crystal layers and is very different from SoLID EC in the choice of material and thus the construction process. Currently the SoLID collaboration is pursuing the possibility of manufacturing the scintillators in China. Two groups, Shandong University (SDU) and Tsinghua University (THU), are participating in the SoLID EC R&D, and they have developed local contact with the CCNU group to learn their experience in module assembly. The SDU group has extensive experience with scintillator production in China and cosmic ray testing of the scintillator's light yield, and is in a good position to lead the prototype R&D for SoLID EC.

## 11 MRPC

### 11.1 Overview

The Multi-gap Resistive Plate Chamber (MRPC), which will be used as the time of flight (TOF) system, is located in front of the forward-angle calorimeter. Several MRPCs have been recently used in RHIC STAR and LHC ALICE as their TOF systems [239–242] and the typical time resolution for these detectors is better than 80 ps. Most importantly, as a gas chamber, the MRPC does not need PMTs for readout so it can work inside a magnetic field. For the SoLID-SIDIS configuration, the total path length is around 8 meters from the target and the flight time is calculated by comparing the timing signal to the beam RF signal. With a time resolution of 100 ps, we can identify pions from kaons at a rejection factor of 20:1 with momenta up to 2.5 GeV/c. Compared with the MRPCs used at STAR and ALICE, the MRPC for SoLID receives a higher flux rate, approximately 10 kHz/cm<sup>2</sup>. Tsinghua University has developed a new type of low resistivity glass with a bulk resistivity on the order of 10  $\Omega$ cm. The rate capability of the high rate MRPC assembled with this type of glass can reach 50 kHz/cm<sup>2</sup> [243, 244]. We propose to construct the high rate SoLID-MRPCs with this low resistive glass.

### 11.2 Structure of the MRPC Prototype

The layout of the MRPC is shown in Fig. 109. The inner diameter of the detector plane is about 1 meter and the outer diameter is 2 meters. The area of the disk is about 10 m<sup>2</sup>. The whole detector consists of 50 super modules and each super module consists of 3 MRPC modules. There is overlap between MRPC modules and super modules to avoid blind areas.

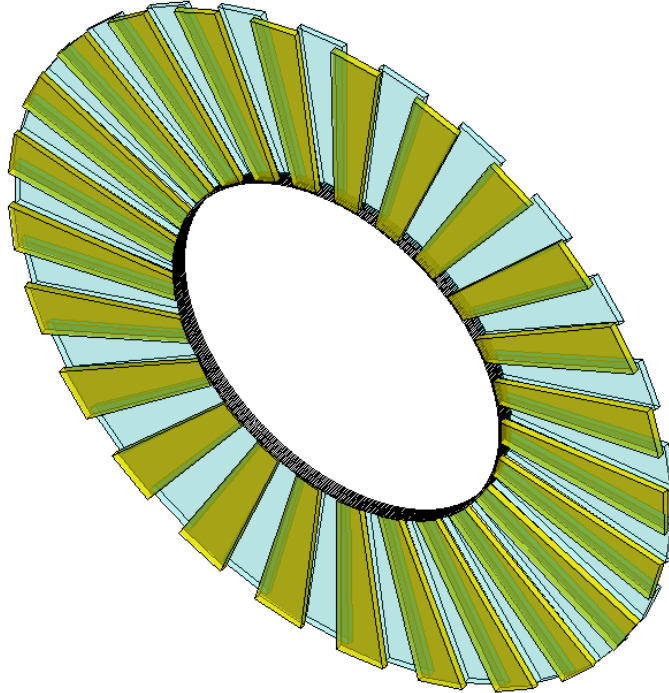


Figure 109: The layout of MRPC TOF

A prototype of the MRPC has been assembled and its structure is shown in Fig. 110. This

trapezoidal module is assembled with our low-resistivity glass. The module has ten gas gaps and the width of each gap is  $250\text{ }\mu\text{m}$ . The outer glass is  $1.1\text{ mm}$  thick and the inner glass is  $0.7\text{ mm}$  thick. Colloidal graphite is sprayed on the surface of the outer glass and the surface resistivity is about  $5\text{ M}\Omega\text{cm}$ . Fig. 111 shows the structure of the readout strips. Each module consists of 11 strips and the width of each strip is  $25\text{ mm}$  with a  $3\text{ mm}$  gap. The shortest strip is  $13\text{ cm}$  and the longest is  $17\text{ cm}$ . This prototype will be similar to the smallest module of the three modules in one super module. With this design, the whole detector will consist of 1650 strips, and the total number of readout channels is 3300 since each strip has readouts on both ends.

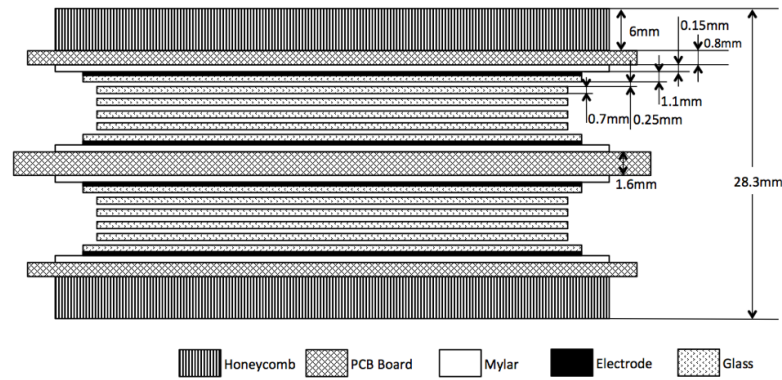


Figure 110: The structure of the MRPC prototype

### 11.3 Gas system

The MRPC uses a mix of Freon 90% R134 freon, 5% Isobutane and 5% SF6. The mix is in itself non flammable but since Freon and SF6 are green house gases we are planning for recycling system for the gas similar to what was used for PHENIX Hadron Blind Detector.

### 11.4 Cosmic Ray Test

The cosmic ray test system for the MRPC prototype consists of a cosmic ray telescope and a VME based DAQ system. The telescope consists of three  $20\text{ cm} \times 5\text{ cm} \times 5\text{ cm}$  scintillators and two  $4\text{ cm} \times 2\text{ cm} \times 1\text{ cm}$  scintillators. These five scintillators were used to trigger on cosmic rays. The layout of the cosmic ray telescope and the prototype is shown in Fig. 112. Two of the larger scintillators and one of the smaller scintillators are above the module, and the rest are below the module. PMT0 through PMT4 were used for basic coincidence triggering and to provide the reference time. The two small scintillators are used to measure the efficiency of the module. The width of the area subtended by the small scintillators is smaller than the width of a MRPC strip. Since this module would be tested with an electron beam at JLab (see later discussion), the cosmic test is only for checking primary performance parameters, such as dark current, noise, efficiency and time resolution. With a high voltage setting of  $13.2\text{ kV}$ , the dark current is less than  $10\text{ nA}$  and the noise rate is a few  $\text{Hz/cm}^2$ . Fig. 113 shows the efficiency plateau. It can be seen that the efficiency can reach 98% and the plateau region is larger than  $600\text{ V}$ . Fig. 114 shows the relation between charge and time after slewing correction. The time spectrum after correction is shown in Fig. 115. The time jitter of four PMTs is  $87\text{ ps}$ , so the resolution of the MRPC can reach  $50\text{ ps}$ . All of these show that the MRPC module has good performance.

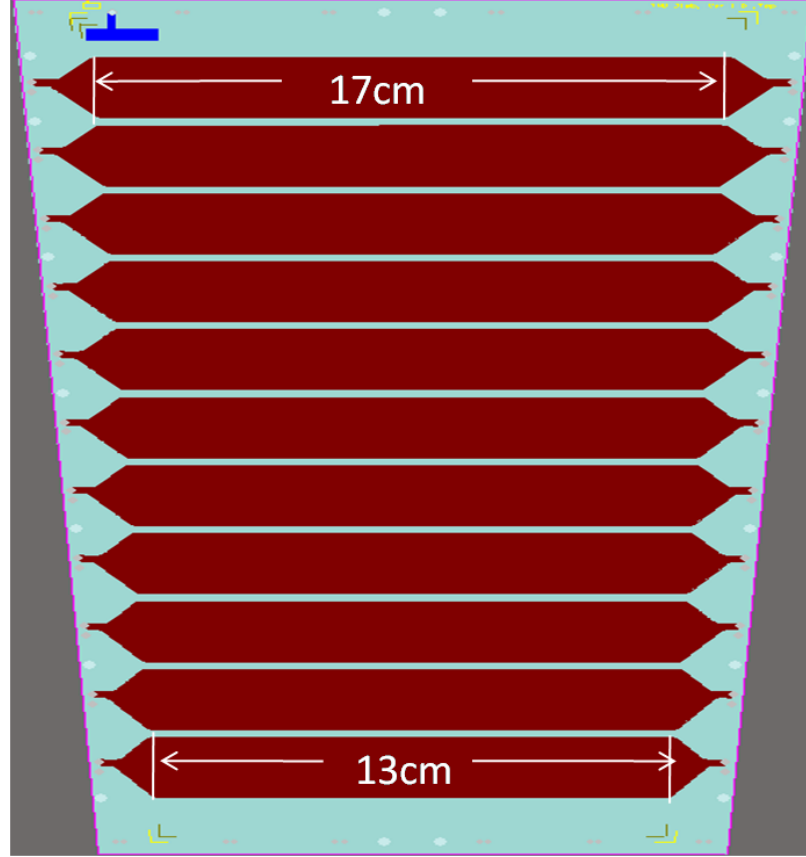


Figure 111: The structure of the readout strips

## 11.5 Beam Test at Hall A

### 11.5.1 Test Setup

The setup of the beam test is shown in Fig. 116. The beam was mainly for the JLab g2p experiment [245]. Our test setup stood about 10 m to the side. There was an electron beam passing through our trigger system and the backgrounds were mainly soft photons, electrons and neutrons. The background intensity was stronger than the main electron beam. A thick concrete shield was used to suppress background particles striking the MRPC. A diagram of the DAQ is shown in Fig. 117. The trigger system was very similar to that of the cosmic test system. One small scintillator ( $5\text{ cm} \times 5\text{ cm} \times 1\text{ cm}$ ) was read out by PMT 0 and each of two long scintillators ( $10\text{ cm} \times 5\text{ cm} \times 1\text{ cm}$ ) was read out on both ends (by PMTs 1–4). The coincidence of PMT0 and PMT4 provided the trigger signal of the system. The delayed coincident signal also acted as the gate signal of the flash ADC and the stop signal of the TDC. PMT1~PMT4 provided the reference time of the system. A CAEN V775 TDC was used to record the time signal and a flash ADC, JLAB FADC 250, was used to record the charge signals. A VME scaler was used to record the time interval between two triggers. From this time interval we can get the signal rate to study the rate capability of the detector.

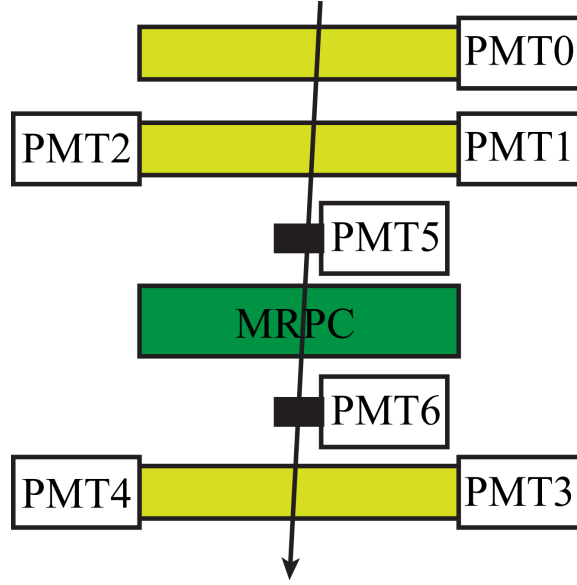


Figure 112: Layout of the test setup

### 11.5.2 HV Scan Result

MRPCs were conditioned under high voltage for a few hours in order to reach a stable, low dark rate working region. The electronics threshold was set to 30 mV. The dark current was less than 8 nA and the rate of the module was less than 10 Hz/cm<sup>2</sup> at 108 kV/cm. The coincidence of PMT1–PMT4 provided the T0 of the test system, with a time jitter of about 100 ps. In order to find the optimum working voltage of the counters, the efficiency and time resolution were scanned as a function of the applied voltage for a ‘low’ flux of  $\bar{\phi} \sim 1\text{--}4$  kHz/cm<sup>2</sup>. The results are summarized in Fig. 118. The counters showed large efficiency plateaus above 600 V, and time resolutions were as good as 75 ps. It can be seen that the time resolution obtained from cosmic rays is better than that from the electron beam test, because the time jitter of T0 in the beam test was larger than that in the cosmic test.

### 11.5.3 Rate Scan Result

The rate depended on background intensity. From the scaler we can get the signal rate of the MRPC. Fig. 119 shows the signal rate change with time in runs 188 and 193 respectively. The rate was not stable in each run. From these runs, we obtained different rates from 1 to 16 kHz/cm<sup>2</sup>. These two runs were combined to analyze the rate performance. The results are shown in Fig. 120. It can be seen even when the flux rate reaches 16 kHz/cm<sup>2</sup>, the efficiency is still higher than 94% and the time resolution is close to 80 ps. So this module meets the requirement of the SoLID TOF system.

The evolution of the charge distribution can be seen in Fig. 121 for this MRPC. The charge is obtained from the sum of its two ends. It can be seen that, with increasing flux, the average charge decreases and the spectrum shifts down to lower charges as expected.

## 11.6 Radiation hardness and aging

Aging and radiation hardness tests were carried out. For the low conductivity glass, no change in resistivity were seen for neutron fluence up to  $10^{14}/\text{cm}^2$  as show in Figure 122. The glass was



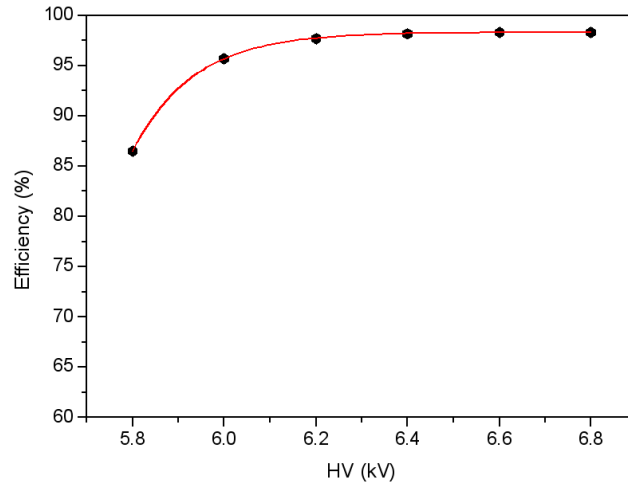


Figure 113: Efficiency plateau of the MRPC

also applied with 1000V for about 32 days with integrated charge of  $1C/cm^2$  (about 2 years of continuous running in SIDIS conditions), and its resistivity remained stable. The module was tested using a X-ray source. the chamber was exposed to X-ray for 35 days which corresponded to about  $0.1C/cm^2$ . No change in amplitude and efficiency were observed at the end of the test as show in Figure 123.

## 11.7 Conclusions

A high rate MRPC was planned to construct the time of flight system for the SoLID-SIDIS program, and a prototype has been designed and constructed. The trapezoidal prototype module assembled with low resistivity glass has  $10 \times 0.25$  mm gas gaps and 11 readout strips. The width of the strips is 2.5 cm with an interval of 3 mm. This module was tested using cosmic rays and also tested using electron beams in Hall A of JLab. The results show its rate capability of larger than  $16 \text{ kHz/cm}^2$ . This module has a very promising time resolution. The time resolution can reach 50 ps in cosmic test and is about 75 ps in the beam test. The chambers behaved very stably during the test. A detailed aging study was performed to assure the stability over a long running time. The performance of the prototype meets the requirement of the SoLID-TOF system.

## 11.8 R&D Plan for Better Time Resolution

A R&D effort by the Chinese collaboration, jointly for SoLID, sPHENIX and EIC, for the next generation MRPC aims at 20 ps resolution. Tsinghua University is planning to develop a prototype in the next year. Beam test and finalization of detector and electronics will be done the following year.

Obtaining good timing resolution also depends on the electronics, both preamplification of signals and digitization:

EIC R&D at BNL is using 7 GHz bandwidth TI LMH5401 [179] amplifiers for preamplifiers. Tsinghua University will also develop its own amplifier chip which could drive lower costs and give a more compact footprint for the electronics with a multichannel amplifier chip.

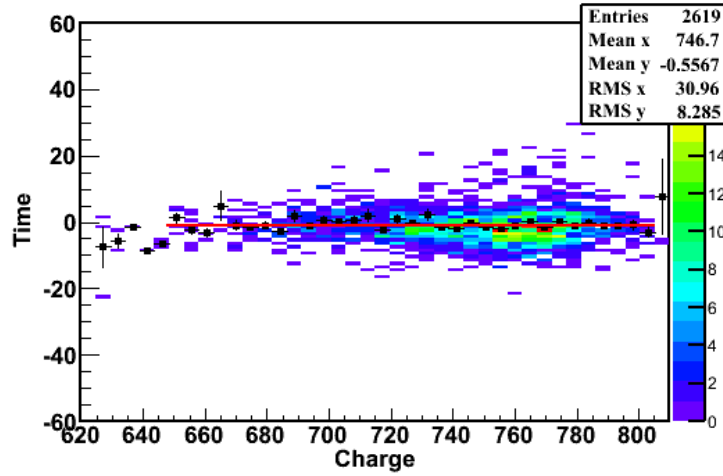


Figure 114: The relation between charge and time after slewing correction

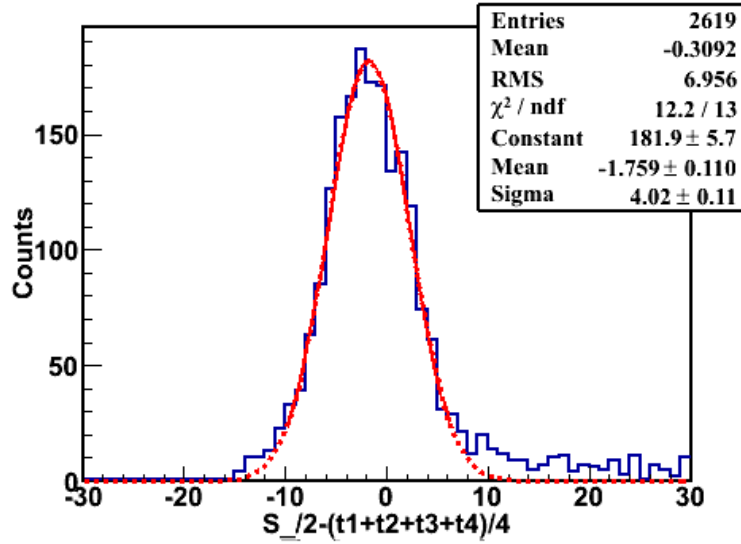


Figure 115: Time spectrum after correction

New sampling electronics, development of which is being motivated by MCP PMTs, can reach picosecond level timing resolution for multi-photons. The system is based on Switched Capacitor Arrays (SCAs), which continuously sample the detector signal on a circular array of capacitors. Sampling frequencies up to 10 GSamples/s have been reached. With a good calibration, a timing resolution of 1 ps has been achieved. The following Table 17 summarizes the different available chips.

One of the main drawbacks of the SCA is the inherent dead time to allow readout of all the samples for each trigger. A multi level array design will be implemented in the next generation of

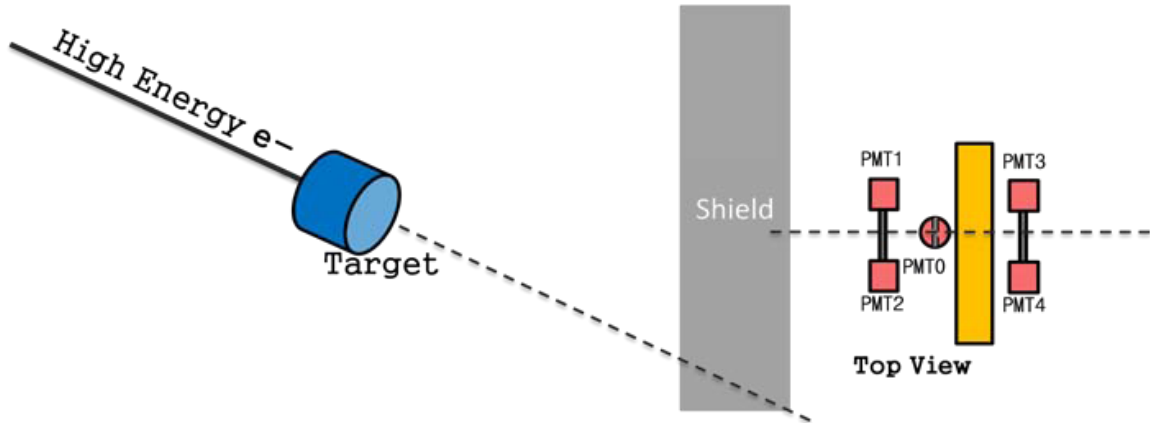


Figure 116: Setup of beam test in Hall A

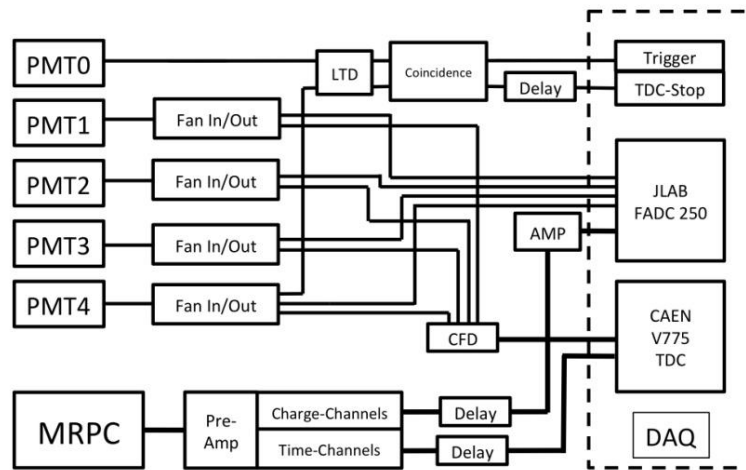


Figure 117: Diagram of the DAQ system

DRS5 or PSEC5 chips. There is a joint effort from HEP/NP and a commercial company to offer a commercial modular system based on the future PSEC5. This is currently the best option with costs which could go as low as \$15 per channel.

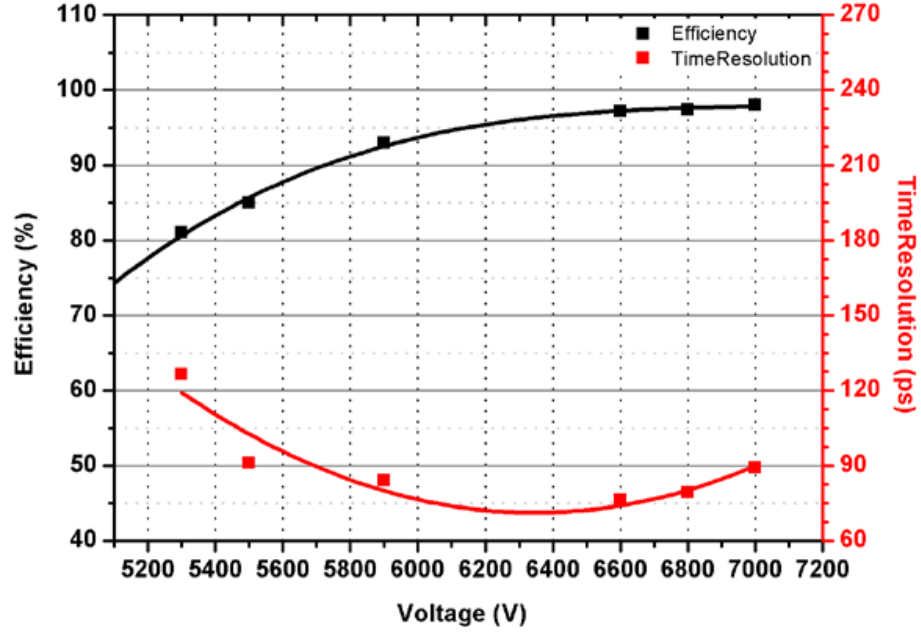


Figure 118: Time resolution and efficiency change versus applied voltage

Chip	Sample Frequency GHz	Bandwidth GHz	Samples	Channels	Readout MHz	Resolution ps
PSEC4	4 to 15	1.5	256	6	40 to 60	9
SAMPIC	3 to 8.2	1.6	64	16 or 8	80	5
DRS4	0.7 to 5 GHz	0.950	1024	9	33	1
DRS5	10	3	4096	32	300 ?	5 ?
PSEC5	5 to 15	1.5 to 2	32768	4	500?	5?

Table 17: Table summarizing the characteristics of different sampling chips available and future generation ones for DRS5 and PSEC5

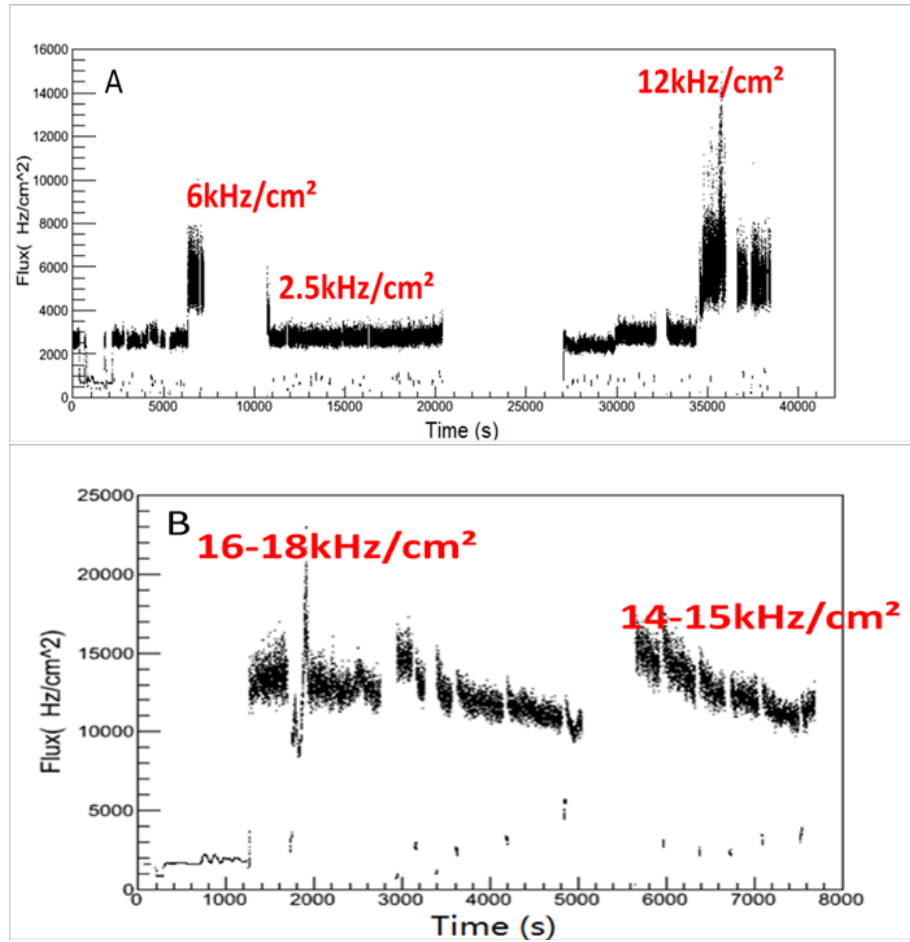


Figure 119: Signal rate changes with time. (A) shows run 188 and (B) shows run 193. The MRPC was located 5 meters from the target. There is shielding in front of the detector in (A), no shielding in front of the detector in (B).

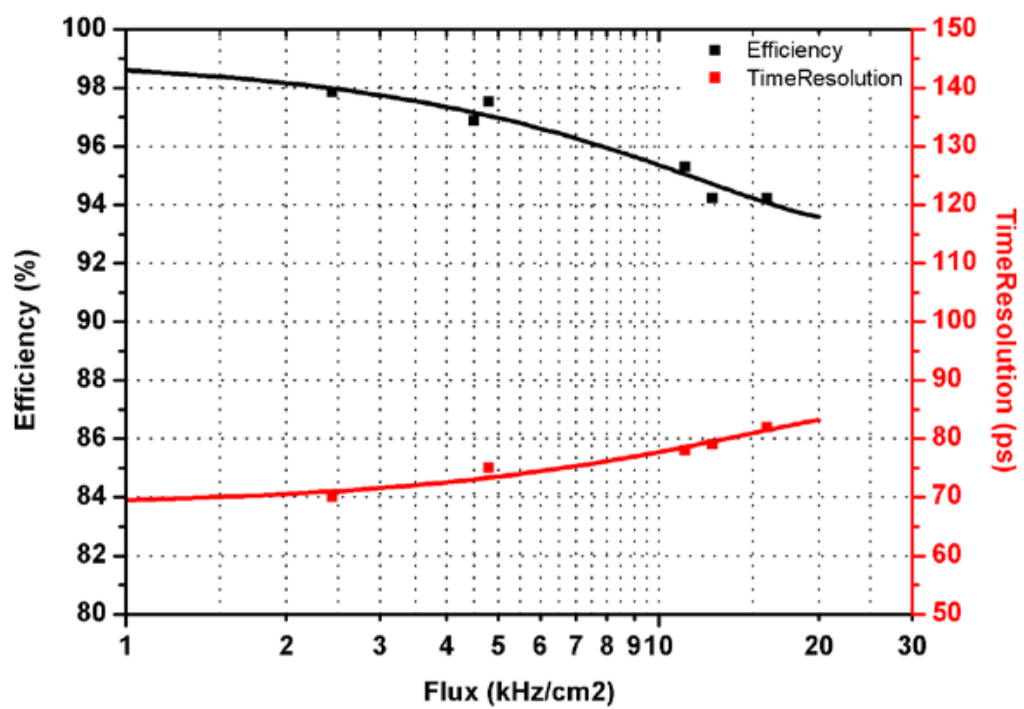


Figure 120: Measured efficiencies and time resolutions as a function of the particle flux.

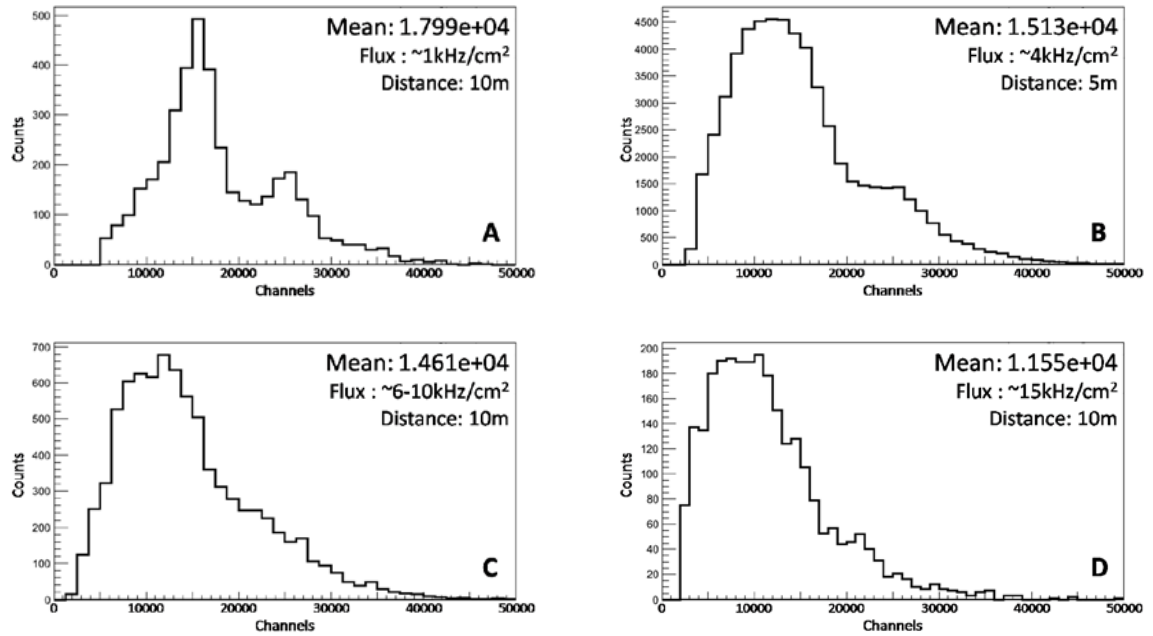


Figure 121: Charge distribution at various fluxes over one readout strip. Flux increases from figure A to D.

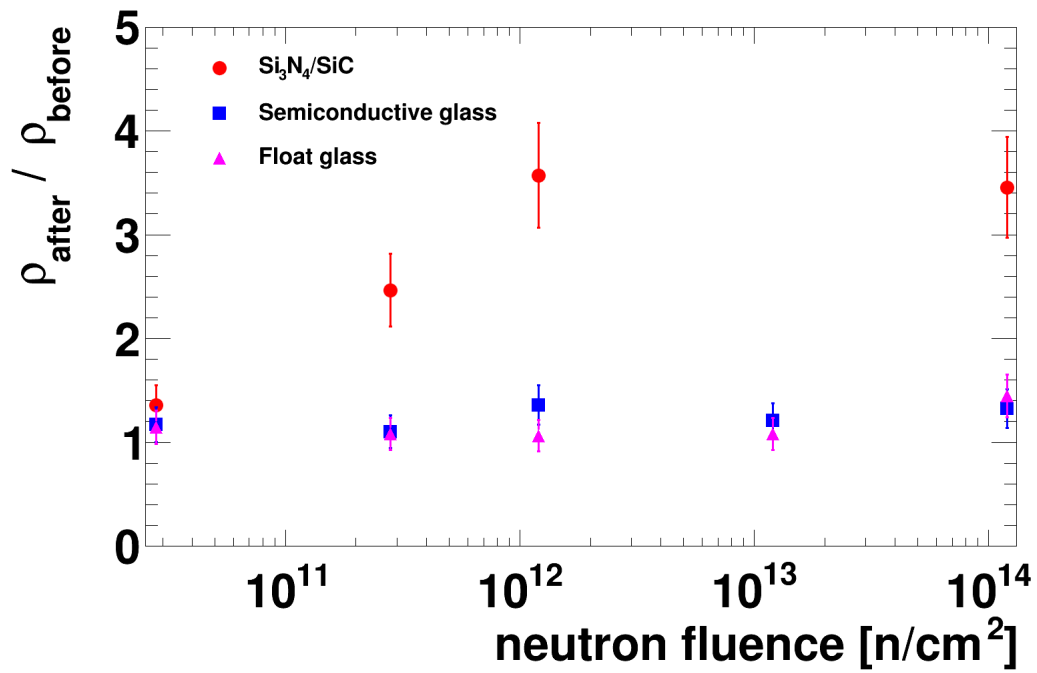


Figure 122: Change in glass resistivity as a function of neutron fluence, where the semiconductive glass is what we use.

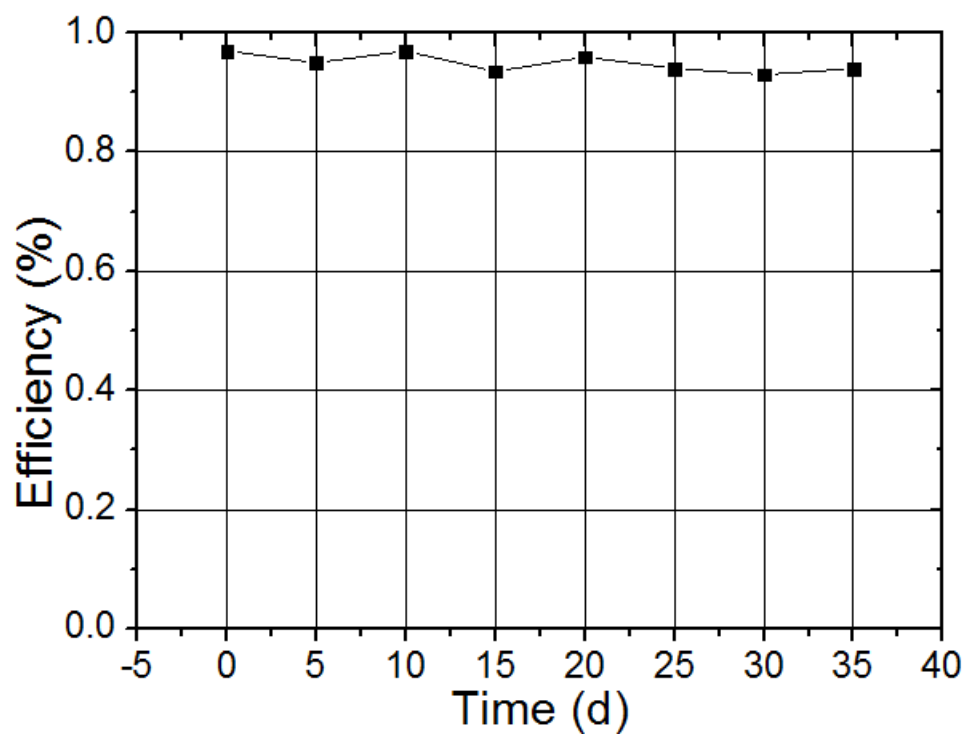


Figure 123: Chamber efficiency as a function of x-ray irradiation days



## 12 Simulation and Reconstruction

### 12.1 End-to-End Software Framework

At the time of this writing, research is underway to identify a comprehensive software framework for SoLID. A framework should be chosen early in the software development cycle, where SoLID is now, to provide a common programming interface (API) for all software components. If chosen well, the API will stay constant, or at least backward compatible, throughout the project’s life-time so that early investments in code development will continue to pay off. Additionally, it is important at this stage to identify software features and capabilities that will be needed for SoLID data analysis, to the extent foreseeable now. Such feature requirements should be well matched to the specifics of the SoLID experiments, such as data volumes, detector types and configurations, and analysis methods. Retrofitting capabilities that were initially overlooked is often difficult and wasteful because doing so may invalidate original design assumptions, requiring large parts of the first-generation software to be re-written. Conversely, choosing a framework with too many features typically results in overly complex, bloated software that is difficult to learn and faces user resistance.

With these goals in mind, we have developed the following requirements for the SoLID software framework; it should

1. support all major components of the physics data processing chain, *viz.* simulation, digitization, reconstruction and physics analysis, within a *consistent* development and run-time environment (“end-to-end framework”);
2. allow multi-pass data processing, where the output of one analysis pass can be used as the input for the next pass—an essential capability to minimize the need for reprocessing large data sets;<sup>4</sup>
3. allow multiple processing chains in a single job, for example to run different track fitting, PID or physics analysis algorithms on the same data in a single processing pass;
4. support interactive analysis of reconstructed quantities with ROOT, since ROOT will most likely be the data analysis package best known to and preferred by future SoLID collaborators;
5. save extensive metadata to its output, for example database parameters used in previous analysis stages (if practical) and detailed information about data provenance;
6. support parallel computing, *i.e.* multi-threading and/or distributed processing;
7. be written in C++, as most SoLID collaborators are well-versed in that language; and
8. be readily available at this time, so that development can start without delay;

Given limited manpower, the effort needed to develop a new framework from scratch that satisfies the above set of requirements would be prohibitive. As experience in other collaborations shows [246–249], frameworks with comparable capabilities are invariably complex and may take the better part of a decade to mature. Therefore, it is practically unavoidable, and certainly wise, to build the analysis software for a specific experiment on already existing packages, unless truly unusual or novel requirements arise. Of course, we are not the first to discover this. Motivated by the

---

<sup>4</sup>This is typically achieved in physics frameworks by a clear separation of data and algorithms, where the data objects are persistable and saved to intermediate files. Regarding object persistence, the ROOT streamer model represents the state of the art in the field.

increasing complexity of software in the field, various collaborations worldwide have, over the past decade or two, put considerable effort into developing high-quality, general-purpose frameworks aimed at processing the event-type data prevalent in nuclear and particle physics experiments. The present trend in HEP is a collaborative approach toward software, where already-developed, widely tested frameworks are increasingly shared by similar experiments and re-used for new ones [250]. Practically no modern software in the field does without ROOT [251] in regard to interactive analysis, visualization and object persistency, while a number of choices exist for event processing frameworks that support simulation and reconstruction.

Obviously, we do not expect to find a perfect framework that satisfies all our criteria fully. Generally, however, a good event processing framework should stand out by a superior technical design and reliance on widely adopted, state-of-the-art technologies (*e.g.* support for C++11/14, ROOT object persistency). To minimize development time and maximize user adoption, the right mix of features, excellent documentation and a large body of available example code would clearly be beneficial.

At present, we are evaluating a number of different NP and HEP data analysis frameworks that are popular and readily available. Specifically, we have been studying Podd (JLab Hall A/C) [252], Clara (JLab Hall B) [246], JANA (JLab Hall D) [247], Fun4All (PHENIX/sPHENIX at BNL) [253], FairRoot (GSI) [248], and *art* (FNAL) [249]. Of these, FairRoot, a package developed for the heavy-ion program at the future FAIR facility at GSI in Darmstadt, Germany, and *art*, the framework developed for and adopted by the Intensity Frontier experiments at Fermilab, appear to be the most promising candidates for long-term use by SoLID. Both frameworks satisfy the majority of the SoLID requirements listed above, are mature, sufficiently rich in features, sufficiently flexible for general-purpose simulation and analysis tasks, well supported, and serve a large user community that is unlikely to dissolve over the next decade.

Both the FairRoot and *art* collaborations participate in the monthly ROOT planning meetings; as stakeholders, they provide direct input to the ROOT team to help improve compatibility of the respective frameworks with ROOT. We interpret this as an additional encouraging sign for the expected longevity of these two frameworks in particular.

Currently, neither FairRoot nor *art* are multi-threaded, but as of 2017 a major effort is underway by the core development team at Fermilab to implement multi-threading in *art* [254]. This feature is expected to become available in 2018. The heavy dependence of FairRoot on ROOT, with its many global variables, on the other hand, effectively rules out a future multi-threaded version of FairRoot. Instead, the GSI FAIR experiments are considering moving to a new, concurrent and distributed framework, ALFA [255], which will presumably be in the upgrade path of FairRoot. This option may or may not materialize in time for SoLID. ALFA could also form the basis of an extension of SoLID software to distributed computing.

We are in the process of prototyping and testing simulation and analysis routines with several frameworks to gain experience with the frameworks' relative benefits. A decision as to which framework to adopt for SoLID, if any, will be made at an appropriate time.

An estimate of the manpower required for implementing the complete SoLID simulation and reconstruction software can be found in Appendix C.

## 12.2 Simulation

### 12.2.1 Simulation Software

Development of the SoLID spectrometer requires the detailed evaluation of different solenoidal fields, optics from those fields, backgrounds from multiple sources, possible detector and baffle

geometries, detector responses, and tracking. Overall, a figure-of-merit must be calculated for different configurations for quantitative comparison. It is also necessary that such simulations be done in a coherent fashion and validated as well as possible. Because details of the design have not been finalized, it must also be flexible enough to be quickly adapted to different configurations.

Initial simulations for SoLID were done using a combination of GEANT3 and COMGEANT. However, these are FORTRAN based and GEANT3 is no longer actively maintained. The decision was made to offer a modern design based on Geant4 [257] to handle particle propagation and interactions. This is a well-supported framework and offers a variety of physics packages, such as simulation of low-energy electromagnetic backgrounds. However, the detector geometries, how magnetic field maps are specified, input parameters, and output formats must all be developed on top of this framework. Because this is being done with a new simulation package, it is necessary to also compare and reconcile the output between GEANT3 and Geant4.

To accomplish all these goals, we have adopted a simulation suite, GEMC, which was successfully developed and employed for similar CLAS12 simulations [258]. It utilizes Geant4 and includes facilities for external event generators, output to a compact style similar to that utilized by JLab data acquisition systems, and a flexible framework to specify arbitrary detector geometries. A framework for specifying sensitive detectors, processing particle hits, and generating output is also included. The geometry and sensitive detector types are read in at run time allowing for easy modification of designs. Advanced visualization abilities are available, which provides a useful debugging tool.

As described in Sec. 4, magnetic field maps for GEMC can be produced using the Poisson Superfish package [259] developed at LANL or TOSCA [260]. The POISSON package allows for the calculation of azimuthally symmetric magnetic fields (relevant for the solenoidal spectrometer). Because both the optics and the fields in the detector regions are relevant, accurate optimization of the iron yoke is important. More detailed field maps produced by TOSCA will be used for the next stage of design.

The overall software design is based on a modular philosophy which is general enough to allow many different software components to interact with each other. This needs to encompass ideas such as external event generators, ROOT analysis scripts, raw hit digitization, and tracking analysis. A schematic is given in Fig. 124. Detailed discussions of the individual components follow in later subsections and Sec. 12.1.

GEMC and generally Geant4 provide the predominant simulation component in modeling secondary physics processes (such as multiple scattering) and propagation through a magnetic field. Physics generators provide information on the initial particle type, position, and momentum to the simulation for each event and are described in Sec. 12.2.3. These can take more than one form and we allow for general text file input and internal generators within GEMC. Magnetic field maps are described over a grid using text files. GEMC allows for various coordinate systems to be used in the grids and handles all interpolation and lookup.

Detector Description including geometries and materials are defined in a tabular structure which can be store in text files or SQL database. GEMC is built as a library and linked to a code called "solid\_gemc" to have detector responses and output file formats customized for SoLID simulation. This gives access to all of the functionality within GEMC, but allows us to modify and add components as we need them.

Output from GEMC is through EVIO, which is a binary format developed at Jefferson Lab. Libraries are available to provide decoding. These files can be converted to ROOT files through available tools or used by higher level analysis packages, such as the detector digitization.

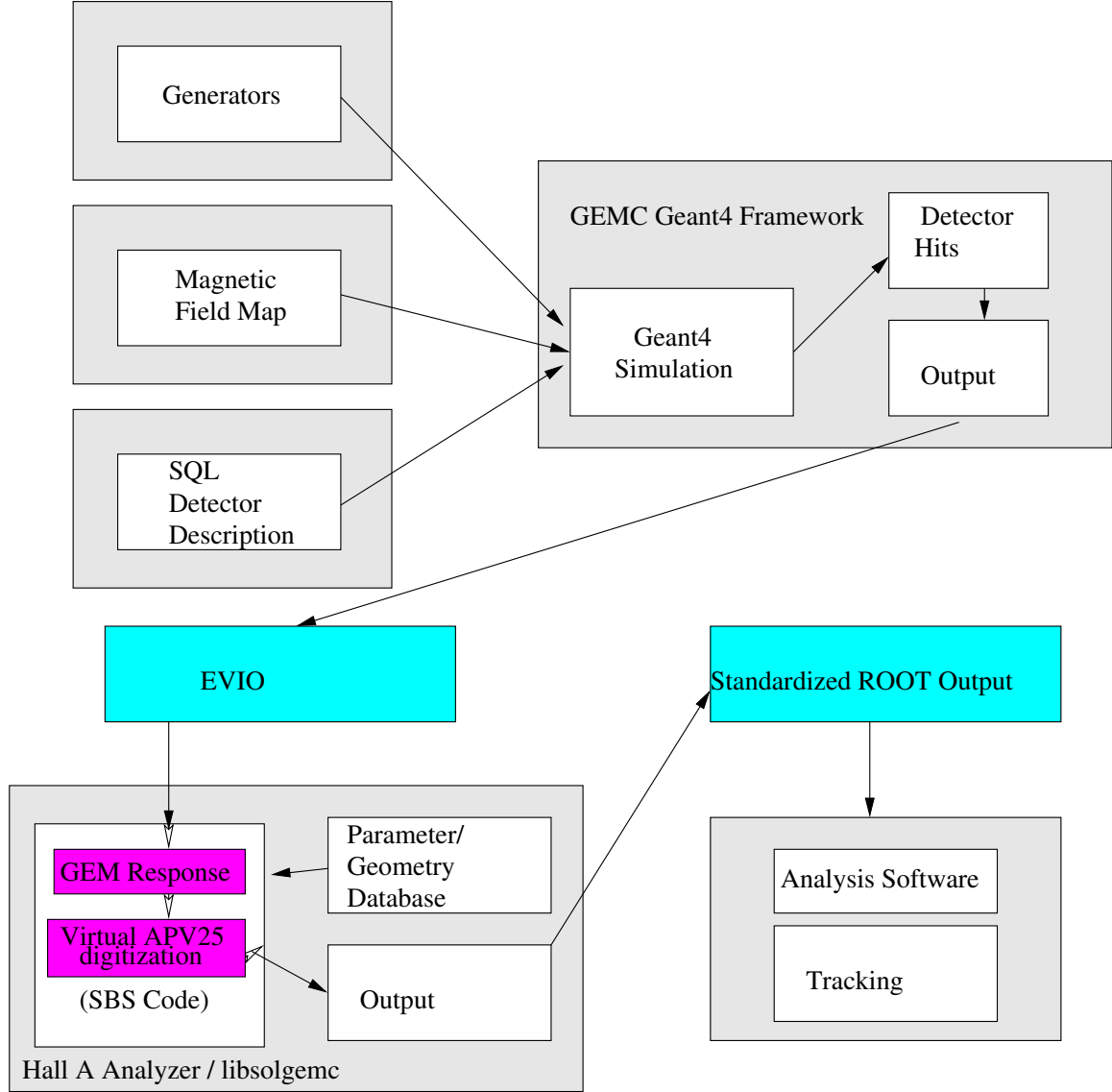


Figure 124: Schematic of the simulation and software framework.

### 12.2.2 Simulation Status

Significant progress has been made with the SoLID simulation, which has allowed realistic performance studies of the core measurements and other important issues. The SoLID simulation has been taking advantage of the new GEMC development. The simulation of each individual subsystem has been developed by different groups using the same framework, and then all subsystems are combined into the whole SoLID simulation without any code change at run time. We can also choose to turn off a subsystem or replace it with a different version in the whole simulation for testing. The entire code, including the production and development version, is kept in a version control system.

The materials in non-detector subsystems have been implemented. Detector subsystems have materials and responses tailored to themselves. In addition to studies done by different groups for subsystems, we also produce the whole simulation output for various overall studies of characteristics such as acceptance, background rates and trigger performance to ensure consistent results.

The simulation output is stored in ROOT trees. Each detector has a standalone tree, and different trees are linked by the same tree index for one event. Then each tree is analyzed by a standalone ROOT script. Combining the set of ROOT scripts, we can analyze all SoLID sub-detectors and perform the overall studies mentioned above.

In general, the SoLID simulation is an effort which will last the entire SoLID lifetime. We are still at its early stage. The simulation code will evolve with the Geant4 and GEMC development. SoLID's detector and engineering design will also evolve and they can be easily transferred into the simulation by a CAD model. Detector prototyping and tests will give direct input to the simulations and in turn improve the overall SoLID design.

The SoLID collaboration may adopt the *art* event-processing framework as its software framework. *art* currently uses generic Geant4 as its simulation engine and allows a flexible middle layer. We are exploring the possibility of using GEMC for the simulation layer of *art*.

### 12.2.3 Physics Event Generators

Beyond the physics included in Geant4, several generators have been implemented to study specific processes. The interface between the generator and GEMC is the LUND format (or an extension of it), which is a text-based file containing event-by-event information of the initial particle configuration. These generators allow for an extended target and randomly sampled position to simulate a fast-rastering system. The generators implemented presently are

- Deep inelastic scattering cross sections from the CTEQ6 parton distribution fits [262].
- Charged and neutral pion production based on empirical fits to SLAC data [263] using the Weizsäcker-Williams approximation.
- Charged and neutral pion production based on the modified Hall D background generator
- Elastic scattering from protons and neutrons based on dipole parameterizations.

The modified Hall D background generator gives better pion background results matching existing data. The original Hall D photo-production generator uses various experimental data to generate photo-production cross sections on a proton target for photon energies below 3 GeV [266, 267]. It uses a modified version of PYTHIA to generate cross sections of photo-production for photon energies above 3 GeV [266, 267]. The Hall D generator is only a photo-production event generator. SoLID requires an electro-production generator. Hadron production in electron scattering on a nucleon target can originate either from real bremsstrahlung photons radiated in the target or from the interaction of the virtual photon with the nucleons. The virtual contribution is calculated in the Equivalent Photon Approximation [268]. The bremsstrahlung contribution is implemented following PDG-2012 [269, 270]. A more detailed overview of the hadron generators used for SoLID simulation is available from [265].

Additional generators are planned, which includes extending the present generators to include initial radiative and multiple-scattering effects. Additionally, self-analyzing hyperon decay processes are a potential systematic and must be evaluated as well. Background rates for processes included in Geant4 can be evaluated by simulating sufficient numbers of individual electrons passing through the target.

### 12.2.4 GEM Digitization

GEM digitization is a crucial aspect in evaluating hit tracking under realistic conditions. The method implemented is based on an approach by the Super-BigBite collaboration, which takes the individual ionization events in the GEM drift region, and produces a charge signal across several readout strips based on a realistic model with parameters tuned to real data.

A track passing through a GEM in Geant4 will record energy deposition events caused by ionization which are then amplified through the GEM foils, resulting in a detectable signal over several readout strips, Fig. 125. Within the simulation, the individual ionization events are written into the output and are post-processed through an independent library built upon the Hall A analyzer analysis software [252]. The digitization and track reconstruction can then be developed within a single framework similar to what could be used for analysis of real data.

A full description of the digitization process can be found in Ref [273]. To summarize, from the individual ionization hits, an average number of hole/electron pairs are determined by sampling a Poisson distribution based on the ionization energy  $W$ , such that  $n_{\text{ion}} = \Delta E/W$ . The physical spread of the resulting charge cloud is described by a simple diffusion model assuming a constant drift velocity, where the Gaussian width of the cloud is given by

$$\sigma_s(t) = \sqrt{2Dt} \quad (13)$$

where  $D$  is the diffusion constant and  $t$  is the time from ionization. Variation in the amplification of the GEM signal is described by a Furry distribution

$$f_{\text{Furry}} = \frac{1}{\bar{n}} \exp\left(-\frac{n}{\bar{n}}\right) \quad (14)$$

where  $\bar{n}$  is the average number of ionization pairs. The previous formalism provides a realistic (unnormalized) charge distribution over an area which can then be associated with a set of GEM readout strips.

The final component of the digitization is to reproduce the time-shaping of the electronics components. For this application, we have assumed the use of APV25 electronics developed at CERN (see Sec. 7). The time-dependent digitized signal  $S(t)$  is produced by convoluting the charge signal with the form

$$S(t) = A \frac{t}{T_p} \exp(-t/T_p) \quad (15)$$

which provides a good parameterization of real data, Fig. 126. The parameters are chosen to represent real data and the time constant  $T_p$  is roughly 50 ns, providing a full-width half-max of about 100 ns.

The advantage to using such a shaping signal is that three samples can be used to deconvolute the longer, shaped signal to suppress out-of-time background hits. Assuming the form given in Eq. 15, the signal in time sample  $k$  is given by

$$s_k = w_1 v_k + w_2 v_{k-1} + w_3 v_{k-2} \quad (16)$$

where weights  $w_i$  are proportional to

$$w_1 \sim e^x/x, w_2 \sim 2/x, w_3 \sim e^{-x}/x. \quad (17)$$

To obtain a more reliable result from the track reconstruction, it is crucial to simulate the responses of GEM detectors and related electronics to a highly realistic level. Such an effort was

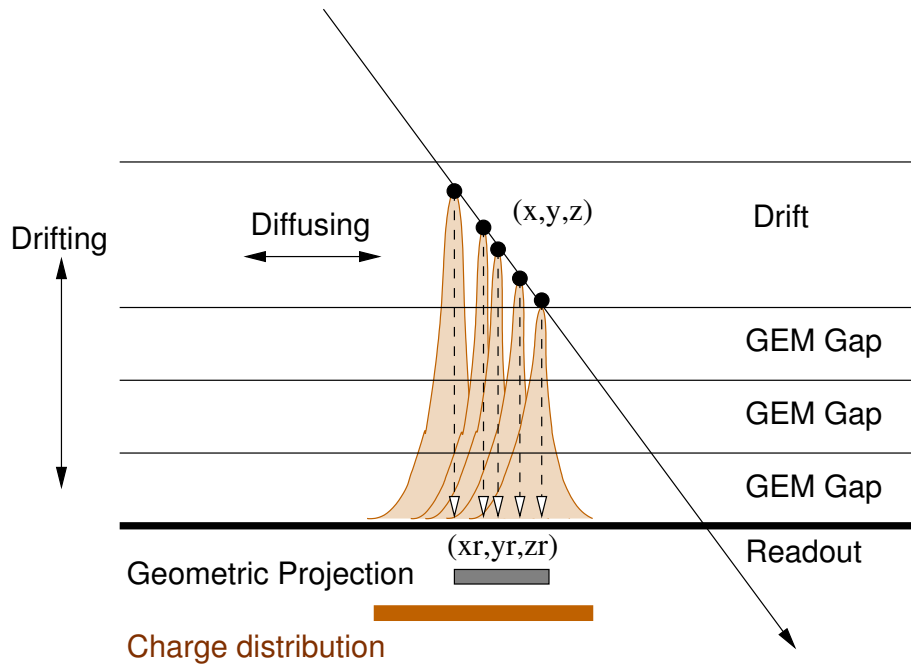


Figure 125: Diagram of the concept behind GEMs using electron avalanching and detection through a set of readout strips.

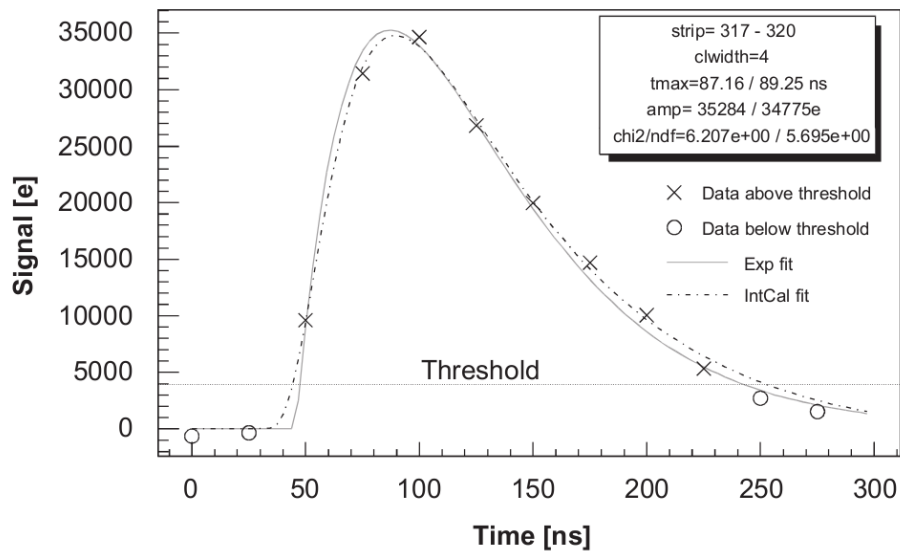


Figure 126: Representation of the signal vs. time response for an APV25 module.



PVDIS GEM occupancies			
Plane	Total strip number (u+v) per sector	Raw Occupancy (%)	Noise filtered Occupancy (%)
1	1156	21.17	9.97
2	1374	10.35	5.11
3	1374	8.81	4.42
4	2287	3.07	1.64
5	2350	2.79	1.50

Table 18: PVDIS GEM average occupancies with LD2 target estimated by digitizing its whole simulation data. The raw occupancy with only pedestal cut and the noise filtered occupancy with 3 samples are shown.

SIDIS $^3\text{He}$ GEM occupancies		
Plane	Total strip number (u+v) per sector	Raw Occupancy (%)
1	906	2.37
2	1020	7.98
3	1166	3.40
4	1404	2.24
5	1040	2.03
6	1280	1.52

Table 19: SIDIS  $^3\text{He}$  GEM average occupancies estimated by digitizing its whole simulation data. The raw occupancy with only pedestal cut is shown, Because only 1 sample is used, there is no noise filtering from multiple samples.

recently carried out, based on the existing SoLID GEM digitization program, by comparing simulated results with actual GEM detector experimental data from beam tests and highly ionizing x-ray test at UVa. The digitization parameters were fine tuned based on this study to work for both highly ionizing low energy photon signals and for MIP signals. This is critical for a reliable simulation of SoLID conditions as much of the background hits in SoLID GEM detectors are due to low energy photons.

By using the tuned digitization code, we digitized the whole simulation for PVDIS setup with LD2 target, SIDIS setup with  $^3\text{H}$  target, and the  $J/\phi$  setup with LH2 target. The same set of simulation data are used for acceptance and trigger study including all detector response. The GEM geometry and material are modeled carefully in simulation the according to the latest design and prototype. The things missing are dead areas by spacers and frames, and the possible overlap over different sectors, which we plan to add in the next round of simulation. Both the simulation and our test have shown that the dominant GEM background is caused by low energy photons which have only a few percents probability to deposition energy and fire GEM, but a huge rate. The occupancy is obtained as the average number of readout strips fired within 275 ns time window divided by total number of strips in the readout plane in one of 30 sectors. Both u and v strips are counted. The results are shown in Table 18, 19 and 20. The noise filtering from 3 samples is applied where it's available.



$J/\psi$ GEM occupancies			
Plane	Total strip number (u+v) per sector	Raw Occupancy (%)	Noise filtered Occupancy (%)
1	906	7.68	4.65
2	1020	14.4	9.28
3	1166	8.82	5.49
4	1404	7.00	4.30
5	1040	5.92	3.78
6	1280	4.58	2.95

Table 20:  $J/\psi$  GEM average occupancies estimated by digitizing its whole simulation data. The raw occupancy with only pedestal cut and the noise filtered occupancy with 3 samples are shown.

## 12.3 Reconstruction

### 12.3.1 Tracking

SoLID track reconstruction requires an accurate and efficient track finder able to identify signal tracks in a high-noise environment and sufficiently fast for the level-3 trigger. In addition, an accurate and robust track fitter is required in order to optimize the resolutions for the vertex variables and other track-related variables.

In order to satisfy the requirements, a Kalman Filter (KF)-based track finding and track fitting algorithm is being developed and tested with digitized GEM simulation data. A Kalman Filter is a recursive fitting algorithm [271]. In contrast to the well-known least-squares fit that provides only one set of parameters after fitting, the track parameters of the KF can evolve along the trajectory. There are three basic steps for the KF. First, it predicts the measurement on the next measurement site by propagating the current track parameters. Second, the covariance matrices of current track parameters are propagated along the trajectory. And last, it filters the next measurement in order to improve the track parameters at the next measurement site. The local field information and errors due to multiple scattering can be collected during the first two steps of the algorithm. Thus, given that particle tracks in the SoLID detector will cross both fringe and uniform field regions, it is expected to perform better than other algorithms that explicitly require a globally uniform magnetic field.

The KF can be easily extended into acting as a track finder as well, achieving concurrent track finding and fitting. This is done by adding two steps to the standard KF algorithm. First, an algorithm is needed to search for seeds, which are track segments that provide initial estimated track parameters. These seeds are used to initialize the KF. Second, a set of arbitration rules need to be applied before filtering to identify hits belonging to the track. A straightforward rule is to require that the hit on the next measurement site fall within a window around the prediction. An alternative rule is to cut on the  $\chi^2$  increment when a candidate hit is added [272].

The whole simulation including all SoLID subsystems in their different respective configurations is used for the tracking studies. Both signal tracks from various event generators and background produced by low energy particles, mostly photons, are included in the simulation data.

At present, the track finding algorithm is being developed and tested for the different SoLID configurations. For the SIDIS  $^3\text{He}$  configuration, using only one time-sample from the APV25 and GEM digitization, both the efficiency of the track finder and the probability of identifying all correct hits of a track typically exceeds 90% for electron tracks in both the forward angle and the large angle regions. For the PVDIS and  $J/\psi$  configurations, using three time-samples from the

APV25 and GEM digitization, the efficiency is about 85% for electron tracks. The track finder also achieves a reasonable execution speed. We will study the possibility of using the current track finding algorithm with looser conditions to improve the reconstruction speed for the planned level-3 data reduction farm.

The track fitting algorithm is also being developed and tested for different SoLID configurations. The kinematic dependence of the reconstruction resolution of the track parameters for the SIDIS  $^3\text{He}$  configuration is shown in Figure 127 as an example. Resolution values averaged over the kinematic ranges, obtained for the SIDIS  $^3\text{He}$  and PVDIS configurations, are summarized in Table 21.  $J/\psi$  results are similar to SIDIS  $^3\text{He}$  results. In these studies, energy loss is included for all materials, except for materials in the dead areas of the GEM planes. Low energy photon background in the GEMs is also not included. Both of them could worsen the resolution. To make our current results conservative, we multiply all values by a safety factor of 1.5 when applying them to various physics studies. We will update the results with all effects included in near future.

All SoLID physics programs are using these track resolutions in their studies by directly applying the full kinematic dependent results.

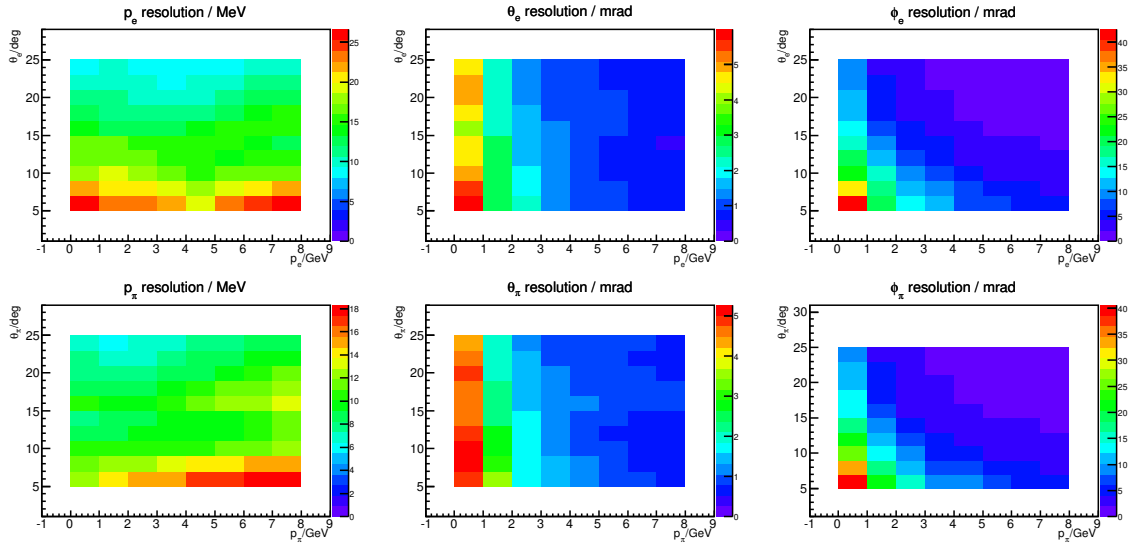


Figure 127: SIDIS  $^3\text{He}$  resolutions by track fitting studies with most of material energy loss and without background. The upper panels are the resolution of the electron kinematics. The lower panels are those of the pion kinematics. The variables are defined in lab frame with beam line as the  $z$ -axis.

	$\theta$ angle (mrad)	$\phi$ angle (mrad)	Vertex $z$ (cm)	$p$ (%)
SIDIS $^3\text{He}$ fwd angle ( $e$ )	1.3	5.7	0.9	1.7
SIDIS $^3\text{He}$ fwd angle ( $\pi$ )	1.2	5.2	0.9	1.1
SIDIS $^3\text{He}$ large angle ( $e$ )	1.0	1.7	0.5	1.2
PVDIS ( $e$ )	0.8	1.7	0.3	1.2

Table 21: Averaged resolutions by track fitting with most of material energy loss and without background

### 12.3.2 Additional Reconstruction Algorithms

Many existing detector reconstruction algorithms available in the Hall A analyzer [252] or in other packages should be reusable for SoLID, for instance the Cherenkov photoelectron yield analysis and the calorimeter clustering algorithm. While the basic physics algorithms can be adopted without much change, code will have to be developed to support the cylindrical geometry of SoLID as well as the individual local detector geometries. Furthermore, a likelihood-based particle identification scheme or similar should be written. Development of calibration software tuned to the SoLID detectors will be necessary as well.

A high-level overview of the necessary algorithm development tasks can be found in Appendix C, specifically in the spreadsheet referenced in that section [347].

## 13 Integration and Expected Performance

### 13.1 Overview

System integration incorporates several tasks : 1) Quality control of the engineering of the apparatus so that all the pieces fit and so that the system satisfies *all* of the experimental program with minimal turnover between experiments; 2) Integration of the detectors so that they work together and form efficient triggers, and so that we can predict the combined PID performance; 3) Control of calibrations and systematic errors; and 4) Commissioning plans.

In a preliminary engineering study done at Argonne National Lab by Paul Reimer, scenarios for assembling and disassembling of the apparatus have been developed which allow for switching rapidly between PVDIS and SIDIS, as well as for allowing other experiments to share Hall A during the SoLID running era. We believe we can switch between running setups in approximately three months.

For the second topic, we have made a study of the combined particle ID using the gas Cherenkov and the calorimeters, see Figure 128 where the resulting  $\pi/e$  ratios are shown. A similar PID performance was achieved by the Hermes spectrometer [274]. Our study was performed by using the pion rejection factor and electron efficiency as a function of the scattered angle and momentum for both detectors for both the PVDIS and SIDIS configurations based on Geant simulations of the current detector designs. The results here, shown for PVDIS, are preliminary since the detector designs and the analysis strategies are still evolving. Nevertheless, the preliminary results are encouraging and show that we can likely meet the requirements for the error in the pion contamination, which is  $10^{-3}$  for entire experimental program. We believe it may be possible to combine some information with the shower shape in a multi-variable analysis to further improve the pion rejection. We are also still considering the issues of rate dependence and pileup on the pion rejection factor.

In the following sections, we will present the study of the acceptance, efficiency, systematics, and calibration for various experiments.

### 13.2 SIDIS Program

The acceptance and efficiencies of the SIDIS configuration with a 40 cm long polarized  $^3\text{He}$  target was studied using the whole simulation. The particles detected by the detectors were compared to those of the original particles from a full-length target. We have good electron detection efficiency from all sub-detectors. They vary slightly across the phase space and the average efficiency values are shown in Table 22. The acceptance is  $\sim 0.7$  due to the two target window collimators. Figure 129 shows the combined effect of acceptance and efficiency (except tracking). We will continue to fine-tune the design and the reconstruction algorithm to improve the efficiency.

Table 22: Average electron detection efficiencies of all SoLID sub-detectors and the total SoLID efficiency.

Detector	EC	Cerenkov	Scintillator pad and MRPC	GEM tracking	Total
average efficiency	95%	95%	98%	90%	80%

We have conducted a careful study of the systematic uncertainties of the SIDIS experiments and the results are presented below.

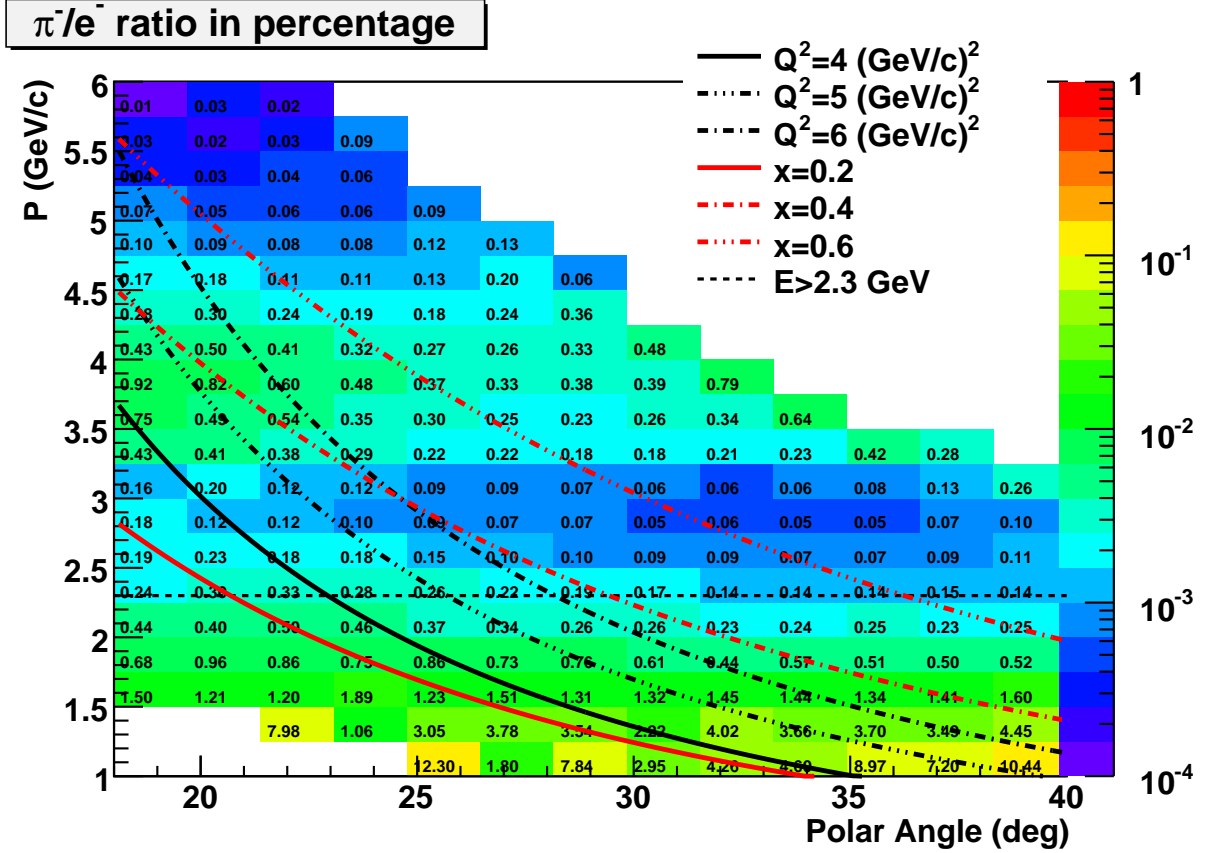


Figure 128: The  $\pi^-/e^-$  ratio from combined Cherenkov and Calorimeter detector performance as a function of the scattered momentum  $P$  and polar angle  $\theta$ . The numerical values are the ratios corresponding to that cell in  $(P, \theta)$ . The curves indicate various regions of  $Q^2$   $x$  or scattered energy  $E$ .

The SIDIS cross section is in general expressed as [275]

$$\frac{d\sigma}{dx dy dz dP_{h\perp}^2 d\phi_h d\phi_S} = \frac{\alpha^2}{xyQ^2} \frac{y^2}{2(1-\varepsilon)} \left(1 + \frac{\gamma^2}{2x}\right) [F_{UU}(x, z, Q^2, P_{h\perp}) + \text{asymmetric terms}]. \quad (18)$$

In the simulation, we model the SIDIS cross section by assuming factorization to express the structure function as a convolution of TMD distribution and fragmentation functions

$$F_{UU}(x, z, Q^2, P_{h\perp}) = x \sum_a e_a^2 \int d^2k_\perp d^2p_\perp \delta^{(2)}(P_{h\perp} - p_\perp - zk_\perp) f_1^a(x, k_\perp) D_1^a(z, p_\perp). \quad (19)$$

The unpolarized TMD distribution function  $f_1(x, k_\perp)$  and fragmentation function  $D_1(z, p_\perp)$  are parameterized as

$$f_1(x, k_\perp) = f_1(x, Q^2) \frac{e^{-k_\perp^2/\langle k_\perp^2 \rangle}}{\pi \langle k_\perp^2 \rangle}, \quad (20)$$

$$D_1(z, p_\perp) = D_1(z, Q^2) \frac{e^{-p_\perp^2/\langle p_\perp^2 \rangle}}{\pi \langle p_\perp^2 \rangle}, \quad (21)$$

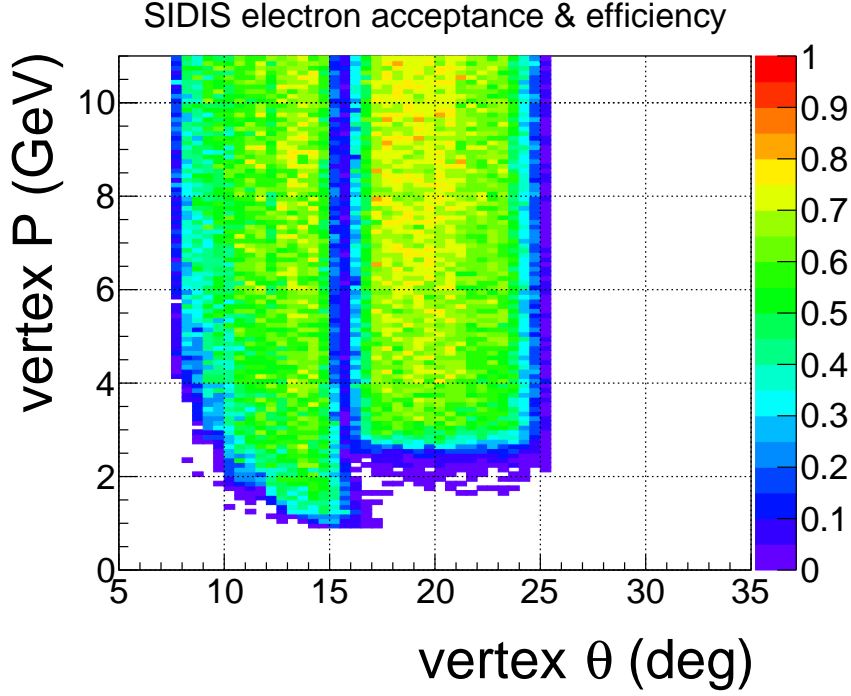


Figure 129: Electron acceptance and efficiency (except tracking) of SoLID SIDIS with the 40 cm  $^3\text{He}$  target and two target window collimators. The result for  $J/\psi$  has a similar shape, but higher values because it has a 15 cm long target and no collimator.

where  $f_1(x, Q^2)$  and  $D_1(z, Q^2)$  are collinear distribution and fragmentation functions. In our simulation, we use CT14 leading order collinear PDF parameterization [276] and DSS leading order collinear FF parameterization [277]. The two parameters describing the transverse momentum dependence are chosen as  $\langle k_\perp^2 \rangle = 0.25$  and  $\langle p_\perp^2 \rangle = 0.20$  [278]. For the three leading twist single spin asymmetry (SSA) terms, the Sivers, the Collins, and the pretzelosity, we use the phenomenological models [279–281] as inputs to the simulation. To take into account the detector efficiency effect, we use 85% of the statistics for the estimation of the uncertainties.

Taking the advantage of the  $2\pi$  azimuthal coverage, we are able to reduce the systematic uncertainties associated with luminosity and detection efficiencies by defining the target single spin asymmetry as

$$A_{UT}(\phi_h, \phi_S) = \frac{2}{P_1 + P_2} \frac{\sqrt{N_1(\phi_h, \phi_S)N_2(\phi_h, \phi_S + \pi)} - \sqrt{N_1(\phi_h, \phi_S + \pi)N_2(\phi_h, \phi_S)}}{\sqrt{N_1(\phi_h, \phi_S)N_2(\phi_h, \phi_S + \pi)} + \sqrt{N_1(\phi_h, \phi_S + \pi)N_2(\phi_h, \phi_S)}}, \quad (22)$$

where the subscripts 1, 2 represents a target spin flip pair.  $N_1(\phi_h, \phi_S)$  and  $N_1(\phi_h, \phi_S + \pi)$  are taken at the same time with target polarization  $P_1$ , while  $N_2(\phi_h, \phi_S)$  and  $N_2(\phi_h, \phi_S + \pi)$  are taken at the same time with target polarization  $P_2$ . Thus, the luminosity at different times will cancel. Since  $N_1(\phi_h, \phi_S)$  and  $N_2(\phi_h, \phi_S + \pi)$ ,  $N_1(\phi_h, \phi_S + \pi)$  and  $N_2(\phi_h, \phi_S)$  are taken in the same detector region, the acceptance and detector efficiency will also cancel to first order. The time-dependent detector efficiencies will be monitored with single electron and pion rates. With a  $^3\text{He}$  target spin flip rate of 1/(10 minutes) (20 minutes for each pair), we expect to control the time-dependent detector efficiency uncertainty to better than 1%. In 48 days with 11 GeV beam,

we will have 3456 pairs, and in 21 days with 8.8 GeV beam, we will have 1512 pairs. Then, the systematic uncertainty of the raw asymmetry is estimated as  $1.0\%/\sqrt{3456} = 1.7 \times 10^{-4}$  for 11 GeV data, and  $1.0\%/\sqrt{1512} = 2.6 \times 10^{-4}$  for 8.8 GeV data. With a proton (ammonia) target spin flip rate of 1/hour (2 hours for each pair), we expect to control the time-dependent detector efficiency uncertainty to under 2%. In 55 days with 11 GeV beam, we will have 660 pairs giving an estimated systematic uncertainty of  $2.0\%/\sqrt{660} = 7.8 \times 10^{-4}$ . In 27.5 days with 8.8 GeV beam, will have 330 pairs, and the systematic uncertainty is estimated as  $2.0\%/\sqrt{330} = 1.1 \times 10^{-3}$ . The derived absolute systematic uncertainties of the SSA data associated with the raw asymmetry are obtained by dividing these numbers by the target polarization and the dilution factor in each bin.

The knowledge of the target polarization is at the 3% level. This translates to a 3% relative systematic uncertainty of the SSA data. The knowledge of the target polarization direction is about 0.2 degree. The corresponding uncertainty of the target polar angle translates into  $6 \times 10^{-6}$  relative uncertainty of the SSA. The uncertainty of the target azimuthal angle is included in the uncertainty of the azimuthal angle  $\phi_S$  together with the detector resolution effect.

The systematic uncertainties associated with detector resolutions are estimated based on the track fitting studies. The resolutions of the kinematic variables in the Trento convention for each bin are obtained by Monte Carlo sampling according to the resolutions of the lab frame variables shown in Figure 127. The resolutions of the kinematical variables in the Trento convention are summarized in Table 23. The systematic uncertainty associated with the resolution mostly come from the uncertainties of the azimuthal angles  $\phi_h$  and  $\phi_S$  which affect the separation of the SSA terms. It is estimated by smearing the pseudo-data according to the resolution, separating the SSA term with the smeared pseudo-data, and then comparing them to the model input of the simulation. The absolute systematic uncertainty of the SSA due to the resolution is less than  $1 \times 10^{-4}$ , which is negligible compared to the other uncertainties.

$E_{\text{beam}} (\text{GeV})$	$x$	$z$	$Q^2 (\text{GeV}^2)$	$P_{h\perp} (\text{GeV})$	$\phi_h (\text{rad})$	$\phi_S (\text{rad})$
11	0.002	0.003	0.02	0.006	0.015	0.006
8.8	0.002	0.004	0.02	0.006	0.018	0.006

Table 23: Resolution of kinematical variables (in the Trento convention) with the  $^3\text{He}$  target setup.

Nuclear effects contribute to the systematic uncertainty when we extract the SSA of the neutron from  $^3\text{He}$  data. We derive the SSA of the neutron from that of  $^3\text{He}$  as

$$A_n = \frac{A_{^3\text{He}} - 2P_p f_p A_p}{P_n f_n}, \quad (23)$$

where the SSA of proton  $A_p$  will also be measured with SoLID in the same kinematic region. We assign 10% relative uncertainty of the knowledge of the proton SSA. The  $f_{p/n}$  are the dilution factors associated with the hydrogen and the  $^3\text{He}$  target, respectively. The light-front spectral function of  $^3\text{He}$  including the final state interaction effect was recently developed [282]. With a theoretical calculation of the nuclear effect of the SSAs in the SoLID kinematic region [283], we estimate that the relative uncertainty in the extraction of the neutron SSAs due to the nuclear effect is about 4~5%.

The random coincidence background is estimated using single electron and single pion rates. By assuming a 1 ns time resolution, we choose a plus-minus three-sigma time window of 6 ns. For the  $^3\text{He}$  target, we also apply a three-sigma vertex cut according to the track fitting results. As the SIDIS signal rate drops with increasing  $P_{h\perp}$ , we summarize the signal background ratio with

respect to  $P_{h\perp}$  in Table 24. The relative systematic uncertainties due to the random coincidence background are estimated by varying the background rate by 20% for each bin.

$P_{h\perp}$ (GeV/c)	[0.0, 0.2]	[0.2, 0.4]	[0.4, 0.6]	[0.6, 0.8]	[0.8, 1.0]	[1.0, 1.2]
11 GeV beam ( $\pi^+$ )	110	160	150	105	75	40
11 GeV beam ( $\pi^-$ )	120	160	140	90	70	50
8.8 GeV beam ( $\pi^+$ )	75	95	80	50	45	
8.8 GeV beam ( $\pi^-$ )	65	95	75	50	45	

Table 24: The ratio of SIDIS signal and random coincidence background within 6 ns. These values are estimated with the  $^3\text{He}$  target. Similar results are obtained for the proton target.

The radiative correction effect of SIDIS is simulated with HAPRAD, which was developed based on the QED calculation to one-loop level [284, 285]. The systematic uncertainties from the radiative corrections are estimated by varying the model parameters  $\langle k_{\perp}^2 \rangle$  and  $\langle p_{\perp}^2 \rangle$  of the SIDIS model in our simulation by a factor of 2 (multiplied and divided). This gives relative uncertainties of about 2.5% for the 11 GeV data and about 2% for the 8.8 GeV data. A summary of the systematic uncertainties is in table 25.

Table 25: The systematic uncertainties on the asymmetry measurements of SIDIS.

Systematic (abs.)		Systematic (rel.)	
Raw asymmetry	0.0014	Target polarization	3%
Detector resolution	< 0.0001	Nuclear effect	(4 – 5)%
		Random coincidence	0.2%
		Radiative correction	(2 – 3)%
		Diffraction meson	3%
Total	0.0014	Total	(6 – 7)%

### 13.3 PVDIS Program

#### 13.3.1 Acceptances, efficiencies, and systematic uncertainties for PVDIS

We now have a full Monte Carlo simulation that includes all elements of the PVDIS apparatus, layer by layer energy deposition in the electromagnetic calorimeter (EC) and optical physics in the light gas Cherenkov (LGC). At present we have preliminary GEM responses and tracking under realistic backgrounds, both of which are under continued development. We now also have recent data from newly constructed GEMs which are being employed at Jefferson Lab to refine our simulations. For the present results, true values of track hit positions in the GEMs are used. Neither the GEMs nor the calorimeter are segmented in the simulation. However, since the GEM sector boundaries will be far from the baffle-defined signal regions and the tracks entering the EC will not be parallel to the module boundaries, the effects of GEM and EC segmentation on our acceptance are expected to be negligible.

Input events to the Monte Carlo are electrons from a DIS generator using cross sections from CTEQ6 parton distribution fits [286]. Our analysis integrates primary electrons which reach the active area of the EC after passing through the active areas of all five GEMs and the front window of the LGC. The acceptance is shown in Figure 130 as a function of  $p$  and  $\theta$  (left panel) and as a



function of  $Q^2$  and  $x_{bj}$  (right panel). Lines on these plots show the boundaries of the kinematic region of interest:  $Q^2 > 6 \text{ GeV}^2$ ,  $W > 2 \text{ GeV}$ , and  $x_{bj} > 0.55$ . Our acceptance in this region is typically 40%.

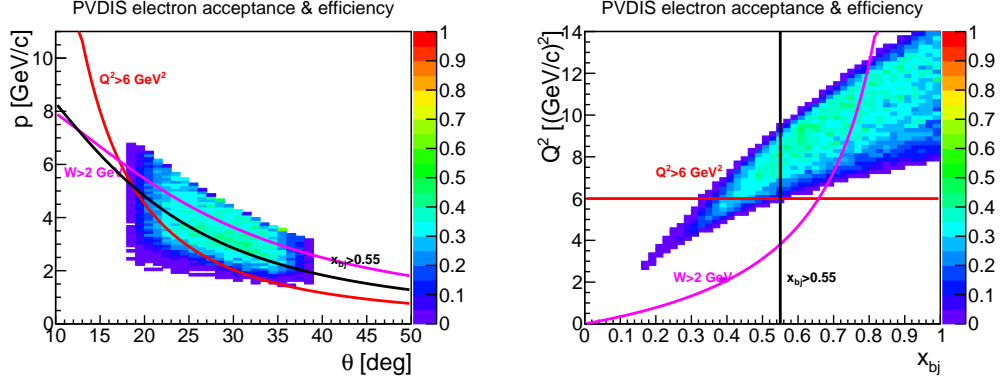


Figure 130: Left: PVDIS acceptance and efficiency as a function of  $p$  and  $\theta$ . Right: PVDIS acceptance and efficiency as a function of  $Q^2$  and  $x_{bj}$ . Curves show bounds of the kinematic range with  $Q^2 > 6 \text{ GeV}^2$ ,  $W > 2 \text{ GeV}$ , and  $x_{bj} > 0.55$ .

Contributions to the efficiency are as follows:

*Calorimeter:* Efficiency of  $\sim 95\%$  as reported in subsection 10.7.

*LGC:* With the changes of the radiator gas and PMT quantum efficiency, new studies of the LGC efficiency need to be undertaken. Requiring  $\geq 2$  photoelectrons in each of  $\geq 2$  PMTs in the sector matching the EC yields 96% efficiency.

*Tracking:* The GEM detection efficiency is 97% per plane. From our studies using a tree search algorithm with realistic and correlated superimposed backgrounds and our current model of digitization, a track finding efficiency of  $\sim 90\%$  appears to be achievable. Development of the track finding software is continuing.

Combining the above contributions yields an estimate of 82% for our overall efficiency.

The systematic errors on our measurement of the parity violating asymmetry are summarized in Table 26.

The systematic error on the polarization of the beam  $\Delta P/P$  is required to be better than 0.4% [287]. The best achievable precision of such measurements is 0.6% at present, but 0.4% are considered to be within reach [288]. The dominant systematic error in [287] is the laser polarization, which was estimated to be 0.3% but is given in [288] to be below 0.2%. The higher analyzing power and large-angle characteristics of the 11 GeV beam relative to the Qweak 1 GeV beam result in a better precision for SoLID. We also expect better to understand the systematic errors of the polarimetry by building on the experience of the MOLLER experiment, where polarimetry plays a particularly important role.

The radiative corrections are similar to those computed for the HERA experiments [289]. Many of the important radiative corrections come from tails of events at larger  $x$ , which are small for the SoLID high- $x$  kinematics. We have assembled a team including A. Aleksejevs, S. Barkanova and W. Melnitchouk, who will assist in performing the necessary calculations. We estimate an error of 0.2% from radiative corrections.

Finally, systematics on the asymmetry due to reconstruction errors, including DAQ issues and particle identification, will be kept to the 0.2% level. The pion contamination is expected to be

below 1% for most bins and the required corrections should be valid to at least 10% of that. Work on the DAQ is in progress to demonstrate that the pile-up and dead-time corrections can be kept to below 0.15%.

The total systematic error is 0.6%, unchanged from the proposal value, allowing sufficient sensitivity to meet our physics goals.

Polarimetry	0.4
$Q^2$	0.2
Radiative corrections	0.2
Reconstruction errors	0.2
Total	0.6

Table 26: Summary of PVDIS systematic errors, in percent.

### 13.3.2 Kinematics, Resolution and Calibration for PVDIS

In this section, we describe the general method of measuring the momentum  $p$  and the scattering angle  $\theta$  of each track. In addition, we discuss the resolution of  $x$ , and  $Q^2$ , the relevant variables for the analysis. Finally, we discuss the calibration of the average value of  $Q^2$ . The most critical requirements are the the  $x$  resolution is on the order of 0.01 to avoid kinematic smearing and that the average  $Q^2$ , which is proportional to the asymmetry, is calibrated to 0.1%.

The method that we use to reconstruct the tracks, determining the scattering angle and momentum, is easiest to understand in the approximation of a uniform field. Based on this method, we can explain our alignment tolerances and systematic errors. We then show how to make the corrections for the realistic case. These corrections do not alter most of the tolerances.

First, we look at the track in the  $x$ - $y$  plane. This is given in Figure 131. All we require is hits in two GEM detectors. The one closest to the target is labeled GEM<sub>*i*</sub> and the other is GEM<sub>*j*</sub>. Since the beam is small (300  $\mu\text{m}$  by 250 $\mu\text{m}$ ), it provides a third point which is sufficient to determine the radius of curvature  $\rho$  of the helix. The transverse momentum of the electron is then  $\kappa/\rho$ , where  $\kappa$  is a constant proportional to the magnetic field. The transverse distance between the beam and the first GEM is  $R$  and between the two GEM's is  $D$ . The angle between the line segments  $R$  and  $D$  is  $(\psi + \delta)/2$ . From the diagram, we have

$$\frac{1}{\rho} = \frac{2(\sin(\psi/2) + \sin(\delta/2))}{(R + D)} \approx \frac{\psi + \delta}{R + D}, \quad (24)$$

where the approximation is for small angles. Since

$$\frac{\sin(\psi/2)}{\sin(\delta/2)} = \frac{R}{D}$$

and  $(\psi + \delta)/2$  is measured, Eq. 24 can be evaluated exactly.

For the helix, the angle  $\theta$  between the trajectory and the  $z$ -direction is constant, and thus is the scattering angle. If  $\Delta z$  is the difference in the  $z$ -coordinates of the GEM's, then

$$\tan \theta = \frac{\rho}{\Delta z} \sin^{-1} \frac{D}{\rho} \approx \frac{D}{\Delta z}. \quad (25)$$

From the approximation, we see that the error in  $\rho$  contributes little to the error in  $\theta$ .

Finally, we note that

$$Q^2 = 4E \frac{\kappa}{\rho} \tan(\theta/2).$$

Thus the fractional error in  $Q^2$  is the sum in quadrature of the fractional errors in  $\rho$  and  $\theta$ .

Thus with two GEM points and a narrow beam, we can reconstruct the important variables for DIS. In addition, the distance  $r$  from the first GEM to the beam line in the  $x$ - $y$  plane and the azimuthal angle of the first GEM hit are measured. The first can be used to determine the  $z$ -coordinate of the interaction, which can be used as a check that the track is valid and also determine if it came from the front or rear target windows.

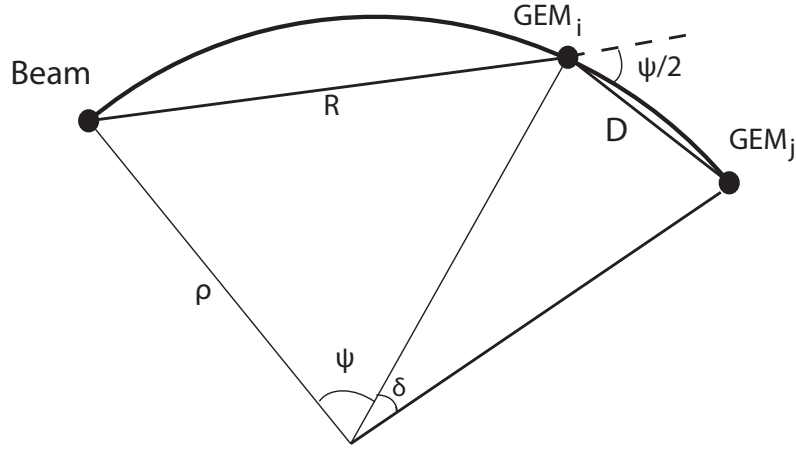


Figure 131: Projection of the track in the  $x - y$  plane. The projected radius of curvature is  $\rho$ .

For realistic magnetic fields, we generated with our Monte Carlo many trajectories and determined the discrepancies with Eqs. 24 and 25. These discrepancies could be parameterized in terms of the measured variables  $\psi + \delta$ ,  $D$ ,  $R$ , and  $r$  and used as corrections. With the corrections,  $\rho$  and  $\theta$  can be determined from the GEM hits with a precision better than 0.1%.

Rather than  $\psi + \delta$ , we used the angle  $\alpha$  between the line segment  $R$  and the line joining the beam with the hit in  $\text{GEM}_j$ . Then

$$\alpha \approx \frac{\psi + \delta}{2} \frac{D}{R + D},$$

and

$$\frac{1}{\rho} = \frac{2\alpha}{D}.$$

Thus our precise and realistic equation for  $\rho$  is

$$\frac{1}{\alpha\rho} = \frac{2}{D} + F_\rho(R, D, r, \Delta z). \quad (26)$$

An important feature is that the angle  $\alpha$  only appears in the left side. This feature is useful for our momentum calibration method shown below. For  $\theta$ ,

$$\tan \theta = \frac{D}{\Delta z} + F_\theta(R, D, r, \Delta z, \alpha). \quad (27)$$

There are two effects that contribute to  $F_\theta$ . The first is the approximation in Eq. 25. The second is the fact that radial components of the magnetic field change the angle that the trajectory makes with the  $z$ -axis. Thus  $F_\theta$  depends slightly on  $\alpha$ .

Since  $F_\rho$  and  $F_\theta$  are small, the errors in their arguments do not contribute significantly to the errors in  $\rho$  or  $\theta$ . The requirements for calibration can be obtained from the leading approximations.

The momentum resolution, which is dominated by multiple scattering, mostly in the air, is about 1%, independent of momentum. The angular resolution, dominated by GEM resolution, is about 0.5%. The resolution in  $Q^2$  is 1.5% and in  $x$  is 1%. The  $z$ -resolution is 7 mm. These numbers are obtained with our simulation with realistic GEM signals.

The first step in momentum calibration is alignment of the GEM trackers. To make estimates of the systematic errors in track momentum reconstruction we use artificial displacements of GEM hits in our simulation. In the simple case of a uniform field and a thin target the minimum distance between the beam axis and the line through two GEM hits is linearly related to  $1/p$ . That distance is of order 10 cm, implying a need to calibrate the GEM transverse positions to  $\sim 100 \mu\text{m}$  in order to achieve a systematic error on the relative momentum  $\Delta p/p$  of order  $10^{-3}$ .

For a more realistic estimate we use a Monte Carlo simulation incorporating a realistic field and a long target to study the effects on our momentum and angle reconstruction of all elementary displacements: lateral and transverse position shifts, and rotations in and perpendicular to the detector plane, of one or both GEMs. Results are shown in Table 27. Due to the symmetry of the apparatus,  $Q^2$  is insensitive to all these misalignments to first order except for single GEM angular displacement in-plane. We find that we need to understand transverse GEM positions relative to straight tracks to within about  $200 \mu\text{m}$ , and absolute positions parallel to the beam axis at the level of about 3 mm.

1/p and $\theta$ residuals for GEMs 1, 4					
transform	GEM(s)	$\delta p(\text{mean})$	$\delta p(\text{width})$	$\delta \theta(\text{mean})$	$\delta \theta(\text{width})$
transverse displacement	1, 4	-0.01%/mm	0.77%/mm	0.00%/mm	0.00%/mm
	4	0.00%/mm	0.76%/mm	0.00%/mm	0.08%/mm
longitudinal displacement	1, 4	0.05%/mm	0.00%/mm	0.00%/mm	0.00%/mm
	4	0.08%/mm	0.01%/mm	0.06%/mm	0.00%/mm
in-plane rotation	1, 4	0.00%/mrad	0.00%/mrad	0.00%/mm	0.00%/mm
	4	<b>1.61%/mrad</b>	0.15%/mrad	0.01%/mm	0.01%/mm
out-of-plane rotation	1, 4	0.00%/mrad	0.08%/mrad	0.00%/mm	0.03%/mm
	4	0.00%/mrad	0.09%/mrad	0.00%/mm	0.06%/mm

Table 27: Momentum and angle reconstruction sensitivities to various displacements of GEMs 1 and 4: transverse, longitudinal, and rotational (in and perpendicular to the detector plane) displacements of both GEMs or of GEM 4 only. “ $\delta p(\text{mean})$ ” and “ $\delta \theta(\text{mean})$ ” are the changes in the mean of the  $1/p$  and  $\theta$  residuals and “ $\delta p(\text{width})$ ” and “ $\delta \theta(\text{width})$ ” are the changes in those residuals’ width per unit displacement. Due to detector symmetry, the displacement to which we are most sensitive is single GEM in-plane rotation.

Within a GEM, strip positions relative to one another will be known to within  $25 \mu\text{m}$ . With standard surveys, relative strip positions within a full GEM plane can be established to better than  $500 \mu\text{m}$ . To achieve our resolution goal and to monitor possible motion of the tracking chambers, straight-through electrons with the magnetic field off and low energy photons with the field off and on will be used to calibrate the relative transverse positions of the GEMs with the required precision. A thin carbon target about 10 cm upstream of the LD<sub>2</sub> target has lines of sight to most of the area of the GEMs, as shown in Figure 132. For x-ray studies, an absorber ring with holes, or conversely a set of absorbing beads mounted on a ring of light material, will provide the fiducials.

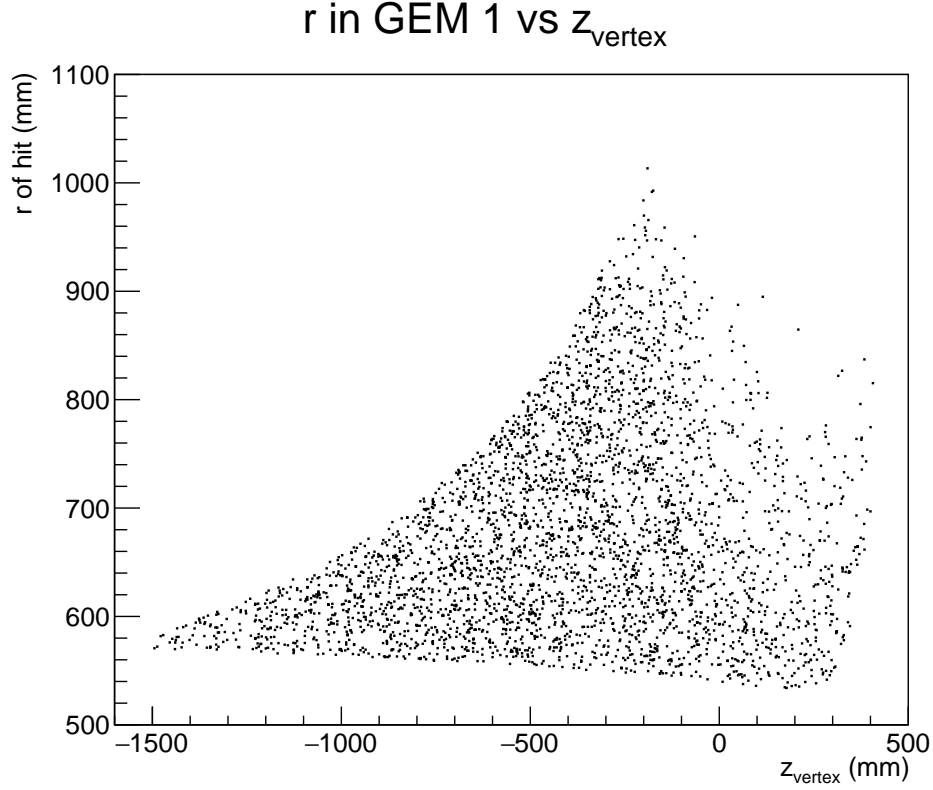


Figure 132: Radial coordinates of photon hits in GEM 1 versus vertex  $z$  position. Most of the detector area is covered for vertex at  $z = -200$  mm, corresponding to a position about 10 cm upstream of the LD<sub>2</sub> target. Similar results are seen in the other GEMs.

Once the positions of the GEMs are known, the magnetic field is calibrated as follows. First a map is obtained with a precision of about 1%. With this map the radial fields are known well enough so that  $F_\theta$  can be precisely determined. To improve the calibration of the momentum to the 0.1% level, we use electron hydrogen elastic scattering data at beam energies of 4.4 and 6.6 GeV as well as at different magnetic field settings. Since the beam energy is known to better than 0.1% and the angle can be measured to that precision, the location of the elastic peak provides a calibration of the magnetic field. One issue is that for one beam energy, there is only one track energy at each angle, whereas for DIS, the angle and energy are much less correlated. However, the correction  $F_\rho$  in Eq. 26 is independent of  $\alpha$ , so a single momentum at each angle is sufficient. In other words, the importance difference between two similar fields is the value of  $\int B_z ds_\perp$  which is a scale factor for all momenta. Hence a single momentum from the elastic scattering is sufficient to make a precise

correction.

Clean separation of the elastic peak will be required. Figure 133 shows results from simulations where the green histograms are elastics and the blue histograms are the inelastic background from a Christy-Bosted parameterization [290]. Target and detector materials were included and momenta were smeared by 1% to simulate detector resolution. At both energies the elastic peaks are cleanly resolved. Rates are ample for calibration; see Figure 134. At 6.6 GeV, the integrated rate is about 150 Hz per  $\mu\text{A}$  of beam current. At 50  $\mu\text{A}$ , sufficient data can be collected in only a few minutes.

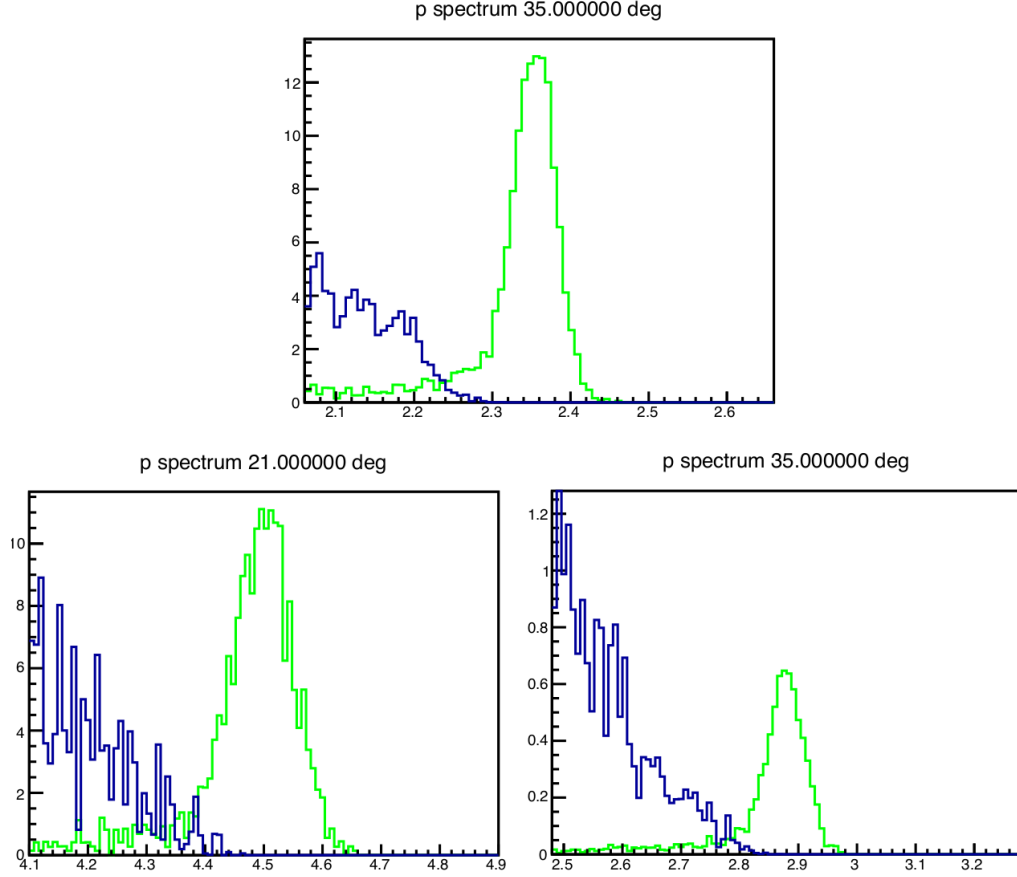


Figure 133: Elastic (green) and inelastic (blue) spectra for 4.4 GeV (top) and 6.6 GeV (bottom) electrons on a hydrogen target, at scattering angles of  $21^\circ$  (bottom left) and  $35^\circ$  (top and bottom right).

### 13.4 $J/\psi$ Program

Recent simulation studies of  $J/\psi$  production have been performed including approximate radiative effects. External bremsstrahlung was applied to both the incident and scattered electrons. The incident electron radiation loss is calculated with the peaking approximation through the target material up to the reaction vertex. The external radiative loss for the scattered electron is calculated within the framework of Geant4/GEMC and folded into the total resolution smearing of the track. Internal bremsstrahlung is calculated according to the  $Q^2$  dependent equivalent radiator method, and applied

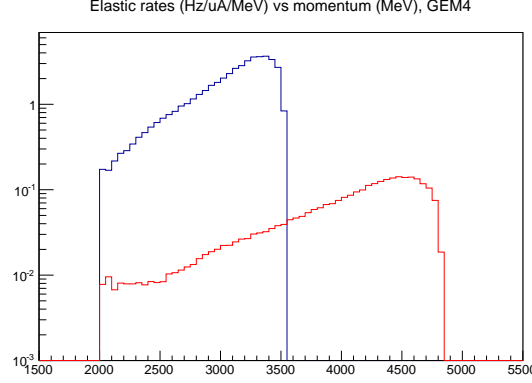


Figure 134: Elastic rates at GEM 4 for 4.4 GeV/c (blue line) and 6.6 GeV/c (red line) electrons on LH2, as a function of momentum in MeV/c. Rates are in Hz per  $\mu\text{A}$  per MeV/c. Target and detector materials are included.

to both the incident and scattered electrons. These radiative calculations are well known and widely used and have historically described radiative losses with reasonable precision. A more robust and explicit calculation would allow for a more precise unfolding of the radiative losses, however such an endeavor is non-trivial and would require a significant investment of manpower. For the approximate calculations, one can see in Figure 135 the effects of bin-migration along  $W$ , and the estimated correction needed to recover the unradiated cross-section. The plotted calculations were simulated with a 4-fold coincidence; the 3-fold coincidence has identical radiative losses (incident electron, scattered electron). Additionally, the internal radiative corrections in the equivalent radiator method are near zero when in the quasi-real photon kinematics of the 2-fold coincidence measurement. We plan to continue developing our radiative corrections procedure with exact calculations, accurate unfolding, and tests of model dependence.

A physics generator which includes acceptance effects was developed for the experiment proposal and has since been extended to include resolution effects and the radiation effect approximations outlined above.

Because the  $J/\psi$  experimental configuration is very similar to the SIDIS setup: a target position offset by 35 cm being the only difference. the acceptance and efficiencies are in-line with the SIDIS  $^3\text{He}$  program shown in Figure 129 and Table 22. The only difference is that the  $J/\psi$  setup has higher acceptance because its 15 cm long LH2 target requires no collimators as SIDIS  $^3\text{He}$

As stated in the original proposal, we expect the systematic uncertainty to be dominated by the acceptance ( $<10\%$ ), with an additional contribution of a few percent from sub-detectors, luminosity, target windows and background contaminations. We take the total systematic uncertainty to be 11%. Without radiative corrections of the data, systematics due to bin migration can be estimated from Figure 135. However, much of these systematics can be corrected by accurately simulating and properly unfolding the radiative effects (see section above).

An updated analysis of the  $J/\psi$  experiment's di-lepton trigger from the decay lepton pairs and triple lepton trigger with additional scattered electron were preformed, similar to what the PVDIS and SIDIS  $^3\text{He}$  programs have done. This simulated trigger study included the signal and combinatorial background from leptons, pions, and additional hadrons over both forward and large angle acceptance including the most up-to-date EC, LGC, and SPD response. The resulting di-lepton trigger and triple lepton trigger are calculated to have a coincidence rate about 60 kHz and 30 kHz

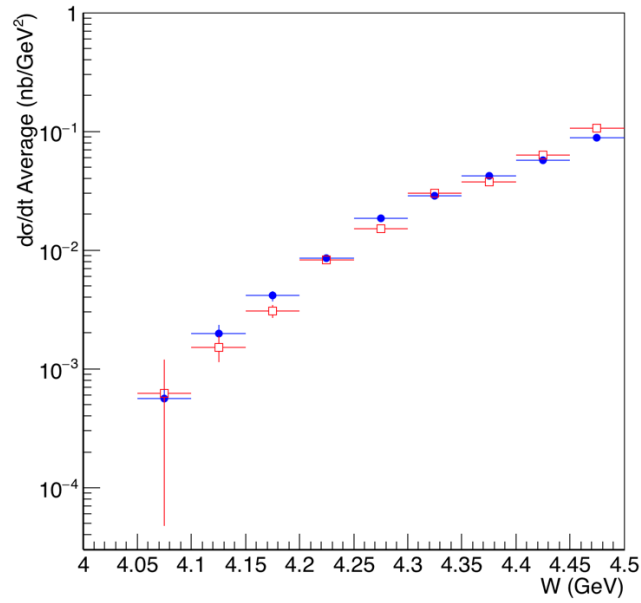


Figure 135: Simulation of cross-section including acceptance effects but no additional radiative losses (blue circles) for comparison with the expected cross-section measurement including acceptance smearing and all radiative effects listed in the text (red squares).

respectively. The triple lepton trigger will be our main trigger and it's also possible to take some pre-scaled di-lepton trigger to preserve photoproduction data. We are working on improving the trigger rate estimation and fine tuning the trigger design to see what's the best way to maximize the physics program under reasonable trigger limit.



## 14 Data Acquisition

### 14.1 Introduction and Requirements

The SoLID detector is a large acceptance detector designed to run at high luminosity. The detector will operate in two basic configurations: the parity-violating electron scattering (PVDIS) configuration and the semi-inclusive deep inelastic scattering (SIDIS) configuration. The experiments planned under these configurations have in common a large number of channels (over 160,000 GEM tracking channels and over 4,000 trigger/particle ID channels), high background rates, and high trigger rates.

We use the whole detector simulation with various experimental configurations to study the trigger as mentioned in Section 12.2. The high energy primary particles are from event generators such as a single electron generator, a SIDIS pion generator and the modified HallD hadron generator. All secondary particles are generated by Geant4. Low energy particles, primarily from electromagnetic processes, are produced by Geant4 directly from beam electrons on the target. The response in various detectors are examined event by event according to a given trigger configuration. Low energy background and pile up effect are taken into account. The expected trigger rates are shown in Table 28 for different experimental setups. (The trigger simulation will be updated as the simulation tools are improved and additional information becomes available from JLab 12 GeV data and DAQ tests.)

The SIDIS configuration, with an expected trigger (coincidences and accidentals) rate of  $\sim 100$  kHz and total data rate of over 3 GB/s represents the greatest challenge for SoLID data acquisition. For PVDIS, the DAQ requirement is more modest as the  $\sim 450$  kHz rate is divided among 30 parallel DAQ systems, following the segmentation provided by the baffle system. However, there are additional challenges as the DAQ systems for adjacent sectors must communicate trigger information and data for events where calorimeter showers extend into adjacent sectors.

We present here a conceptual design for a DAQ system based on modest evolution of current technology, much of which has been developed at JLab. Considering the large number of channels, the rate requirements and the availability of new electronics developed for the Hall D GlueX detector, a pipelined electronics approach has been chosen. These electronics continuously digitize the detector signals, keeping the data in several microsecond deep buffers which can be retrieved after a trigger is received. With these electronics, the First Level Trigger (L1) is generated primarily from prompt data streams from Flash Analog to Digital Converters (FADC). This gives the ability to reprogram trigger algorithms without the need for re-cabling.

Experiment	PVDIS	SIDIS $^3\text{He}$	$J/\psi$
Trigger rate (expected) (kHz)	$15 \times 30$	100	30
Data rate (GB/s)	$0.2 \times 30$	3.4	4.0
Running time (days)	169	125	60
Total data (PB)	175	73	42

Table 28: Rates, run times and data total estimates for the PVDIS, SIDIS  $^3\text{He}$  and  $J/\psi$  experiments. For PVDIS, there are 30 sectors each of which has a separate DAQ.

#### 14.1.1 SIDIS Trigger and Rate Estimate

Three experiments, E12-10-006 [291], E12-11-007 [292], and E12-11-108 [293], have been approved to measure single and double asymmetries of semi-inclusive deep-inelastic scattering (SIDIS) ( $e, e'\pi^\pm$ ) with SoLID. As these experiments have similar reaction channels, they can share the same DAQ system design. The required overall luminosity of E12-10-006 and E12-11-007 is  $10^{37}/\text{cm}^2/\text{s}$ , which is an order of magnitude higher than that of E12-11-108. Therefore, we will use E12-10-006 as an example to illustrate the requirements of the SIDIS DAQ. The goal of the SIDIS DAQ is to satisfy the requirement of  $\sim 100$  kHz trigger rate, see Section 14.2.1 for more information about the limit.

The SIDIS process requires the detection of both the scattered electron and the leading pion. Therefore, a single electron trigger or a coincidence trigger of the electron and the hadron would satisfy this need. The electron trigger for the large angle detector will be provided by the E&M calorimeter at a threshold of about 3 GeV. Such a trigger is sensitive to both high energy electrons and high energy photons (mostly from the  $\pi^0$  decay). A set of scintillator paddles, added in front of the calorimeter, are incorporated into the trigger in coincidence, significantly suppressing triggers from high energy photons.

The electron trigger at the forward angle detectors will be formed by a coincidence of the Gas Cerenkov detector, the E&M calorimeter, the scintillator paddle detector (SPD) and the Multigap Resistive Plate Chamber (MRPC). Considering the kinematics of the scattered electrons from the DIS process (e.g.  $Q^2 > 1 \text{ GeV}^2$ ), a position dependent energy threshold with a lower limit of 1 GeV in the E&M calorimeter will be used.

The single electron trigger rate was estimated from simulation to be 116 kHz for the forward angle calorimeter in coincidence with the Gas Cerenkov, SPD and MRPC. Adding 32 kHz for the large angle calorimeter in coincidence with the SPD gives a total single electron rate of 148 kHz. In order to keep the Level-1 trigger rate below 100 kHz, we plan to form a coincidence trigger between the electron trigger and the charged hadron trigger with a 20 ns time window. The charged hadron trigger using the calorimeter with the SPD and the MRPC is 20 MHz. The SIDIS processes including charge pions and misidentified neutral pions and protons, have coincidence trigger rate of 27 kHz. Other multiple hadron process can also contribute to coincidence rate of 12 kHz. Excluding the true coincidence from SIDIS and multiple hadron process, we estimate the accidental coincidence rate 46 kHz with a 20 ns time window. Some single electron trigger will also be acquired. These will be prescaled to about 15 kHz such that the total trigger rate remains below 100 kHz.

#### 14.1.2 $J/\psi$ Trigger and Rate Estimate

The E12-12-006 experiment is designed to measure the cross section of the  $p(e, e'J/\psi)p$  reaction at an unpolarized luminosity of  $1.2 \times 10^{37} N/\text{cm}^2/\text{s}$  with a proton target. A coincidence trigger between the electron and positron from  $J/\psi$  decay will allow both electroproduction and photoproduction reactions to be recorded. By using an electron trigger similar to the SIDIS configuration, with a different radial dependent EC trigger threshold, a rate of 60 kHz is estimated. Adding the scattered electron into trigger to form a triple coincidence will reduce the trigger rate by a factor of 2 to 30 kHz.

#### 14.1.3 PVDIS Trigger and Rate Estimate

The PVDIS measurement is based on the asymmetry of inclusive electron scattering between incident electrons of opposite helicity states. To achieve the needed statistical accuracy of this parity violating asymmetry, high rates will be required in the detector. The rate over the whole detector

is expected to be of the order of 500 kHz, above the trigger rates that can be handled by the JLAB electronics. As the measurement is of singles inclusive electrons, the detector electronics can be divided into 30 sectors (corresponding to the baffle arrangement) each with a separate trigger, giving an acceptable rate for each sector. For each sector, the trigger will be a coincidence between the gas Cerenkov and electromagnetic calorimeter. Based on our simulations of the inclusive electron rate and accidentals (with a 30 ns coincidence window) between singles in the electromagnetic calorimeter and the Cerenkov counter, the estimated trigger rate is 15 kHz per sector.

## 14.2 DAQ Hardware and Trigger

The DAQ system for SoLID will use modules recently developed for Hall D by the JLab Physics Division Fast Electronics and Data Acquisition groups. These include flash ADCs (FADC250), VXS Trigger Processors (VTP) and Global Trigger Processors (GTP), Sub-System Processors (SSP), Trigger Supervisors (TS), Trigger Interface (TI), and Signal Distribution (SD) modules.

Analog signals are digitized by the JLab FADC250, a 16-channel 12-bit flash analog to digital converter sampling at 250 MHz. The input signals are continuously recorded into a memory with a depth of up to 8  $\mu$ s with event data latched by a trigger. The system is dead-timeless as long as the latched data can be readout as fast as it is generated.

In addition to making data available for readout when triggered, the FADC250 is capable of sending continuous digitized data over high speed VME switched Serial (VXS) lanes on the backplane connector. This data, a 16 bit word per module every 4 ns, could be a digital sum of the 16 channels of the ADC or more complex information.

Each crate will have a VXS Trigger Processor (VTP) which receives a 16 bit word from each FADC250 every 4 ns. The VTP processes the data stream from each module in the crate to generate a 32-bit word every 4 ns. This word, which could be, for example, a sum of all the channels in the crate or a bit pattern, is sent upstream via a 10 Gbps optical link to a Sub-System Processor (SSP) board which gathers trigger data from multiple crates. All the SSP boards send their information to the Global Trigger Processor (GTP) which generates the level one (L1) trigger.

The GTP sends the trigger to the Trigger Supervisor (TS) which makes sure the system is ready to accept a trigger and sends the accepted signal to Trigger Distribution boards which are linked to the Trigger Interface (TI) boards in each crate via optical links as represented in Fig. 136. The trigger and synchronization clock signals are then sent back to individual crates and payload modules through Trigger Distribution (TD) boards and Signal Distribution (SD) boards which distribute the signals to electronics such as the FADCs. Once a trigger is generated, the full resolution data which is still in the pipeline, is readout out using a serial VXS link at a data rate of 8 Gbit/s correspond to 1 GB/s. As this is a point to point connection, the aggregate full crate bandwidth is 16 GB/s, giving plenty of headroom for FADC readout.

### 14.2.1 GEM readout

The plan for readout of the GEM detectors is to use the CERN Scalable Readout System (SRS) [294] which is based on the APV25 [295] front end chip. The APV25 chip is a shaper amplifier circuit that samples 128 channels at 40 MHz, storing the most recent 192 samples of amplifier output in a switched capacitor analog memory array. When a trigger is issued the corresponding slice in time is frozen, allowing a look back in time of up to 4  $\mu$ s. With such a pipeline design, the system is deadtimeless as long as the trigger rate is well under the 40 MHz sample rate. Readout of the chip by the front end electronics is also done at 40 MHz. For each trigger, 128 channels are readout with additional control signals making a total of 141 signals to be transferred. The chip has the ability to

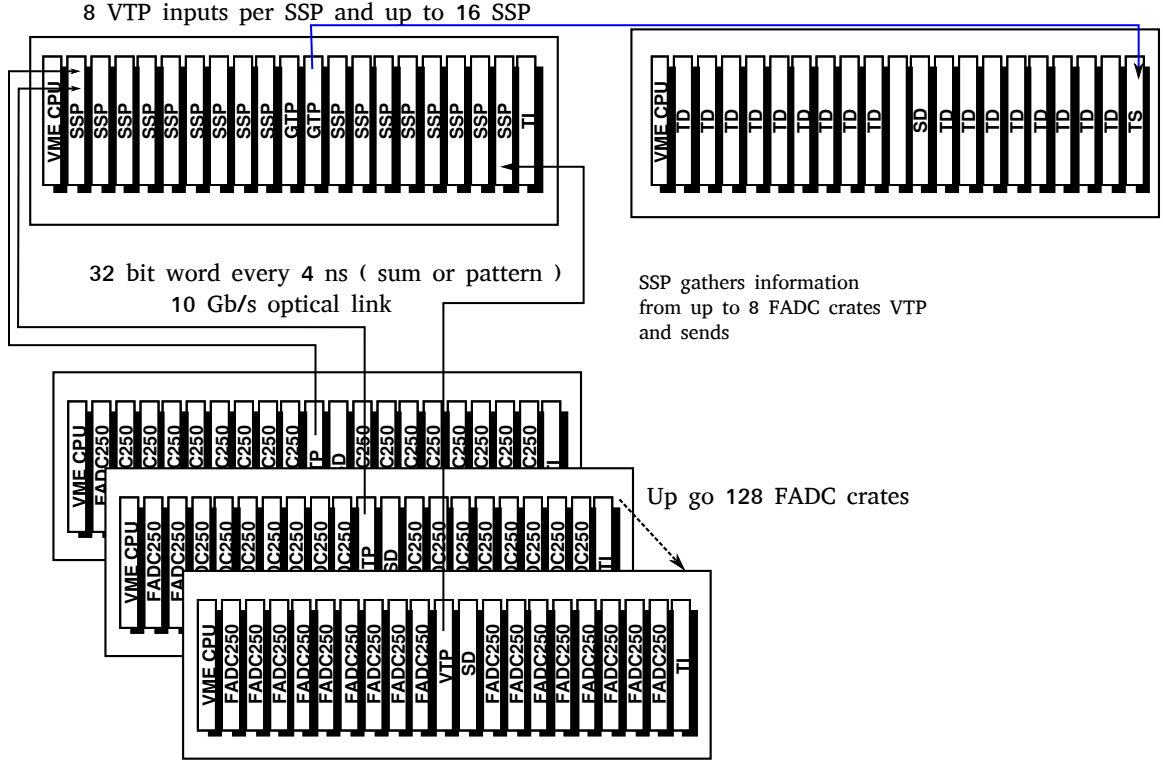


Figure 136: Standard Triggering scheme using the JLAB pipeline electronics

record 1 sample per trigger or 3 samples in case of high background. The signal is transferred in an analog form to the front end card where it is digitized by a flash ADC. In the case of one sample it will take :

$$141 * 25 = 3.6 \mu s$$

to transfer the data from the chip. This time is tripled to 10.6  $\mu s$  for 3 sample readout. This data transfer rate is ultimately limiting the trigger rate capability of the chip to 91 kHz in 3 sample mode and 280 kHz in single sample mode. All the data is digitized on the front end board with pedestal subtraction and zero suppression.

The SRS system, developed by the RD51 collaboration, gathers all the common high level digital functions of a typical readout system : triggering, buffering, data transfer and event building. To use the APV25, a chip specific adapter is needed. Such an adapter card is available which links to the the hybrid board that holds the APV25 using HDMI cables. This card has 8 FADCs reading out 8 APVs chips, digitizing 2048 channels of detectors per board. These boards interface with the SRS Front-End Card (FEC). The FEC card process the digitized data and can transfer the data directly to a computer through Gigabit Ethernet. These FECs are mounted in Eurocrates which each can hold up to 8 FECs. For larger systems, a Scalable Readout Unit (SRU) can be used to gather data from multiple FECs. In this case data is transferred from the FEC to the SRU using a custom protocol over standard CAT6 ethernet cables. The data gathered by the SRU is sent to a computer over 10 Gigabit Ethernet. As each FEC can communicate individually to a computer or a SRU, the system is highly scalable and modular. As many FECs can be added as need to readout all the detector channels.

GEM readout systems based on the APV25 are currently in use at JLab (Heavy Photon Search, Proton Radius Experiment and the Super Bigbite Spectrometer). The experience with these exper-

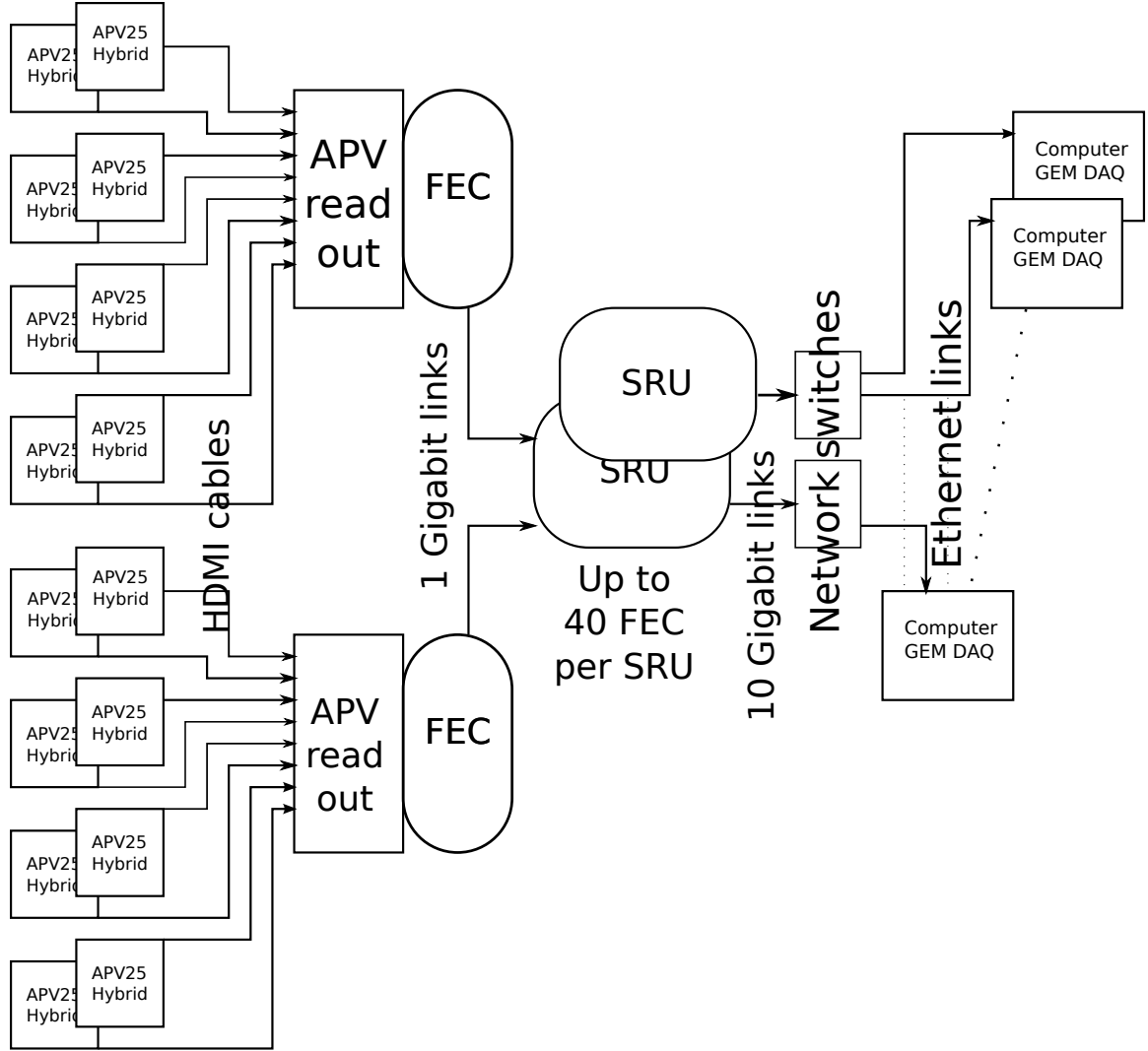


Figure 137: Standard SRS architecture which will be used for SIDIS experiment

iments indicates that a readout system based on the APV25 can be built that supports the trigger and data rates required by SoLID. A variety of other GEM readout front end chips are under development. The collaboration will monitor these developments for improvements in cost, performance and DAQ rate.

#### 14.2.2 SIDIS Configuration

The SIDIS experiment will use a similar detector setup as the PVDIS experiment with the addition of more detectors. Scintillator planes will be used to reduce the photon background as the PVDIS baffles will be removed. A Heavy Gas Cerenkov and a MRPC will be added for  $\pi/K$  separation. The PVDIS crates will serve as the basis of the SIDIS DAQ, but the signals from the VTP will be sent to the SSP and GTP in an additional crate to make a coincidence trigger. The additional detectors will be instrumented with FADCs for the Heavy Gas Cerenkov and TDCs for the MRPC.

Based on current simulations, the size of each event is expected to be about 31.1 kBytes including signals from all detectors. So for a SIDIS  $^3\text{He}$  rate of 100 kHz (coincidences plus prescaled

Detector	Channel
EC Shower	1800
EC Preshower	1800
SPD	300
Light Gas Cerenkov	270
Heavy Gas Cerenkov	480
MRPC	3300

Table 29: Detector channel counts for the SIDIS and  $J/\Psi$  experiments, excluding the GEMs.

singles) a data rate of 3110 MB/s is expected.

The SIDIS experiment trigger formula is

**forward angle electron trigger** Forward Angle Calorimeter *AND* Light Gas Cherenkov *AND* SPD *AND* MRPC

**large angle electron trigger** Large Angle Calorimeter *AND* SPD

**forward angle charged particle trigger** Forward Angle Calorimeter *AND* SPD *AND* MRPC

**coincidence** electron trigger (large *OR* forward) *AND* forward angle charged particle trigger

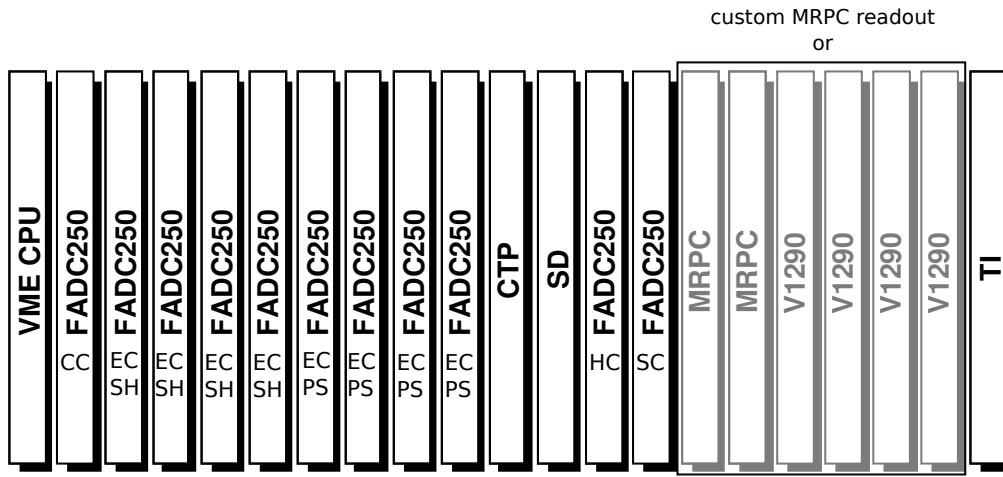
The SIDIS experiment and  $J/\Psi$  will use the same detector configuration, cabling, DAQ and trigger hardware. The only difference is that the DAQ will be configured to trigger on a high energy electron and a pion for SIDIS while for  $J/\Psi$  it will trigger on 2 high energy leptons.

**MRPC readout** The current plan for MRPC readout is to develop a custom electronics module for the readout of the 1550 MRPC strips. It will be a custom designed TDC that digitizes 3300 channels of MRPC. (Strips are readout at both ends.) The baseline solution will be to use a chip similar to the NINO chip which is an amplifier discriminator chip. This chip generates a discriminated signal with a time resolution on the order of 10 ps with a logic output width proportional to the time the pulse is above threshold which allows amplitude information for time walk correction. In order to include the MRPC in the trigger, a new module, the VETROC board, developed by the JLab electronics group will be used.

**SIDIS GEM rates** As the DAQ for the SIDIS experiments can not be segmented in to a separate DAQ chain for each sector, the event size is an important factor in keeping the DAQ throughput below limits to the overall data rate that can be recorded. The occupancy of the detector is fairly low when using the on-board deconvolution which is the default running mode for SIDIS. By reading in one sample mode, we expect the allowed trigger rate to be about 200 kHz. We are planning to use several SRUs to concentrate the signal from the SRS front end cards. The SRU module gathers all the FEC signals and sends the data to a 10 Gbit ( $\sim 1.2$  GB/s) Ethernet port. To have a safety margin, 4 SRUs will be used to handle the rate.

### 14.2.3 PVDIS Configuration

**Calorimeter trigger for PVDIS** There are currently two options to generate a Level-1 (L1) trigger from the calorimeter. The standard option is to use the sum of the 16 FADC channels which is computed and sent to the VTP every 4 ns. The VTP can add all the FADC sums, generating a global



Optical link 10 Gbps  
1250 MB/s

Figure 138: SIDIS FADC crate layout

Chamber	Occupancy	Hits per sector	Hits detector
1	2.37	21.5	644.2
2	7.98	81.4	2441.9
3	3.4	39.6	1189.3
4	2.24	31.5	943.5
5	2.03	21.1	633.4
6	1.52	19.4	583.7
Total hits		6435.9	193076.8
Event size 1 sample (Kbytes)		945.3	28408.4
Data rates 100 kHz (Mb/s)		94.5	2840

Table 30: SIDIS GEM occupancies and event size for GEM

Table 31: Channel counts of individual detectors for PVDIS for one sector

Detector	Module Type	Number of Channels	Number of Modules
Electromagnetic Calorimeter (EC)	FADC	122	8
Light Gas Cherenkov (GC)	FADC	9	1
GEM	SRS	4700	1

sum for each crate and generating a trigger when that sum exceeds a threshold. Another scheme was devised for the Heavy Photon Search experiment in Hall B. In this scheme 16 bits of data for each of the 16 FADC channels is sent every 32 ns as in Fig. 141. These data contains both the signal amplitude, and the timing (to a 4 ns resolution) of any threshold crossing. With the VTP receiving a signal from all the calorimeter elements, it can compute the signal sum, in parallel, of every possible cluster of one central and 6 surrounding blocks. This approach of triggering on the cluster sum can reduce the number of triggers coming from background and improve online pion rejection.

Particles near the edge of a sector will likely shower into calorimeter blocks in the adjacent sector. In order to avoid inefficiencies near the edges of sectors, VTPs for neighboring sectors will share information through bidirectional optical links as shown in Fig. 140. Once the VTP receives all the FADC data from its own crate and the two adjacent crates, it either computes the total sum or performs cluster searching to generate trigger. If the cluster trigger method is used, a 64 bit pattern containing the FADC channels to be readout will be generated by the VTP and transferred to the Flash ADC using the trigger data path. A new firmware for the FADC will be developed to take this pattern into account allowing each FADC to only read the channels that are part of a cluster in order reduce event sizes.

**Gas Cerenkov trigger** Both Cerenkov detectors are divided into 30 sectors. The most straightforward way to generate a Cerenkov trigger is to put all the channels of a given sector (9 for the light gas and 16 for the heavy gas) into one FADC board and generate the trigger in the VTP by putting a threshold on the sum of the PMT signals. To improve efficiency at the interface between two sectors one can include a threshold on the sum of the two adjacent sectors. If the combinatory background is too large, a clustering scheme similar to that discussed for calorimeter could be used. The efficiency and background of the different schemes has been evaluated in the full simulation of the digitized background. This simulation shows that a simple trigger based on PMTs sums works and has a sufficient efficiency.

In order to estimate the per event size of data from the GEMs, the GEM signal and the APV25 digitization process were modeled in a simulation. This simulation is detailed in the simulation section 12.2.4 of this document. The total number of GEM strips firing in a 25 ns window was computed without and with deconvolution. The last column are the results coming from the GEM digitization Section 18.

**PVDIS GEM rates** For PVDIS, we are interested in the data rate per sector. The numbers in Table 32 are evaluated for 20 kHz (15 kHz rate + 5 KHz of safety margin). Even though occupancies are high, the data rates for PVDIS are reasonable (about 80 MB/s per sector) and simulations show that tracks can be efficiently identified if 3 sample readout is used. The 3 sample readout will allow for more effective offline rejection of pile up. The deconvolution and filtering are also able to significantly reduce the occupancy and event size. Using the SRS system, each FEC can transfer up to 1Gbps through its Ethernet link.

### 14.3 Event size from FADC

The FADC samples are 12 bits at 250 MHz. In the case of PVDIS, since pile up is going to be significant, we plan to record the entire waveform. As pulses are 40 ns wide, we will record 10 samples for each detector channel. The event size per FADC events have a 4 byte block header, a 4 byte block trailer, a 4 byte event header and pack 2 samples into each 4 byte word. For a 10 sample size, the event size per module is thus  $(12 + 4 \times (10n/2))$  bytes where  $n$  is the number of channels firing.



Chamber	Occupancy (%)	Hits	Occupancy with noise cut (%)	Hits after noise cut
1	21.2	244.8	10.0	115.2
2	10.3	142.2	5.1	70.2
3	8.8	121.0	4.4	60.7
4	3.1	70.2	1.6	37.5
5	2.8	65.6	1.5	35.2
Total hits		643.8		159.8
Event size 3 samples (Kbytes)		7.9		3.9
Data rates 20 kHz 3 samples (Mb/s)		159.8		79.2

Table 32: PVDIS GEM occupancies and event size for GEM

The FADC simulation with digitization is still being developed. Given the size of a sector, the event size will be estimated with a maximum of 2 clusters of 7 for shower and 2 clusters of 3 preshower and assuming all 9 PMTs of the Cerenkov fire all the time. With this assumption the event size is 1160 bytes per event.

With the trigger rate of 20 kHz, this gives 23.2 MB/s data rate, well under the VME320 back-plane transfer rate limit of 200 MB/s.

In the case of SIDIS, the occupancy on the detector is small enough that only pulse integrals need to be recorded. The estimated event size using the occupancies from the simulation is 31.2 KBytes, which gives an aggregate data rate, including GEMs, of 3110 MB/s at 100 kHz for all 30 crates.

#### 14.4 Data rates,event size,tape SILO footprint and L3 Farm

Experiment	Event Size ( kBytes)	L1 trig Rate (kHz)	Data Rate MByte/sec
PVDIS	146.4	20	2928
SIDIS	31.2	100	3360
JPsi	133	30	3990

A JLab network upgrade, completed in 2014, provided two 10 Gigabit Ethernet links between the Hall A counting house and the computer center. Additionnal fibers are available making it possible to upgrade the link up to 40 Gigabit/sec by using 4 fibers before SoLID running is planned. Silo (tape storage) upgrades are planned to accommodate Hall D data, allowing for 12 petabytes per year. Currently the SILO system can hold up to 11,240 tapes giving, with compression, a current capacity of 47 PB using LTO6 drives. The computer center out year budgets include plans to add a second silo, giving a storage capacity of 22,480 tapes and 48 drives. Assuming the evolution of LTO technology (shown in table below), a fully upgraded data storage center will have a capacity of 1840 PB and handle data rates up to 52.8 GB/sec. Assuming the silo is fully upgraded it could hold up to 919 PB of data in the LTO10 technology with a 13.2 GB/s data rate per drive frame or 26.4 GB/s for the whole system. Each drive frame can have up to 12 drives, A second two frame silo system is already budgeted to be deployed when needed. This would give a total capacity of 1840 PB and data transfer rate  $13.2 \text{ GB} \times 4 = 52.8 \text{ GB/s}$ , accomodating the needs of SoLID and the other halls.

LTO tape drive evolution.

LTO version	4	5	6	7	8	9	10
Availability	2008	2010	2012	2015	2018	2020	2023
Capacity/tape (TB)	0.8	1.5	2.5	6.25	12.8	25	48
Data rate/driver (MB/s)	120	140	200	300	472	708	1,100
Compression	2	2	2	2.5	2.5	2.5	2.5

Assuming 28 week of running, and assuming the usual 50% efficiency, every experiment longer than 98 days will span over 2 fiscal years giving an average tape cost per year of 120 K\$, a cost which can be accommodated by the hall operations budget. The total amount of data from all SoLID running will total to about 380 PB representing about 20 % of the future silo size.

## 14.5 Hall DAQ installation

The DAQ for both the SIDIS and PVDIS configurations will be located in the hall. As is typically done, a shielded bunker will be constructed to house the data acquisition electronics, protecting it from beam induced radiation. This bunker will contain  $\sim 15$  racks containing 32 VXS crates and the crates containing the GEM front-end cards.

Approximately 4500 coaxial cables (RG58) will connect the PMT based detectors to the ADCs in the bunker. Additionally,  $\sim 200$  ribbon cables will connect the on-detector MRPC discriminators to TDCs in the bunker and HDMI cables will connect the detector mounted GEM chips to the front end cards.

### 14.5.1 Experiment switch over

Switch over of the DAQ electronics between the PVDIS and SIDIS setups will be relatively straightforward. Changing to the PVDIS setup, the VTP module in each sector's crate will connect directly to the TI module in that crate to give an L1 trigger signal for that crate and the corresponding GEM electronics. The unused SSP, TD and TS, and VTP modules as well as ADC and TDC modules for detectors not in PVDIS will be removed from the hall to avoid extra radiation dose.

## 14.6 Managing data rates

Managing total data rates for SoLID will require careful system design to avoid bottlenecks. While the PVDIS configuration has the highest overall trigger and data rate, the segmentation of SoLID into 30 nearly independent sectors allows for natural parallelization. The data rate per sector is a few hundred MB/s. The parallel data paths can be preserved through the event builder (that combines VME and GEM data), to temporary disk storage, through parallel network paths, and through an L3 farm before merging into a smaller number of paths for storage on tape.

The SIDIS configuration is more challenging as the data for each event which is spread over 30 VME systems and 30 sectors of GEMs must be combined to build events. It is presently not feasible to build events from these 60 sources into single data stream of over 3 GB/s. This can be overcome with the option in CODA of multiplexing events to multiple event builders. A possible architecture would have up to 60 ROCs pushing data to several primary event builders so that each event builder handles a more modest data rate. (One event builder for the VME crates and several event builders for the GEM data.) Each of these primary event builders, which contain a fraction of each event, would feed, in round robin fashion, several secondary event builders. Each secondary event builder would build complete events, but only have a fraction of a given runs events saved

to its disk cache. This architecture is scalable such that bottlenecks can be mitigated by using a sufficient number of primary and secondary event builders.

## **14.7 Summary and Pre R&D plans**

The conceptual design of the SoLID data acquisition system is based on hardware that has all ready seen use with beam at JLab. While SoLID's trigger rate and total data rate exceed what has been achieved by detectors such as GlueX and HPS, it is expected that it is feasible to meet the requirements with careful system design, hardware firmware improvements and upgrades to the CODA software. The DAQ component of the SoLID Pre R&D will serve to understand the capability and limitations of the conceptually designed system. Some of the specific items to address in Pre R&D include:

- Test single VXS crate to acquire data at 100 kHz.
- Test acquisition of GEM data from one sector at 100 kHz with data rate of 100 MB/sec.
- Mockup 60 ROC system and multiple event builders and establish ability to handle throughput of 4GB/sec at 100 kHz trigger rate.
- Provide prototype small scale DAQ system for detector beam tests.
- Test trigger and data sharing scheme between adjacent sector PVDIS DAQ systems.



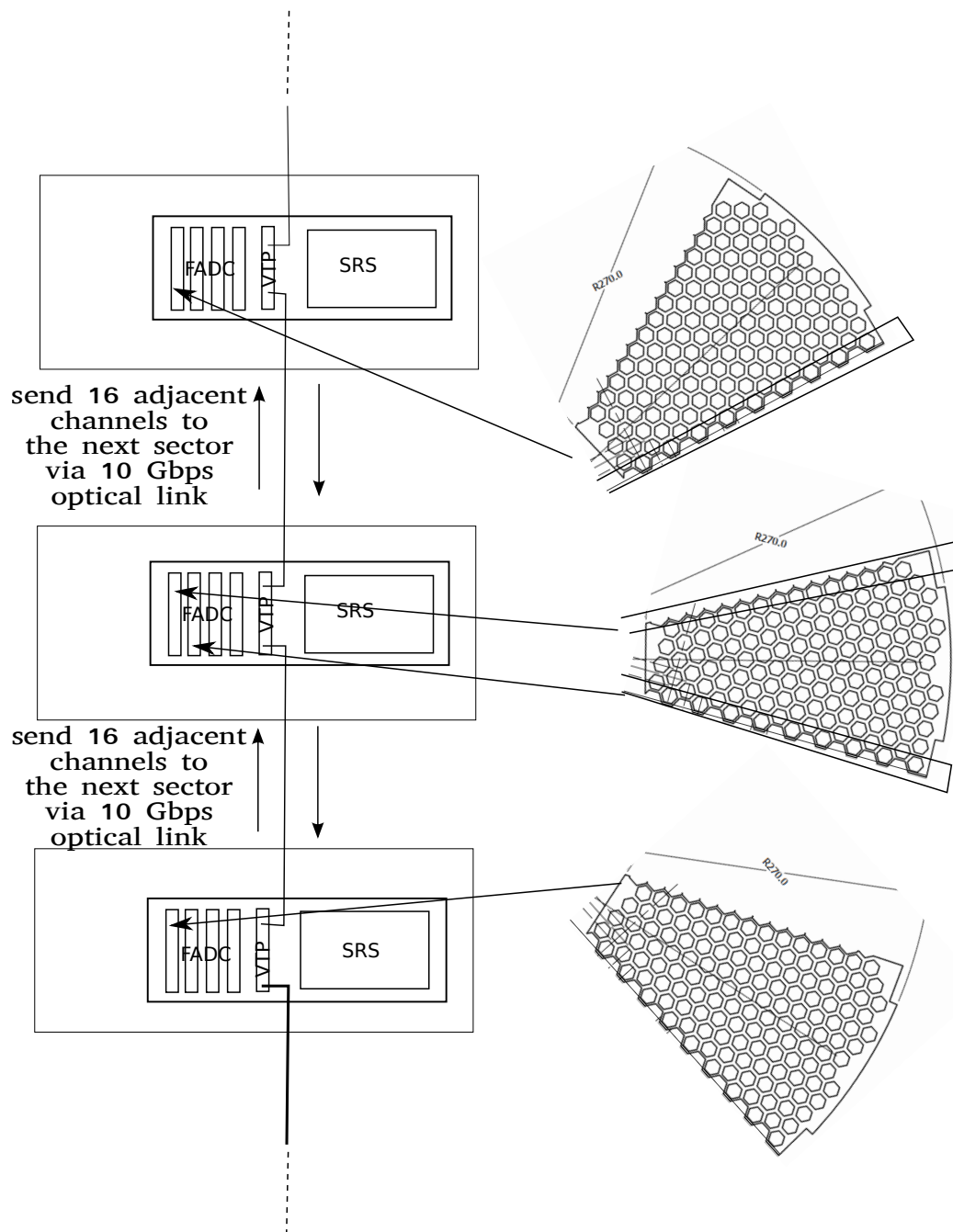


Figure 140: PVDIS specific electron trigger

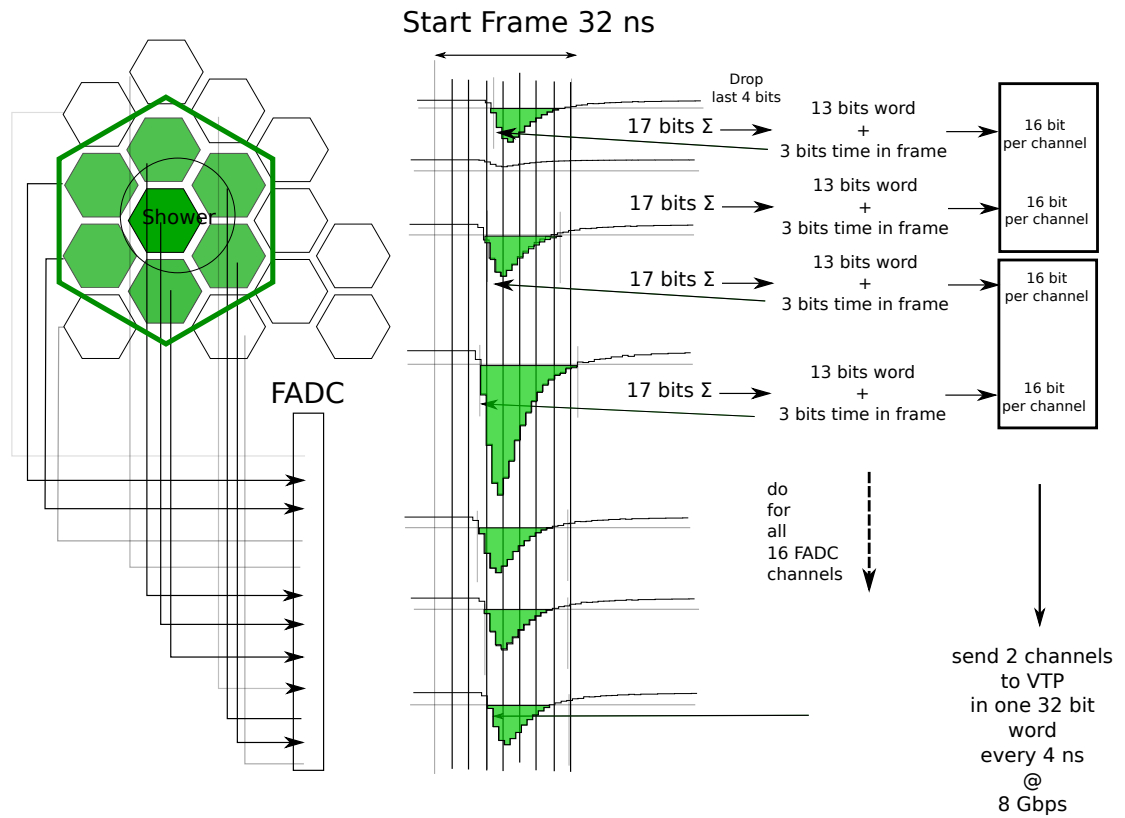


Figure 141: Calorimeter clustering scheme using the HPS algorithm. All calorimeter signals are sent to the FADC.

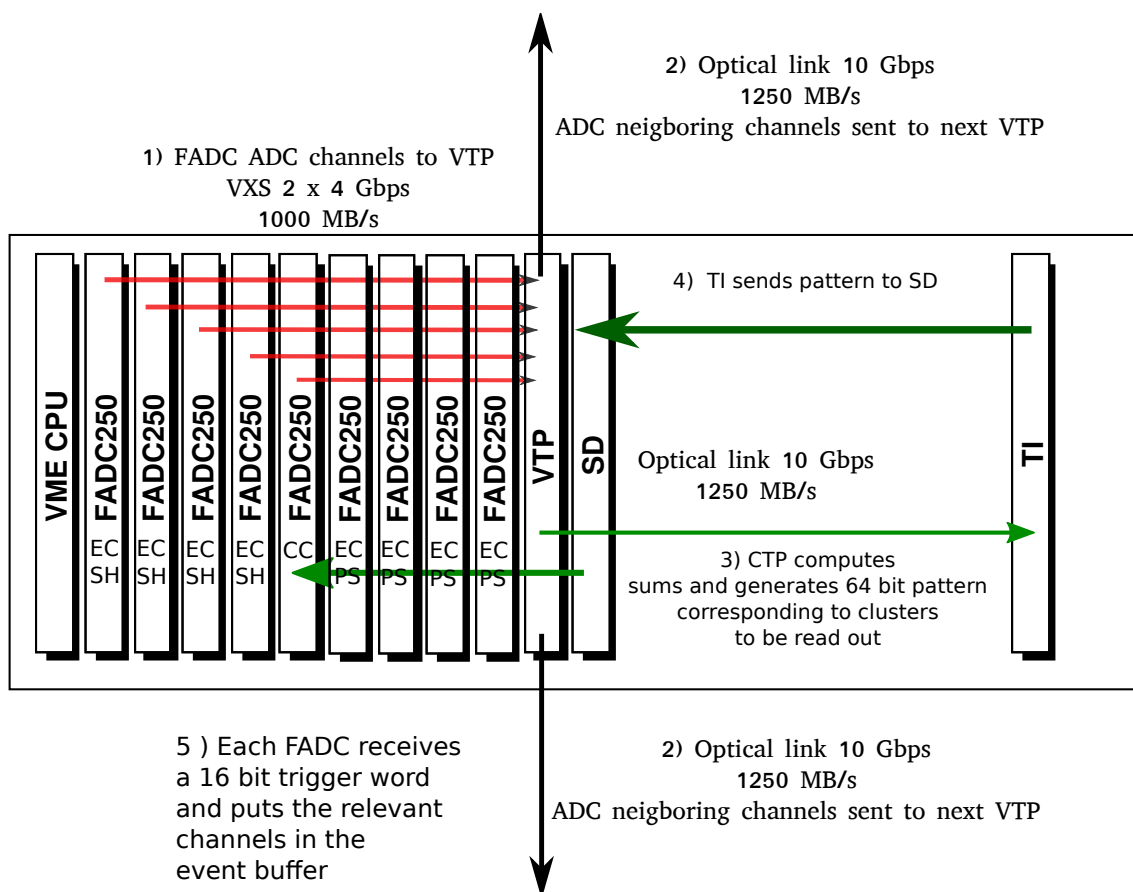
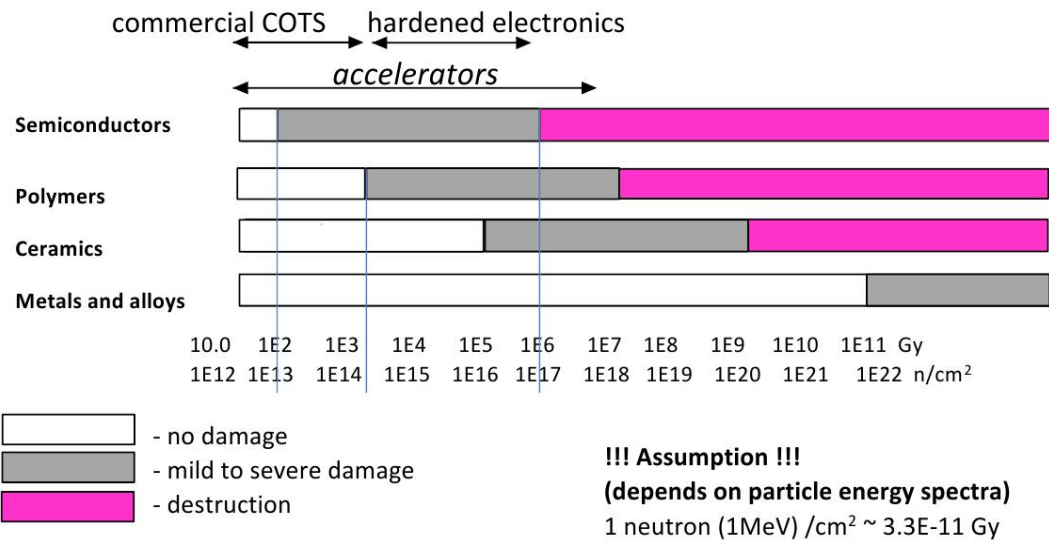


Figure 142: PVDIS FADC crate layout

## 15 Radiation damage estimates and Activation

The simulation and background calculation software for SoLID is using the two simulation packages with independent code base (Geant4 and FLUKA [298] [299]). This allows independent cross checks both in geometry and in physics modeling. At the same time the two codes each provide unique capabilities expanding the overall reach. FLUKA provides useful tools that simplify the study of radiation damage and estimates but the physics processes present in the simulation lack of direct electro-nuclear dissociation and fragmentation models. Such electro-nuclear reactions are dominant in the neutron production from the Liq.D target at high energies (see figure 148). If one just considers the neutron photo-production, both codes (GEANT4 and FLUKA) have really good agreement with experimental cross section, as shown in figure 146 and 147. A full simulation and tests are underway in order to construct a better and common target background generator for both simulation packages (see figure 148). To have a first idea of the tolerance of different material to radiation damage, see figure 143. As a weighting factor to estimate the effect of radiation damage on



© Lockheed Martin

Figure 143: Estimate of the tolerance of different material to different level of radiation exposure given in Gy and  $\frac{\text{neutron}(1\text{MeV})}{\text{cm}^2}$ . This is just a first order approximation and a detailed analysis of each equipment is needed in order to establish the correct radiation tolerance of each detector/material

electronics I used, in parallel to the calculation of full Dose estimates, the Displacement damage in silicon, on-line compilation curves by A. Vasilescu (INPE Bucharest) and G. Lindstroem (University of Hamburg). This curves assume that the damage effects by energetic particles in the bulk of any material can be described as being proportional to the so called Non Ionizing Energy Loss and normalize the damage in Silicon to the one caused by a 1 MeV neutron (more details can be found here [301]).

### 15.1 Radiation damage to GEM electronics

A simulation in order to test the radiation level on the GEM foils has been done. Comparison to estimated radiation level of the CMS experiment, which shares the part of the electronics most sus-



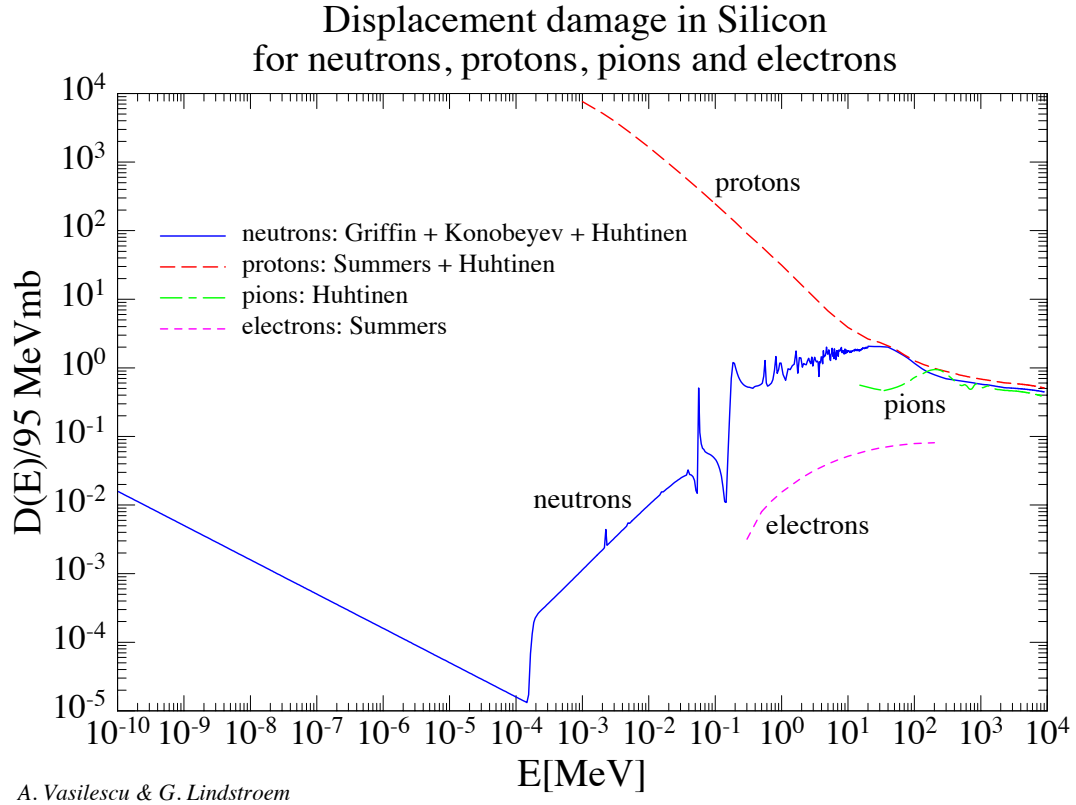


Figure 144: Not Ionizing Energy Loss curves to 1MeV equivalent damage in Silicon for electrons, pions, neutrons and protons

ceptible to radiation damage for the GEM chambers detectors, permitted us to establish a radiation limit flux for our expected running time. Already with our first conceptual design of the shielding we are able to reach tolerable radiation levels also in the first layer of the GEM chambers (the one that is supposed to sustain the higher radiation fluxes). This result is show in figure 149

## 15.2 Power deposited

A detailed study of the power deposited in the SoLID spectrometer has been done in order to detect areas of possible activation. In these areas, in order to define possible activations, the FLUKA simulation has been used as a tool, and particle fluxes were provided by GEANT4 for areas where was the particle fluxes estimated by FLUKA were known to be incorrect. FLUKA in fact provides many good tools for activation and radiation estimates, but lacks in direct electro-nuclear dissociation-fragmentation models and has limitations in producing more complex geometry, like the Baffle design for the PVDIS experiment in SoLID. In the following study of activation, GEANT4 has been used as a common input for an estimate of the background radiation in areas where direct electro-nuclear dissociation-fragmentation models are important.

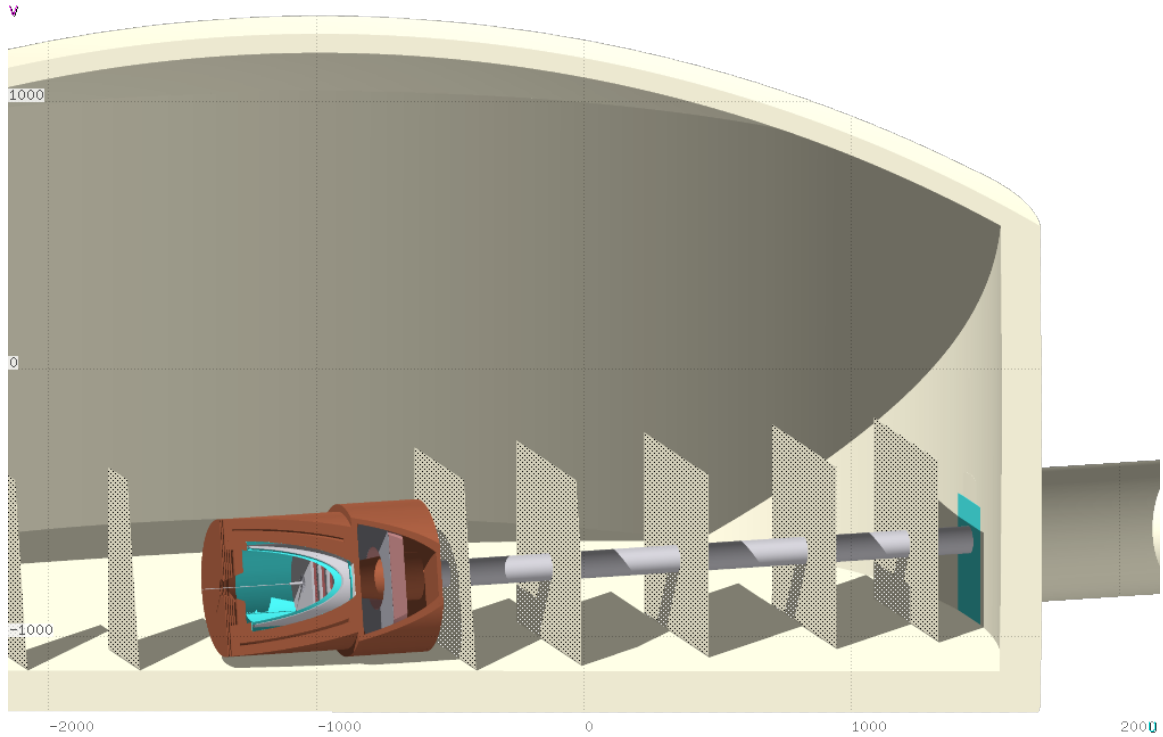


Figure 145: FLUKA simulation for the PVDIS experiment with SoLID.

### 15.2.1 Power in 1st baffle (due to Möllers), (Cooling, activation)

The first baffle, due to his proximity to the Deuterium target in the PVDIS configuration for SoLID, has a power deposition of  $\sim 8W$  for a beam current of  $50\mu A$  and an energy of  $6.6GeV$ . The high production of neutrons from the Deuterium target can be an ulterior source for activation in the baffle. For this reason an investigation of the possible activation has been done. In this study has been considered at the same time the radiation coming from the target and from the baffle itself that “self-irradiate” different parts of its structure. The impact of Activation due to the utilization of different materials have been directly studied (see [150](#) for the first baffle: In order to optimize the computing time and avoid issues of pixelization due to the detailed shape of the baffle, a single block of material was used in this study. Since the solid angle coverage seen by the main source of radiation (the target) of the baffle used in this study is not the same, the radiation calculated should be scaled accordingly or used as an extra safety factor due to our relying just on simulations.

These results (see show the Dose equivalent radiation spatial distribution for 3 different cooling times. This study (see figure [150](#) ) shows, for example, that, in order to survey the area in proximity of the first baffle, one should wait around 1 day of cooling, in order to reach level of radiation tolerable. The Residual nuclei activated in the Lead baffle are shown for the same cooling time in the bottom plots of figure [151](#).

### 15.2.2 Power in exit hole in magnet (elastics) (Cooling, activation)

Another spot for possible activation will be the part close to the exit hole of the magnet. Further investigation will need to be done, after a final design of the magnet will be reached, but it is expected to be less important than the activation on the first baffle, due to the not proximity to the target and to the less intense and less localize radiation. This situation has been investigated and

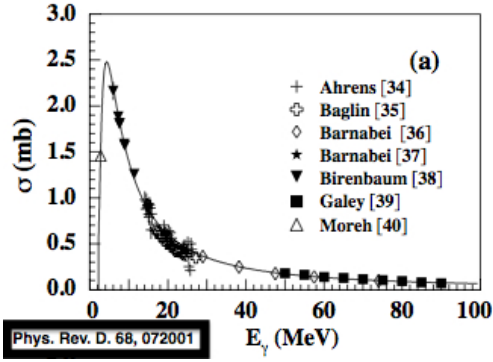


Figure 146: Neutron cross section for photo-production [300]

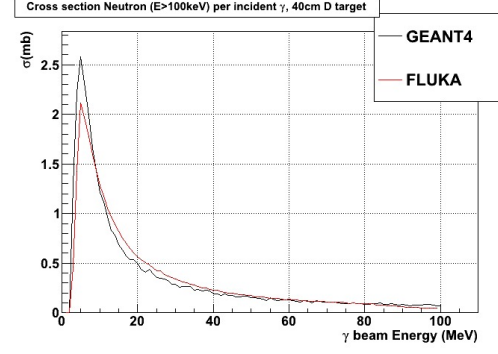


Figure 147: Test for Neutron cross section for photo-production with FLUKA and GEANT4

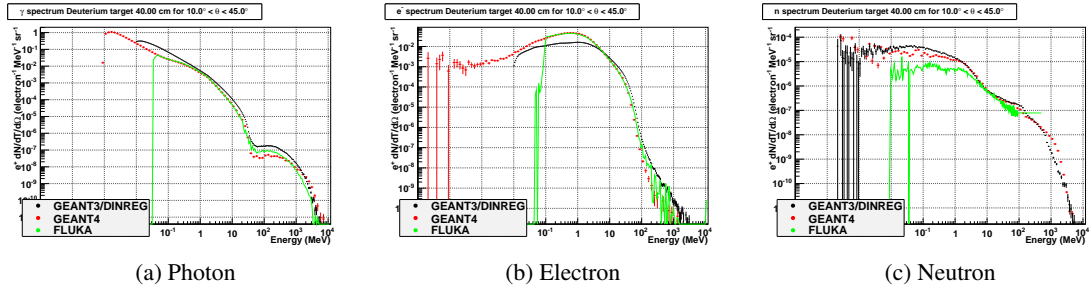
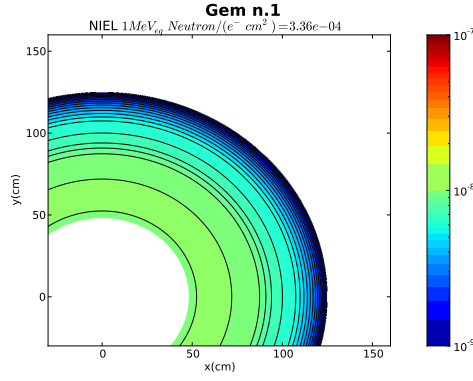


Figure 148: Background comparison produced from GEANT3(DINREG), GEANT4 and FLUKA with 40cm of Liquid Deuterium. Here is plotted the  $\frac{d^2N}{dT d\Omega}$  per incoming electron in the angle range of  $10^\circ < \theta < 45^\circ$  for  $\gamma$ (a),  $e^-$ (b) and  $n$ (c)

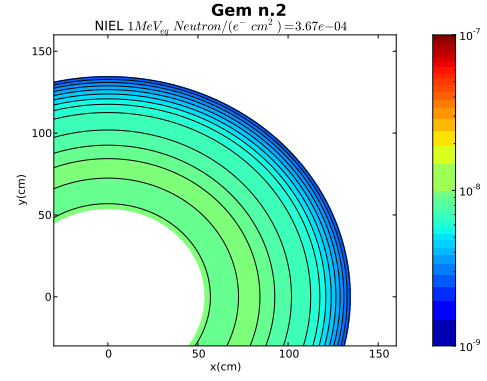
compared to the PVDIS design, because it is the one with the expected higher activation of all the configuration with SoLID, with the proximity of the lead baffles to the target (see this section at page 182). This has been done in order to compare power deposition to have a first idea of possible activation areas. The levels of power deposited in the exit hole of the magnet are at least lower by one order of magnitude respect to the one expected in the first baffle, as shown in figure 152a and 152b. The integrated value (using the cylindrical symmetry) over the higher area of power deposition in the exit hole of the magnet has a maximum of  $\sim 0.9W$  per cm in the  $z$  direction over the full internal section of the exit hole with  $r_{xy} < 40cm$  (color scale of  $\sim 3E-04$  in figure 152a). This compares to a full power deposition on the first baffle of  $\sim 20W$ , running in the same conditions. A power deposition estimate for the beam-line downstream is shown in figure 152b. As one can see in 153c, is considerably smaller the impact of the configurations like SIDIS to the activation in this area.

### 15.2.3 Power in the entrance surface of the magnet (Cooling, activation) (external target configurations)

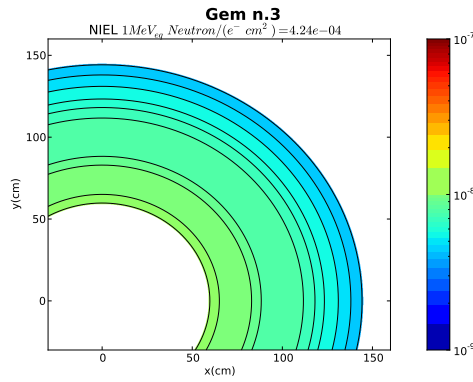
With configuration like SIDIS that have the target positioned outside the magnet, there is a consistent power deposition in the front part of the magnet. Some simulation has been done in order to estimate the possible activation in this area. The results of these studies are presented in figure 153 and show the areas of power deposition in the magnet and in the front surface of the magnet. As expected



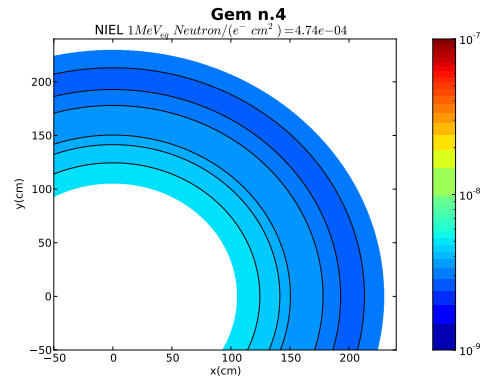
(a) NIEL weighted 1MeV equivalent neutron flux per  $cm^2$  per incident electron on the 1<sup>st</sup> GEM foil



(c) NIEL weighted 1MeV equivalent neutron flux per  $cm^2$  per incident electron on the 2<sup>nd</sup> GEM foil



(b) NIEL weighted 1MeV neutron equivalent neutron flux per  $cm^2$  per incident electron on the 3<sup>rd</sup> GEM foil



(d) NIEL weighted 1MeV equivalent neutron flux per  $cm^2$  per incident electron on the 4<sup>th</sup> GEM foil

Figure 149: The CMS experiment dose rates are expected to be of the order of 10 MRad( $SiO_2$ ) ( $5 \times 10^{13} \frac{n}{cm^2}$ ). This translate for us, assuming 2000 hours of beam at  $100\mu A$ , in a flux of  $\sim 1.1 \times 10^{-8} \frac{1MeVeqn}{e^-cm^2}$ . This put us on the same level of radiation that the APV25 chip was built to tolerate

the areas of possible activation is the area more exposed to the target radiation and the collimator positioned in front of the nose-cone of the magnet.

#### 15.2.4 Heat load in magnet cryostat

A detailed design of the Cryogens and coils of the CLEO II solenoid has been obtained and was constructed a detailed model that replicates key components of the magnet (see Fig.154). Particular attention was put in well represent:

1. the 3-5 mm of stainless steel which is the inner bore of the cryostat
2. the 3-5 mm of aluminum thermal shield 3-5 cm beyond (1)
3. the 6+ mm of stainless steel which is the helium vessel
4. any winding forms left at the inner diameter of the coils

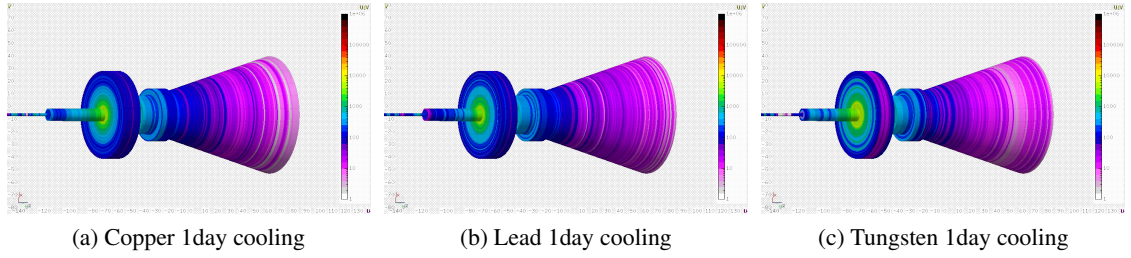


Figure 150: First Baffle: Activation study has been calculated for 3 different Cooling times (here is just shown after 1day), after an assumed exposure to the beam of 3 separate full weeks interleaved by a down time of 4 days. (150a, 150b,150c) The dose is expressed in  $mrem/h$  and here is shown their spatial distribution.

5. the copper matrix in which the Nb-Ti is embedded. Typical conductors of the era were 66-80% copper with balance Nb-Ti (2:1 to 4:1 Cu:SC).

After updating the design, a detailed calculation was done with the PVDIS configuration with Deuterium as its target: This configuration, with the Deuterium target inside the magnet, is the one between the different SoLID configurations which presents the highest flux of neutrons on the Coils. An integrated dose was calculated and determined using the cylindrical symmetry of the system and the flux calculated per  $cm^2$  on the more susceptible parts of the magnet. An integrated dose of  $10^{17} \frac{MeV_{neutron}}{cm^2}$  is needed in order to start to see some modification on the Critical Current ( $I_c$ ) of the magnet. A map of the integrated dose for the PVDIS and  $D_2$  case was created and presents peaks for the integrated fluxes around  $10^{14} \frac{MeV_{neutron}}{cm^2}$ , well below the tolerance level of the magnet. As a consequence, also if it is not known what is the current level of exposure reached by the CLEO-II solenoid, the full scientific outreach that is planned at this moment with SoLID does not seem to be going to affect considerably the lifetime of the coils of the magnet (see Fig. 155).

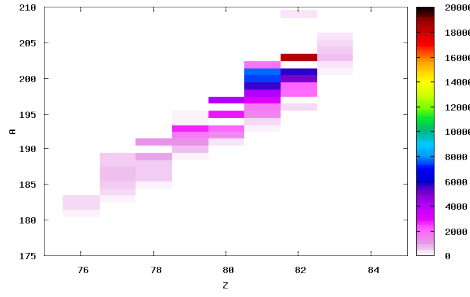
### 15.3 Estimates for radiation damage in the Hall

A study has been done in order to address possible radiation damage areas with the current SoLID design with no further shielding in place. This work has been done in order to address and pinpoint areas that will need to be further investigated when a final design for the magnet and electronics will be reached.

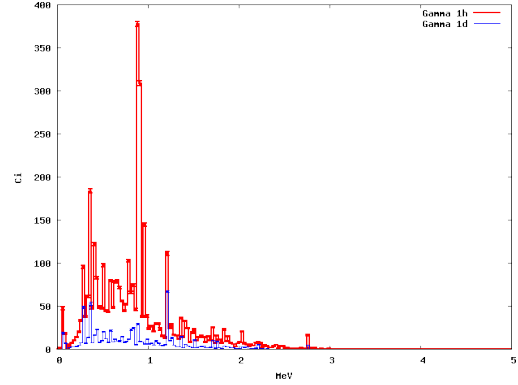
#### 15.3.1 Radiation damage to electronics in Hall

The results of the different simulations run suggest that the design of a shielding structure to minimize the radiation in the Hall seems not to be a priority. With the current different layouts of the multiple configuration possible with the SoLID spectrometer. In this study the magnet has been placed in a dome structure of concrete that mimics the presence of the Hall (It is important to consider that the SoLID spectrometer will not be placed in an open environment, but in an Hall full of equipments, with relative reflectivity that could cause an enhancement of the radiation present in the Hall). Different features of these results are in common with the different configurations for SoLID:

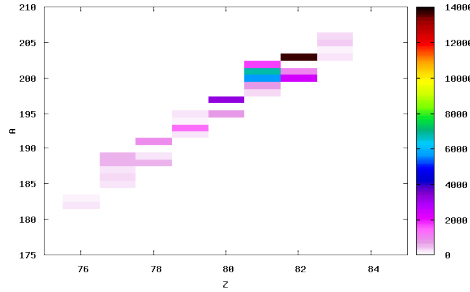
- The radiation damage estimated with the simulation is, as expected, consistently lower in the area outside the SoLID spectrometer respect to the one inside the magnet.



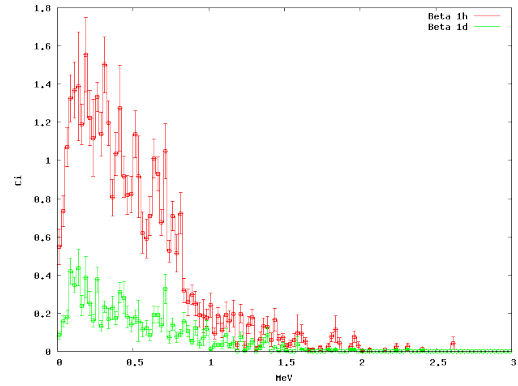
(a) Residual Nuclei for Lead Target after 1hour cooling (Z vs A)



(c) Photon Energy spectrum in Curie due to activation at 2 different cooling times



(b) Residual Nuclei for Lead Target after 1day cooling (Z vs A)



(d) Electron Energy spectrum in Curie due to activation at 2 different cooling time

Figure 151: (151a, 151b) The Residual decaying Nuclei are shown as a function of Z,A in the first baffle assumed constructed on Lead. The Gamma and Beta activity is also shown for the same decaying time (151c, 151d). Determining the activity permits in establishing different needs for shielding at different times of the experimental running (repair or decommissioning)

- In the downstream part of the Hall, the predominant part of the radiation that escape the magnet is present in the last part of the beam-line, enhancing the choice of keeping in the upstream section of the Hall the existing left and right arm spectrometers existing in Hall-A.
- The configurations that have the target area external to the solenoid have also an high radiation area in the proximity of the target

The configuration that gives the higher radiation estimates in this simulation study, is the PVDIS configuration with Deuterium target. The radiation damage estimate in this configuration is investigated in detail in the next section.

### 15.3.2 Radiation from beam pipe

The main source of radiation leaking from the magnet to the Hall is from the beam pipe downstream. In order to quantify the leaking with the different layouts with SoLID, different simulation have been carried out. The one that presents the biggest impact on possible damage to electronics is the PVDIS

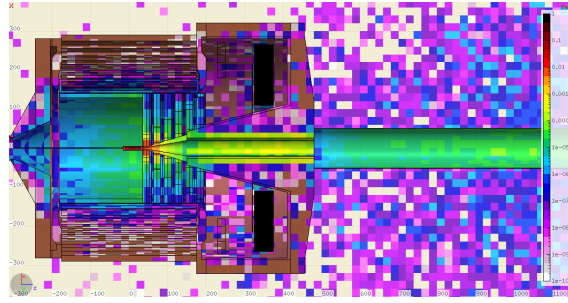
configuration with 40cm Liquid Deuterium target, but the localization of the leakage (close to the beam-line, see figures [156b](#) ,[156c](#) and [156d](#)), and the low level of radiation present, suggest that a shielding construction is not needed. A further factor of 10 reduction, if needed, can probably be reached placing shielding material on the hot areas, around the beam-line, if this area, will be used during the experiment, reaching levels of radiation compatible also to commercial electronics.

### 15.3.3 Radiation with external targets

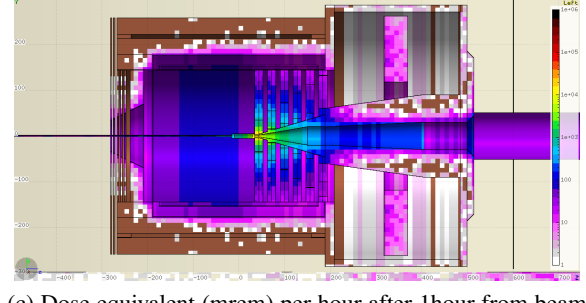
Some of the configuration with the SoLID spectrometer, position their target in the proximity of the entrance of the magnet. Simulations have been done in order to evaluate possible high radiation areas for electronics. An example for the possible areas of high radiation with these layouts for the experiments is shown in figure [157](#) (SIDIS configuration with  $^3He$  target) and figure [158](#) ( $J/\Psi$  configuration with  $H_2$  target).

More details and plots on the studies can be found in [[302](#)].

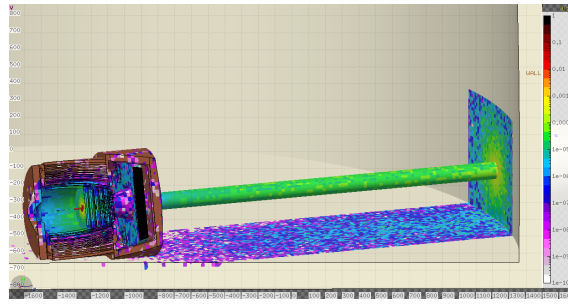




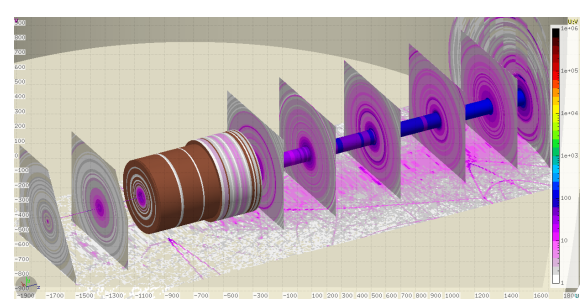
(a) Energy deposited (W) per  $cm^3$  for PVDIS configuration and Liquid Deuterium target



(c) Dose equivalent (mrem) per hour after 1 hour from beam exposure for PVDIS configuration and Liquid Deuterium target



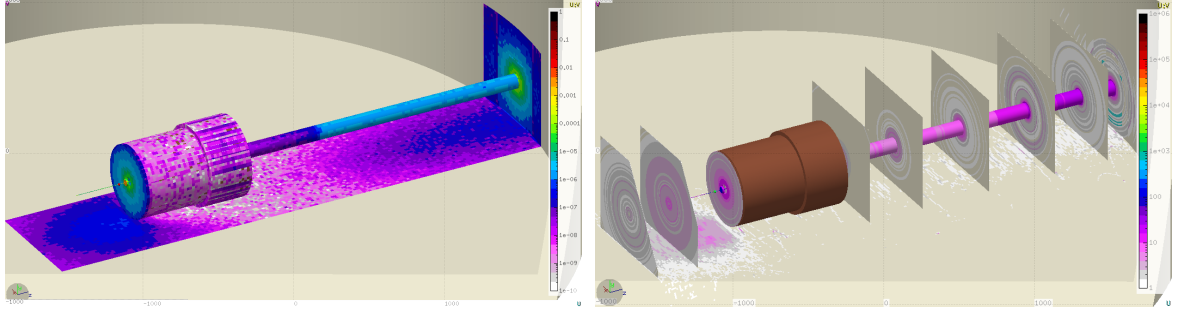
(b) Energy deposited (W) per  $cm^3$  for PVDIS configuration and Liquid Deuterium target (Hall view)



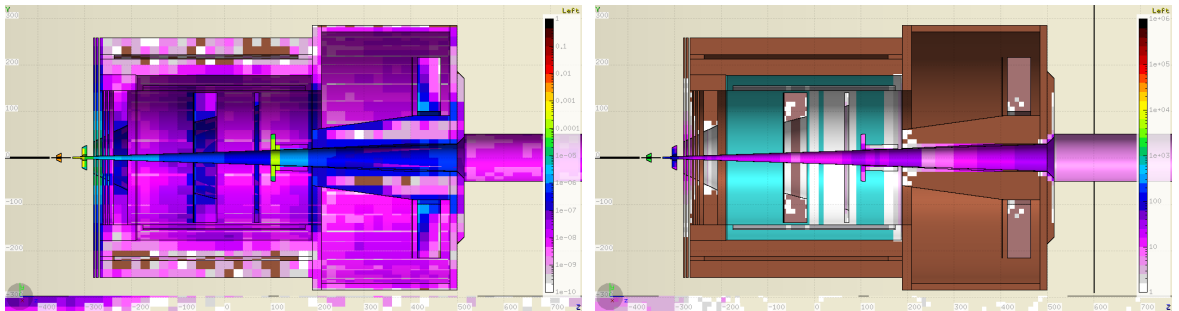
(d) Dose equivalent (mrem) per hour after 1 hour from beam exposure for PVDIS configuration and Liquid Deuterium target (Hall view)

Figure 152: Energy deposited (W) per  $cm^3$  (152a and 152b) considering running condition with Liquid Deuterium target and electron beam current of  $100\mu A$ . The spectrum is averaged in blocks of size of  $20cm \times 20cm \times 20cm$  in order to boost statistics, since this simulation with the complex SoLID design is very high demanding in CPU time. One can see how the power deposited in the first baffle region is considerably higher respect to the one expected in the exit hole of the magnet. In order to obtain the integrated power deposition for the expected beam time for the PVDIS configuration (2000h), multiply the values of the plots by  $7.2E+06$ . Activation dose equivalent (mrem) rate per hour (152c and 152d) expected with the same configuration after 1 hour from beam exposure (  $100\mu A$  for a month ). This study has been done in order to simulate condition in the Hall during running time. For a more accurate description of the activation expected in the baffle area, see figure 150





(a) Energy deposited (W) per  $cm^3$  considering SIDIS running condition with  $^3He$  target and electron beam current of  $15\mu A$  exposure for SIDIS configuration and  $^3He$  target (Hall view)  
(b) Dose equivalent (mrem) per hour after 1 hour from beam exposure for SIDIS configuration and  $^3He$  target (Hall view)



(c) Energy deposited (W) per  $cm^3$  considering SIDIS running condition with  $^3He$  target and electron beam current of  $15\mu A$  exposure for SIDIS configuration and  $^3He$  target (Inside the magnet)  
(d) Dose equivalent (mrem) per hour after 1 hour from beam exposure for SIDIS configuration and  $^3He$  target (Inside the magnet)

Figure 153: Energy deposited (W) per  $cm^3$  (153a 153c) considering running condition with  $^3He$  target and electron beam current of  $15\mu A$ . In order to obtain the integrated power deposition for the expected beam time for the SIDIS configuration (3000h), multiply the values of the plots by  $1.08E+07$ . The main part of the energy is deposited, as expected, in the target area and in the collimator positioned in front of the nose-cone part of the magnet. The energy deposited in the exit hole of the magnet is considerably lower than with the PVDIS configuration. Activation dose equivalent (mrem) rate per hour (153b and 153d) expected with the same configuration after 1 hour from beam exposure (  $15\mu A$  for a month ). This study has been done in order to simulate condition in the Hall during running time.

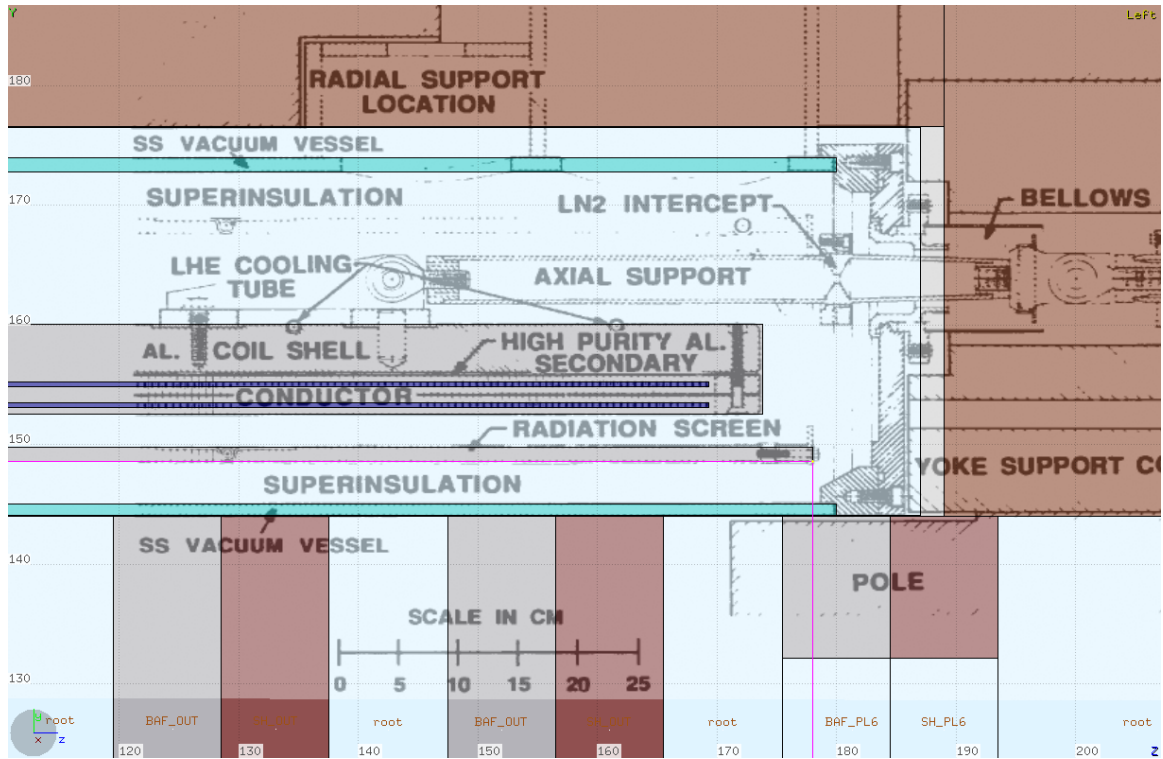


Figure 154: Existing engineering design for the CLEO magnet are put in comparison with the simulation design used for this study.

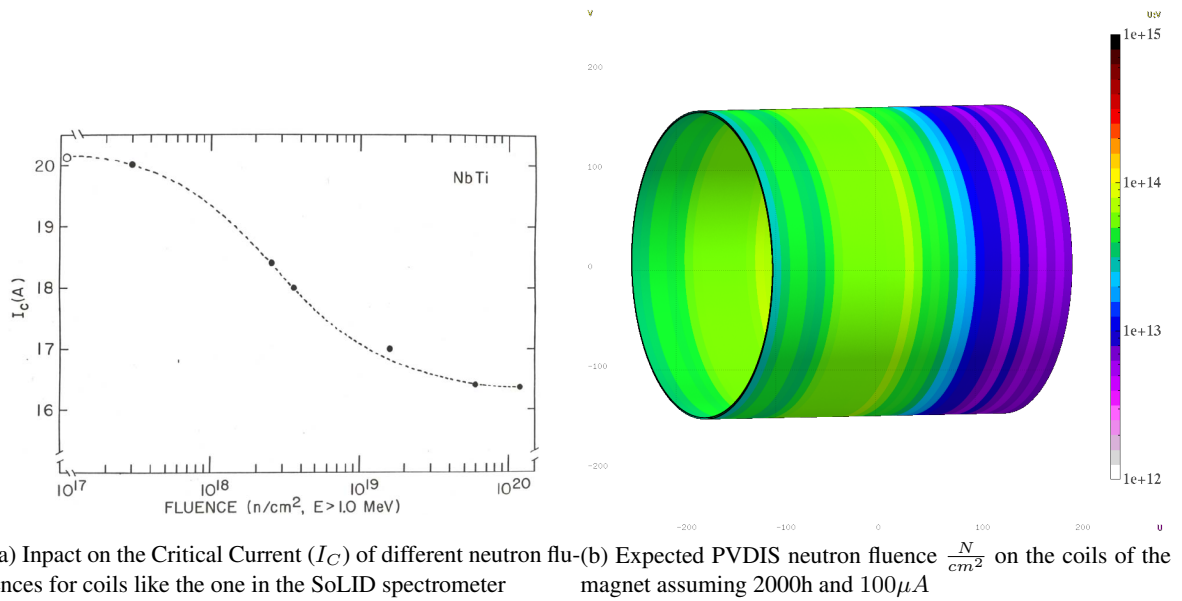
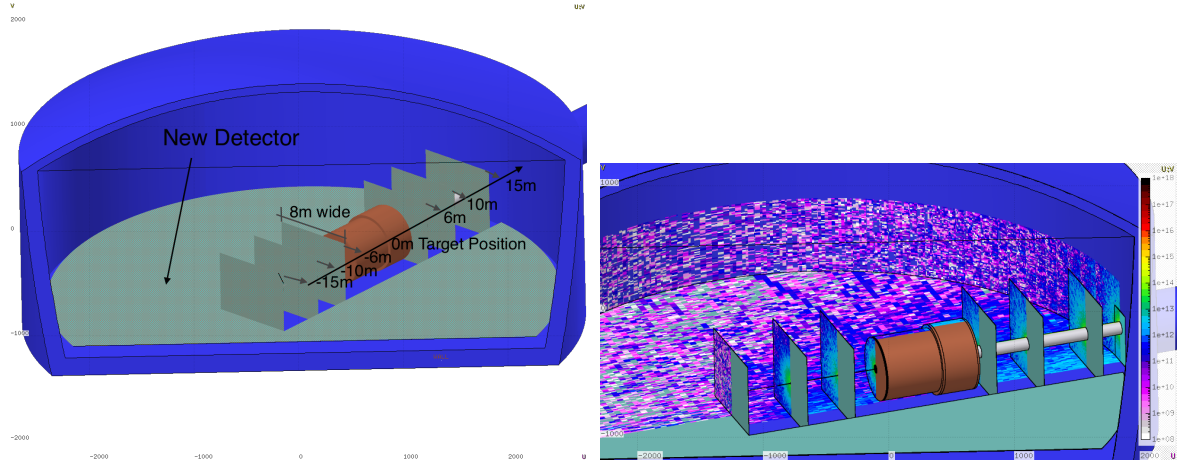
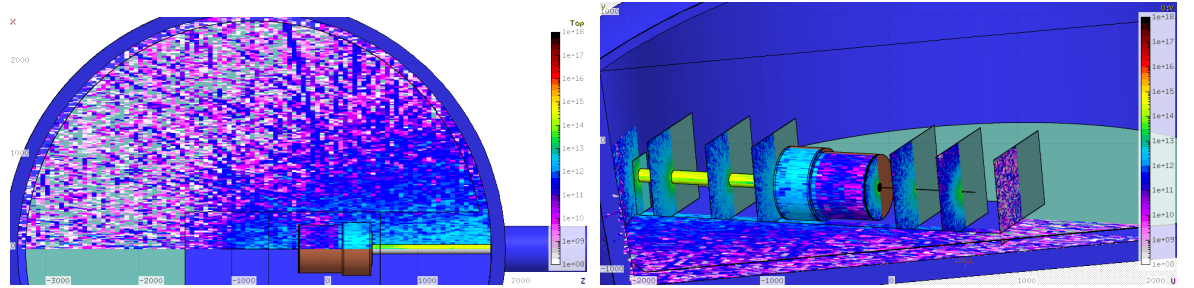


Figure 155: Expected exposure of the Solid magnet coil and expected impact of neutron fluence on Nb-Ti based coil for the Critical Current of the superconducting magnet.



(a) Position of the different planes where in the next plots (b) Estimate of radiation damage in the Hall with the SoLID spectrometer and the PVDIS configuration: A different view planes are put at different positions perpendicular to the beam-line; A plane is also put parallel to the floor at 1m of height



(c) Estimate of radiation damage in the Hall with the SoLID spectrometer and the PVDIS configuration: A different view (d) Estimate of radiation damage in the Hall with the SoLID spectrometer and the PVDIS configuration: A different view

Figure 156: Estimate of radiation damage in the Hall with the SoLID spectrometer and the PVDIS configuration. The leading part of radiation present in the Hall for the SoLID spectrometer is leaking through the downstream part of the beam-line assembly. In this plot is shown the 1MeV Neutron equivalent flux per  $cm^2$  on the volumes surfaces estimated for 2000h of continuous running with a beam current of  $100\mu A$  (This is the expected beam-time with the PVDIS configuration). In order to better show the behavior of the radiation leaking, different plane of observation have been inserted (at a distance from the target of  $\Delta z = -15m$ ,  $\Delta z = -10m$ ,  $\Delta z = -6m$ ,  $\Delta z = 6m$ ,  $\Delta z = 10m$ ,  $\Delta z = 15m$  (see Fig. 156a). The level of radiation leaking increases as one moves farther from the target, reaching a maximum  $\leq 10^{15} \frac{N_{1MeV}}{cm^2}$ . These levels of radiation is on the “mild to severe” damage range for commercial semiconductors ( as one can see comparing them with Estimate of the tolerance of different material plots 143). This area is not expected to carry any delicate equipment. On the upstream section of the beam-line, the level of radiation leaking is tolerable to also commercial equipment (not rad-hard). A comparable plot of this one, with a projection plane on the zy axis, is show in figure 156c

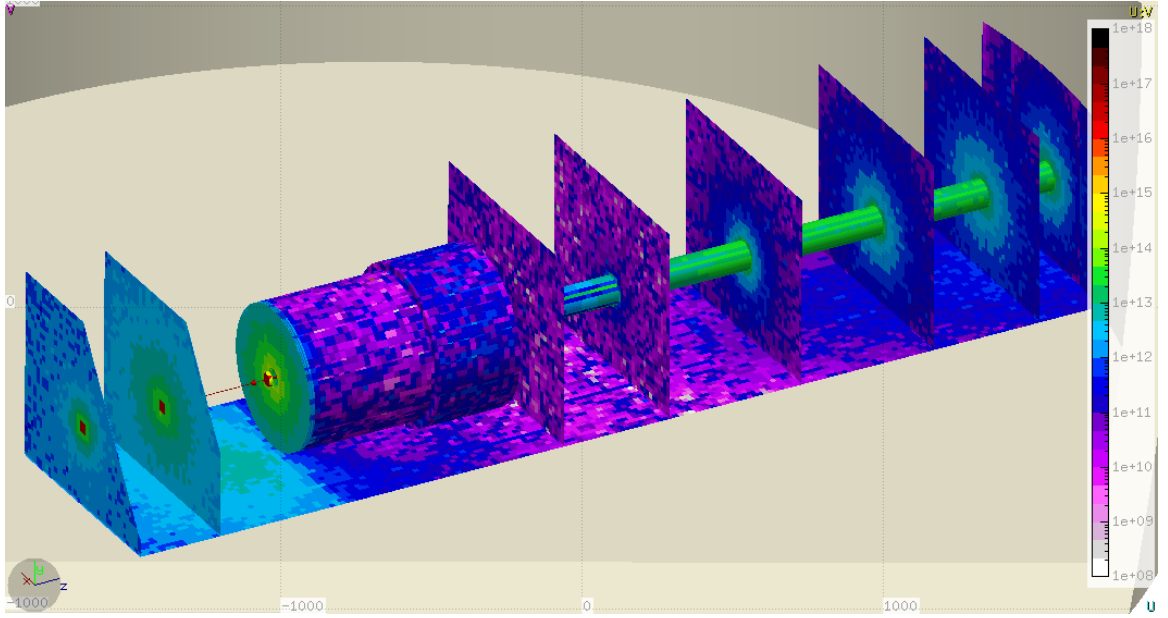


Figure 157: Estimate of radiation damage in the Hall with the SoLID spectrometer and the SIDIS  $^3\text{He}$  configuration. The leading part of radiation present in the Hall for the SoLID spectrometer is originating from the target area and the closer surface of the magnet. In this plot is shown the 1 MeV Neutron equivalent flux per  $\text{cm}^2$  on the volumes surfaces estimated for 3000h of continuous running with a beam current of  $15\mu\text{A}$  (This is the expected beam-time with the SIDIS configuration). In order to better show the behavior of the radiation leaking, different planes of observation have been inserted (at a distance from the center of the Cryostat of the magnet of  $\Delta z = -10\text{m}$ ,  $\Delta z = -6\text{m}$ ,  $\Delta z = 6\text{m}$ ,  $\Delta z = 10\text{m}$ ,  $\Delta z = 15\text{m}$ ,  $\Delta z = 20\text{m}$ ,  $\Delta z = 24\text{m}$ ). The level of radiation leaking increases as one moves farther from the target, reaching a maximum  $< 10^{14} \frac{\text{N}_{1\text{MeV}}}{\text{cm}^2}$ . These levels of radiation is on the “mild to severe” damage range for commercial semiconductors ( as one can see comparing them with Estimate of the tolerance of different material plots [143](#)). This area is not expected to carry any delicate equipment.

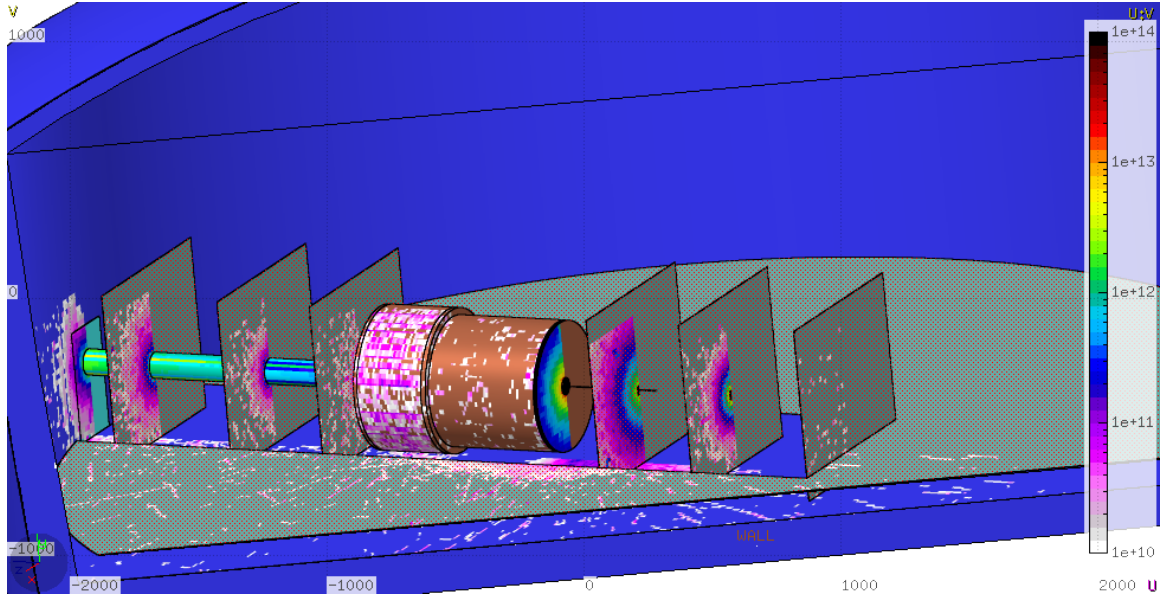


Figure 158: Estimate of radiation damage in the Hall with the SoLID spectrometer and the  $J/\Psi$  configuration with a 15cm Liquid Hydrogen target. The leading part of radiation present in the Hall for the SoLID spectrometer is originating from the target area and the closer surface of the magnet. In this plot is shown the 1MeV Neutron equivalent flux per  $cm^2$  on the volumes surfaces estimated for 60 days of continuous running with a beam current of  $3\mu A$  (This is the expected beam-time with the  $J/\Psi$  configuration). In order to better show the behavior of the radiation leaking, different planes of observation have been inserted (see Fig. 156a for reference of the position of each plane). The Color scale is different than in the previous cases in order to enhance the details in the desired region.

## 16 Slow Controls

Slow Controls typically covers the “infrastructure support” systems and logging for the detector package as a whole. This includes real-time controls and status monitoring of power, vacuum, temperatures, etc., in addition to integrated safety interlocks and alarm functions. Typical measurement and response times for such systems are on the order of a 100s of milliseconds to seconds. More rapid response times are also available if needed. Common examples of slow controls involve the high- and low-voltage power supplies for all detector apparatuses, gas composition and flow regulation, control of gain-monitoring systems, etc.

This section *excludes* any discussion of slow controls for the target and solenoid magnet. Slow controls for those systems will be designed and implemented by their respective working groups. The systems covered here involve only the SoLID detector subsystems.

Due to the obvious interdependence between the hardware and the software used to control it, details of several slow control components will need to wait until the hardware design is better developed (*eg.* gas systems). We will give an overview of some baseline requirements and expectations that the Collaboration will abide by to ensure slow controls development and implementation will proceed smoothly.

It is understood that any fast interlocks (*i.e.* millisecond level or faster) that cross system boundaries need to be identified at the design stage. Examples may include tripping high-voltage if the gas flow is interrupted for the GEM system, disabling the flammable gas flows in the event of a fire alarm, etc.

### 16.1 General Requirements

The Collaboration agrees that all components must be able to interface with the EPICS (Experimental Physics and Industrial Control System) environment already present at Jefferson Lab. This imposes a common mid-level API for inter-system communication and allows the systems to take advantage of the well supported EPICS infrastructure at JLab. This includes local expert support from other experimental Halls (particularly Halls B & D), and the Accelerator Division for any necessary PLC, software and/or hardware IOC development, as well as taking advantage of JLab’s EPICS data archiver “MYA”.

### 16.2 Frontend GUIs

The graphical interface employed for all systems is expected to be based on the Control Systems Studio (CSS) environment. This is an Eclipse-based toolkit that is slowly replacing the legacy EDM/MEDM GUIs developed during JLab’s 6 GeV period. Hall D and Hall B already make extensive use of the CSS toolkit, and Hall C will be migrating its legacy M/EDM GUIs as time permits.

The BEAST alarm handler, part of the CSS system, will be used to monitor EPICS variables and alert shift crew and/or external experts of problems.

Systems that require lower-latency response times than softIOCs and EPICS polling systems can provide will investigate the CompactRIO (cRIO) standard successfully used in Halls B & D.

The Hall B slow controls development experience, in particular, has been well documented by those involved and will provide an excellent local repository of interface code and management processes that SoLID can leverage.

### 16.3 High/Low Voltage Controls

High Voltage hardware will be standardized as much as possible. CAEN and Wiener systems are both in use at JLab. They each come with integrated EPICS support and pre-existing software support on-site. Detector, sub-detector, and individual channel control and monitoring will be provided. Legacy LeCroy HV systems will *not* be supported.

### 16.4 DAQ Crate Control

It is desired to have realtime monitoring of VME and other data acquisition crate power systems and temperatures. All DAQ crates are expected to provide an integrated ethernet interface and EPICS support. Examples of such hardware include the Wiener 60xx series in common use across JLab.

### 16.5 Gas Systems Requirements

In addition to the necessary EPICS interface, the Collaboration agrees that the various gas sub-systems (Cerenkovs, GEMs, MRPC) will standardize any hardware that requires software support. This includes items such as mass flow controllers (MFCs) and hardware process controllers, etc. This will allow for a common spares inventory and simplify control software development and maintenance.

### 16.6 Detector Systems

The following list runs through the various sub-detectors and summarizes the necessary slow controls.

- **EC:** HV control and monitoring.
- **FA/LASPD:** HV control and monitoring.
- **GEM Tracking:** HV/LV control and monitoring. The non-recirculating gas system will use Ar/CO<sub>2</sub> at STP and will employ a basic gas mixer system with flow monitoring and control.
- **LGC:** HV control and monitoring. The CO<sub>2</sub> gas employed operates at STP and will be served by a simple non-recirculating “flow-through” system.
- **HGC:** HV control and monitoring. The C<sub>4</sub>F<sub>10</sub> gas employed is expensive and used in large quantities. Such a system will require a somewhat sophisticated recapture/purification/recirculation infrastructure involving PLC/IOC controls that remain to be designed.
- **MRPC:** HV/LV control and monitoring. The MRPC gas system employs a 5% SF<sub>6</sub> + 90% R134 + 5% Isobutane mix that will likely require a recapture/recirculation infrastructure also involving a PLC/IOC system. This is still to be designed.

In addition to the above items, gain-monitoring systems have been discussed that would also require some nominal controls. It is not expected that such systems would be a significant burden.



## 17 Electron Beam Polarimetry

The interpretation of the measurement of the parity-violating asymmetry relies on precise correction for finite beam polarization, with an accurate absolute normalization to 0.4% accuracy at both 11 GeV and 6.6 GeV. This will be achieved using two independent measurement techniques with independent sources of calibration errors, which can be directly cross-checked to high precision. This is an ambitious goal. The most precision electron beam polarimetry result to date in a physics publication is the 0.5% Compton polarimetry result by the SLD collaboration [303]. Compton polarimetry is well-suited for the energy and intensity of the upgraded Jefferson Lab beam. Plans for upgrading the existing Hall A Compton polarimeter to achieve 0.4% precision are described below.

The best candidate for a second, high-precision, independent measurement is Møller polarimetry. The use of iron foils in high magnetic fields can provide a precision well better than 1%, and may prove to be more precise to the level of 0.5%.

### 17.1 Compton Polarimetry

Compton polarimetry is a very promising technique for high precision polarimetry at beam energies above a few GeV. Beam interactions with a photon target are non-disruptive, so Compton polarimetry can be employed at high currents as a continuous polarization monitor. The photon target polarization can be measured and monitored with a very high precision, and the scattering between a real photon and free electron has no theoretical uncertainty, such as the atomic or nuclear effects which can complicate other measurements. Radiative corrections to the scattering process are at the level of 0.3% and are very precisely known. While the SLD collaboration result, with a precision of 0.5%, demonstrates the feasibility of very high accuracy Compton polarimetry, that measurement was ultimately limited by the inability to detect individual scattered particles (due to the pulsed beam) and the high Bremsstrahlung background in the photon detector due to the proximity to the interaction region. Conditions at JLab are favorable for both of these concerns. The existing apparatus and plans for future improvements are described below.

### 17.2 The Hall A Compton Polarimeter Baseline Upgrade

As pictured in Fig. 159, the Hall A Compton polarimeter [304] is located in a chicane, about 15 meters long, just below the beamline. After modification of the bend angle to accommodate 11 GeV running with the existing chicane magnets, the electron-photon interaction point will be 21 cm below the primary (straight-through) beamline. After passing the electron-photon interaction point, the electron beam is bent about 3.5 degrees by the third chicane magnet and then restored to the main beamline. The scattered electrons are separated from the primary beam and detected using silicon microstrips, just before the fourth chicane magnet. Scattered photons pass through the bore of the third chicane magnet to be detected in a calorimeter.

The photon target is a 0.85 cm long Fabry-Perot cavity crossing the electron beam at an angle of  $1.4^\circ$ . The laser system can be configured for infrared (1064 nm) or green (532 nm) light, and has achieved power levels of 10 kW of green light for polarimetry measurements. The laser light is polarized using a quarter-wave plate, and can be toggled between opposite polarizations of highly circularly polarized light. The feedback loop which locks the laser to the cavity resonance can be disabled to enable backgrounds from all non-Compton-scattering processes. To reduce overhead from the time required to re-lock the cavity, the transition between laser states is typically performed with a period of 1-2 minutes. The polarization of the transmitted light from the locked cavity and



the reflected light from the unlocked cavity are each monitored and can be used to characterize the laser polarization at the interaction point.

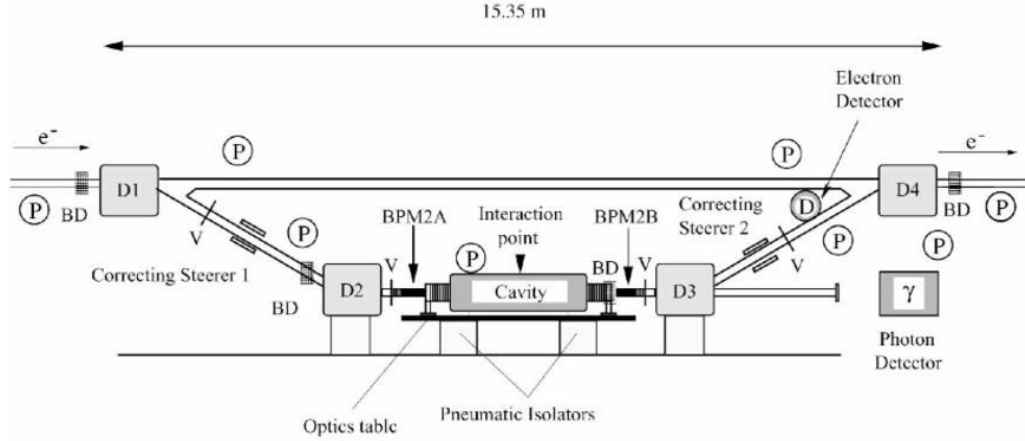


Figure 159: Schematic of the Hall A Compton polarimeter. Figure from [304].

The vacuum in the interaction region is at the level of few  $\times 10^{-8}$  torr, implying a photon background rate due to Bremsstrahlung scattering from residual gas of around  $5 \text{ Hz}/\mu\text{A}$ . The dominant source of background in the photon detector is thought to be tails of the beam halo distribution interacting with the apertures in the interaction region. In contrast, for the electron detector the background is thought to be dominated by energy tail or position halo of the primary beam since electrons from aperture scattering would presumably not cleanly transit the third dipole. When well-tuned, the background rates in the photon and electron detectors have been seen to be roughly similar: around  $<100 \text{ Hz}/\mu\text{A}$  in recent use. At 11 GeV, with a 10 kW IR cavity, the Compton-scattered rates would be approximately  $20 \text{ kHz}/\mu\text{A}$  and the asymmetry will range from 17.8% to -4% over the energy spectrum. At 6.6 GeV, a 10 kW green cavity will be used, which will provide a rate of  $13 \text{ kHz}/\mu\text{A}$  with an asymmetry ranging from 20.9% to -4.7%. If backgrounds remain comparable to recent operation, statistical precision of 0.4% would be possible in less than 5 minutes, depending on the specific detection and analysis approach which is considered.

Electrons are detected in a set of 4 planes of silicon microstrips located just before the 4th dipole. Each microstrip instruments 192 strips with a pitch of  $240 \mu\text{m}$ . Custom readout electronics pre-amplify and discriminate signals from the microstrips, implement a simple tracking algorithm to reduce non-directional backgrounds, and count hits in each strip over specified integration gates corresponding to the helicity pattern of the electron beam. Presently, this system is operating at low efficiency with poor signal size for a minimum ionizing track compared to environmental noise on individual strips. The baseline upgrade would include an improvement in this system to achieve high efficiency and high signal-over-noise for the microstrip readout. The use of diamond microstrips, such as were recently successfully used for the Hall C Compton polarimeter [305], is under consideration. Such diamond microstrips are more difficult to procure and in principle are more challenging to instrument than silicon strips, however, they are more radiation hard and less susceptible to low-energy photon backgrounds.

The calorimeter for detecting scattered photons lies about 7 meters downstream of the interaction point. The strong forward boost of scattered photons leads to a tightly collimated photon beam ( $<1 \text{ mrad}$ ), so the calorimeter size is determined by consideration of energy resolution through

shower loss. The photon calorimeter is a GSO crystal scintillator of 6 cm diameter and 15 cm length, with a single photomultiplier tube. The PMT signal is split between two parallel data acquisitions: one with a fast-counting, buffered ADC self-triggered on pulses from the photon detector, and the other utilizing a 250MHz flash ADC (fADC) to integrate the total signal over periods corresponding to the helicity pattern of the electron beam. The fADC system can also record a very low rate of individual pulses for calibration. Each of these dual readouts can be analyzed independently. The fast counting ADC readout and the sample pulses in the fADC system can both be triggered using the electron detector, providing an electron-photon coincidence spectrum for calibration.

### 17.3 Upgrades Beyond the Baseline

There are several issues which must be addressed, related either to operation at the higher beam energy or to the very high level of precision which is proposed.

- The electron beam halo — a term meant to describe a long tail on the momentum or position distribution of the beam — is expected to be larger at 11 GeV compared to 6 GeV operation, due to synchrotron light emission in the recirculation arcs which will increase the momentum-normalized beam emittance. For Compton polarimetry, a tail on the beam energy distribution is directly responsible for the dominant backgrounds in electron detection, while scattering of beam halo from narrow apertures in the interaction region is thought to dominate backgrounds in photon detection.
- The measurement of the laser polarization must be performed with very high precision.
- The total power of synchrotron radiation emitted by the beam in the chicane arcs will be more than an order of magnitude higher compared to Compton measurements in the 6 GeV era, and this radiation spectrum will be significantly stiffer. Dilution from this radiation would complicate photon and electron detection.
- Photon detection must provide a well-characterized and linear response for photons in an energy range from about 3 GeV to low energies and over a large variation in signal rate, while being radiation hard and also insensitive or shielded from the synchrotron radiation power.

These issues are addressed by several modifications which go beyond the baseline 11 GeV upgrade, listed below and described in the following sections. These improvements are expected to allow us to achieve the precision goals listed in Table 33.

- **Laser system** A larger crossing angle for the photon and electron beams would allow larger electron beam apertures, and reduce backgrounds in the photon detector. This increase in crossing angle comes at the expense of lower luminosity, leading to a tradeoff in signal rate and background rate. With the high cavity power that has been achieved with this laser system, we do not expect to be limited by laser power even at increased crossing angle. The decision on crossing angle can be made when more is known about beam conditions at 11 GeV. The beamline through the chicane magnets is one inch inner diameter, which is about a factor of three larger than the aperture required by the present laser crossing angle. The luminosity would drop roughly linearly with crossing angle, and even with a factor of 1/3 the statistical power of the signal rate for a 10 kW cavity would still be sufficient assuming a reduced background fraction.

In addition to the option to increase this crossing angle, a system for measuring laser polarization inside the resonant optical cavity (although not while locked to resonance) must

Relative error (%)	electron	photon
Position asymmetries*	-	-
$E_{Beam}$ and $\lambda_{Laser}$ *	0.03	0.03
Radiative Corrections*	0.05	0.05
Laser polarization*	0.20	0.20
Background / Deadtime / Pileup	0.20	0.20
Analyzing power Calibration / Detector Linearity	0.25	0.35
Total:	0.38	0.45

Table 33: *Goals for systematic errors for the Hall A Compton polarimeter at 11 GeV. Topics marked \* are common systematic errors between the photon and electron analyses, while the others are largely independent between the detector systems.*

be developed and used, along with a thorough study of all optical components, to improve knowledge of the photon polarization.

- **Chicane Modification** The synchrotron light power on the photon detector will be significantly reduced by installing shims to increase the fringe fields of the chicane dipole magnets in the interaction region. This would also soften the synchrotron energy spectrum, making shielding more effective. The effect of synchrotron light on the electron detector is being investigated, with the possibility to add some baffling to limit reflection into the detector.
- **Photon Detector** The photon detection system used for recent running will be replaced with a detector better matched to the Compton photon energy spectrum for 11 GeV operation.

These upgrades are described in more detail below.

### 17.3.1 Laser System and Luminosity

As described above, in the current configuration of the Hall A Compton, the electron beam interacts with green (532 nm) light in a resonant optical cavity at a crossing angle of about  $1.4^\circ$ . After accounting for the length of the optical cavity (about 85 cm) and the finite size of the cavity mirror, it is necessary to enforce an aperture on the electron beam of  $\pm 5$  mm. It is thought that this narrow aperture is the dominant source of background for 6 GeV running. At higher energies, synchrotron light emission in the accelerator recirculation arcs will increase the beam emittance and presumably lead to significantly larger backgrounds from this aperture scattering. In present use of the Compton polarimeter, frequent beam tuning is required to maintain operation with the signal-over-background  $> 10$ . A large background signal is often associated with large fluctuations over the period of time in the laser on/off cycle used to measure backgrounds. This reduces the measurement precision, and potentially introduces a significant systematic error through instability in the phototube under large variations in rate. For this reason, it is desirable to keep the signal-over-background ratio large.

The aperture can be widened only by increasing the laser crossing angle which would also lower the luminosity. Although the baseline upgrade plans do not make provision for changing this crossing angle, operability at 11 GeV may require larger apertures. At a finite crossing angle  $\alpha$ , the luminosity for a continuous-wave electron and photon beam, with intersecting electron and photon

waists sizes  $\sigma_e$  and  $\sigma_\gamma$ , is given by:

$$\mathcal{L} \approx \frac{1 + \cos \alpha}{\sqrt{2\pi}} \frac{I_e P_\gamma}{ek_0 c} \frac{1}{\sqrt{\sigma_e^2 + \sigma_\gamma^2}} \frac{1}{\sin \alpha} \quad (28)$$

Here  $P_\gamma$  is the power of the photon beam,  $I_e$  is the current in the electron beam, and  $k_0$  is the photon energy scattered at the kinematic maximum limit of colinear backscattering. As an example: at 10000 W stored power at 532 nm, the Compton scattering rate would be about 12 kHz/ $\mu$ A at  $1.4^\circ$  crossing angle and about 4.8 Hz/ $\mu$ A at  $3.5^\circ$ . At the expense of approximately a factor of 2.5 in luminosity, that larger crossing angle would allow a  $\pm 0.5$  inch aperture, comparable to the maximum aperture allowed by the 1" beam pipe diameter in the bore of the existing dipole magnets in the chicane.

With an available laser power of 10 kW, the polarimeter is not expected to be limited by low signal rates even at the larger crossing angles. However, the drop in luminosity with increasing crossing angle suggests that any change must be optimized from the point of view of signal-over-background. Until beam tests at higher beam energies are preformed to form reliable estimates of background levels, it is prudent to design for both large crossing angle and large luminosity.

We propose the use of an infrared cavity storing 10 kW of optical power at 1064 nm for operation at beam energy above 8.8 GeV, and a cavity storing 10 kW of optical power at 532 nm for beam energies at 6.6 GeV and below. The primary disadvantages to the longer photon wavelength are the reductions in analyzing power and softening of the energy spectrum (17% analyzing power and 1.8 GeV maximum photon energy for IR at 11 GeV, compared to 32% and 3 GeV for 532 nm). The advantages for the IR system would be a greater available luminosity and system reliability. While the cross-section is very similar between the two photon energies, at 1064 nm there are twice as many photons per unit energy. At 10 kW, an IR cavity would provide a rate of 9 kHz/ $\mu$ A at the increased crossing angle to allow the full  $\pm 0.5$ " electron beam aperture, or 23 kHz/ $\mu$ A at the original design  $1.4^\circ$  crossing angle. The 532 nm system requires an additional stage to frequency-double the original 1064 laser light. Without this doubling stage, the IR system can inject higher power to the cavity, enabling higher cavity power or the same cavity power with reduced cavity gain. A lower gain cavity will typically be more robust, and and less sensitive to radiation damage of the cavity optics. At beam energies below 8.8 GeV, the improvement in analyzing power and higher scattered photon energy endpoint are worth the possible trade-off in ease of operability.

Precision electron beam polarimetry also requires precise determination of the polarization of the photon target. This has proved to be the dominant systematic error contribution in recent Hall A Compton polarimeter measurements, in part because the use of a high-gain resonant cavity significantly complicates this determination. In a resonant cavity, the polarization state of the stored light can not be directly measured without destroying the resonance. For the present Hall A polarimeter, the laser polarization is inferred from measurements of the light that transmits through the cavity. A transfer function, relating the polarization of light in the Compton Interaction Region (CIP) to the polarization measured in the transmitted beam outside the vacuum vessel, is determined from measurements with an un-locked cavity. The highly-reflective cavity mirrors must be removed for these measurement, and the cavity must be open to air, which implies a relaxation of stress-induced birefringence of the vacuum entrance and exit windows. Contributions from birefringence in the cavity mirror substrate and stress on the vacuum windows can be characterized separately, but as a practical matter these corrections are difficult to determine with high precision. For the Hall A polarimeter, previous studies have quoted the uncertainty in beam polarization to be 0.35%, but in recent operation the uncertainty could not be bounded to better than 0.7%.

An improved technique has been used in Hall C to control the laser polarization uncertainty. The

polarization of light arriving at the cavity entrance can be inferred from light reflected back from the cavity and analyzed with the same apparatus used to create the initial polarization state, measuring a single power level [306]. This technique was employed in Hall C to maximize the circular polarization of light injected in the cavity and to monitor the polarization during the run. It was verified to work by two methods. In the first, with the cavity under vacuum in running conditions, a scan over a broad range of initial polarization states was performed, and the recorded analyzed reflected power was shown to be well described by the simple hypothesis of optical reversibility. A more direct verification was made with the cavity opened, directly measuring the polarization of the injected light in the cavity and correlating this with the analysis of the reflected light. The correlation is shown over the full range of the scan, and zoomed in for measurements at maximum circular polarization, in Fig. 160. In operation, the Hall C Compton polarimeter ran with the reflected light very near minimum, with an implied uncertainty on the circular polarization within the cavity of 0.1%.

These studies demonstrate that this technique may provide knowledge and monitoring of the circular polarization in the cavity to the level of 0.1%. An *in situ* measure of the polarization would be a valuable confirmation of this procedure. Modifications to the interaction region will be made to allow an insertable, vacuum-compatible analysis assembly for measurements of the beam in the CIP. The power level for such measurements will necessarily be very low, as the highly reflective mirrors of the cavity will attenuate incident light, but such a direct measurement would include all effects of birefringence and depolarization in the injection of optical power into the cavity.

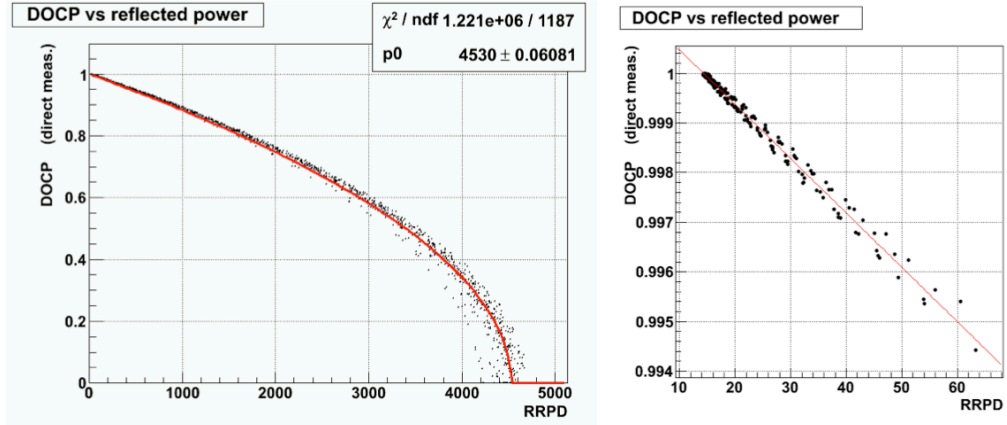


Figure 160: Measured degree of circular polarization in the Hall C Compton laser cavity vs. the polarization-analyzed reflected light, measured over a broad scan of initial polarization states. The figure on the right is zoomed in the region of maximum circular polarization.

### 17.3.2 Alternative Laser System

An alternative laser system has also been considered, based on the use of a short-pulse RF laser synchronized to the electron bunch frequency. Such a system would concentrate laser power on the electron bunches, in effect creating an electron-photon collider. For a laser with narrow pulse structure ( $\approx 10$  ps) and repetition frequency sub-harmonic to the electron beam ( $f_{laser} = 499$  MHz

/  $n$  with integer  $n$ ), the the ratio of luminosity for the same average power goes as:

$$\frac{\mathcal{L}_{pulsed}}{\mathcal{L}_{CW}} \approx \frac{c}{f_{beam} \sqrt{2\pi}} \frac{1}{\sqrt{\sigma_{e,z}^2 + \sigma_{\gamma,z}^2 + \frac{1}{\sin^2 \alpha/2} (\sigma_e^2 + \sigma_\gamma^2)}}. \quad (29)$$

Here  $f_{beam}$  is the electron repetition rate and  $\sigma_{e,z}$  ( $\sigma_{\gamma,z}$ ) is the longitudinal size of the electron (laser) pulse. For the parameters relevant to the proposed system, this corresponds to an enhancement of luminosity per unit power of between 20-50. Commercially available mode-locked laser systems has been identified providing 45 W at 1064 nm, with 100 MHz repetition rates and 10 ps pulse widths. Assuming an average injected power of 30 W at the  $3.6^\circ$  crossing angle, such a pulsed laser would provide 330 Hz/ $\mu$ A with a single-pass beam, that is, without the resonant optical cavity.

Although the relatively low rates would be expected to be a disadvantage, it may turn out to be operable depending on the characteristics of the 11 GeV electron beam. The statistical precision (0.4% in about 3 hours) would be sufficient for a high precision measurement. The primary advantage of such a system would be a more straightforward determination of the laser polarization, relative to a high-gain optical cavity. There are other advantages as well. Locking and unlocking a cavity takes time, so to maintain a high duty factor for a cavity system the locked and un-locked periods used to determine backgrounds are long ( $\approx 1$  minute) relative to the fluctuations in the background. On the other hand, a laser can be turned off or deflected to a dump quickly, so background measurements for such a single pass system could take place quickly, potentially providing superior control of background fluctuations even if the signal-over-background ratio is smaller. Similarly, without the requirement to maintain the delicate balance of signal levels necessary to robustly lock a high-gain cavity, systematic studies varying laser power or position would be simplified.

Should the rate from such a system be unmanageably small relative to backgrounds, it could be roughly doubled using a “butterfly” cavity to recirculate the exit beam through the interaction point. A more powerful option would be a hybrid system in which the RF pulses are stored in a resonant optical cavity. A moderate cavity gain  $\approx 20$  would double the Compton signal rate compared to the 10 kW, gain  $\approx 3000$  CW default design. At such a low gain, the cavity lock would be relatively easy to acquire, potentially enabling more rapid background measurements than the high-gain system. The polarization measurement would also likely be simpler than for a high-gain cavity system, as the injection beam in the interaction region would still be similar to the beam stored through relatively few resonant reflections.

Such a cavity would require the dual resonance condition of being both an integral number of optical and RF wavelengths. This is not a particularly difficult condition to maintain. The injection laser must be mode-locked to ensure coherence between pulses. Locking mode-locked lasers to Fabry-Perot cavities has been actively pursued over the last decade in development studies for Compton-based X-ray sources [307, 308] and for a polarized positron source for the ILC [309, 310], with significant technical success beyond the requirements for this proposed system.

The above discussion demonstrates the utility and technical feasibility of the alternative proposal for a 10 ps pulse length, 100 MHz, 1064 nm laser system operating either as an injection laser for a gain  $\approx 20$  resonant cavity or as a 30 W single-pass system. This alternative proposal would require new investment for acquisition of the injection laser and high-power optics. In addition, the possibility of time-dependent polarization in the short RF laser pulse may additionally complicate the laser polarization determination. The alternative system remains as a backup should complications in determining the laser polarization inside the high-gain laser cavity prove to be insurmountable.

### 17.3.3 Chicane Magnet Modification

At 11 GeV, significant synchrotron radiation is emitted when the electron beam is bent in a magnetic field. The total radiated power rises as  $\beta^4$  for the same bend radius. At 11 GeV, this radiation load will be a significant background in the photon detector and may overwhelm the signal from Compton scattering. Figure 161 shows the energy spectrum of synchrotron light attenuated by lead shielding between 1–5 mm thick, depending on the beam energy. On the left, the spectrum for 11 GeV with unmodified magnets is compared to calculations for the recent runs of HAPPEX-III (3 GeV) and PV-DIS (6 GeV). On the right, the energy spectrum (“Fringe 2”) is shown when iron extensions, 15 cm in length, are added to the dipole magnets in order to provide an extended region of reduced field. This reduced magnetic field produces synchrotron light with lower energy range and with reduced intensity, for the portion of the electron beam trajectory that projects to the photon detector. With this modification, the bending strength of the magnet remains the same but the synchrotron light radiated into the detector is reduced by a factor of  $10^4$ , to a level comparable to HAPPEX-III. The magnetic field extensions were modeled using TOSCA, and have been constructed. Field measurements have been taken to verify the magnetic model for both the integral  $Bdl$  and the shape of the fringe field with and without the field extensions. These field extension pieces have been built and will be ready for installation at the start of 11 GeV operations.

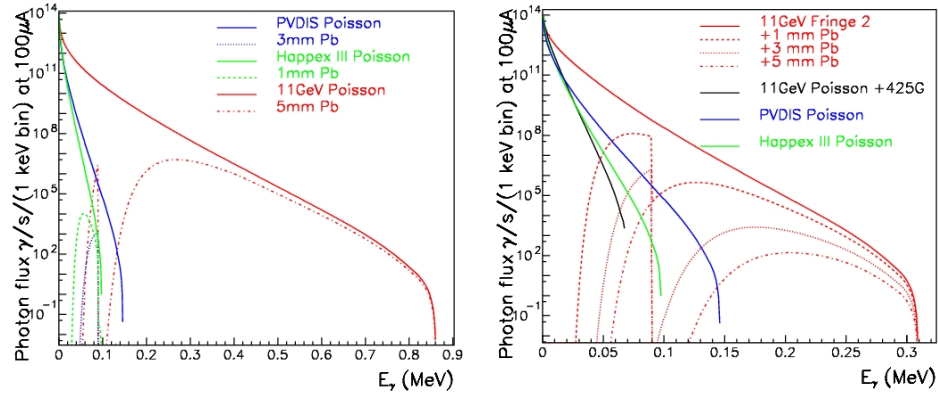


Figure 161: Energy spectrum of synchrotron radiation penetrating lead shielding of thickness listed. Plot on left shows unmodified chicane magnets, plot on right shows energy spectrum for proposed magnetic shims which reduce the field for the bend radiating into the Compton photon detector acceptance. Note the different horizontal scales between the plots.

### 17.3.4 Photon Detection

The specific calorimeter to be employed is not yet determined. The present calorimeter is a GSO crystal scintillator, which has excellent light yield suitable for measurements at low energies. The crystal is too small to contain most showers at higher energies, and a new calorimeter will be required for precision measurements at 11 GeV. In the past, Hall A has used an undoped lead tungstate ( $\text{PbWO}_4$ ) array. This may be suitable for 11 GeV operation; the relatively low light yield for  $\text{PbWO}_4$  is not an issue for higher photon energies of the proposed measurements or for the integrating measurements, and the high speed of this material reduces pile-up issues in counting measurements. Designs for multi-layer sampling calorimeters, using either scintillation or Cherenkov light, will also be considered.



## 17.4 Systematic Uncertainties

While the proposed system should assure operability and sufficient statistical precision at 11 GeV, the challenge will be achieving an absolute measurement of beam polarization with a precision of 0.4%. Table 33 summarizes the goals for various contributions to systematic uncertainty. The first four rows list sources of uncertainty which are highly or completely correlated between the electron and photon analyses. Other potential systematic errors arise in detector readout or calibration and are mostly or entirely decorrelated between the analyses. Each of these separate categories of potential systematic uncertainty: correlated, electron-only, and photon-only, will be discussed in the following sections.

### 17.4.1 Sources of Correlated Error

Any error associated with the Compton scattering process will be a common source of systematic error between the electron- and photon-detector analyses. One example lies in the energy normalization of the scattering process. The analyzing power is a function of both electron energy and photon energy, so these must be precisely determined. The photon wavelength will be determined to better than 0.1 nm and the electron energy to 0.05%, which leads to an uncertainty at the level of 0.03%. A similarly small uncertainty will come from radiative corrections, which are calculable [311] with high precision and will contribute at the level of  $10^{-3}$ .

Helicity-correlated changes in luminosity of the laser/electron interaction point can introduce a false asymmetry. Various causes of luminosity variation must be considered, such as electron beam intensity, beam motion or spot-size variation. The control of helicity-correlated beam asymmetries is now a standard technology at Jefferson Lab, and typically achievable results (few part per million intensity, 10's of nanometers beam motion,  $<10^{-3}$  spot size changes) will suitably constrain the electron-photon crossing luminosity variations. Another possible source of false asymmetry would be electronics pickup of the helicity signal, which could potentially impact an integrating photon analysis. However, the demands of the primary experiment for isolation of the helicity signal exceed those for polarimetry by several orders of magnitude. In addition, the laser polarization reversal provides an additional cancellation for asymmetries correlated to the electron beam helicity. For these reasons, beam asymmetries are expected to be a negligible source of uncertainty in this measurement.

A more significant potential source of error comes from the uncertainty in the photon polarization. As described above, the determination of photon polarization will be improved with the analysis of light reflected from the cavity input mirror, which will allow precise control and measurement of the polarization state injected into the cavity. This will be supplemented by an insertable stage to measure the polarization in the interaction region directly. The circular polarization of the laser will be determined and cross-checked with a precision of 0.2%. If studies do not demonstrate that this can be achieved within the high-gain cavity, the alternative laser system will need to be developed.

### 17.4.2 Systematic Errors for the Electron Detector

The electron detector is composed of 4 planes of silicon microstrips normal to the electron beam trajectory and positioned on the low-energy side of the beam trajectory in the dispersive chicane. Electrons which have given up energy to a scattering process are separated from the primary beam by the third chicane dipole, and the energy of a detected electron is implied by the distance of the track from the primary beam with a dispersion of about 0.45% of the beam energy per millimeter. Models of the chicane magnets are used to calculate the electron energy as a function of position



in the detector. The effects of electronics noise and non-directional backgrounds are reduced by triggering on tracks which are restricted to very small angles relative to the beam. The trigger can be adjusted for the range of track angles and number of planes used in the track, including a single plane trigger. The efficiency of individual strips can also be measured using data from the multiple planes.

The silicon detector may also be sensitive to synchrotron light, and while the detector is not in line-of-sight to synchrotron emission in dipole 3, synchrotron photons rescattered in the beam pipe may be a problem. The 11 GeV upgrade includes a gate valve installed on the straight-through beam pipe, to block synchrotron light from the first dipole of the chicane during operation of the polarimeter.

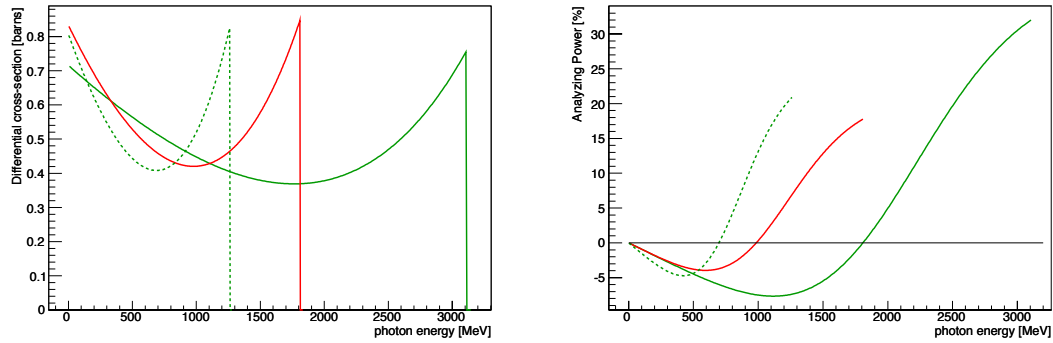


Figure 162: *The cross-section and asymmetry plotted versus Compton scattered photon energy for the Hall A polarimeter at 11 GeV for 532 nm (green solid line) and 1064 nm (red line) laser options, and at 6.6 GeV for the 532 nm laser (green dotted line).*

The cross-section and asymmetry as a function of Compton scattered photon energy is plotted in Figure 162 for 11 GeV electron beam. The Compton edge (the kinematic endpoint of the Compton energy spectrum) is observed in the electron detector and used to calibrate the distance of the detector from the primary beam. In addition, the asymmetry as a function of photon energy  $k$  exhibits a zero crossing. Determining the location of this asymmetry zero crossing (0xing) provides a second absolute energy calibration point, so together the Compton edge and 0xing can be used to calibrate two parameters: the detector location relative to the beam and the strength of the magnetic field in dipole 3. In this way, survey results and magnetic field maps serve as a cross-check to a beam-based self-calibration of the Compton energy spectrum. The precision of this calibration is limited by delta-ray production in the microstrips, which distorts the measured spectrum, and efficiency variations between the microstrips.

In operation at low beam energies, the 0xing is close to the primary beam: for HAPPEX-II, the separation was approximately 5 mm. At this proximity, background rates were extremely sensitive to beam tuning in the injector and RF phase corrections in the linacs, presumably due to energy tails. At 11 GeV with the IR laser, the 0xing will be around 16mm from the primary beam, which should allow for robust operation. The analyzing power for the measured electron distribution can be very accurately determined with use of this self-calibration, with the systematic error dependent upon the specifics of the analysis approach.

For an example of a specific analysis technique, consider an asymmetry measured from the Compton edge to some selected cut-off in the electron spectrum. This would need to be compared to the theoretically expected average asymmetry, which would be sensitive to the energy cut-off

threshold. In an analysis that computed a single count-rate asymmetry from the integrated rate from the Oxing to Compton edge, an error in determining the Oxing would act approximately as a dilution effect (as the asymmetry is small in the neighborhood of the Oxing). While there may be statistical variation in determining the Oxing, this would be merely a source of statistical noise. If the systematic bias in determining the Oxing is estimated to be within  $1/10$   $\mu$ strip width (about  $25\text{ }\mu\text{m}$ ), this would imply a systematic bias in the analyzing power of about 0.15%. While this is a useful estimate of the error due to energy calibration, this analysis relies on integrating the rate-weighted average asymmetry over the accepted energy range, and so would likely suffer a larger contribution of systematic error due to efficiency variations in the  $\mu$ strips.

Other analysis techniques which would be less sensitive to efficiency variations would rely on averaging asymmetries over a range of strips, rather than averaging the count rate. In this case, both energy calibration points are needed to determine the expected asymmetry at each  $\mu$ strip. Because the Compton edge will be extracted from the rate spectrum, efficiency variation between the silicon strips must be minimized and well-known to avoid biasing this determination. In addition, careful study of the contribution of delta-ray production, which distorts the asymmetry spectrum at the Oxing and the rate spectrum at the Compton edge, will also be important. Here also, a high strip efficiency will be helpful, by providing a high-efficiency for vetoing events with multiple tracks. Strip-by-strip efficiencies can be calculated by comparing track-hit efficiency between the multiple planes of the  $\mu$ strip detector, and comparisons between planes can also help benchmark corrections for delta-ray production. A uniform and high-efficiency detector will be an important component of this system.

It is worth noting a measurement using only the last, single silicon strip at the Compton edge will be capable of 0.4% statistical precision on time-scales of around one hour. The rate of change of the asymmetry in this region is only 0.5% / mm. Locating this strip, relative to Compton edge, to a little better than half its own width should provide a robust accuracy on the analyzing power better than 0.4%. This technique would be sensitive to determination of the location of the Compton edge, but otherwise very insensitive to other calibration parameters.

Similarly, if the electron detector can be moved close to the primary beam (about 9 mm from the primary beam for the IR laser at 11 GeV) the asymmetry minimum could be detected. The statistical power is much lower in this region, with a single strip requiring 20 hours to achieve 0.4% statistical precision on the polarization (assuming signal-noise ratio of 10:1). However, here the asymmetry is not changing with position, so there is minimal calibration error in selecting a strip in this minimum. Beam position and angle may vary the asymmetry minimum over hundreds of microns during this time span, but such changes can be tracked using beam position monitors or the Compton edge, and the analyzing power varies by only about 0.4% of itself over a range of  $\pm 300\text{ }\mu\text{m}$ , suggesting minimal corrections will be necessary.

Cross-checks between calibrations and techniques should provide convincing evidence that the system is well understood. Given these considerations, it seems likely that the calibration of the electron detector will be understood at the level of 0.3% or better.

Regardless of the analysis, contributions from deadtime and pileup will need to be understood. The fast-counting DAQ can take very high rates with low deadtimes, and deterministic deadtime intervals are enforced in readout and acquisition electronics stages. While the total Compton-scattered data rates may as high as 1 MHz, rates in individual strips will be reduced by segmentation to  $<15\text{ kHz}$ , which will allow dead-time and pile-up systematic errors to be controlled at the level of 0.2%. The high statistical power of the measurement is of significant use here; high precision studies can be performed to benchmark models of the readout system against changes in the laser power or the parameters of the triggering (preamp levels, logical gate lengths, coincidence levels, etc).

Backgrounds are also a potential but small source of systematic uncertainty. Backgrounds are studied with the laser cavity unlocked, allowing both the background level and asymmetry to be well determined. However, high backgrounds could impact the systematic error due to deadtime or pile-up corrections. There is also the possibility of backgrounds from Compton-scattered electrons, which can produce delta rays when scattering in the detector or in its shielding. These tracks can themselves be sufficiently forward-going to pass the trigger, thus changing the analyzing power as a function of energy. Simulation will be used to avoid such problems, and studies of track distribution and electron-tagged photon energy spectra can be used to identify such effects in the data.

Finally, it is perhaps obvious, but worth stating, that beam properties at 11 GeV will be important for the precision of the electron detector analysis. If simulations reveal that halo backgrounds for the electron detector are likely to be large in the region  $\sim 15$  mm from the primary beam, then the green laser option would be required for high precision polarimetry. Using 532 nm light in a cavity would put the zero-crossing about 33 mm from the primary beam. It is also worth noting that the single-strip analyses would also be improved with the higher resolution and larger asymmetries (and larger distances from the primary beam) available from a green laser.

### 17.4.3 Systematic Errors for the Photon Detector

The precise determination of the analyzing power as a function of energy is more difficult for the photon calorimeter than for the electron detector due to the width and shape of the detector response function. In order to fit the asymmetry as a function of detected photon energy, the analyzing power must be calculated as a convolution of the response function with the theoretical analyzing power curve. The response function shape and energy calibration can be simulated, and studied using the photon tagging through coincidence triggers with the electron detector.

In general, determining the effect of a low-energy threshold on the analyzing power depends sensitively on the shape of the response function; at low energies this is a major source of uncertainty. At high energies, the improved resolution and consistency of the response function shape over the range of interest should significantly reduce this problem. As noted above, the photon calorimeter will be upgraded to better contain showers from high energy photons, with the primary objective to provide a response function which scales linearly over a broad range of energy.

The pulse-counting analysis in the photon detector is also sensitive to pile-up, which distorts the asymmetry distribution. Background and rate distributions will serve as inputs to simulation for corrections to the analyzing power. In the current Hall A analysis, pile-up corrections are estimated at the level of 1%, and the effect can be controlled at a level better than 10% of itself. Deadtime corrections, which can vary significantly with background conditions, will also represent a potential systematic uncertainty.

Uncertainties related to the threshold, response function shape, absolute energy calibration, deadtime and pile-up can also be eliminated by integrating the photon calorimeter signal, without threshold [312]. These previous problems are then replaced with a requirement on the linearity of the average response to the photon energy. Because the analyzing power integral is energy-weighted, the statistical figure-of-merit is not badly degraded by the negative asymmetry region at low photon energies.

The PREX experiment, with a beam energy near 1 GeV, relied on the integrating photon method for polarimetry at the level of 1% precision. Simulations of the photon response function were sufficient to control the analyzing power uncertainties for those measurements. The dominant uncertainty in the asymmetry measurement arises from variation in the photomultiplier response with changes in average rate which introduces a systematic error through background subtraction.

At high energies, with the ability to study response function with the electron-detector-tagged

photon beam over a large fraction of the energy range, the photon detector analyzing power normalization uncertainty in the range of 0.3% should be achievable. Characterization of the phototube response as a function of rate and pulse-size will also be important. As described above, Bremsstrahlung scattering from apertures in the interaction region, coupled with the characteristics of the 11 GeV electron beam, present a possible source of background.

## 17.5 Summary of Compton Polarimetry

The prospects for 0.4% Compton polarimetry are excellent. This ambitious goal will require vigorous and dedicated efforts to reduce sources of systematic uncertainty. It is expected that some significant fraction of data production time will be used for studies of the Compton polarimeter system which are not disruptive to the experiment, for example, scans of detector positions, laser power and polarization, and data acquisition parameters. The scattering asymmetry at 11 GeV is relatively large which, for some analysis approaches, will provide statistical precision at the level of  $\sim 0.5\%$  in a few minutes of data collection. Given this high statistical power, these studies will be an effective method for constraining many of the possible experimental systematic uncertainties.

The future use of the Hall A polarimeter at 11 GeV will be a very different situation from the recent operation. The dominant systematic errors in recent operation lay in the determination of the analyzing power and laser polarization. Operating at lower energies the asymmetries were significantly lower and therefore the statistical power was worse. In addition, the limits of systematic uncertainty had not been pushed by demands of the experiment precision.

The 0-Xing “self-calibration” of the electron detector was attempted for the first time for the HAPPEX-II and HAPPEX-He measurements. The situation was complicated due to the low beam energy of around 3 GeV, which not only reduced the average asymmetry but also reduced the ratio of Compton-scattered photon energies and the electron energies. At 3 GeV, the zero-crossing was about 5 mm from the primary beam, which was as close as the electron detector could get to the beam. Geometric efficiencies at the edge were a significant complication in this approach. In addition, the microstrip detector was damaged and displayed low and uneven efficiency, which complicated the analysis. The estimated systematic errors for that analysis which were not associated with these efficiency issues are consistent with Table 33. A similar technique has been successfully employed in the Hall C Compton polarimeter at 1 GeV, where a larger chicane and green laser were used to optimize for the low beam energy during the Qweak experiment. While analysis is ongoing, the current status indicates that the ultimate precision will be significantly better than 1%.

For the photon detector, the integration readout method has been successfully used in the HAPPEX-3 and PREX experiments, with the primary limitations being the characterization of the phototube response over the range of signal levels. The rapid access to high statistical power expected for 11 GeV operation, which is so powerful for cross-checking potential sources of systematic uncertainty, has never before been available to the Hall A Compton. Coincidence measurements between the photon and electron detectors will also provide a significant cross-check to the response function and energy calibrations. As described above, recent improvements in available laser power, analysis techniques, laser polarization measurements, and the favorable kinematics of the higher electron beam energy have opened the door to 0.4% precision Compton polarimetry for the SoLID program.

## 17.6 Møller Polarimetry

This section describes our plans for precision Møller polarimetry in Hall A. Møller polarimetry will provide a useful cross check on beam polarization measurements performed with Compton scattering, gathering high statistics in a short amount of time and with different attendant systematic

errors. The principal challenge is to achieve high precision ( $\sim 0.5\%$  on the beam polarization) through careful control of the systematic effects.

Electron-electron scattering, with arbitrary spin orientation for the beam and target, has been calculated in lowest order QED by many authors [313–316], and the basic formulas for (non parity-violating) polarized Møller scattering are given in many places. For example, following [317], the cross section at high energies in the center of mass frame can be written as

$$\frac{d\sigma}{d\Omega_{\text{cm}}} = \frac{\alpha^2}{s} \frac{(3 + \cos^2 \theta)^2}{\sin^4 \theta} [1 - P_{\text{long}}^{\text{B}} P_{\text{long}}^{\text{T}} A_{\text{long}}(\theta) - P_{\text{tran}}^{\text{B}} P_{\text{tran}}^{\text{T}} A_{\text{tran}}(\theta) \cos(2\phi - \phi_B - \phi_T)] \quad (30)$$

Here,  $s = (2E)^2$  for electron energy  $E$ ,  $\theta$  is the scattering angle,  $P_{\text{long,tran}}^{\text{B,T}}$  are the longitudinal and transverse polarizations of the beam and target electrons,  $\phi$  is the azimuthal scattering angle, and  $\phi_{\text{B,T}}$  are the azimuthal angles of the beam and target polarizations. The analyzing powers are

$$A_{\text{long}}(\theta) = \frac{(7 + \cos^2 \theta) \sin^2 \theta}{(3 + \cos^2 \theta)^2} \quad \text{and} \quad A_{\text{tran}}(\theta) = \frac{\sin^4 \theta}{(3 + \cos^2 \theta)^2} \quad (31)$$

which are maximized at  $\theta = 90^\circ$  with  $A_{\text{long}}(90^\circ) = 7/9$  and  $A_{\text{tran}}(90^\circ) = 1/9$ . The electron laboratory scattering angle for  $\theta = 90^\circ$  is  $(2m/E)^{1/2}$ , rather small for GeV electron beams.

A Møller polarimeter makes use of Eq. 30 to measure the beam polarization vector  $\vec{P}^{\text{B}} = (P_{\text{long}}^{\text{B}}, P_{\text{tran}}^{\text{B}})$  by incorporating a target with a known electron polarization vector  $\vec{P}^{\text{T}} = (P_{\text{long}}^{\text{T}}, P_{\text{tran}}^{\text{T}})$  into a spectrometer to detect one or both of the scattered electrons. By reversing the beam polarization vector  $\vec{P}^{\text{B}} \rightarrow -\vec{P}^{\text{B}}$ , one can deduce its magnitude, and perhaps its direction, through the analyzing powers (31). The ideal Møller polarimeter, for determining longitudinal beam polarization  $P_{\text{long}}^{\text{B}}$ , is set at  $\theta = 90^\circ$  with maximal (minimal) target longitudinal (transverse) polarization  $P_{\text{long(tran)}}^{\text{T}}$ .

We describe two techniques for getting as close as possible to the ideal Møller polarimeter. One is based on iron foil targets, in which the outer atomic electrons are polarized, and the other is based on an atomic hydrogen target. In the case of the iron foil target design, polarimeters at Jefferson Lab have already described control of systematic errors near the 0.5% level. We describe upgrades already in progress in Hall A in preparation the general 12 GeV program at Jefferson Lab which will enable that level of performance. While potentially very precise, such a polarimeter requires calibration from a body of magnetization studies with iron, and this normalization has never been cross-checked to the required precision. In addition, iron foil polarimeters require dedicated measurements at low current, and so measured polarization must be interpolated between spot measurements and extrapolated to the high currents used for production. Møller polarimetry with an atomic hydrogen target, in contrast, would be able to provide a continuous, non-invasive polarization measurement and would not require external calibration for accuracy at the few  $10^{-3}$  level, but would be a new technology requiring significant technical R&D.

The strategy for Møller polarimetry, therefore, is to complete the upgrade of the Hall A iron foil polarimeter and seek to maximize the accuracy of this device. A cross-calibration with the upgraded Compton polarimeter should demonstrate that normalization of the target foil polarization is under control. The atomic hydrogen polarimeter option could be pursued if it is needed to confirm results of those studies.

## 17.7 The Hall A Upgrade: “High Field” Iron Foil Targets

Nearly all high energy Møller polarimeters operated to date [321, 322, 325–330] make use of tilted ferromagnetic foil targets. High permeability alloys coupled with  $\sim$ few hundred gauss magnetic

Variable	Hall C	Hall A:	Hall A:
		High Field Foil	Hydrogen
Target polarization	0.25%	0.25%	0.01%
Target angle	‡	‡	*
Analyzing power	0.24%	0.20%	0.10%
Levchuk effect	0.30%	0.20%	*
Target temperature	0.05%	0.05%	*
Dead time	‡	0.10%	0.10%
Background	‡	0.10%	0.10%
Others	0.10%	0.10%	0.30%
Total	0.47%	0.42%	0.35%

☆: Not applicable      ‡: not estimated

Table 34: *Systematic error summary for Møller polarimeters at JLab, including anticipated uncertainties for future prospects. The Hall C polarimeter [318] uses a high field pure iron target [319, 320] with a simple two-quadrupole spectrometer. Uncertainties quoted for that system are taken from a publication detailing calibration of the analyzing power. The current Hall A Møller polarimeter [321, 322] uses a tilted ferromagnetic allow target, and a spectrometer with a dipole magnet following three quadrupoles. A high-field pure iron target upgrade is underway with plans for an additional quadrupole in the spectrometer for high energy operation. Uncertainties for this system are the expected performance after the upgrade. Research and development for a hydrogen gas target [323, 324] provides the basis for a second continuously-running high precision polarimeter to complement the Compton apparatus.*

fields preferentially polarize in the plane of the foil, so tilting the foil at a moderate angle gives a substantial longitudinal target polarization. Calculating the effective polarization, however, is typically the limiting systematic error, and such devices cannot ultimately do better than several percent precision.

A different approach [318], implemented in Hall C at Jefferson Lab, using a high magnetic field perpendicular to the foil plane [319, 320], has reported 1% precision on the beam polarization. It is this target design that we are adopting for SOLID, and indeed are already preparing to implement in Hall A.

Below we describe the principles of “high field” iron foil targets, the plans for redesign of the scattering chamber, and modifications to the existing spectrometer including simulations for operation at high energy.

### 17.7.1 Ferromagnetic Foil Targets

Materials respond to external magnetic fields because atomic electrons, with spin and orbital angular momentum, align themselves to an applied field. However, with a Bohr magneton equal to  $5.8 \times 10^{-5}$  eV/tesla, the magnetic energy at several tesla is still much smaller than the thermal energy at room temperature, so the effects of magnetic fields in most materials (“diamagnetism” and “paramagnetism”) are quite small.

Ferromagnetism, on the other hand, is a quantum mechanical phenomenon in which a subset of atomic electrons in some elements and alloys spontaneously align. These alignments happen in localized domains, which themselves are randomly oriented. However, the application of relatively

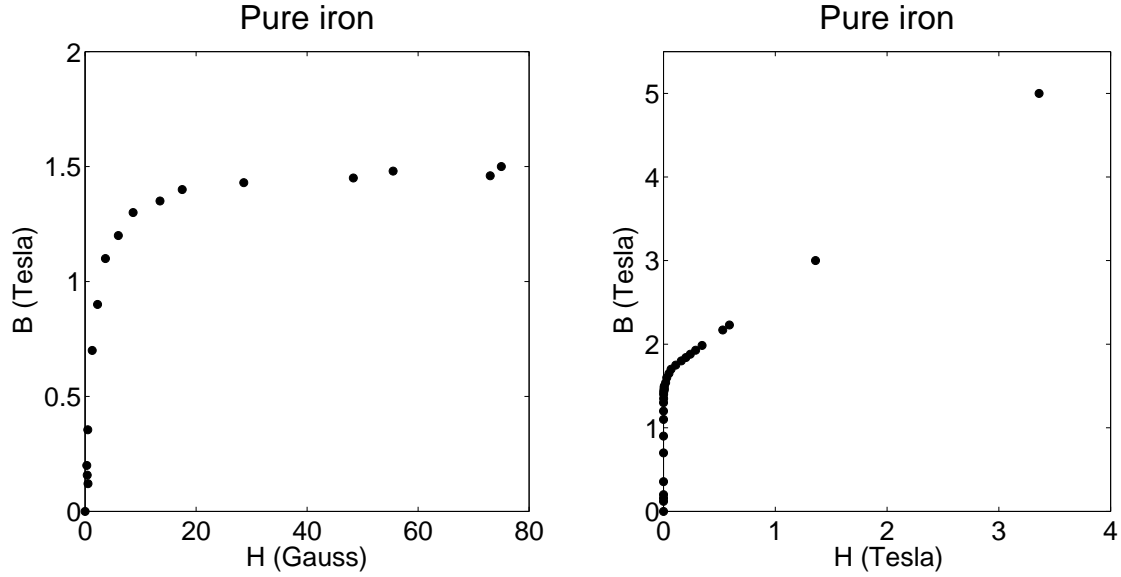


Figure 163: Magnetization curves for pure iron, from <http://www.fieldp.com/magneticproperties.html>. We use CGS units, so both  $B$  and  $H$  are properly measured in Gauss, but 1 Tesla =  $10^4$  Gauss. Both plots are of the same data set, but the horizontal scale is much expanded on the right.

small magnetic fields cause the domains themselves to line up, leading to large induced magnetic fields.

Magnetostatics (in CGS units) is governed by the equations  $\vec{\nabla} \cdot \vec{B} = 0$  and  $\vec{\nabla} \times \vec{H} = 4\pi\vec{j}/c$  where  $\vec{B}$  is the magnetic field,  $\vec{j}$  is the free current density, and  $\vec{H}$  absorbs the magnetic response of the medium. To be precise,  $\vec{H} \equiv \vec{B} - 4\pi\vec{M}$  where the magnetization  $\vec{M}$  is the magnetic dipole moment per unit volume. It is the magnetization  $\vec{M}$  that we interpret, ultimately, as the polarization of target electrons.

For *linear* materials (which *do not* include ferromagnets), we define the magnetic permeability  $\mu$  through  $\vec{B} = \mu\vec{H}$ . It is nevertheless a habit to speak of  $\mu$  for ferromagnetic materials in terms of vector magnitudes, that is  $B = \mu H$ . For most materials,  $\mu$  is a constant slightly larger than unity. In ferromagnets, however,  $\mu$  is a strong function of  $H$  and can be very large.

Figure 163 shows magnetization data for pure iron. At several tens of gauss of “applied” field  $H$ , the magnetic field  $B$  saturates at  $\sim 1.5$  tesla because the domains are aligned. The resulting magnetization corresponds to  $\sim 2$  Bohr magnetons per iron atom, that is, roughly two electrons worth of magnetic dipole moment in *each* iron atom. As  $H$  reaches and exceeds several tesla, the magnetization field simply adds directly to the applied field. The value of  $\mu$  rises to several thousand for a few gauss, and then decreases to unity for fields much greater than saturation.

Møller polarimeters using “low field tilted” foil targets operate in the region where  $\mu \gg 1$ . In fact, they generally make use of special alloys that have exceptionally high values of  $\mu$ , that is, saturate at relatively low values of  $H$ . In this case  $\vec{B} = 4\pi\vec{M}$  to a very good approximation. Since  $\vec{\nabla} \cdot \vec{B} = 0$  implies that perpendicular components of  $\vec{B}$  are continuous across the foil surface, and since  $B = H$  outside the foil is hundreds of times smaller than the magnetization, the only way to meet the boundary condition is for  $\vec{M}$  to point in the plane of the foil. (Of course, this argument breaks down if the foil is at right angles to the applied field.) Thus a target tilted at some angle, say  $\sim 20^\circ$  provides a dominantly longitudinally polarized target for an incident electron beam in the



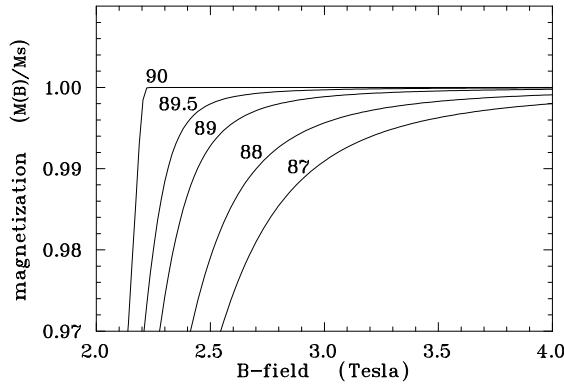


Figure 164: Simulations of foil magnetization for angles between the foil plane and the B-field direction close to 90 degrees. Errors due to imperfect alignment or a slight warp of the foil could produce such a result. Taken from [319, 320], which uses a calculation [335] of magnetization curves for uniformly magnetized prolate ellipsoidal domains.

same direction as the applied field.

The limiting precision of polarimeters using such targets, however, is extracting the target electron spin polarization from the magnetization. The ratio of “spin” magnetization  $M_s$  to the total can be written as [331]  $M_s/M = 2(g' - 1)/g'$ , with  $g'$  close to, but somewhat less than 2. The attendant uncertainties in  $g'$  for the alloys used in tilted target applications, limit one’s knowledge of the target polarization to several percent.

Measurements in *pure* iron or nickel, however, point to very precise knowledge of their magnetization parameters [332, 333]. The approach used by the Basel/Hall C group [318–320] is to not only use pure iron foil targets, but to polarize them with a very high (several tesla) field, provided by superconducting coils. This overcomes limitations of a not-so-large value of  $\mu$  for pure iron.

It is important to note that the magnetization of the foils in the strong longitudinal field has not been measured, but is taken from published data on the properties of bulk iron, which claims an accuracy of  $\sim 0.1\%$ . The orbital contributions to the magnetization of about 5% can be evaluated and subtracted using the magneto-mechanical factor, measured by other dedicated experiments [334]. With strong external fields of 3-4 T several additional correction of about 0.5% have to be made to compensate for extra orbital momenta and other complex effects. These corrections are temperature dependent. It will be important to carefully evaluate the literature on these measurements and their interpretation to verify that the uncertainty is not larger than a few  $10^{-3}$ . For example, it is apparent that the anomalous magnetic moment of the electron has not been accounted for in recent publications, amounting to a correction of more than 0.2% to the target electron spin polarization.

Calculations of the longitudinal magnetization of a foil placed perpendicularly (or nearly so) to an applied field are quite difficult. Figure 164, taken from [319, 320], shows the magnetization (relative to its maximum value) of a pure iron foil as a function of applied magnetic field, for different angles between the field and the normal to the foil. To be sure, this calculation is in fact of a model of non-interacting prolate ellipsoidal domains [335], and the extent to which it applies to a pure iron foil is not clear.

A polarimeter based on this “high field” target was constructed in Hall C at Jefferson Lab [318]. The device has performed well, with experimenters claiming accuracy of 1% or better on the longitudinal beam polarization. Much of the updated design of the Hall A Møller polarimeter is based on the Hall C experience.

### 17.7.2 Simplified Møller Scattering Target Assembly

Quite a number of small, systematic effects need to be considered in order to achieve 0.5% uncertainty on the longitudinal beam polarization. For example, Figure 164 gives an idea of the tolerance



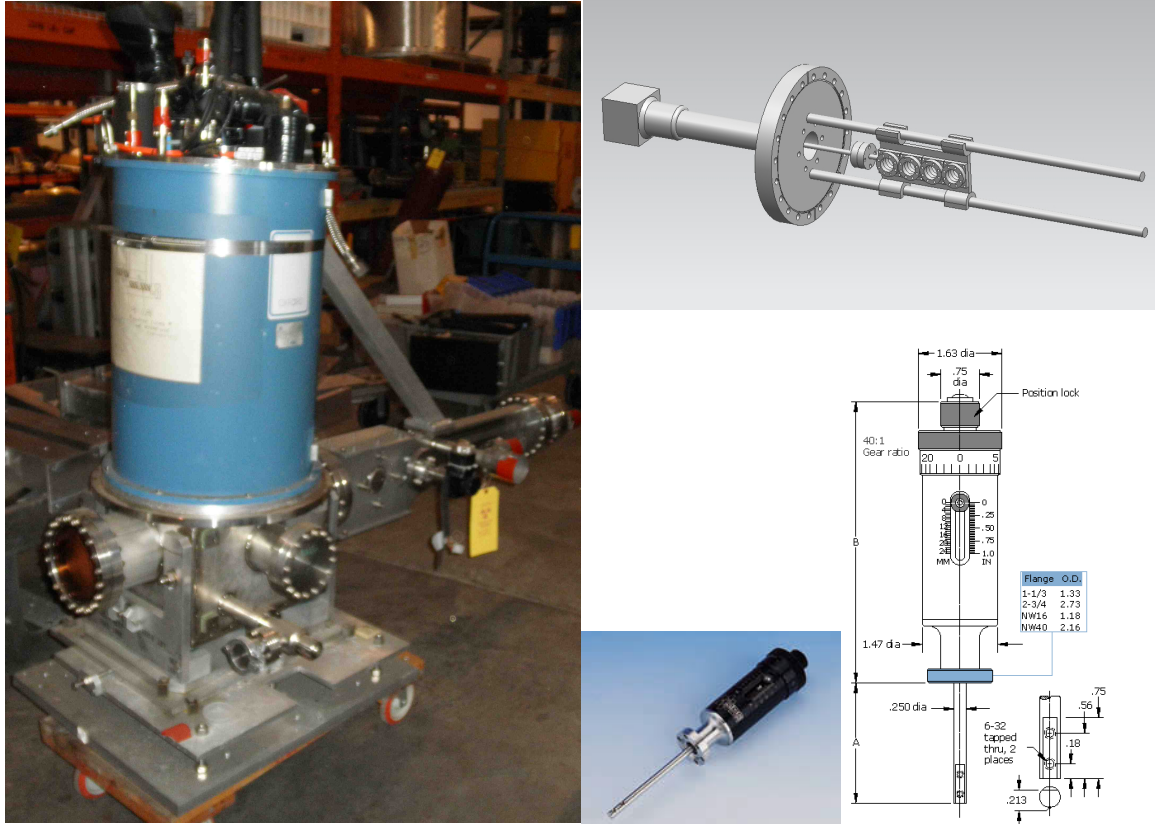


Figure 165: *Left*: Existing Hall A target chamber with ladder actuator extending off to the right. The magnet cryogenic system sits on top of the chamber. Our plan is to replace the actuator assembly, here shown supported by a boom attached to the cryo system. *Right*: Design concept for a new ladder actuator system, based on the Hall C design, along with a photo and schematic of the MDC660034 linear motion feedthrough.

needed on iron target alignment. In order to be assured of at least 99.8% of the maximum target polarization for a field of  $\sim 3$  T, the tolerance on the foil angle misalignment is  $\sim 1^\circ$ .

Figure 165 includes a photograph of the high-field foil target chamber previously in place in Hall A, and some details of our current plans for the upgrade. Our plan is to retain the cryogenic magnet system and the target chamber and overall adjustment mechanism, but to replace the target actuator assembly. Originally designed to provide adjustments in many degrees of freedom, the existing actuator assembly proved unwieldy for regular use. It was also very heavy, and required stabilization through a connection to the dewar for the cryogens. The redesign relies on precision construction with fewer adjustable degrees of freedom, and will be much lighter.

In order to interpret the target polarization to high precision, it is imperative that the foil be saturated. This can be confirmed by studying the Møller scattering asymmetry as a function of applied magnetic field. The cryogenic magnet is limited to fields less than 4 T, so according to Fig. 164 we need to have the target angle precise to about  $1^\circ$ . It would be useful to in fact confirm the behavior suggested by the figure, by making these measurements with the target arm rotated by various angles close to  $90^\circ$ .

## **18 Supports and Infrastructure**

### **18.1 Magnet Support**

The initial plan used for estimating the cost is to build a stationary frame and distribute the approximate 1000 ton load of the modified CLEO-II magnet section using eight 200 ton energpac jacks. Steel plates and large steel blocks and/or large I-beams will be used to distribute the load out over a safe area. The 200 ton jacks will be used for vertical alignment and have locking rings which allow for a full mechanical connection and not rely on hydraulic pressure for stationary support.

### **18.2 Endcap Support Structure and Motion Mechanism**

The endcap will have a support structure that cradles each half the cylindrical ring. The structure will be integrated into a track system that is mounted to steel plates resting upon the concrete floor. The initial design concept for the track system requires a set of longitudinal (downstream direction) tracks for moving the endcap away from the magnet. A second set of tracks that would separate the endcap halves in the lateral direction would ride on top of the longitudinal tracks. The endcap support structure would then be attached to the top lateral track system. Motion can be achieved by using hydraulic or electric cylinders to push and pull the entire system into position.

### **18.3 Support Structure for Equipment Located Inside Cryostat Bore**

The magnet will be located adjacent to the existing Hall A center pivot/target mount area and will have limited access to the front of the magnet. The insertion of the large angle detector packages that will reside internal to the cryostat will be accomplished from the downstream side of the magnet using a supporting framework to roll the packages in and out. This will require the detector hut to be moved downstream to allow access to the cryostat.

An internal frame system is needed to mount the lead baffles in the PVDIS experiment. See Figure 166. The frame cannot come into contact with the inside bore of the cryostat. This requires the frame to span the entire length of the cryostat and mount to the return yoke iron. The rails of the frame will be fabricated from 4 inch diameter schedule 80 welded stainless steel pipe. Either 304 or 316 grade stainless is acceptable. The downstream end of the rails will have a hemispherical cap and a stainless steel foot welded on and will be bolted to the downstream collar. The upstream end of the rail will either be bolted or welded to an annular stainless steel plate. The upstream end of the frame will be mounted to the frontcup (magenta body inside the red front collar). Since the frontcup has to be movable to balance the magnetic field on the coils the annular plate will be attached to the frontcup with studs. This will allow the rail framework to remain stationary if the frontcup has to be adjusted. The same rail system can be used for the SIDIS experiment for mounting the large angle calorimeter and GEMs.

### **18.4 Power Requirements**

The projected electrical power load is 1.6MVA, maximum current for magnet at 3266A. The present power consumption for Hall A is less than 1 MVA. So upgrade to the Hall substation to have 2 MVA is required. (MOLLER Experiment has included the cost (\$300k) for this in their MIE).

The CLEO-II magnet is designed to have a low cryogenic heat load with passive cooling. The HRS arms will not be operational during SoLID, so it is expected that the refrigeration heat load will be less than needed for HRS. The refrigeration need for the cryotarget is discussed in the target section (Section 5).

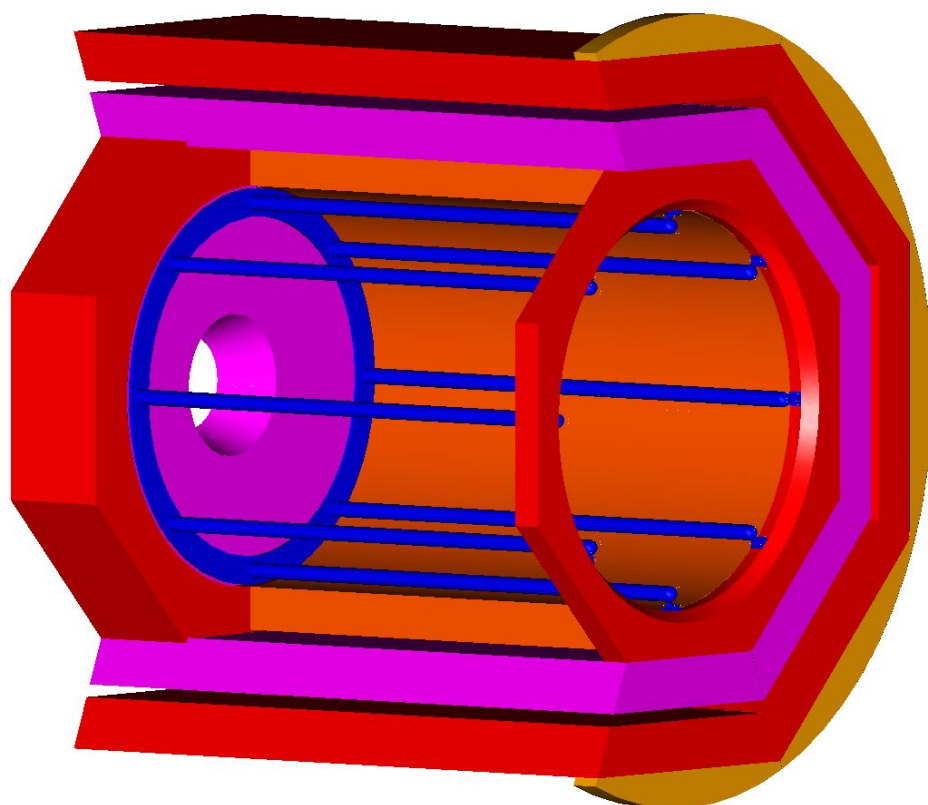


Figure 166: The internal rail system will be used to mount all parts inside the barrel, including PVDIS baffle, SIDIS large angle calorimeter and GEM's

## **19 Installation**

### **19.1 Experimental Layout**

An initial check of the experimental equipment layout in Hall A has been done and no major obstructions have been found. The experiment layout puts the HRS arms at 90 degrees to the beamline on the left and right. The target is at the nominal pivot location with the center of the CLEO-II magnet 350 cm downstream of the target center. The SoLID magnet and detectors encompass an area of 5.8 meters in diameter and 7.3 meters long. With the magnet on beamline center, clearance to the Hall floor ranges from 10 to 38 cm. This is sufficient area to support the load. The weight of the CLEO-II magnet, detector hut and detectors is estimated to be 1300 tons. The floor in this installation region is designed for 250 tons for a 12 square foot pad.

### **19.2 Magnet Moving and Placement**

In evaluating the use of the CLEO magnet for SoLID consideration is given to how the CLEO magnet can be transported into Hall A and how Hall A structurally meets the requirements of CLEO. The footprint of SoLID utilizing the CLEO magnet will be approximately a 1000 ton load with dimensions of 24 feet long by 19 feet in diameter. Hall A is 164 feet in diameter. In the area required to install SoLID, the floor is constructed to carry 250 to 500 tons per 12 square feet.

The existing Hall A equipment consists of the two High Resolution Spectrometers mounted at the center pivot and all related infrastructure. To accommodate installation of SoLID the target will need to be mounted 115 cm downstream from the existing support location in order for the magnet to clear the HRS bearing assembly. Placing the CLEO magnet on beamline height gives 15 inches clearance to the floor for adequate support and alignment. The location of the HRS arms during SoLID have two options: remove the existing beam line and move both HRS arms to beam left locations or place both HRS arms 90 degrees to the beam line. The second option allows more clearance for SoLID during operation but requires more planning and infrastructure modifications during installation. These options will be studied further.

The bird's eye view Figure 167 and the back side Figure 168 show the SoLID in Hall A with two HRS arms on the side. The SoLID detector hut is cut in half and the right side of the return yoke layers are removed showing the cryostat in orange color.

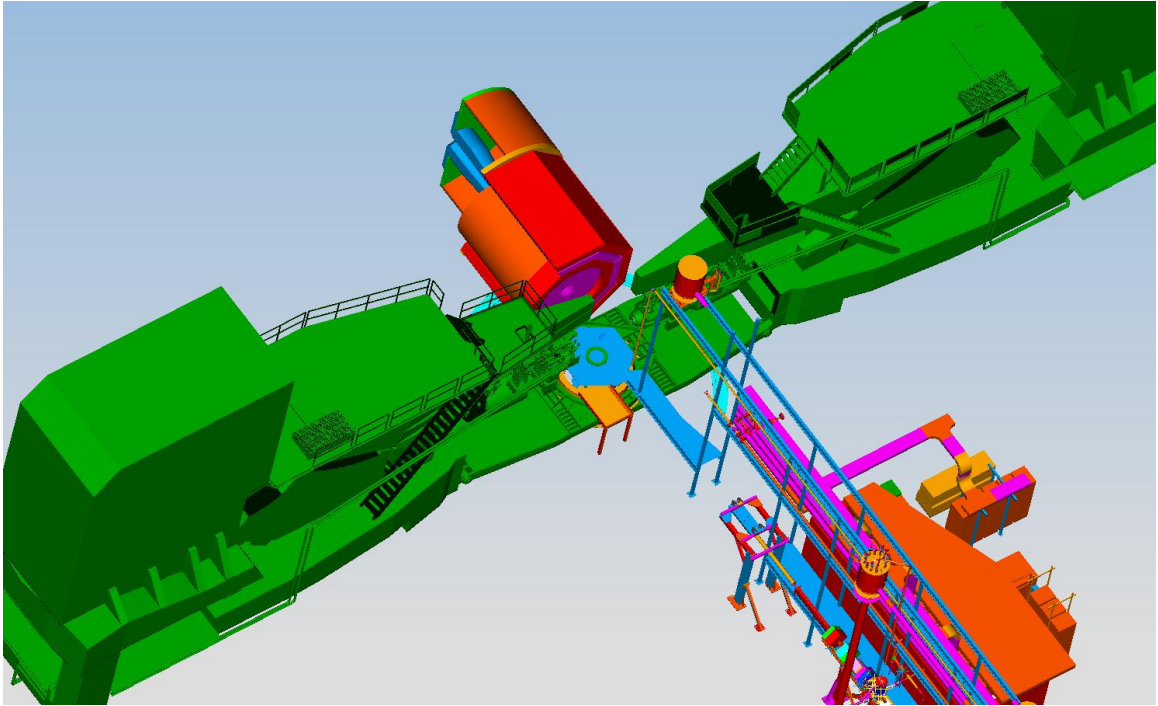


Figure 167: The bird's eye view of SoLID in Hall A

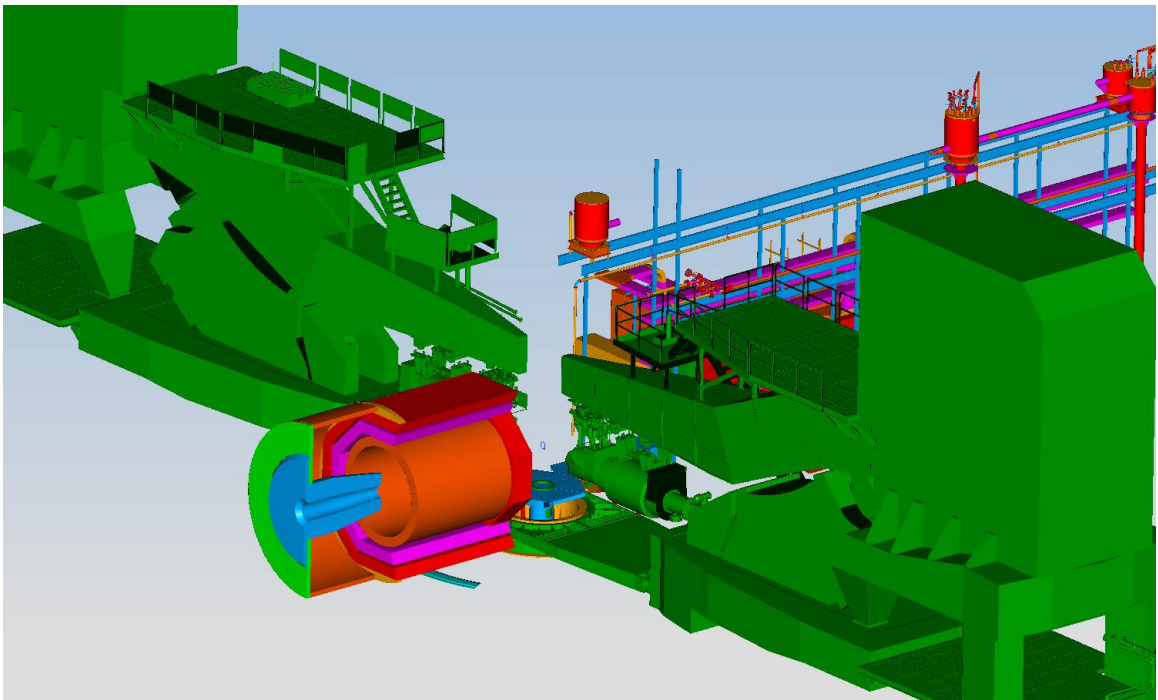


Figure 168: The back side view of SoLID in Hall A



The CLEO-II magnet was disassembled and loaded on trucks for shipping by the Cornell personnel with oversight by Jefferson Lab. The coils and cryostat of the CLEO-II magnet have arrived at JLab in 2016 and the exterior steel is being shipped as of Spring 2017.

We have identified all of the parts of the CLEO magnet, with sizes and weights. We have identified specifically the parts to reuse in building the SoLID magnet, and these have a total weight of 1,053k lbs. The cryostat (35k lbs) and power supply are stored in an environment-controlled area of approximately 400 square feet. Jefferson Lab projects the use of the CMSA site for storage of all parts.

In developing the installation plan for SoLID, the largest part to transport is the cryostat. The cryostat is 12.3 feet long, 11.8 feet in diameter and weighs 22 tons. The height of the truck ramp into Hall A is limited to 17 feet in height. This will require the cryostat to be moved into the Hall on a roller structure rather than a flatbed type truck. This type of procedure has been completed several times at Jefferson Lab. See Figure 169, Figure 170, and Figure 171.

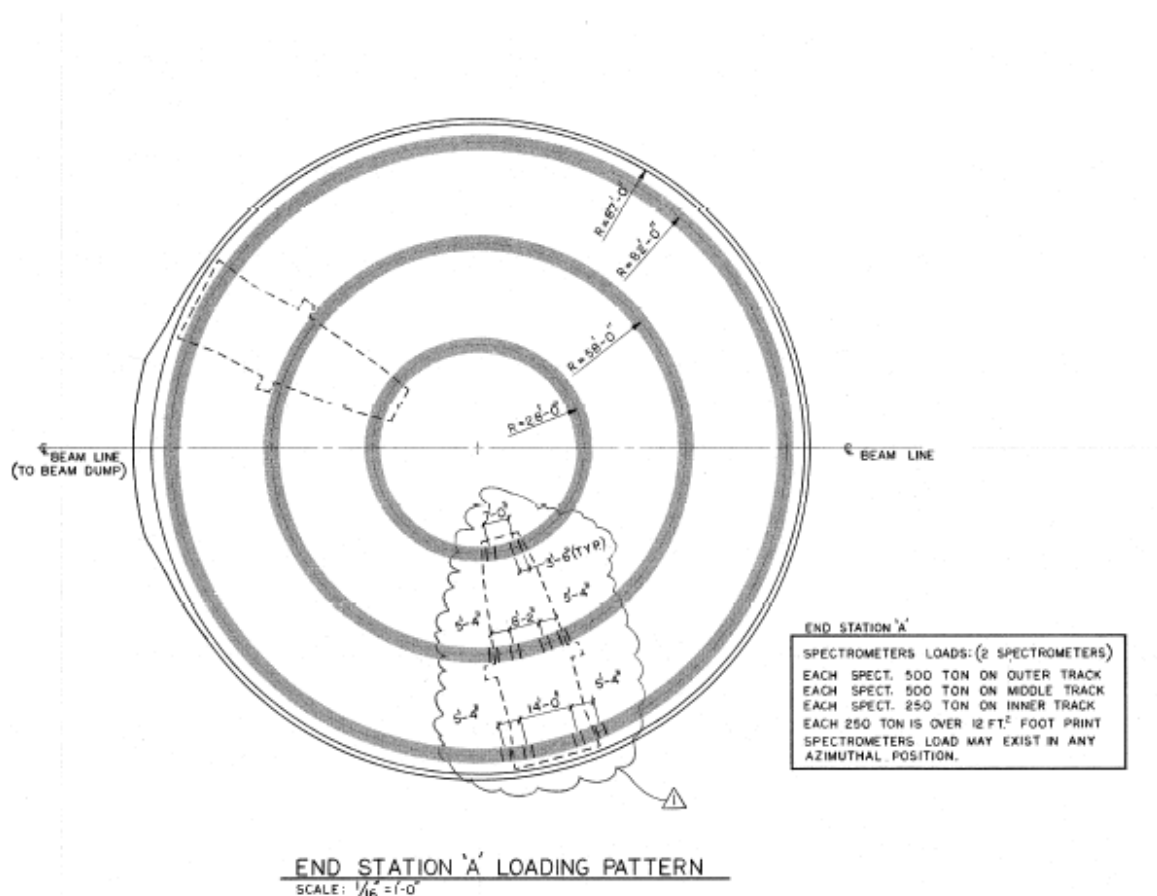


Figure 169: Hall A loading pattern.

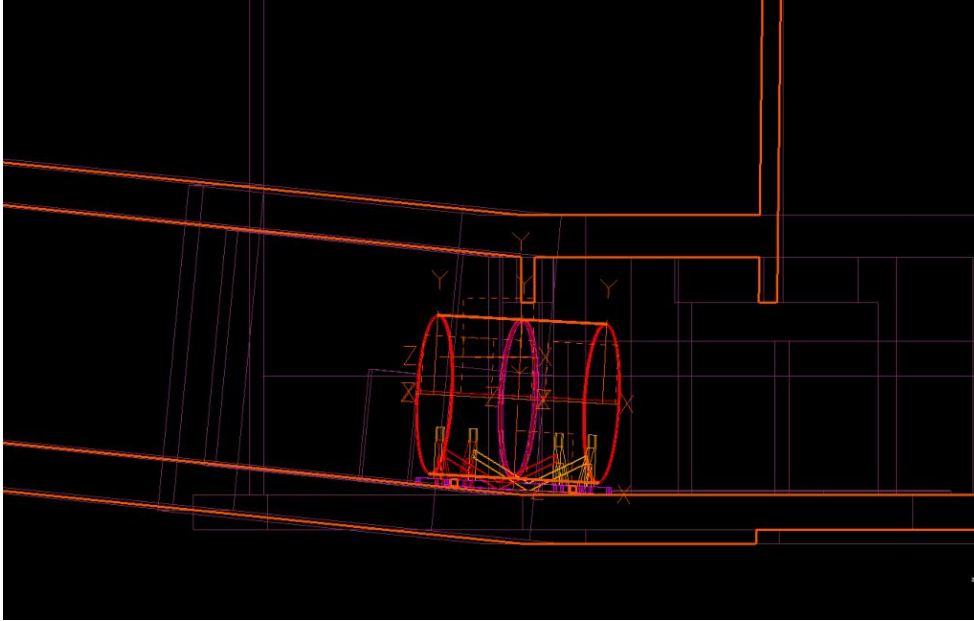


Figure 170: The plan of moving CLEO cryostat through Hall A ramp.

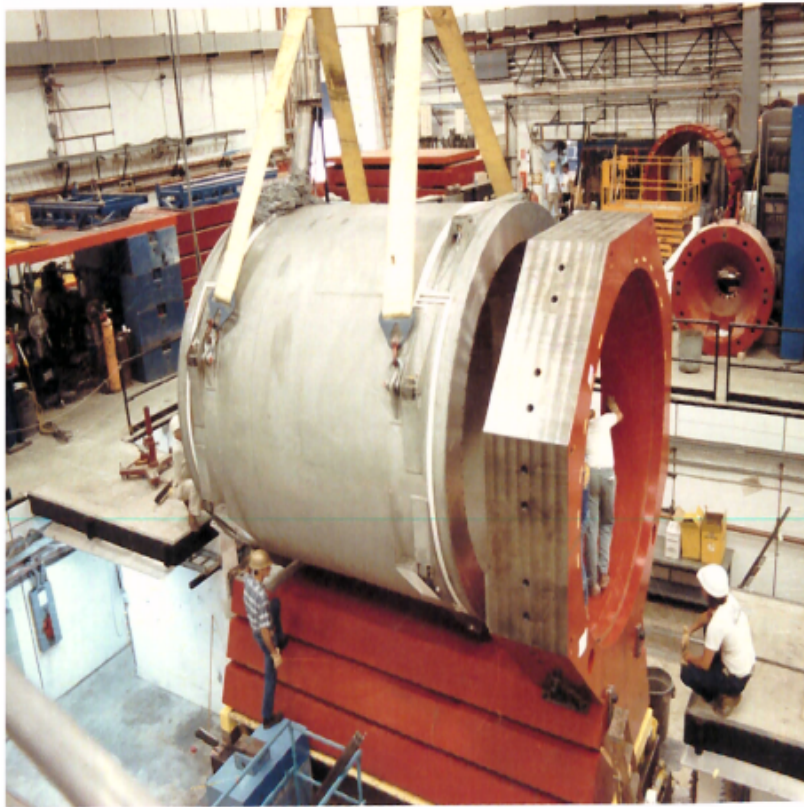


Figure 171: CLEO cryostat lifted during the installation at Cornell.

### 19.3 Helium Dewar Support and Upper Access Platform

An upper personnel access platform that is capable of supporting the helium dewar will be mounted to the top of the magnet. A similar platform was used for the CLEO II experiments. See Figure 172.

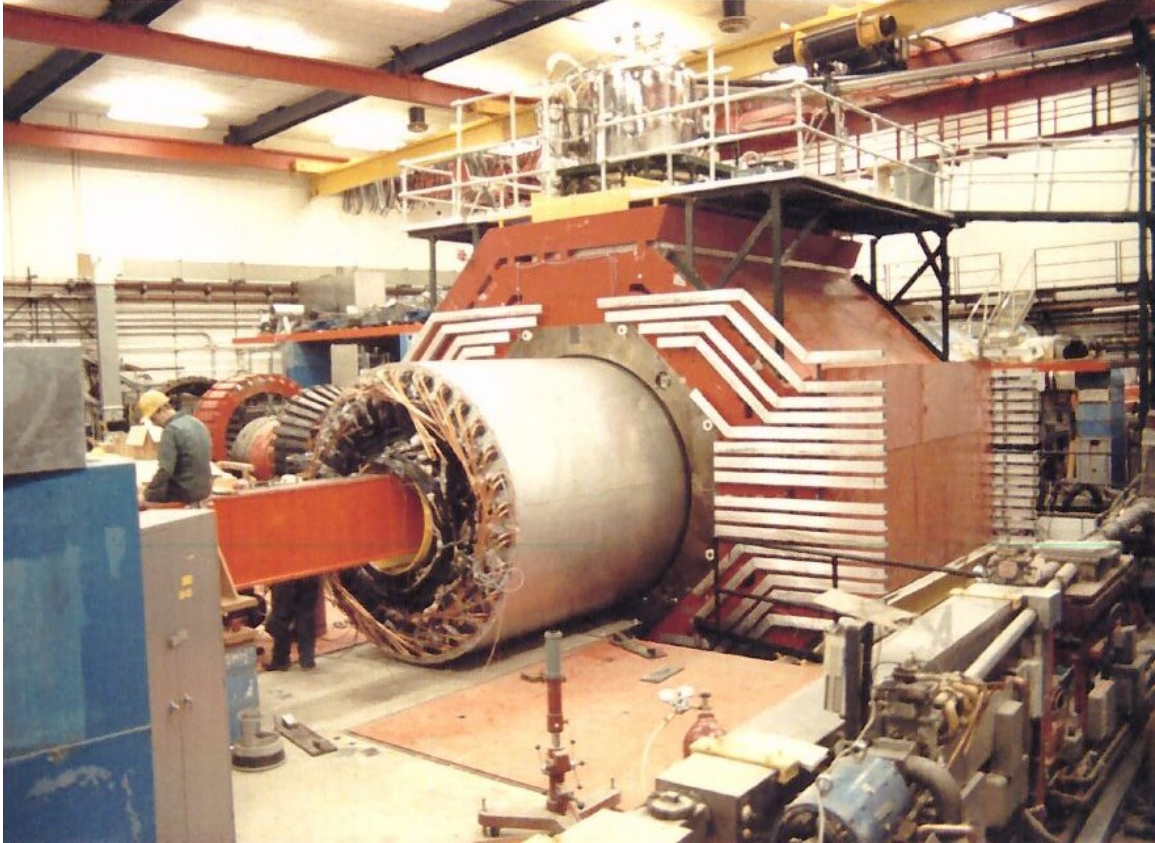


Figure 172: Helium dewar support upper access platform and detector loading inside of cryostat.

### 19.4 Endcap Forward Angle Detector Package Installation Structure

The basic design concept for the detectors mounted inside the endcap will have them supported by individual rails mounted to the inner circumference of the cylindrical ring and on rails attached to the outer horizontal circumferential surface of the nose if needed. The heavy gas Cherenkov will be separated into six sections with each section utilizing two rails to attach the section to the outer circumference of the endcap. A counterweight balanced installation device that is slung from the crane can be used to orient and position each section onto the rails. Personnel access to the endcap will be through man lifts and/or a specialized scaffolding as needed.

### 19.5 Large Angle Detector and Baffle Installation Mechanism

An installation mechanism is needed to load the large angle detector packages and baffle system into the internal support structure mentioned in the last section. This mechanism will likely be mounted to the longitudinal track system used for the endcap movement and can utilize the tracks for rolling the detectors and baffles into the cryostat and transferring the load to the internal frame. Depending



on the final design of the detectors and baffle system the support could be a simple beam that runs through the middle of the detectors and baffles. See Figure 172 for similar approach at BNL

## **19.6 Light Gas Cherenkov Installation Structure**

The light gas Cherenkov will mount to the external downstream end of the magnet and will not traverse with endcap. When the endcap is in the operational position the light gas Cherenkov will be enclosed within the cylindrical ring along with the rest of the forward angle detectors. The light gas Cherenkov detector will be made up of six pie shaped sections that will need to be bolted to the downstream side of the magnet. A space frame similar to a scaffolding system would hold and position each section while being attached to magnet. The space frame would attach to the rail system and could be movable along the rails if needed. The space frame will be suitable for personnel access to allow workers to perform the installation and maintenance of the detectors.

## 20 Project Status and Proposed Management Organization

The SoLID spectrometer was initially proposed in 2009 for two experiments: SIDIS experiment (PR12-09-014, later became E12-10-006) and the PVDIS experiment (PR12-09-012, later became E12-10-007). Both experiments aim to achieve high precision which require very high statistics. A spectrometer/detector system with a large acceptance and also able to handle high luminosity is needed. Therefore SoLID is designed to have a large solid angle and broad momentum acceptance and can handle luminosity up to  $10^{39}\text{s}^{-1}\text{cm}^{-2}$  with a baffle system in the PVDIS configuration and  $10^{37}\text{s}^{-1}\text{cm}^{-2}$  without a baffle system in the SIDIS configuration. With these unique features, SoLID is ideal for inclusive and semi-inclusive DIS experiments and is also good for measurements of certain exclusive reactions. The SoLID base equipment consists of a solenoid magnet (CLEO-II magnet), tracking detectors (GEMs), electron PID detectors (electromagnetic calorimeter and light gas Cherenkov detector) and hadron PID detectors (MRPC, heavy gas Cherenkov and EC), DAQ system, supporting structure and infrastructure needed for the spectrometer. Leveraging the unique capabilities of SoLID, currently, there are five high impact (four “A” rating and one “A<sup>−</sup>”) experiments approved using SoLID, including a near threshold  $J/\psi$  production experiment in addition to three SIDIS and one PVDIS experiments. Three more run-group proposals were also approved.

The pre-conceptual design has gone through many iterations, including careful studies, detailed simulations, pre-R&D testings and a number of internal reviews. Among the various internal reviews, it is worth mentioning the two brainstorming sessions in September 2011 and January 2012, organized by the JLab physics division, and the dry run review in June 2012 with external experts (outside SoLID collaboration, including people from outside JLab). A formal pre-conceptual design report was submitted to the JLab management in July 2014. A Director’s Review was held in February 2015. These reviews helped greatly in optimizing, improving and finalizing the conceptual design. Detailed simulations with realistic background (including neutron backgrounds) and pre-R&D activities focusing on the major challenges have significantly improved the reliability of the conceptual design.

### 20.1 Collaboration and Organization

The SoLID collaboration has more than 250 members from over 70 institutions over 13 countries. SoLID has attracted international attention with many groups committed to make significant contributions, including noticeably the contributions to the R&D efforts for large detector projects (GEMs, MRPC and EC) from several Chinese groups and Heavy Gas Cherenkov detector from the Regina group in Canada.

The proposed SoLID Organization Chart is shown in Figure 173.

#### **Project Manager**

Function: The Project Manager (PM) will be in charge of executing the project and report to JLab management. The collaboration will provide advice and oversight, and members of the collaboration will work under the PM in various roles to execute the project. For example, all subsystems coordinators will report to the PM. The PM has the authority and responsibility to manage the SoLID project.

Jian-ping Chen is the initial PM.

#### **Executive Board**

Function: The Executive Board (EB) makes decisions on scientific and organizational choices, and provides high level oversight on all matter pertaining to preparation and operation of the SoLID project.

The Chair of EB is the science leader, and is the principle contact between the collaboration

and the lab management/DOE. The Chair will provide oversight and input to the PM for the SoLID project. The Chair, together with the PM, is responsible for the performance and assessment of all subsystems.

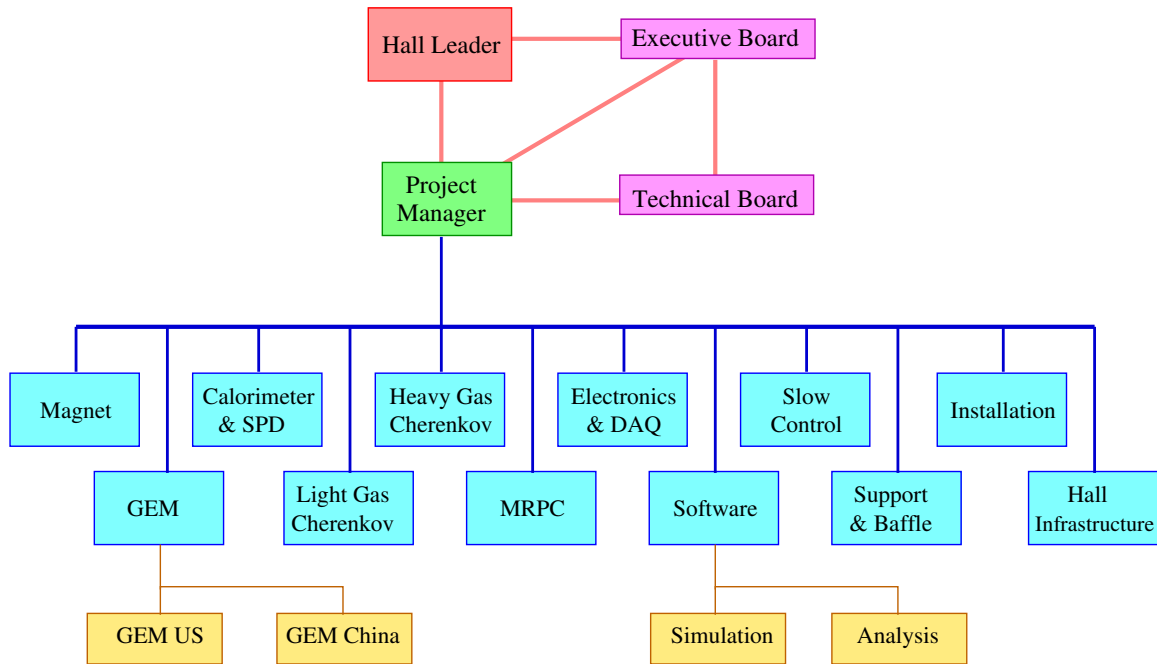


Figure 173: SoLID Organization Chart

Initial members are the senior spokespeople plus the Hall Leader (ex-officio) and the PM (ex-officio): Paul Souder (PVDIS), Haiyan Gao (SIDIS), Zein-Eddine Meziani ( $J/\psi$ ), Thia Keppel (Hall Leader, ex-officio) and Jian-ping Chen (PM, ex-officio).

Paul Souder is the 1st Chair. It is expected that the Chair position will rotate.

#### Technical Board

Function: The technical Board (TB) advises the PM on all aspects of the Project, including any changes in cost, scope or schedule.

The TB will have a group of (usually senior) collaborators who represent the full range of required technical expertise and usually a representative from each subsystem is expected to be on this board. This group will be appointed by the EB. In addition, the TB will include the PM and also project engineers when they are appointed. The membership of the TB can be periodically adjusted by the EB as the situation warrants.

The chair of the TB will be the PM. All EB members who are not already in the TB are ex-officio members, along with the Hall leader.

Initial members: Jian-ping Chen (Chair), Paul Souder, Haiyan Gao, Zein-Eddine Meziani, Thia Keppel (ex-officio); Alexandre Camsonne, Eugene Chudakov, Tom Hemmick, Xiaodong Jiang, Nilanga Liyanage, Bob Michaels, Xin Qian, Paul Reimer, Yi Wang, Zhengguo Zhao, Xiaochao Zheng

#### Sub-System Lead Coordinators and Institutions

- **Magnet:** Robin Wines / Paul Reimer; JLab, Argonne
- **GEM-US:** Nilanga Liyanage / Bernd Surrow ; UVa, Temple

- **GEM-China:** Zhengguo Zhao / Xiaomei Li; USTC, CIAE, Lanzhou, Tsinghua, IMP
- **Calorimeter:** Xiaochao Zheng / Wouter Deconick / Chufeng Feng; UVa, W&M, Shandong (China), Argonne
- **Light Gas Cherenkov:** Zein-Eddine Meziani / Michael Paolone; Temple
- **Heavy Gas Cherenkov:** Haiyan Gao / Zhiwen Zhao / Garth Huber; Duke, Regina (Canada)
- **MRPC:** Yi Wang / Alexandre Camsonne; Tsinghua (China), JLab, Duke, Rutgers
- **DAQ/Electronics:** Alexandre Camsonne / Ron Gilman; JLab, Stony Brook, Rutgers
- **Simulation:** Seamus Riordan / Zhiwen Zhao ; Argonne, Duke, UVa, Syracuse, Stony Brook, Temple
- **Reconstruction and Analysis:** Ole Hansen; JLab
- **Slow Control:** Brad Sawatzky; JLab
- **Supporting Structure and Baffle:** Robin Wines / Seamus Riordan; JLab, Argonne
- **Hall Infrastructure Modification:** Robin Wines / Jessie Butler; JLab
- **Installation:** Jessie Butler / Robin Wines; JLab, all user groups.

The names listed are the coordinators for sub-systems. Institutions working on and responsible for the sub-systems are also listed. Details of the responsibilities are described in the summary for each sub-system. The list reflects the current situation and it is expected to be modified as more groups join the effort as the SoLID project moves forward.

## 20.2 Cost estimation

Cost estimation has gone through many iterations in the last a few years. Procurement cost and manpower estimations were first performed by the coordinators of subsystems. There are variations in assumptions, including the number of years to complete the project. The final estimation made adjustments to keep consistency for all subsystems in the assumptions. The length of the project is assumed to be 4 years. Most of the procurement costs were estimated based on quotations from vendors. Manpower were estimated from comparison with similar projects. JLab manpower was estimated initially based on the estimation of similar projects from other halls. They were revised later using the actual manpower used at the end of project completion in Hall D. The JLab budget office provided valuable assistance in the cost estimation.

## Bibliography

- [1] Z. B. Kang, A. Prokudin, P. Sun and F. Yuan, Phys. Rev. D **93**, 014009 (2016).
- [2] Z. Ye, N. Sato, K. Allada, T. Liu, J.P. Chen, H. Gao, Z. B. Kang, A. Prokudin, P. Sun, and F. Yuan, Phys. Lett. B. **767**, 91-98 (2017).
- [3] D. Wang *et al.* (PVDIS Collaboration), Nature **506**, 67 (2014).
- [4] E. Eichten, K. D. Lane and M. E. Peskin, Phys. Rev. Lett. **50**, 811 (1983).
- [5] J. Erler, C. J. Horowitz, S. Mantry and P. A. Souder, Ann. Rev. Nucl. Part. Sci. **64**, 269 (2014).
- [6] S. Durr *et al.*, Science **322**, 1224 (2008).
- [7] Wang, Qian, Liu, Xiao-Hai and Zhao, Qiang, Phys. Rev. D **92**, 034022 (2015).
- [8] S. An et al, NIM A **594**, 39 (2008).
- [9] Mickey Chiu et al, Progress Report of (Sub) 10 Picosecond Timing Detectors for Generic Detector R&D for an Electron Ion Collider, [https://wiki.bnl.gov/conferences/images/c/c8/ERD10\\_Report\\_2015-06.pdf](https://wiki.bnl.gov/conferences/images/c/c8/ERD10_Report_2015-06.pdf).
- [10] M. Boglione, L. Gamberg, J. O. Gonzalez-Hernandez, T. C. Rogers and N. Sato, Phys. Lett. B **766**, 245 (2017).
- [11] European Muon, J. Ashman *et al.*, Phys. Lett. **B206**, 364 (1988).
- [12] B. W. Filippone and X.-D. Ji, Adv. Nucl. Phys. **26**, 1 (2001), hep-ph/0101224.
- [13] S. E. Kuhn, J. P. Chen, and E. Leader, Prog. Part. Nucl. Phys. **63**, 1 (2009), 0812.3535.
- [14] X. Artru and M. Mekhfi, Z. Phys. **C45**, 669 (1990).
- [15] P. J. Mulders and R. D. Tangerman, Nucl. Phys. **B461**, 197 (1996), hep-ph/9510301.
- [16] D. Boer and P. J. Mulders, Phys. Rev. **D57**, 5780 (1998), hep-ph/9711485.
- [17] X.-d. Ji, J.-P. Ma, and F. Yuan, Phys. Lett. **B597**, 299 (2004), hep-ph/0405085.
- [18] K. Hidaka, E. Monsay, and D. W. Sivers, Phys. Rev. **D19**, 1503 (1979).
- [19] J. P. Ralston and D. E. Soper, Nucl. Phys. **B152**, 109 (1979).
- [20] R. L. Jaffe and X.-D. Ji, Phys. Rev. Lett. **67**, 552 (1991).
- [21] V. Barone, Phys. Lett. **B409**, 499 (1997), hep-ph/9703343.
- [22] C. Bourrely, J. Soffer, and O. V. Teryaev, Phys. Lett. **B420**, 375 (1998), hep-ph/9710224.
- [23] J. Soffer, Phys. Rev. Lett. **74**, 1292 (1995), hep-ph/9409254.
- [24] W. Vogelsang, Phys. Rev. **D57**, 1886 (1998), hep-ph/9706511.
- [25] G. R. Goldstein, R. L. Jaffe, and X.-D. Ji, Phys. Rev. **D52**, 5006 (1995), hep-ph/9501297.
- [26] J. Ralston, private communications.

- [27] QCDSF, M. Gockeler *et al.*, Phys. Lett. **B627**, 113 (2005), hep-lat/0507001.
- [28] H.-X. He and X.-D. Ji, Phys. Rev. **D52**, 2960 (1995), hep-ph/9412235.
- [29] B. Q. Ma, I. Schmidt, and J. Soffer, Phys. Lett. **B441**, 461 (1998).
- [30] L. P. Gamberg and G. R. Goldstein, Phys. Rev. Lett. **87**, 242001 (2001), hep-ph/0107176.
- [31] I. C. Cloet, W. Bentz, and A. W. Thomas, Phys. Lett. **B659**, 214 (2008), 0708.3246.
- [32] M. Wakamatsu, Phys. Lett. **B653**, 398 (2007), 0705.2917.
- [33] B. Pasquini, M. Pincetti, and S. Boffi, Phys. Rev. **D72**, 094029 (2005), hep-ph/0510376.
- [34] J. C. Collins, Nucl. Phys. **B396**, 161 (1993), hep-ph/9208213.
- [35] Belle, K. Abe *et al.*, Phys. Rev. Lett. **96**, 232002 (2006), hep-ex/0507063.
- [36] HERMES, A. Airapetian *et al.*, (2010), hep-ex/1006.4221.
- [37] HERMES, A. Airapetian *et al.*, Phys. Rev. Lett. **103**, 152002 (2009), 0906.3918.
- [38] HERMES, A. Airapetian *et al.*, Phys. Rev. Lett. **94**, 012002 (2005), hep-ex/0408013.
- [39] COMPASS, M. G. Alekseev *et al.*, (2010), 1005.5609.
- [40] COMPASS, V. Y. Alexakhin *et al.*, Phys. Rev. Lett. **94**, 202002 (2005), hep-ex/0503002.
- [41] D. W. Sivers, Phys. Rev. **D41**, 83 (1990).
- [42] X. Qian *et al.*, Phys. Rev. Lett. **107**, 072003 (2011).
- [43] G. L. Kane, J. Pumplin, and W. Repko, Phys. Rev. Lett. **41**, 1689 (1978).
- [44] M. Anselmino, M. Boglione, and F. Murgia, Phys. Lett. **B362**, 164 (1995), hep-ph/9503290.
- [45] J. C. Collins, Phys. Lett. **B536**, 43 (2002), hep-ph/0204004.
- [46] A. V. Belitsky, X. Ji, and F. Yuan, Nucl. Phys. **B656**, 165 (2003), hep-ph/0208038.
- [47] D. Boer, P. J. Mulders, and F. Pijlman, Nucl. Phys. **B667**, 201 (2003), hep-ph/0303034.
- [48] S. J. Brodsky, D. S. Hwang, and I. Schmidt, Phys. Lett. **B530**, 99 (2002), hep-ph/0201296.
- [49] X.-d. Ji and F. Yuan, Phys. Lett. **B543**, 66 (2002), hep-ph/0206057.
- [50] L. P. Gamberg, G. R. Goldstein, and K. A. Oganessyan, Phys. Rev. **D67**, 071504 (2003), hep-ph/0301018.
- [51] M. Burkardt, Phys. Rev. **D69**, 057501 (2004), hep-ph/0311013.
- [52] M. Burkardt, Phys. Rev. **D72**, 094020 (2005), hep-ph/0505189.
- [53] S. J. Brodsky and S. Gardner, Phys. Lett. **B643**, 22 (2006), hep-ph/0608219.
- [54] J. Huang *et al.*, Phys. Rev. Lett. **108**, 052001 (2012).
- [55] T.-C. Meng, J.-C. Pan, Q.-b. Xie, and W. Zhu, Phys. Rev. **D40**, 769 (1989).

- [56] M. Anselmino, M. Boglione, and F. Murgia, Phys. Rev. **D60**, 054027 (1999), hep-ph/9901442.
- [57] A. Bacchetta, A. Schaefer, and J.-J. Yang, Phys. Lett. **B578**, 109 (2004), hep-ph/0309246.
- [58] Z. Lu and B.-Q. Ma, Nucl. Phys. **A741**, 200 (2004), hep-ph/0406171.
- [59] L. P. Gamberg, G. R. Goldstein, and M. Schlegel, (2007), 0708.2580.
- [60] A. Bacchetta, F. Conti, and M. Radici, Phys. Rev. **D78**, 074010 (2008), 0807.0323.
- [61] B. Pasquini and F. Yuan, Phys. Rev. D **81**, 114013 (2010).
- [62] F. Yuan, Phys. Lett. **B575**, 45 (2003), hep-ph/0308157.
- [63] D. Amrath, A. Bacchetta, and A. Metz, Phys. Rev. **D71**, 114018 (2005), hep-ph/0504124.
- [64] A. Bacchetta, L. P. Gamberg, G. R. Goldstein, and A. Mukherjee, Phys. Lett. **B659**, 234 (2008), arXiv:0707.3372 [hep-ph].
- [65] H. H. Matevosyan, A. W. Thomas, W. Bentz, Phys. Rev. D **86**, 034025 (2012), arXiv:1205.5813 [hep-ph].
- [66] A. Kotzinian, H. H. Matevosyan and A. W. Thomas, arXiv:1403.5562 [hep-ph].
- [67] A. Metz, Phys. Lett. **B549**, 139 (2002).
- [68] J. C. Collins and A. Metz, Phys. Rev. Lett. **93**, 252001 (2004), hep-ph/0408249.
- [69] L. P. Gamberg, A. Mukherjee, and P. J. Mulders, Phys. Rev. **D77**, 114026 (2008), 0803.2632.
- [70] G. R. Goldstein and L. Gamberg, (2002), Transversity and meson photoproduction Proceedings of ICHEP 2002; North Holland Amsterdam, p. 452 (2003), hep-ph/0209085, Published in Amsterdam ICHEP 452-454.
- [71] Z. Lu and B.-Q. Ma, Phys. Rev. **D70**, 094044 (2004), hep-ph/0411043.
- [72] H. Avakian *et al.*, Phys. Rev. D **78**, 114024 (2008).
- [73] J. She, J. Zhu, and B.-Q. Ma, Phys. Rev. D **79**, 054008 (2009).
- [74] B. Pasquini, S. Cazzaniga, and F. Yuan, Phys. Rev. D **78**, 034025 (2008).
- [75] S. Boffi, A. V. Efremov, B. Pasquini, and P. Schweitzer, Phys. Rev. **D79**, 094012 (2009), 0903.1271.
- [76] V. Barone, Z. Lu, and B.-Q. Ma, Phys. Lett. **B632**, 277 (2006), hep-ph/0512145.
- [77] V. Barone, A. Prokudin, and B.-Q. Ma, Phys. Rev. **D78**, 045022 (2008), 0804.3024.
- [78] M. Anselmino *et al.*, Phys. Rev. **D75**, 054032 (2007), hep-ph/0701006.
- [79] COMPASS, E. S. Ageev *et al.*, Nucl. Phys. **B765**, 31 (2007), hep-ex/0610068.
- [80] COMPASS, M. Alekseev *et al.*, Phys. Lett. **B673**, 127 (2009), 0802.2160.
- [81] M. Anselmino *et al.*, Eur. Phys. J. **A39**, 89 (2009), 0805.2677.

- [82] M. Anselmino *et al.*, Phys. Rev. **D72**, 094007 (2005), hep-ph/0507181.
- [83] M. Anselmino *et al.*, (2005), hep-ph/0511017.
- [84] M. Anselmino *et al.*, Phys. Rev. **D71**, 074006 (2005), hep-ph/0501196.
- [85] J. C. Collins *et al.*, Phys. Rev. **D73**, 014021 (2006), hep-ph/0509076.
- [86] V. Barone, A. Drago, and P. G. Ratcliffe, Phys. Rept. **359**, 1 (2002), hep-ph/0104283.
- [87] Jefferson Lab Experiment E12-10-006, Spokespersons: Chen, Gao (contact), Jiang, Peng, and Qian.
- [88] Jefferson Lab Experiment E12-10-006, Spokespersons: Chen, Huang (contact), Qiang, and Yan.
- [89] Jefferson Lab Experiment E12-11-108, Spokespersons: Allada, Chen, Gao (contact), Li, and Meziani.
- [90] D. Crabb *et al.*, Phys. Rev. Letts. **64**, 2627 (2008).
- [91] C. Keith *et al.*, Nucl. Inst. Meth. **A501**, 327 (2003).
- [92] G. S. Atoian *et al.*, Nucl. Inst. Meth. **A531**, 467 (2004).
- [93] G. S. Atoian *et al.*, Nucl. Inst. Meth. **A584**, 291 (2008).
- [94] M. Anselmino and A. Prokudin, private communications.
- [95] J. Huang and Y. Qiang, *Maximum likelihood estimation of asymmetry and angular modulation for transversity (2010)*, URL <http://www.jlab.org/jinhuang/Transversity/MLE.pdf>.
- [96] Z. Ye *et al.*, Phys. Lett. B **767**, 91 (2017).
- [97] T. Hobbs and W. Melnitchouk, Phys. Rev. D **77**, 114023 (2008) [arXiv:0801.4791 [hep-ph]].
- [98] D. Wang *et al.* [PVDIS Collaboration], Nature **506**, no. 7486, 67 (2014).
- [99] S. Mantry, M. J. Ramsey-Musolf and G. F. Sacco, Phys. Rev. C **82**, 065205 (2010) [arXiv:1004.3307 [hep-ph]].
- [100] M. R. Buckley and M. J. Ramsey-Musolf, Phys. Lett. B **712**, 261 (2012) [arXiv:1203.1102 [hep-ph]].
- [101] E. Eichten, K. D. Lane and M. E. Peskin, Phys. Rev. Lett. **50**, 811 (1983).
- [102] F. E. Close and A. W. Thomas, Phys. Lett. B **212**, 227 (1988).
- [103] E. Sather, Phys. Lett. B **274**, 433 (1992).
- [104] E. N. Rodionov, A. W. Thomas and J. T. Londergan, Mod. Phys. Lett. A **9**, 1799 (1994).
- [105] G. P. Zeller *et al.* [NuTeV Collaboration], Phys. Rev. Lett. **88**, 091802 (2002) [Erratum-ibid. **90** 239902 (2003)].
- [106] J. T. Londergan and A. W. Thomas, Phys. Lett. B **558** 132 (2003).



- [107] J. T. Londergan and A. W. Thomas, J. Phys. G **31** 1151 (2005).
- [108] M. Gluck, P. Jimenez-Delgado and E. Reya, Phys. Rev. Lett. **95** 022002 (2005).
- [109] I. C. Cloet, W. Bentz and A. W. Thomas, Phys. Rev. Lett. **102**, 252301 (2009) [arXiv:0901.3559 [nucl-th]].
- [110] W. Melnitchouk, I. R. Afnan, F. Bissey and A. W. Thomas, Phys. Rev. Lett. **84** 5455 (2000).
- [111] W. Melnitchouk and A. W. Thomas, Phys. Lett. B **377** 11 (1996).
- [112] S. I. Alekhin, Phys. Rev. D **63** 094022 (2001).
- [113] S. Kuhlmann *et al.*, Phys. Lett. B **476** 297 (2000).
- [114] S. J. Brodsky and G. A. Miller, Phys. Lett. B **412**, 125 (1997).
- [115] S. J. Brodsky, I. A. Schmidt, and G. F. de Téramond, Phys. Rev. Lett., **64**, 1011 (1990).
- [116] M. E. Luke, A. V. Manohar, and M. J. Savage. Phys. Lett. B **288**, 355 (1992).
- [117] A. B. Kaidalov and P. E. Volkovitsky, Phys. Rev. Lett., **69**, 3155 (1992).
- [118] G. F. de Téramond, R. Espinoza, and M. Ortega-Rodriguez. Phys. Rev. D **58**, 034012 (1998).
- [119] V. I. Shevchenko, Phys. Lett. B **392**, 457 (1997).
- [120] A. Hayashigaki, Prog. Theor. Phys., **101**, 923 (1999).
- [121] K. Yokokawa, S. Sasaki, T. Hatsuda, and A. Hayashigaki, Phys. Rev. D **74**, 034504 (2006).
- [122] T. Kawanai and S. Sasaki, Phys. Rev. D **82**, 091501 (2010).
- [123] K. Tsushima, D. H. Lu, G. Krein, and A. W. Thomas, Phys.Rev. C **83**, 065208 (2011).
- [124] K. Tsushima, D. H. Lu, G. Krein, and A. W. Thomas, AIP Conf. Proc. **1354**, 39 (2011).
- [125] M. Binkeley et al., Phys. Rev. Lett. **48**, 73 (1982).
- [126] B. H. Denby et al., Phys. Rev. Lett. **52**, 795 (1984).
- [127] M. D. Sokoloff et al., Phys. Rev. Lett. **57**, 3003 (1986).
- [128] R. Barate et al, Z. Phys. C **33**, 505 (1987).
- [129] P. L. Frabetti et al., Phys. Lett. B **316**, 197 (1993).
- [130] S. Aid et al., Nucl. Phys. B **472**, 3 (1996).
- [131] J. Breitweg et al., Z. Phys. C **76**, 599 (1997).
- [132] S. Aid et al., Nucl. Phys. B **472**, 2 (1996).
- [133] U. Camerini et al., Phys. Rev. Lett. **35**, 483 (1975).
- [134] B. Gittelman et al., Phys. Rev. Lett. **35**, 1616 (1975).
- [135] B. Knapp et al., Phys. Rev. Lett. **34**, 1040 (1975).

- [136] R. L. Anderson, *Excess Muons and New Results in  $\Psi$  Photoproduction*, SLAC-PUB-1471.
- [137] D. Kharzeev, nucl-th/9601029.
- [138] D. Kharzeev, H. Satz, A. Syamtomov, and G. Zinovjev, Eur. Phys. J. C **9**, 459 (1999).
- [139] S. J. Brodsky, E. Chudakov, P. Hoyer, and J.M. Laget, Phys. Lett. B **498**, 23 (2001).
- [140] A. Sibirtsev, S. Krewald, and A. W. Thomas, J. Phys. G **30**, 1427 (2004).
- [141] M. A. Shifman, A. I. Vainshtein, and V. I. Zakharov, Phys. Lett. B **65**, 255 (1976).
- [142] V. A. Novikov, M. A. Shifman, A. I. Vainshtein, and V. I. Zakharov, Nucl. Phys. **B136**, 125 (1978).
- [143] . A. Shifman, A. I. Vainshtein, and V. I. Zakharov, Nucl. Phys. **B136**, 157 (1978).
- [144] A. Sibirtsev and M. B. Voloshin, Phys. Rev. D **71**, 076005 (2005).
- [145] R. B. Baldini, S. Pacetti and A. Zallo, arXiv:0812.3283 [hep-ph].
- [146] M. Ablikim *et al.* (BESIII Collaboration), Phys. Rev. Lett. **108**, 112003 (2012).
- [147] Gryniuk, Oleksii and Vanderhaeghen, Marc”, Phys. Rev. D **94**, 074001 (2016).
- [148] J. J. Wu, R. Molina, E. Oset, and B.-S. Zou, Phys. Rev. Lett. **105**, 232001 (2010).
- [149] P. Bosted *et al.*, Phys. Rev. C **79**, 015209 (2009).
- [150] Contact Person: E. Chudakov, PAC32 PR12-07-106 The A-dependence of  $J/\Psi$  Photoproduction near Threshold.
- [151] Contact Person: Z.-E. Meziani, PAC39 [https://www.jlab.org/exp\\_prog/proposals/12/PR12-12-006.pdf](https://www.jlab.org/exp_prog/proposals/12/PR12-12-006.pdf).
- [152] Contact Person: P. Souder, PAC34 <http://hallaweb.jlab.org/collab/PAC/PAC34/PR-09-012-pvdis.pdf>.
- [153] Contact Person: H. Gao, PAC34 <http://hallaweb.jlab.org/collab/PAC/PAC34/PR-09-014-transversity.pdf>.
- [154] Contact Person: J. Huang, PAC37 [http://www.jlab.org/exp\\$\\$\\_{prog}/PACpage/PAC37/proposals/Proposals/NewProposals/PR-11-007.pdf](http://www.jlab.org/exp$$_{prog}/PACpage/PAC37/proposals/Proposals/NewProposals/PR-11-007.pdf).
- [155] Contact Person: H. Gao, PAC38 [http://wwwold.jlab.org/exp\\$\\$\\_{prog}/proposals/11/PR12-11-108.pdf](http://wwwold.jlab.org/exp$$_{prog}/proposals/11/PR12-11-108.pdf).
- [156] X. Qian et al., Phys. Rev. C **81**, 055209 (2010).
- [157] S. J. Brodsky et al., Phys. Lett. B **498**, 23 (2001).
- [158] K. Schilling and G. Wolf, Nucl. Phys. **B61**, 381 (1973).
- [159] R. Fiore et al., Phys. Rev. D **80**, 116001 (2009).
- [160] Aaij, Roel et al. (LHCb Collaboration), Phys. Rev. Lett., **115**, 072001 (2015).

- [161] C. Adloff et al., Eur. Phys. J. C **13**, 371 (2000).
- [162] L. W. Whitlow, Ph. D. thesis, Stanford University, SLAC-Report-357 (1990).
- [163] Developed by J. W. Lightbody and J. S. O’Connell in 1988.
- [164] D. E. Wiser, Ph. D. thesis, Univ. of Wisconsin (1977).
- [165] X. Qian, Ph. D. thesis, Duke University.
- [166] T. Abe, Computer Physics Communications **136**, 126 (2001).
- [167] PYTHIA, <http://projects.hepforge.org/pythia6/>, 2006.
- [168] Y. Kubota et al., Nucl. Instr. and Meth. A **320** (1992).
- [169] Poisson Superfish, [http://laacg1.lanl.gov/laacg/services/download\\_sfp.html](http://laacg1.lanl.gov/laacg/services/download_sfp.html).
- [170] G. Atoian et al., Nucl. Instr. and Meth. A **584**, 291 (2008).
- [171] W. Anderson et al., arXiv:1103.4277 [physics.ins-det].
- [172] B. Azmoun et al., IEEE Trans. Nucl. Sci. **56-3**, 1544 (2009).
- [173] C. Lu and K. T. McDonald, Nucl. Instr. and Meth. A **343**, 135 (1994).
- [174] Y. Wang et al., Chin. Phys. C **33**, 374 (2009).
- [175] S. J. Brodsky, P. Hoyer, C. Peterson, and N. Sakai, Phys. Lett. **93B**, 451 (1980).
- [176] S. J. Brodsky, C. Peterson and N. Sakai, Phys. Rev. D **23**, 2745 (1981).
- [177] W. C. Chang and J. C. Peng, Phys. Lett. B **704**, 197 (2011).
- [178] B. W. Adams *et al.*, “A Brief Technical History of the Large-Area Picosecond Photodetector (LAPPD) Collaboration,” arXiv:1603.01843.
- [179] “eRD14: PID Consortium for an integrated program for Particle Identification (PID) at a future Electron Ion Collider,” [https://wiki.bnl.gov/conferences/images/6/6f/ERD14\\_progress\\_report\\_Dec\\_2015.pdf](https://wiki.bnl.gov/conferences/images/6/6f/ERD14_progress_report_Dec_2015.pdf).
- [180] E12-10-007 “Precision Measurement of Parity-violation in Deep Inelastic Scattering Over a Broad Kinematic Range” Contact person: P. Souder.
- [181] E12-10-006, “Target Single Spin Asymmetry in Semi-Inclusive Deep-Inelastic ( $e, e'\pi^\pm$ ) on a Transversely Polarized  $^3\text{He}$  Target at 8.8 and 11 GeV”, Spokesperson: J.-P. Chen, H. Gao (contact), X. Jiang, J.-C. Peng, and X. Qian.
- [182] E12-11-007, “Asymmetries in Semi-Inclusive Deep-Inelastic ( $e, e'\pi^\pm$ ) Reactions on a Longitudinally Polarized  $^3\text{He}$  Target at 8.8 and 11 GeV”, Spokesperson: J.-P. Chen, J. Huang (contact), Y. Qiang, and W.-B. Yan.
- [183] E12-11-108 “Target Single Spin Asymmetry in Semi-Inclusive Deep-Inelastic ( $e, e'\pi^\pm$ ) on a Transversely Polarized Proton Target”, Spokespersons: K. Allada, J.-P. Chen, H. Gao (contact), Z.-E. Meziani, and X.-M. Li.

- [184] M. Anselmino and A. Prokudin, *private communications*. Predictions are based on the extractions of Ref. [185].
- [185] M. Anselmino *et al.*, proceedings of the XVI International Workshop on Deep Inelastic Scattering and Related Subjects, DIS 2008, London, U.K. 2009. e-Print: arXiv:0807.0173.
- [186] W. Vogelsang and F. Yuan, *private communications*.
- [187] B. Pasquini, *private communication*.  
S. Boffi, A. V. Efremov, B. Pasquini and P. Schweitzer, Phys. Rev. **D79**, 094012 (2009) arXiv:0903.1271.
- [188] X. Qian *et al.* (JLab Hall A Collaboration) Phys. Rev. Lett. **107**, 072003 (2011).
- [189] J. Huang *et al.* (JLab Hall A Collaboration) Phys. Rev. Lett. **108**, 052001 (2012).
- [190] X. Qian, Modern Phys. Lett. **A27**, 1230021 (2012).
- [191] Y. Zhang *et al.* Chinese Physics **C36**, 610 (2012).
- [192] L. W. Whitlow, SLAC-Report-357 (1990).
- [193] J. W. Lightbody and J. S. O’Connell, Computers in Physics 2, 57 (1988).
- [194] D. E. Wiser, Ph. D. thesis, Univ. of Wisconsin (1977).
- [195] E12-12-006, “Near-Threshold Electroproduction of  $J/\psi$  with a 11 GeV Beam”, Spokespersons: K. Hafidi, Z.-E. Meziani (contact), X. Qian, N. Sparveris, and Z.-W. Zhao.
- [196] Study of modifying CLEO II magnet for SoLID, E.Chudakov ([https://userweb.jlab.org/~gen/jlab12gev/cleo\\_mag/](https://userweb.jlab.org/~gen/jlab12gev/cleo_mag/))
- [197] Y. Kubota *et al.*, Nucl. Inst. and Meth., **A320** 66 (1992)
- [198] D. M. Coffman *et al.*, IEEE Transactions on Nuclear Science, **37** 1172 (1990)
- [199] X. Qian *et al.*, Phys. Rev. Lett. 107, (2012) 072003. J. Huang *et al.*, Phys. Rev. Lett. 108 (2012) 052001.
- [200] T.D. Averett, *et al.*, Nucl. Instr. and Meth. A 427 (1999) 440.
- [201] J. Maxwell *et al.*, to be submitted to Nucl. Instr. and Meth. A.
- [202] D.G. Crabb, C.B. Higley, A.D. Krisch, R.S. Raymond, T. Roser, and J.A. Stewart, Phys. Rev. Lett. 64, (1990) 2627.
- [203] C.D. Keith, *et al.*, Nucl. Instr. and Meth. A 684 (2012) 27.
- [204] C.D. Keith, *et al.*, Nucl. Instr. and Meth. A 501 (2003) 327.
- [205] Design Report rfq 14231, Oxford Instruments Nanotechnology Tools Ltd.
- [206] F. Sauli, Nucl. Inst. and Meth. **A 386**, 531 (1997).
- [207] B. Ketzer *et al.*, Nucl. Phys. B (Proc. Suppl.) **125**, 368 (2003).

- [208] M. Villa, *et al.*, Nucl. Inst. and Meth. **A 628** 182 (2011).
- [209] M. Alfonsi *et al.*, Nucl. Inst. and Meth. **A 617**, 151 (2010).
- [210] D. Abbaneo *et al.*, Nucl. Inst. and Meth. **A** (2010).
- [211] M.J. French *et al.*, Nucl. Instr. and Meth. **A 466** 359 (2001).
- [212] F.Sauli, RD51-NOTE-2012-007 REVISED 21.09.2012.
- [213] D. Abbaneo *et al.*, RD51-NOTE-2012-012 16.11.2012.
- [214] William Whyte, “Cleanroom Technology: Fundamentals of Design, Testing and Operation” (2001) ISBN 978-0-470-74806-0
- [215] P. Walker, V. Weber, *et al.*, Journal of Photographic Science, **18** 150 (1970).
- [216] J. M. Shaw, J. D. Gelorme, *et al.*, IBM Journal of Research and Development. **41** 81 (1997) ISSN: 0018-8646
- [217] Rensheng Wang, Yan Huang, Zhigang Xiao *et al.*, Nucl. Inst. and Meth. **A701** 54 (2013)
- [218] S. P. Malace, B. D. Sawatzky and H. Gao, “Studies of single-photoelectron response and of performance in magnetic field of a H8500C-03 photomultiplier tube,” JINST **1309**, P09004 (2013) [arXiv:1306.6277 ].
- [219] Composite Mirror Applications, Inc. 1638 S. Research Loop, Suite 100 Tucson, Arizona 85710. <http://www.compositemirrors.com>
- [220] LHCb RICH Technical Design Report, The LHCb Colaboration: [lhcb-rich.web.cern.ch/lhcb-rich/richtdr/tdr.pdf](http://lhcb-rich.web.cern.ch/lhcb-rich/richtdr/tdr.pdf)
- [221] Hamamatsu flat panel type multianode photomultiplier tube assembly H8500 series specifications are found at [http://jp.hamamatsu.com/products/sensor-etd/pd002/pd394/H8500C/index\\_en.html](http://jp.hamamatsu.com/products/sensor-etd/pd002/pd394/H8500C/index_en.html)
- [222] Amuneal Manufacturing Corporation. 4737 Darrah Street Philadelphia, PA 19124, USA. [www.amuneal.com](http://www.amuneal.com)
- [223] GEMC: a GEant4 Monte Carlo. <https://gemc.jlab.org/>
- [224] GEANT4: a toolkit for the simulation of the passage of particles through matter: <http://geant4.cern.ch/>
- [225] M. Artuso *et al.*, Nuclear Instruments and Methods A, 558 373-387 (2006).
- [226] A. Bulla, Ph.D. thesis (1997); E. Fokitis *et al.*, Nuclear Instruments and Methods A 371 255 (1996).
- [227] G.J. Barber *et al.*, Nuclear Instruments and Methods A 593 624-637 (2008).
- [228] JLab approved experiments E-12-09-014 and E-12-10-006  
[http://www.jlab.org/exp\\_prog/proposals/09/PR12-09-014.pdf](http://www.jlab.org/exp_prog/proposals/09/PR12-09-014.pdf)  
[http://www.jlab.org/exp\\_prog/proposals/10/PR12-10-006.pdf](http://www.jlab.org/exp_prog/proposals/10/PR12-10-006.pdf)

- [229] S. P. Malace, B. D. Sawatzky and H. Gao, “Studies of single-photoelectron response and of performance in magnetic field of a H8500C-03 photomultiplier tube,” JINST **1309**, P09004 (2013) [arXiv:1306.6277 ].
- [230] G. S. Atoian *et al.*, Nucl. Instrum. Meth. A **584**, 291 (2008).
- [231] H. Avakian *et al.*, Nucl. Instrum. Meth. A **417**, 69 (1998).
- [232] E. Picatoste Olloqui [LHCb Collaboration], J. Phys. Conf. Ser. **160**, 012046 (2009).
- [233] Y. V. Kharlov *et al.*, Nucl. Instrum. Meth. A **606**, 432 (2009).
- [234] D. A. Morozov *et al.*, J. Phys. Conf. Ser. **160**, 012021 (2009).
- [235] ATLAS Tile Calorimeter Technical Design Report (1996).
- [236] L. Aliaga *et al.* [MINERvA Collaboration], Nucl. Instrum. Meth. A **743**, 130 (2014) doi:10.1016/j.nima.2013.12.053 [arXiv:1305.5199 [physics.ins-det]].
- [237] M. J. Varanda, M. David, A. Gomes and A. Maio, Nucl. Instrum. Meth. A **453**, 255 (2000). doi:10.1016/S0168-9002(00)00642-2
- [238] LHCb Tracker Upgrade Technical Design Report.
- [239] Y. Wang, *et al.*, Nucl. Instr. and Meth. A 538 (2005) 425.
- [240] Y. Wang, *et al.*, Nucl. Instr. and Meth. A 537 (2005) 698.
- [241] A. Akindinov, *et al.*, Nucl. Instr. and Meth. A 602 (2009) 709.
- [242] A. Akindinov, *et al.*, Nucl. Instr. and Meth. A 533 (2004) 74.
- [243] Y. Wang, *et al.*, Chinese Physics C. 33 (2009) 374.
- [244] J.B. Wang, *et al.*, 2012 JINST 7 P10004.
- [245] JLab E-08-027, A. Camsonne, J. P. Chen, D. Crabb and K Slifer, spokespersons; [http://www.jlab.org/exp\\_prog/proposals/08/PR-08-027.pdf](http://www.jlab.org/exp_prog/proposals/08/PR-08-027.pdf)
- [246] V. Gyurjyan *et al.*, J. Phys. Conf. Ser. **331**, 032013 (2011). <https://claraweb.jlab.org/docs/clara>
- [247] D. Lawrence, J. Phys. Conf. Ser. **119**, 042018 (2008). <https://www.jlab.org/JANA>
- [248] M. Al-Turany *et al.*, J. Phys. Conf. Ser. **396**, 022001 (2012). <https://fairroot.gsi.de>
- [249] C. Green *et al.*, J. Phys. Conf. Ser. **396**, 022020 (2012). <http://art.fnal.gov>
- [250] See for example E. Sexton-Kennedy, *A Review of Event Processing Frameworks used in HEP*, Talk at CHEP 2015, <http://indico.cern.ch/event/304944/contributions/1672690/>
- [251] R. Brun and F. Rademakers, Nucl. Instr. Meth. Phys. Res. A **389**, 81 (1997). <http://root.cern/>

- [252] ROOT/C++ Analyzer for JLab Hall A, <https://hallaweb.jlab.org/podd>. Code repository <https://github.com/JeffersonLab/analyzer>
- [253] <https://github.com/sPHENIX-Collaboration/coresoftware>
- [254] <https://cdcv.s.fnal.gov/redmine/issues/15372>
- [255] M. Al-Turany *et al.*, J. Phys. Conf. Ser. **664**, 072001 (2015).
- [256] Fluka, <http://www.fluka.org>
- [257] Geant4, <http://geant4.cern.ch/>
- [258] GEMC, <https://gemc.jlab.org/>
- [259] Poisson superfish, [http://laacg1.lanl.gov/laacg/services/download\\_sf.phtml](http://laacg1.lanl.gov/laacg/services/download_sf.phtml)
- [260] Tosca, <http://www.chilton-computing.org.uk/inf/eng/electromagnetics/p001.htm>
- [261] C. Altunbas *et al.*, Nucl. Inst. Meth. A **490**, 177 (2002).
- [262] J. Huston, H.L. Lai, P. Nadolsky, W.K. Tung, J. Pumplin, and D.R. Stump, JHEP 07 (2002) 012.
- [263] David E. Wiser, and Pions at SLAC Energies,” PhD thesis, Wisconsin University Madison, 1977, <http://wwwlib.umi.com/dissertations/fullcit?p7719743>
- [264] S. Riordan, X. Zheng, Z. W. Zhao and N. Ton, unpublished (2014).
- [265] R. Beminiwattha, [https://hallaweb.jlab.org/DocDB/0002/000212/001/HallD\\_Gen\\_Summary.pdf](https://hallaweb.jlab.org/DocDB/0002/000212/001/HallD_Gen_Summary.pdf)
- [266] Mark Ito, private communication (2014).
- [267] Eugene Chudakov, private communication (2014).
- [268] V. M. Budnev, I. F. Ginzburg, G. V. Meledin and V. G. Serbo, Phys. Rep. **15**, 181 (1975).
- [269] J. Beringer *et al.* (Particle Data Group), Phys. Rev. D **86**, 010001 (2012).
- [270] Yung-Su Tsai, Rev. Mod. Phys. **46**, 815 (1974).
- [271] R. E. Kalman, Transactions of ASME Journ. Basic Engineering **82**, 35 (1960).
- [272] R. Mankel, Rept. Prog. Phys. **67**, 553 (2004).
- [273] M. Capogni, E. Cisbani, G.M. Urciuli, *Note on GEM digitization modeling*, [http://www.iss.infn.it/cisbani/atmp/sbs/ft/gemc/diginote\\_0.2.pdf](http://www.iss.infn.it/cisbani/atmp/sbs/ft/gemc/diginote_0.2.pdf).
- [274] H. Avakian *et.al* Nucl. Instrum. Meth. A**417**, 69 (1998).
- [275] A. Bacchetta, M. Diehl, K. Goeke, A. Metz, P. J. Mulders, and M. Schlegel, JHEP **0702**, 093 (2007).

- [276] S. Dulat *et al.*, Phys. Rev. D **93**, 033006 (2016).
- [277] D. de Florian, R. Sassot and M. Stratmann, Phys. Rev. D **75**, 114010 (2007).
- [278] M. Anselmino, M. Boglione, U. D’Alesio, A. Kotzinian, F. Murgia and A. Prokudin, Phys. Rev. D **71**, 074006 (2005).
- [279] M. Anselmino, M. Boglione, U. D’Alesio, A. Kotzinian, S. Melis, F. Murgia, A. Prokudin and C. Turk, Eur. Phys. J. A **39**, 89 (2009).
- [280] M. Anselmino, M. Boglione, U. D’Alesio, S. Melis, F. Murgia and A. Prokudin, Phys. Rev. D **87**, 094019 (2013).
- [281] C. Lefky and A. Prokudin, Phys. Rev. D **91**, 034010 (2015).
- [282] L. P. Kaptari, A. Del Dotto, E. Pace, G. Salmè and S. Scopetta, Phys. Rev. C **89**, 035206 (2014).
- [283] A. Del Dotto, private communication
- [284] I. Akushevich, N. Shumeiko and A. Soroko, Eur. Phys. J. C **10**, 681 (1999).
- [285] I. Akushevich, A. Ilyichev and M. Osipenko, Phys. Lett. B **672**, 35 (2009).
- [286] J. Pumplin, D. R. Stump, J. Huston, H. L. Lai, P. M. Nadolsky and W. K. Tung, JHEP **0207**, 012 (2002).
- [287] “SoLID Preliminary Conceptual Design Report”, The SoLID Collaboration, unpublished (2014).
- [288] A. Narayan *et al.*, Phys. Rev. X **6**, no. 1, 011013 (2016).
- [289] H. Spiesberger, Phys. Rev. D **52**, 4936 (1995).
- [290] M. E. Christy and P. E. Bosted, Phys. Rev. C **81**, 055213 (2010).
- [291] E12-10-006, “Target Single Spin Asymmetry in Semi-Inclusive Deep-Inelastic ( $e, e'\pi^\pm$ ) on a Transversely Polarized  $^3\text{He}$  Target at 8.8 and 11 GeV”, Spokesperson: J.-P. Chen, H. Gao (contact), X. Jiang, J.-C. Peng, and X. Qian.
- [292] E12-11-007, “Asymmetries in Semi-Inclusive Deep-Inelastic ( $e, e'\pi^\pm$ ) Reactions on a Longitudinally Polarized  $^3\text{He}$  Target at 8.8 and 11 GeV”, Spokesperson: J.-P. Chen, J. Huang (contact), Y. Qiang, and W.-B. Yan.
- [293] E12-11-108 “Target Single Spin Asymmetry in Semi-Inclusive Deep-Inelastic ( $e, e'\pi^\pm$ ) on a Transversely Polarized Proton Target”, Spokespersons: K. Allada, J.-P. Chen, H. Gao (contact), Z.-E. Meziani, and X.-M. Li.
- [294] S. Martoiu, H. Muller and J. Toledo, Conference Proceedings: 2011 IEEE Nuclear Science Symposium Conference Record, 2036 (2011).
- [295] M.J. French *et al.*, Nucl. Instr. and Meth. A **466** 359 (2001).
- [296] A. Neiser *et al.*, Journal of Instrumentation **8**, C12043 (2013).



- [297] E12-12-006, “Near-threshold Electroproduction of  $J/\psi$  with a 11 GeV Beam”, Spokespersons: K. Hafidi, Z.-E. Meziani (contact), X. Qian, N. Sparveris, and Z.-W. Zhao.
- [298] *The FLUKA code: Description and benchmarking* G. Battistoni, S. Muraro, P.R. Sala, F. Cerutti, A. Ferrari, S. Roesler, A. Fassio, J. Ranft, Proceedings of the Hadronic Shower Simulation Workshop 2006, Fermilab 6–8 September 2006, M. Albrow, R. Raja eds., AIP Conference Proceeding 896, 31-49, (2007)
- [299] *FLUKA: a multi-particle transport code* A. Ferrari, P.R. Sala, A. Fassio, and J. Ranft, CERN-2005-10 (2005), INFN/TC\_05/11, SLAC-R-773
- [300] *Photodisintegration of deuterium and big bang nucleosynthesis* K.Y. Hare and others, *Phys. Rev. D* **68**, 072001 (2003)
- [301] *Displacement damage in silicon, on-line compilation* A. Vasilescu and G. Lindstroem available at [http://hepweb03.phys.sinica.edu.tw/opto/Irradiation/Documents/NIEL\\_scaling/gunnar.htm](http://hepweb03.phys.sinica.edu.tw/opto/Irradiation/Documents/NIEL_scaling/gunnar.htm)
- [302] [https://solid.jlab.org/DocDB/0000/000025/001/zana\\_solid\\_radiation\\_and\\_activation\\_mar\\_2017.pdf](https://solid.jlab.org/DocDB/0000/000025/001/zana_solid_radiation_and_activation_mar_2017.pdf)
- [303] K. Abe *et al.* [SLD Collaboration], *Phys. Rev. Lett.* **84**, 5945 (2000) [arXiv:hep-ex/0004026].
- [304] N. Falletto *et al.*, “Compton scattering off polarized electrons with a high finesse Fabry-Perot cavity at JLab,” *Nucl. Instrum. Meth.*, **A459**, 212-425, 2001.
- [305] A. Narayan, D. Dutta, V. Tvaskis and J. W. Martin, *Nuovo Cim. C* **035N04**, 134 (2012).
- [306] N. Vansteenkiste, P. Vignolo, and A. Aspect, “Optical Reversibility Theorems for Polarization: Application to Remote Control of Polarization”, *J. Opt. Soc. Am. A*, Vol. 10, No. 10, (1993) 2240.
- [307] R.J. Loewen, “A compact light source: Design and technical feasibility study of a laser-electron storage ring X-ray source,” SLAC-R-0632 (2003).
- [308] S. Miyoshi *et al.*, Photon generation by laser-Compton scattering at the KEK-ATF, *NIM A* **623** (2010) 576.
- [309] A. Variola *et al.*, The LAL Compton Program,, *NIM A* **608** (2009) S83.
- [310] V. Brisson *et al.*, High finesse Fabry-Perot cavities in the picosecond regime, *NIM A* **608** (2009) S75.
- [311] A. Denner and S. Dittmaier, “Complete  $\mathcal{O}(\alpha_s^2)$  QED corrections to polarized Compton scattering”, *Nucl. Phys. B* **540** 58 (1999).
- [312] M. Friend *et al.*, “Upgraded photon calorimeter with integrating readout for Hall A Compton Polarimeter at Jefferson Lab”, [arXiv:1108.3116 [physics.ins-det]].
- [313] G. W. Ford and C. J. Mullin, “Scattering of Polarized Dirac Particles on Electrons,” *Phys. Rev.* **108**, 477 (1957); Erratum, *Phys. Rev.* **110**, 1485(E) (1958).
- [314] A. M. Bincer, “Scattering of Longitudinally Polarized Fermions,” *Phys. Rev.* **107**, 1434 (1957).

- [315] P. Stehle, “Calculation of Electron-Electron Scattering,” *Phys. Rev.* **110**, 1458 (1958).
- [316] A. Raćzka and R. Raćzka, “Møller Scattering of Arbitrarily Polarized Electrons,” Erratum, *Phys. Rev.* **110**, 1469 (1958).
- [317] G. Alexander and I. Cohen, “Møller scattering polarimetry for high-energy  $e^+e^-$  linear colliders,” *Nucl. Instrum. Meth. A* **486**, 552 (2002) [hep-ex/0006007]. This paper contains the basic formulas for Møller polarimetry, as well as references to calculations of higher order QED corrections.
- [318] M. Hauger *et al.*, “A high-precision polarimeter,” *Nucl. Instrum. Meth.*, vol. A462, pp. 382–392, 2001, nucl-ex/9910013.
- [319] Matthias Loppacher, “Møller Polarimetry for CEBAF Hall C”, Inaugural Dissertation, Universität Basel (1996).
- [320] L. V. de Bever, J. Jourdan, M. Loppacher, S. Robinson, I. Sick, J. Zhao, “A Target for Precise Møller Polarimetry”, *Nucl. Instrum. Meth. A* **400**, 379 (1997).
- [321] A. V. Glamazdin, V. G. Gorbenko, L. G. Levchuk, R. I. Pomatsalyuk, A. L. Rubashkin, P. V. Sorokin, D. S. Dale and B. Doyle *et al.*, “Electron beam Møller polarimeter at JLab Hall A,” *Fizika B* **8**, 91 (1999) [hep-ex/9912063].
- [322] E. A. Chudakov, A. V. Glamazdin, V. G. Gorbenko, L. G. Levchuk, R. I. Pomatsalyuk, P. V. Sorokin, “Electron beam Møller polarimeter at Hall A, JLab”, *Prob.Atom.Sci.Tech.* **40**, 43 (2002)
- [323] E. Chudakov and V. Luppov, “Møller polarimetry with atomic hydrogen targets,” *IEEE Trans. Nucl. Sci.*, vol. 51, pp. 1533–1540, 2004.
- [324] E. Chudakov and V. Luppov, “Moeller polarimetry with atomic hydrogen targets,” *Eur. Phys. J.*, vol. A24S2, pp. 123–126, 2005.
- [325] P. S. Cooper, M. J. Alguard, R. D. Ehrlich, V. W. Hughes, H. Kobayakawa, J. S. Ladish, M. S. Lubell and N. Sasao *et al.*, “Polarized electron Electron Scattering at GeV Energies,” *Phys. Rev. Lett.* **34**, 1589 (1975).
- [326] B. Wagner, H. G. Andresen, K. H. Steffens, W. Hartmann, W. Heil and E. Reichert, “A Møller polarimeter for CW and pulsed intermediate-energy electron beams,” *Nucl. Instrum. Meth. A* **294**, 541 (1990).
- [327] J. Arrington, E. J. Beise, B. W. Filippone, T. G. O’Neill, W. R. Dodge, G. W. Dodson, K. A. Dow and J. D. Zumbro, “A Variable energy Møller polarimeter at the MIT Bates Linear Accelerator Center,” *Nucl. Instrum. Meth. A* **311**, 39 (1992).
- [328] K. B. Beard, R. Madey, W. M. Zhang, D. M. Manley, B. D. Anderson, A. R. Baldwin, J. M. Cameron and C. C. Chang *et al.*, “Measurement of the polarization of a pulsed electron beam with a Møller polarimeter in the coincidence mode,” *Nucl. Instrum. Meth. A* **361**, 46 (1995).
- [329] H. R. Band, G. Mitchell, R. Prepost and T. Wright, “A Møller polarimeter for high-energy electron beams,” *Nucl. Instrum. Meth. A* **400**, 24 (1997).

- [330] P. Steiner, A. Feltham, I. Sick, M. Zeier and B. Zihlmann, “A high-rate coincidence Moller polarimeter,” *Nucl. Instrum. Meth. A* **419**, 105 (1998).
- [331] G. G. Scott and H. W. Sturmer, “Magnetomechanical Ratios for Fe-Co Alloys,” *Phys. Rev.* **184**, 490 (1969).
- [332] J. Crangle and G. M. Goodman, “The Magnetization of Pure Iron and Nickel,” *Proceedings of the Royal Society of London, Series A*, **321**, 477 (1971).
- [333] C. D. Graham, Jr., “Iron and Nickel as Magnetization Standards,” *J. Appl. Phys.* **53**, 2032 (1982).
- [334] G. G. Scott, “Review of gyromagnetic ratio experiments,” *Rev. Mod. Phys.*, vol. 34, pp. 102–109, Jan 1962.
- [335] E. C. Stoner and E. P. Wohlfarth, “A Mechanism of Magnetic Hysteresis in Heterogeneous Alloys,” *Phil. Trans. Royal Soc. London, Series A* **240**, 599 (1948).
- [336] L. G. Levchuk, “The Intraatomic motion of bound electrons as a possible source of a systematic error in electron beam polarization measurements by means of a Møller polarimeter,” *Nucl. Instrum. Meth.*, vol. A345, pp. 496–499, 1994.
- [337] M. Swartz, H. R. Band, F. J. Decker, P. Emma, M. J. Fero, R. Frey, R. King and A. Lath *et al.*, “Observation of target electron momentum effects in single arm Møller polarimetry,” *Nucl. Instrum. Meth. A* **363**, 526 (1995) [hep-ex/9412006].
- [338] D. Gaskell, D. G. Meekins, and C. Yan, “New methods for precision Møller polarimetry,” *Eur. Phys. J.*, vol. A32, pp. 561–564, 2007.
- [339] E. Chudakov and V. Luppov, “Møller polarimetry with atomic hydrogen targets,” tech. rep., JLab, 2005. [http://www.jlab.org/~gen/hyd/loi\\_3.pdf](http://www.jlab.org/~gen/hyd/loi_3.pdf).
- [340] I. F. Silvera, “Ultimate fate of a gas of atomic hydrogen in a liquid-helium chamber: Recombination and burial,” *Phys. Rev. B*, vol. 29, pp. 3899–3904, Apr 1984.
- [341] I. F. Silvera and J. T. M. Walraven, “Stabilization of atomic hydrogen at low temperature,” *Phys. Rev. Lett.*, vol. 44, pp. 164–168, Jan 1980.
- [342] I. F. Silvera and J. T. M. Walraven, “Spin polarized atomic hydrogen,” *Progress in Low Temperature Physics*, vol. X, pp. 139–370, 1986.
- [343] T. Roser *et al.*, “Microwave driven extraction of stabilized spin polarized atomic hydrogen,” *Nucl. Instrum. Meth.*, vol. A301, pp. 42–46, 1991.
- [344] M. Mertig, V. G. Luppov, T. Roser, and B. Vuaridel, “Continuous density measurement of atomic hydrogen by means of a bolometer,” *Rev. Sci. Instrum.*, vol. 62, pp. 251–252, 1991.
- [345] M. D. Miller and L. H. Nosanow, “Possible ”new” quantum systems. ii. properties of the isotopes of spin-aligned hydrogen,” *Phys. Rev. B*, vol. 15, pp. 4376–4385, May 1977.
- [346] M. Poelker, J. Grames, J. Hansknecht, R. Kazimi, J. Musson, *Phys. Rev. ST Accel. Beams* **10**, 053502 (2007).

- [347] [https://hallaweb.jlab.org/12GeV/SoLID/download/doc/Estimated\\_SoLID\\_Offline\\_Effort.ods](https://hallaweb.jlab.org/12GeV/SoLID/download/doc/Estimated_SoLID_Offline_Effort.ods)
- [348] <https://halldsvn.jlab.org/repos/trunk/docs/offline/ProjectProgress/OfflineComputingActivities2013.xlsx>
- [349] EventDisplay3D project in the *art* workbook, available from <https://cdcvs.fnal.gov/redmine/projects/art-workbook>

## Appendix A Summary of Recommendations from the 2015 SoLID Director’s Review and the Responses With Notes Where They Are Addressed

The SoLID Director’s Review was held at JLab on 23-24 February 2015. The committee consisted of: Paul Brindza (JLab), Marcel Demarteau (ANL), Nancy Grossman (ANL), David Mack (JLab), Richard Majka (Yale), Naomi Makins (UIUC), Curtis Meyer (CMU)(chair), Ernest Sichtermann (LBL), William Wisniewski (SLAC) and Bolek Wyslouch (MIT).

A summary of all recommendations made by the committee is provided below, with each recommendation ordered by number to improve readability. We also note briefly below each recommendation what has been done and where it is addressed in the text.”

### A.1 On the physics relevance and risks

**On the completeness and credibility of the discussion of the experimental reach, including statistical, systematic and theoretical uncertainties**

**Recommendation 1: End-to-end simulations with realistic subsystem responses and material budgets, and complete track finding and reconstruction should be developed.**

The simulations of all SoLID subsystems are unified in the GEANT4 based simulation framework, GEMC, with realistic setup and simple responses for all detectors. Digitization for GEM and tracking with field effects are conducted after simulation. (in Section 12)

**Recommendation 2: Acceptances, efficiencies, and systematic uncertainties should be simulated for each of the core measurements.**

Acceptances, efficiencies, and systematic uncertainties for each of the core measurements have been performed with the aforementioned simulation (Section 13).

**Recommendation 3: For the PVDIS measurements, the viability of the elastic scattering calibration procedure, to determine absolute  $Q^2$  should be demonstrated by simulations for similar scattering angles to those probed in DIS, and with realistic misalignments.**

A study was performed with simulation which demonstrated that absolute  $Q^2$  can be determined to the required precision with elastic scattering calibration assuming realistic misalignments (Section 13.3).

**Recommendation 4: Bin migration effects should be simulated for the measurements of the sharply rising  $J/\psi$  production cross section near threshold.**

Bin migration effects were simulated combining radiative effects and track resolution (Section 13.4).

**On the ability to handle the desired luminosities and backgrounds including impacts on both the apparatus and the beam line downstream of the target**

**Recommendation 5: The signal and background trigger rates should be simulated for the  $J/\psi$  measurements.**

We have performed a simulation for both signal and background trigger rates for  $J/\psi$  using the full SoLID simulation similar to what we did for PVDIS and SIDIS. (Section 14).

**Recommendation 6: The dead-time(s) in the DAQ chain should be modeled.**

We have continued to develop the deadtime analysis in the context of experimental impact and verification is ongoing based on experience with the hardware modules (Section 14).

**Recommendation 7: The development of a simulation framework with realistic reconstruction and analysis should be pursued with high priority and increased resources.**

The development of a full simulation package with realistic reconstruction and analysis has continued to be a high priority and focus for the collaboration. We have been progressing to develop a full end-to-end simulation of all SoLID experiments and have been soliciting increased resources to fully realize this. (Section 12).

**On the implications for the relevance of the physics results in the context of possibly competing experiments at both Jefferson Lab and internationally.**

**Recommendation 8: Better comparisons with the expected results on programs such as SBS and particularly CLAS12 are needed to clarify the need for the SoLID SIDIS program. Crisp demonstrations of the improvements possible with SoLID should be developed.**

With the help of theory group, a new method was developed to properly evaluate the impact of future SIDIS measurements on TMDs. Comparisons of SoLID projections with SBS and CLAS12 were performed, which demonstrated significant improvement of SoLID over SBS and CLAS12. (Section 2.2.6)

**Recommendation 9: The SoLID Collaboration should investigate the possibility of kaon identification, especially given their high luminosity.**

We have explored different options for kaon identification, and are pursuing the path of upgrading the MRPC time of flight to reach resolution of 20ps. R&D on the MRPC upgrade is underway. (Section 2.5.2 and 11.8).

**Recommendation 10: The SoLID collaboration should investigate the feasibility of carrying out a competitive GPD program. Such a program would seem particularly well suited to their open geometry and high luminosity. If SoLID's luminosity is sufficiently high to permit a program of precise Double Deeply Virtual Compton Scattering (DDVCS) measurements, it would make a groundbreaking contribution to GPD studies.**

A GPD program has been initiated, including an approved timelike Compton scattering proposal, a proposed deep exclusive meson production proposal presently under review, a letter of intent for DDVCS, and a polarized DVCS measurement under study. (Section 2.5.1).

## **A.2 On the viability of approach and the experimental technique**

**On any R&D required to meet the technical challenges of the experiment**

**Recommendation 11: Develop an overall R&D plan for the project with a timeline.**

We have developed a pre-R&D plan which was submitted to the DOE medium energy nuclear physics program manager in Summer 2016, which received feedback with encouragement. The full R&D plan and project timeline is under development. (Section 20).

**Recommendation 12: Close interaction between the US and Chinese groups in the development of GEM foils to assure good quality control is highly recommended.**

We have continued to work closely with the Chinese groups for GEM foil production through regular meetings and discussions, as well as hosting visiting Chinese researchers at the UVA GEM laboratory. Plans have been developed to ensure produced GEM quality at multiple levels including by sample inspection by the UVA and Temple groups. (Section 7).

**Recommendation 13: Investigate the schedule risk when GEM foils are not produced in a timely way and continue to pursue Tech-Etch as a potential supplier for the foils.**

We have contacted Tech-Etch as a potential backup option and they have indicated they would be able to commit the resources to produce a large order of GEMs in such an event. The CERN workshop also presents an option with the capability to be able to fulfill a large order of necessary GEMs. (Section 7).

**Recommendation 14: The calorimeter group is encouraged to contact other groups (ALICE, LHCb SiPMs and possibly CMS) to understand the detector design choices these groups have made and resources needed for construction.**

Beyond the initial LHCb contact at the beginning of R&D, the calorimeter group has been in contact with the University of Iowa CMS group and Central China Normal University group which assembled modules for the ALICE experiment. We have also acquired relevant technical documents from LHCb and other CERN experiments which have been beneficial in detailing design choices. The design was refined, prototyping modules were constructed by two newly joined groups (Shandong University and Tsinghua University from China) and cosmic and beam tests are ongoing. (Section 10)

**Recommendation 15: The stability tests of the conductivity of the glass for the MRPCs should be extended for a much longer period and the risk associated with the R&D needs to be identified.**

Conductivities of the glass were tested for extended period with large radiation dose of neutron and xray, showed no aging or stability issues. (Section 11).

**Recommendation 16: The collaboration is strongly encouraged to develop an end-to-end realistic simulation and reconstruction to further optimize cost and physics reach and derive clear performance requirements for the individual subdetectors.**

All subsystems simulations have been unified into the same simulation framework with simple reconstruction. We have continued to iterate the designs within the simulation, especially as more engineering resources have become available. For example, studies evolving the detector layouts are being performed as internal mounting and field constraint specifications are developed. (Section 12).

**Recommendation 17: The collaboration is encouraged to explore the power of extended kaon identification (through Cherenkov or TOF).**

The collaboration has identified that the MRPC time of flight option for kaon identification will be the most promising approach. We have initiated R&D on the 20ps MRPC upgrade. (Section 2.5.2 and 11.8).

**On the proposed magnet concept and choice, including magnet configuration modifications (if any), magnet cool-down and infrastructure requirements**

**Recommendation 18: The Committee strongly recommends testing the CLEO magnet coils (cold test), power supply and controls, before installation in Hall A.**

A cold test is planned at reduced operating parameters by Jefferson Lab engineering which will be carried out prior to installation in Hall A. (Section 4.4).

**Recommendation 19: A new magnet power supply should be included in the total cost of SoLID.**

The collaboration is planning for a new power supply for the solenoid and has now included the cost in the budget. (Section 4.4).

**Recommendation 20: Evaluate the schedule impact of mapping the magnetic field in situ in Hall A.**

Field mapping and analysis has been estimated by Jefferson Lab engineering and estimates of necessary workforce and cost have also been evaluated and included. (Section 4.4).

**On the proposed detector concept and associated electronics and data acquisition**

**Recommendation 21: The plans for the High Level Trigger and the needs for slow control need to be worked out in detail and the implications for resources need to be evaluated.**

Development of the hardware trigger in particular for the complicated SIDIS trigger has continued and further details are included. (Section 14)

Slow controls have now been integrated into the experiment design and budget and a responsible subsystem coordinator has been assigned. (Section 16).

**Recommendation 22: The implications of the need for these resources in the context of availability of resources at the laboratory need to be understood.**

Consideration of further details of lab resources are presented in Section 14 and Appendix C. The collaboration has been in active communication with the JLab computing center about the needs for SoLID including data volumes and analysis.

**Recommendation 23: Closer communication with the other JLab experiments and the JLab computing center is strongly encouraged.**

We have closer communication with other JLab groups and the computing center. Software and computing resource needs have been further evaluated, especially related to larger JLab 12 GeV projects. (Section 12.1 and Appendix C).

**Recommendation 24: Having a functional simulation and reconstruction routines as soon as possible should be a high priority in the software effort. Such software will pay off many times over in experimental design and avoiding pitfalls.**

Development of the simulation and using that to develop and test reconstruction algorithms has been a high priority of the collaboration. We have had postdocs and students dedicated to these efforts and have been requesting further resources to meet short term goals. (Section 12).

#### **On the beam line design, including collimation and shielding**

**Recommendation 25: Complete radiation calculations to determine activation and absorbed dose on components of concern and mitigate as appropriate.**

We have completed initial radiation calculations for all the experiments in Geant4 as well neutron dose and activation studies in FLUKA. These continue to be iterated as design details become available. (Section 15).

**Recommendation 26: It should be confirmed that the baffle design, including the support structure, is optimized for background rejection and signal acceptance. Furthermore the baffle design should minimize generation of secondary backgrounds.**

Optimization studies and baffle refinement have been completed with material, acceptance, background, and secondary production in the figure of merit. Detailed evaluation of baffle supports are ongoing with engineering. (Section 6).

#### **On the cryogenic and polarized target system concepts and integration**

No recommendation was presented in the report.

#### **On the beam polarimetry requirements.**

No recommendation was presented in the report.

### **A.3 On the understanding, completeness, and credibility of the resources needed for the SoLID project.**

#### **On the experience, expertise and quantity of the scientific and technical manpower for the project**

**Recommendation 27: Compare the resource levels you have assumed in some key areas (particularly in software, data acquisition and project management) to make sure the estimates align with other similar projects or there is a good reason they do not.**



Further details in required software resources based on other large scale experiments at Jefferson Lab and outside of the lab have been considered. Communicating with JLab fast electronics, DAQ and IT groups to have a better estimation of resource level for DAQ. (Section 14 and Appendix C).

**Recommendation 28: Redo the cost estimate using an average cost per type of resource.**

A new full cost estimate is anticipated to be performed after a DOE science review.

**Recommendation 29: Create a high level resource loaded schedule to get a more realistic schedule, funding and resource profile. This will also allow JLab to better determine their ability to support the FTE needs.**

A high level resource loaded schedule is anticipated to be performed after a DOE science review.

**Recommendation 30: Revisit the comments of the 2012 Internal Review Report in conjunction with the recommendations from this report.**

We revisited those comments and they are addressed in multiple sections of this document.

**On utilities (power, cabling, LCW, cryogenics) requirements for the project**

**Recommendation 31: A cost benefit analysis for any systems being reused should be carried out, including the magnet power supply.**

A cost-benefit analysis was performed and the only reused components will be the iron yoke and cryostat. Cost for a new power supply, controls, transfer lines, and supports have been included in the budget. (Section 4.4).

**Recommendation 32: Appoint a small team to facilitate the integration planning for SoLID.**

Integration has been a consideration in the development of the subsystems. A full team will be assigned after a DOE science review.

**On requirements from Jefferson Lab on for instance engineering needs, electron beam, polarized source, and cryogenic target requirements**

**Recommendation 33: We strongly recommend tests at JLab of the CLEOII magnet coils (cold test), ideally with the new power supply and controls, before installation into the hall.**

A cold test is planned at reduced operating parameters by Jefferson Lab engineering which will be carried out prior to installation in Hall A. (Section 4.4).

**Recommendation 34: An effort should be made to clearly specify resources required from JLab that are not explicitly in the project (effort, non-effort, equipment, building space, etc.).**

Many of these resources have been identified and it is an ongoing process within the collaboration. (Section 4.4 and 19).

**On general experiment installation and alignment issues, including potential interaction with other Hall A programs and operations**

**Recommendation 35: The project should develop a preliminary resource loaded schedule for the installation and the corresponding space-management plan for the hall floor.**

A preliminary plan has been outlined for installation of the magnet and major subsystems. (Section 19).

**Recommendation 36: The project should start planning the process of how to change from one SoLID configuration to another in order to better understand the time and effort involved and if there are any potential issues such as radiation levels.**

Based on the initial radiation studies, a preliminary plan is made and details will continue to be refined. (Section 15 and 19).

## Appendix B Summary of Subsystems

In responding to the recommendations from JLab physics division, we add this section, aiming to provide a brief description of the key assumptions for each subsystem, namely where the subsystem will be built, which groups will build it, where the fund comes from, how long it will take and what is needed from JLab to support it. Anything unique to the system which drives the project will also be listed.

### B.1 Magnet

The solenoid magnet provides the magnetic field required for measuring the momentum of the track in the experiment. The detectors for SoLID will be mounted on the magnet yoke. The collaboration has identified the CLEO-II magnet as the one to be used for SoLID after modifications. The JLab Hall A engineering team, with assistance from JLab Engineering Division and also from the SoLID collaboration, is responsible for the transportation and modification of the magnet.

The coils and cryostat of the magnet have arrived at JLab and the exterior steel is being shipped. The transportation (disassembling and shipping) the magnet from Cornell to JLab and initial refurbishing to verify the magnet is in good state for specific modifications for physics experiments is covered from the JLab Physics Division (operation fund). The cost for refurbishing and modifications specific to SoLID is to be part of the SoLID MIE to DOE.

The refurbishing and modification specific to SoLID will take 2.5 years. JLab will perform most of the work. Space will be needed at JLab for refurbishing, modification and storage. We will also need JLab support for the cryogenic and control systems.

### B.2 GEM

- **Where the system will be built and who will build it:** It is assumed that the SoLID GEM tracker will be built in China by the five member institutions of the Chinese SoLID GEM collaboration: CIAE, LZU, THU, USTC and IMP. The GEM module development, design prototyping and benchmarking would be done in collaboration with the GEM detector groups at the University of Virginia (Liyanage) and Temple University (Surrow). The GEM module and Electronics fabrication activities would be divided among the Chinese collaboration as follows:

- USTC: The main institution for GEM module fabrication, readout electronics development and fabrication.
- CIAE: GEM foil fabrication and GEM module fabrication.
- LZU: GEM module fabrication
- THU and IMP: GEM module fabrication and testing.

- **Who will fund it ?**

The funding for the SoLID GEM tracker will be sought from the Chinese funding agencies. Only the pre R&D funds and R&D funds (of the order of \$ 400 k) for the activities conducted at the University of Virginia and Temple University will be requested from the US DoE.

- **How long will it take ?**

The pre-R&D phase of the project would take at least 2 years. This would be especially true if the GEM foils fabricated in China are to be used for the project as assumed. A well focused

and intense pre-R&D program in China is required to ensure that the manufacturing capabilities and capacities for full size GEM foils, and that GEM module assembly facilities setup and several full size prototype module constructed and tested at each of the five institutions.

After the successful conclusion of the pre-R&D program, it would take at least two more years for the R&D, construction, testing, installation and the commissioning phase.

- **what is needed from JLab to support it ?**

Jlab engineering support will be needed for the design of the GEM module mounting structure, and DAQ support will be needed to integrate the GEM readout into the hall A DAQ framework.

### **B.3 Light Gas Cherenkov**

The light gas Cherenkov prototyping and construction will be done by the Temple University Nuclear Physics Group. All of the construction will be done at Temple, with the possible exception of any specific materials needed to adapt and integrate the subsystem into the larger SoLID detector. Funds for the project will be requested by the group from DOE and/or NSF. The light gas Cherenkov detector will also be designed at Temple University with the expectation that communication with the SoLID project engineers at Jefferson Lab, as well as access to schematics and documentation, will be made available concerning interfacing the sub-detector design with the larger SoLID design.

### **B.4 Heavy Gas Cherenkov**

The Heavy Gas Cherenkov (HGC) will provide the required particle identification of pions in a background of kaons and protons. It will be built by Prof. Haiyan Gao's Medium Energy Physics group from Duke University with engineering and technical help from the Triangle Universities Nuclear Laboratory (TUNL), and by Prof. Garth Huber's group from the University of Regina in Canada.

### **B.5 Electromagnetic Calorimeter and Scintillator-Pad Detector**

The Electromagnetic Calorimeter (EC), in combination with other detectors, provides the main trigger and the particle identification for the SoLID experiments. The EC consists of a Preshower and a Shower portion. The technologies that we chose for the EC – WLS-fiber-embedded scintillator for the Preshower with MAPMT readout and the Shashlyk-type modules for the Shower with regular PMT readout – have both been used in experiments at the LHC. The main goal of the pre-R&D is thus to adopt such technology and to optimize the design configuration of the EC to meet the physics requirement of SoLID, and to determine the best construction institution/site.

The Scintillator Pad Detector (SPD) is needed only by the SIDIS program of SoLID. It consists of a forward- (FA) and a large-angle (LA) parts. Both FASPD and LASPD will serve as a photon veto in order to reduce the photon background to a manageable level. Design of the FASPD is very similar to the Preshower detector of the EC, with WLS fibers embedded in thin scintillators. The LASPD will also provide time-of-flight information and a 150-ps timing resolution is required. The LASPD will thus consists of thick scintillators with direct readout by field-resistant fine-mesh PMTs inside the solenoid.

The pre-R&D stage of EC and SPD will likely take up to two years. The lead institutions on the EC includes University of Virginia (UVa), and the Chinese Shandong University (SDU) and Tsinghua University (THU). The SDU group has extensive experience with scintillator manufacturing

in China, and have produced preshower modules with similar light yield as those produced by the Russian IHEP (the sole manufacturer of EC for nearly all LHC experiments). For Shashlyk modules, both THU and SDU groups have already constructed prototypes and are currently working on improving their light yield. The pre-R&D will focus on increasing the light yield, conducting beam tests to determine their PID performance, and to design an effective mass-quantity construction method.

The SPD will be manufactured by the US Eljen company and further constructed at UVa. Prototype modules have already been made and tested with cosmic rays and their light yield has been characterized. The pre-R&D goal will be to determine the light yield uniformity for the FASPD, and to determine the timing resolution of the LASPD under SoLID-like running conditions.

## B.6 MRPC

The Multi Gap Resistive Plate Chamber (MRPC) will be used by the SIDIS experiment for particle identification by means of time of flight. A MRPC can achieve a timing resolution of 50 ps. Under more realistic conditions with large background rates, timing resolution of 80 ps has been demonstrated.

- Who will build it :  
Tsinghua University
- Where the system will be built:  
In Tsinghua University, Beijing
- Rutgers university will take care of the readout electronics.
- Who will fund it :  
NSFC (China) for the detector; the front end electronics will be funded by the DOE, and also the NSF through Rutgers University.
- How long will it take :  
Two and half years
- What is needed from JLab to support it:  
Beam tests will be needed at JLab including electronics and DAQ system in order to test the detector and optimize it under realistic beam conditions. Since it is planned to include the MRPC in the trigger to reduce the background, a special board from JLab will be required to send the logic signals to the L1 trigger.
- Anything unique to that system that's a project driver : This is the first high rate TOF system in hadron physics experiments and is need for the particle identification.

## B.7 DAQ

The SoLID experiment is a large acceptance detector designed to run at high luminosities. The trigger rates expected for PVDIS are of the order of 600 KHz and for SIDIS up to 100 KHz. This pipelined electronics is crucial to generate a selective trigger in the very large background present in the detector.

- Where the system will be built and who will build :  
The Rutgers University with the group of Prof. Ronald Gilman group will be in charge of the high resolution timing measurement aspects of the development and production for the electronics and help in the testing of the Flash ADCs similar to what was done for Hall D.
- Who will fund it ?  
The electronics will be funded by the DOE request.
- How long it will take  
The project will take 2 years of preRD, 4 years of R%D, production and testing, and installation.
- What is needed from JLAB to support it  
Since SoLID will be using the Jefferson Laboratory Pipelined Electronics, the JLAB Fast electronics group will be largely involved in the development, tests and deployment of the electronics. An estimate of the electronics and DAQ group is summarized in the table in addition of the JLab physics staff person.

## Appendix C Software Development Effort Estimate

A preliminary assessment of the effort required to carry out all SoLID offline computing-related tasks, assuming adoption of the *art* framework [249] as an example, yields approximately 586 FTE-weeks. With contingency and overhead, explained below, this number increases to a total of 976 FTE-weeks, or about 22 FTE-years, assuming 44 work weeks per year per developer. A spreadsheet with this calculation can be found online [347].

This estimate covers simulations, reconstruction, calibrations and alignment, data challenges, production and analysis, where “analysis” represents a baseline set of replay configurations (PVDIS, SIDIS-<sup>3</sup>He, SIDIS-*p*, *J/ψ*), data quality checks, plots, production output variables, corrections, cuts and histograms. Not included in the estimate are DAQ software (firmware, front-end and trigger programming, run control etc.), online analysis and monitoring, and the intellectual effort to understand and interpret the results of the simulations and experimental data analysis. The latter is excluded because it is largely an open-ended creative process.

For each covered area, we have counted the work required to develop the actual software, test the code and validate results, coordinate efforts (meetings, wikis and similar), write and generate user and developer-level documentation, and to configure and monitor offline computing operations (simulation and production passes, data challenges). The time estimates at this point are subjective best guesses, based on our experience with similar efforts. They assume expert developers who are fully familiar with all task requirements, programming languages, framework paradigms, library APIs, tools etc. This yields a sum of 586 FTE-weeks. A contingency of 25% is added to this total to account for missed tasks, time overruns, etc. Furthermore, since developers are never the ideal experts assumed above, we estimated an average “developer efficiency” of 75%, *i.e.* on average each developer is assumed to spend an extra 1/3 of the estimated task time on preparations such as collecting requirements and learning. A more precise estimate of this efficiency factor would have to be made on a task-by-task basis under consideration of the personnel assigned to the task, information which is incomplete at this time. With contingency and overhead, the total effort estimate is 976 FTE-weeks.

In comparison to a similar project, GlueX have estimated their offline computing effort at 1866 FTE-weeks [348]. (This number excludes 110 FTE-weeks that GlueX allocate for “online” tasks (beamline commissioning and monitoring), which is outside of our scope.) It is unclear if the GlueX numbers include developer overhead, *i.e.* the time spent on task preparations and learning discussed above, but given the generous allowances made generally, we assume that they do.

The offline computing manpower requirements estimated by GlueX and SoLID are summarized in Table 35. To make the GlueX estimates comparable to ours, we combined certain line items of the GlueX offline computing effort document [348] as follows:

- The quoted “Simulation” effort includes “Geant3 simulation”, “Geant4 simulation” plus 1/4 of “Integration/QC” and “Coordination” (total of 16.5 FTE-weeks) from the Miscellaneous section.
- “Reconstruction” counts all of “Reconstruction” plus “DAQ Translation”, “Event Viewer”, “Documentation”, “Integration of Slow Controls”, 1/2 of “Recon/analysis code Q/A” and again 16.5 FTE-weeks for integration and coordination.
- “Calibration” is taken as the total of “Calibrations” plus 1/4 of “Integration/QC” (11 FTE-weeks).
- “Production” comprises “DST Generation”, “MC Studies for Detector Optimization” and again 11 FTE-weeks of “Integration/QC”.

- “Analysis” takes all of “Analysis” less 1/2 of “Recon/analysis code Q/A” already counted under “Reconstruction” plus 1/2 of “Coordination”.
- The “Data Challenges” estimate is taken as is.

These allocations make the top-level categories approximately comparable.

Task Group	Labor estimate (FTE-weeks)		Main reasons for difference (see text)
	GlueX [348]	SoLID [347]	
Simulation	192	240	Simulation to be integrated into framework.
Reconstruction	787	355	Adoption of existing framework. Re-use of algorithms. Smaller number of subsystems.
Calibration	275	103	Smaller number of subsystems.
Production	275	155	Standard data format. Re-use of workflow tools.
Analysis	275	100	No PWA analysis and no grid implementation of analysis.
Data Challenges	62	23	No PWA data challenge.
Totals	1866	976	

Table 35: Offline computing manpower requirements estimated by SoLID and GlueX

SoLID estimates a larger simulation effort than GlueX, possibly because GlueX make approximate estimates of time already spent on finished work, while SoLID is using a detailed breakdown of anticipated future tasks. Also, SoLID plans to integrate simulations into the overall software framework, while GlueX’s simulations are standalone.

The estimated SoLID effort for reconstruction is significantly lower than GlueX’s. The difference is to a great extent due to the fact that SoLID proposes to adopt an existing framework rather than write a new one and that SoLID anticipates to reuse well-tested existing algorithms for standard tasks such as track fitting, *e.g.* from the `genfit` library, and calorimeter cluster reconstruction. Documentation effort is reduced in SoLID’s case also due to the already very good user-level documentation of the proposed *art* framework. Furthermore, the difference can be attributed to the smaller number of detector subsystems in SoLID than in GlueX, 5 vs. 7, the lower complexity of these systems (one vs. two tracker systems, Cherenkovs vs. multiple calorimeter systems), and the more challenging multi-particle final state reconstruction and PID in GlueX. Lastly, a SoLID event viewer can be readily assembled from an existing MC geometry with minimal effort (days vs. months) using ROOT’s `TEve` framework within *art*, as demonstrated by *art* example code [349].

Calibration effort for SoLID is also estimated lower than in GlueX, again in part due to fewer main detector systems, smaller channel counts and easier calibration of SoLID’s GEMs vs. GlueX’s drift chambers.

The lower estimated time for Production (DST generation) is attributable to the fact that we do not anticipate spending time on developing and maintaining a custom file format (it is defined by *art*) and expect to be able to reuse the job control and workflow tools currently under development for GlueX and CLAS12.

Finally, SoLID estimates much lower analysis effort than GlueX because no kinematic fitting and PWA analysis is foreseen for SoLID nor is SoLID planning a grid implementation at this point as the JLab compute farm resources are expected to be sufficient for us. For similar reasons, our estimate for data challenges is lower.